UNIVERSITÀ DEGLI STUDI DI SALERNO

UNIVERSITÀ DEGLI STUDI DI SALERNO
Dipartimento di Farmacia

PhD Program
in **Drug Discovery and Development**
XXXVIII Cycle

PhD Thesis in

Isolation, analytical and biochemical characterization of nutraceuticals from traditional and novel foods

Candidate

Dott.ssa *Maria Rosaria Miranda*

Supervisor

Chiar.mo Prof. *Giacomo Pepe*

Co-tutor

Chiar.mo Prof. *Luca Rastrelli*

Coordinator: Chiar.ma Prof.ssa *Alessandra Tosco*

Index

4. Chapter IV: *Allium cepa* L. (Cipollotto Nocerino) leaves extract

Index

6. Chapter VI: Conclusions

1. Chapter I: Research project presentation

1.1 Abstract

In recent decades, growing scientific attention has focused on the role of food-derived bioactive compounds in maintaining health and preventing disease. Beyond their nutritional value, many natural food components exert specific biological activities that modulate key molecular pathways involved in chronic disorders.

These compounds, defined as nutraceuticals, represent a bridge between nutrition and pharmacology, as they combine dietary origin with measurable therapeutic potential.

This evolving perspective has shifted research interest toward the identification and characterization of novel nutraceuticals, particularly those derived from biodiversity-rich environments such as the Mediterranean basin.

The Mediterranean area, recognized as one of the world's most important biodiversity hotspots, represents an exceptional reservoir of structurally diverse bioactive molecules, derived predominantly from plants and traditional agri-food products that reflect the region's rich agricultural heritage.

The preservation and scientific valorization of this biodiversity are therefore essential not only from an ecological standpoint, but also as a strategic approach to discovering innovative health-promoting compounds.

Unlike conventional pharmacological therapies, which often act on single molecular targets and may cause adverse effects, nutraceuticals generally exert multi-targeted actions with a favorable safety profile. Their regular inclusion in the diet represents a proactive and sustainable preventive strategy, and growing evidence supports their role not only in disease prevention but also in modulating disease progression.

Chronic disorders, including cancer, intestinal inflammatory diseases (IBD), metabolic and hepatic dysfunctions, neurodegenerative conditions, and ultraviolet (UV)-induced skin damage, share complex and interconnected pathogenic

mechanisms. These include oxidative stress, endoplasmic reticulum (ER) stress, mitochondrial dysfunction, altered redox homeostasis, and impaired cellular signaling pathways. The multifactorial nature of these conditions often limits the effectiveness of single-target therapies, highlighting the need for multifunctional bioactive compounds capable of modulating multiple pathways simultaneously.

Based on these premises, the present doctoral project aims to isolate, characterize, and biologically evaluate new phytocomplexes derived from traditional Mediterranean products and novel food sources. Through integrated *in vitro* and i*n vivo* experimental models, this research seeks to elucidate the biochemical mechanisms underlying their protective and modulatory effects.

The ultimate objective is to contribute to the development of innovative nutraceutical strategies that support disease prevention and health promotion through a biodiversity-driven and mechanistically grounded approach.

1.2 Introduction

The concept of biodiversity refers to the variety and variability of living organisms at the genetic, species, and ecosystem levels. Beyond its ecological relevance, biodiversity represents a strategic reservoir of natural resources with significant implications for human health.

Italy, and more broadly the Mediterranean area, is one of the regions with the highest biological richness worldwide, characterized by a remarkable degree of endemism and extraordinary floristic diversity. This richness is closely linked to the climatic, geological, and morphological heterogeneity of the territory.

However, agro-industrial development has progressively promoted production models based on genetic uniformity and crop standardization, leading to a gradual erosion of agricultural biodiversity. Such impoverishment is not only an environmental concern but may also affect the nutritional and functional quality of food products (Wilson, 1992; Hofman *et al.*, 2025; Mattas *et al.*, 2023).

In recent decades, increasing attention has been devoted to the idea that the value of food extends beyond its caloric and macronutrient content to include a functional component associated with bioactive compounds (Galland, 2010).

Within this framework, nutraceutical science has emerged as a discipline investigating natural substances that possess both nutritional and pharmacological properties, positioning itself at the interface between food and medicine (Georgiou *et al.*, 2011).

Nutraceuticals are multifunctional molecules, mainly derived from plant matrices, capable of modulating multiple biological pathways and contributing to the maintenance of cellular homeostasis.

Their lies relevance in the possibility of adopting a proactive approach to health, acting before the clinical onset of disease (Santini *et al.*, 2017).

Chronic disorders such as atherosclerosis, diabetes, hepatic steatosis, inflammatory bowel diseases, cancer, and neurodegenerative conditions are often characterized by a subclinical phase dominated by chronic inflammation and oxidative stress, which precedes overt organ damage (Ferro *et al.*, 2022; Chiu *et al.*, 2020; Larussa *et al.*, 2017). These pathophysiological mechanisms are also central in models of damage induced by environmental factors.

In particular, exposure to UV radiation represents a paradigm of chronic injury characterized by increased production of reactive oxygen species, alterations in inflammatory responses, and cellular dysfunction. The convergence of these processes on common molecular pathways, including redox imbalance, activation of pro-inflammatory signaling, and cellular stress responses, highlights how apparently distinct conditions share similar biological bases (Ferro *et al.*, 2022; Wei *et al.*, 2024).

The central role of chronic inflammation and oxidative stress in major degenerative diseases has directed research toward the identification of natural compounds capable of modulating these processes (Nasri *et al.*, 2014).

A growing body of evidence demonstrates that bioactive molecules present in plant matrices, including polyphenols, phytosterols, terpenes, and bioactive peptides, exert antioxidant and anti-inflammatory activities and may contribute to disease prevention and modulation of pathological progression through the regulation of molecular pathways involved in oxidative damage and cellular stress (Basilicata *et al.*, 2019; Vestuto *et al.*, 2022; Arshad *et al.*, 2025).

In light of these considerations, the present doctoral project aims to valorize Mediterranean biodiversity as a source of novel bioactive compounds, evaluating their nutraceutical potential in *in vitro* (two-dimensional and three-dimensional cell cultures) and *in vivo* experimental models. Particular attention is devoted to their antioxidant properties and to their ability to modulate molecular pathways involved in chronic metabolic and oncological disorders, as well as in UV-induced cellular damage.

1.3 General objectives

The overall objective of the present PhD project is the identification, characterization, and development of nutraceuticals derived from natural matrices rich in biologically active compounds (BACs), with potential applications in the prevention and modulation of chronic disorders.

The general aims of the project are:

- *in vitro* evaluation of BACs isolated from traditional Mediterranean matrices, using different cellular models representative of chronic disorders, including metabolic-associated fatty liver disease (MAFLD), cancer and UV-induced skin damage.
- *In vivo* investigation of the mechanistic properties of the most promising extracts identified in cellular models, in order to validate their efficacy and further elucidate their biological activity in complex experimental systems.

1.4 Annual aims

1.4.1 First-year aims

The first year was focused on the investigation of the onconutraceutical potential of a *Lycium barbarum* L. extract (LBE), integrating analytical, biochemical, and cellular approaches. Specifically, the objectives were:

- analytical characterization and evaluation of antioxidant activity of *Lycium barbarum* extract through liquid chromatography-tandem mass spectrometry (LC–MS/MS) profiling and cell-free antioxidant assays.

- In-cell assessment of the onconutraceutical potential of LBE in breast cancer models, exploring its dual pro-oxidant/antioxidant mechanism of action.
- Investigation of pyroptosis induction in MCF-7 breast cancer cells, with particular attention to the involvement of ER stress–related pathways.
- Evaluation of the protective effects of LBE in non-tumorigenic MCF-10A cells, assessing its ability to counteract oxidative stress.

1.4.2 Second-year aims

The second year was dedicated to the investigation of the nutraceutical potential of *Olea europaea* L. leaves extract (OE), from Olevano sul Tusciano, and *Allium cepa* L. (Cipollotto Nocerino*,* CN) leaves extracts, with particular focus on their anti-steatotic activity in a cellular model of metabolic-associated fatty liver disease (MAFLD). Specifically, the objectives were:

- analytical characterization and evaluation of antioxidant activity of OE and CN leaf extracts through phytochemical profiling and cell-free antioxidant assays.
- *In vitro* assessment of the anti-steatotic potential of both extracts in a model of MAFLD, characterized by intracellular lipid accumulation under steatogenic conditions, using the human hepatocellular carcinoma cell line (HepG2).
- Biochemical investigation of their protective mechanisms, evaluating their effects on oxidative stress and lipid metabolism, and exploring whether these activities were potentially mediated by Sirtuin 1 (SIRT1) signaling.

1.4.3 Third-year aims

The third year was dedicated to the evaluation of the photoprotective potential of coffee silverskin extracts (CSS), with particular focus on their ability to counteract UVA-induced skin damage in both *in vitro* and *in vivo* models.

Specifically, the objectives were:

- analytical characterization and evaluation of antioxidant and anti-melanogenic activity of CSS through phytochemical profiling and cell-free assays.
- *In vitro* assessment of the photoprotective effects of CSS extracts in UVA-irradiated HaCaT keratinocytes.

- *In vivo* validation of CSS activity in zebrafish larvae exposed to UVA radiation.
- Biochemical investigation of the molecular mechanisms underlying their protective effects, focusing on the modulation of oxidative stress, lipid peroxidation, and ferroptotic cell death pathways involved in UVA-induced damage.

1.5 Experimental plan

The experimental strategy combined analytical characterization with mechanistic validation in disease-relevant *in vitro* and *in vivo* models representative of redox- and metabolism-driven chronic disorders.

For the breast cancer model, immortalized human tumorigenic MCF-7 cells were used to evaluate the antitumor activity of the polyphenol-rich LBE. Immortalized non-tumorigenic mammary epithelial MCF-10A cells were employed as physiological controls and to compare redox balance in distinct cellular compartments. This approach allowed the assessment of context-dependent redox modulation and the investigation of selective pro-oxidant effects and pyroptosis-related cell death mechanisms in cancer cells.

Metabolic-associated fatty liver disease was modeled using the immortalized human hepatocarcinoma cell line HepG2. Steatotic conditions were induced by treatment with a mixture of oleic and palmitic acids in a 1:2 ratio, mimicking lipid overload. The establishment of the model was confirmed by Oil Red O (ORO) staining, enabling visualization of intracellular lipid droplets accumulation.

Both 2D and 3D culture systems were applied, including spheroid models to more closely mimic tissue-like architecture, and extract activity was evaluated in terms of lipid accumulation, oxidative stress, ER stress markers, and the potential involvement of SIRT1 signaling pathways.

UVA-induced skin damage was investigated using immortalized human keratinocytes cell line HaCaT exposed to UVA radiation at 365 nm with an energy dose of 366 mJ/cm² to induce oxidative imbalance and cellular stress. The same

irradiation conditions were applied *in vivo* in zebrafish larvae at 3 days post-fertilization (3 dpf), allowing the assessment of whole-organism responses.

This integrated *in vitro* and *in vivo* strategy allowed a comprehensive assessment of photoprotective activity, tracing the cascade from UVA-induced reactive oxygen species (ROS) production to protein kinase RNA-like endoplasmic reticulum kinase (PERK)-mediated endoplasmic reticulum stress, nuclear factor erythroid 2-related factor 2 (Nrf2) activation, and the modulation of ferroptosis and melanogenic pathways.

This integrated multi-model design allowed the comparative and mechanistic evaluation of biodiversity-derived phytocomplexes across oncological, metabolic, and UV-induced stress contexts.

1.6 Expected results

The PhD project aims to establish mechanistically grounded experimental platforms for the evaluation of bioactive compounds derived from Mediterranean agri-food matrices. The research is directed toward the identification and biological validation of multifunctional phytocomplexes capable of modulating redox- and metabolism-driven pathways involved in chronic disorders.

Particular emphasis is placed on understanding the biochemical mechanisms underlying their protective effects, in order to support the rational development of innovative nutraceutical strategies.

The key expected outcomes of this doctoral project include:

- development and validation of *in vitro* and *in vivo* experimental models representative of chronic disorders characterized by oxidative stress, metabolic imbalance, and cellular stress responses;
- mechanistic elucidation of the biochemical pathways modulated by Mediterranean agri-food–derived bioactive compounds, including redox regulation, lipid metabolism, ER stress, pyroptosis, ferroptosis, and SIRT1-related signaling;
- identification and biological validation of multifunctional phytocomplexes with context-dependent antioxidant and pro-oxidant activity;

- scientific support for the development of innovative nutraceutical strategies aimed at the prevention and potential adjuvant management of chronic disorders such as cancer, MAFLD, and UVA-induced skin damage;
- valorization of Mediterranean biodiversity and agri-food by-products as sustainable sources of bioactive compounds with health-promoting potential.

1.7 References

Arshad, Z., Shahid, S., Hasnain, A., Yaseen, E. and Rahimi, M. (2025). Functional Foods Enriched With Bioactive Compounds: Therapeutic Potential and Technological Innovations. *Food Science & Nutrition*, 13(10), e71024.

Baan Hofman, J.H., Bannenberg Cavero, C., Dötsch-Klerk, M., Wanders, A.J., van Dooren, C., Feskens, E.J., de Roos, B. and Biesbroek, S. (2025). Food Biodiversity and its Association with Diet Quality and Health Outcomes – A Scoping Review. *Advances in Nutrition*, 16(12), 100551.

Basilicata, M.G., Pepe, G., Rapa, S.F., Merciai, F., Ostacolo, C., Manfra, M., Di Sarno, V., Autore, G., De Vita, D., Marzocco, S. and Campiglia, P. (2019). Anti-Inflammatory and Antioxidant Properties of Dehydrated Potato-Derived Bioactive Compounds in Intestinal Cells. *International Journal of Molecular Sciences*, 23, 6087.

Chiu, H.F., Venkatakrishnan, K. and Wang, C.K. (2020). The role of nutraceuticals as a complementary therapy against various neurodegenerative diseases: A mini-review. *Journal of Traditional and Complementary Medicine*, 10, 434–439.

Ferro, Y., Pujia, R., Mazza, E., Lascala, L., Lodari, O., Maurotti, S., Pujia, A. and Montalcini, T. (2022). A new nutraceutical (Livogen Plus®) improves liver steatosis in adults with non-alcoholic fatty liver disease. *Journal of Translational Medicine*, 1, 377.

Galland, L. (2010). Diet and inflammation. *Nutrition in Clinical Practice*, 6, 634–640.

Georgiou, N.A., Garssen, J. and Witkamp, R.F. (2011). Pharma-nutrition interface: the gap is narrowing. *European Journal of Pharmacology*, 651, 1–8.

Larussa, T., Imeneo, M. and Luzza, F. (2017). Potential role of nutraceutical compounds in inflammatory bowel disease. *World Journal of Gastroenterology*, 23, 2483–2492.

Mattas, K., Raptou, E., Alayidi, A., Yener, G. and Baourakis, G. (2023). Assessing the Interlinkage between Biodiversity and Diet through the Mediterranean Diet Case. *Advances in Nutrition*, 14(3), 570–582.

Nasri, H., Baradaran, A., Shirzad, H. and Rafieian-Kopaei, M. (2014). New concepts in nutraceuticals as alternative for pharmaceuticals. *International Journal of Preventive Medicine*, 12, 1487–1499.

Santini, A., Tenore, G.C. and Novellino, E. (2017). Nutraceuticals: A paradigm of proactive medicine. *European Journal of Pharmaceutical Sciences*, 53–61.

Vestuto, V., Amodio, G., Pepe, G., Basilicata, M.G., Belvedere, R., Napolitano, E., Guarnieri, D., Pagliara, V., Paladino, S., Rodriquez, M., Bertamino, A., Campiglia, P., Remondelli, P. and Moltedo, O. (2022). Cocoa Extract Provides Protection against 6-OHDA Toxicity in SH-SY5Y Dopaminergic Neurons by Targeting PERK. *Biomedicines*, 8, 2009.

Wei, M., He, X., Liu, N. and Deng, H. (2024). Role of reactive oxygen species in ultraviolet-induced photodamage of the skin. *Cell Division*, 19(1), 1.

Wilson, E.O. (1992). *The Diversity of Life* (Questions of Science). Cambridge: Belknap Press, Harvard University Press.

2. Chapter II: *Lycium barbarum* L. extract

Redox-dependent antitumor activity of *Lycium barbarum* L. extract (LBE) in *in vitro* breast cancer models

2.1 Abstract

Lycium barbarum, commonly known as goji berry or wolfberry, is recognized not only for its nutritional value but also as a source of bioactive compounds, including polysaccharides, carotenoids, polyphenols, and flavonoids.

These constituents are associated with antioxidant, anti-inflammatory, immunomodulatory, and anticancer effects. Although several goji-derived fractions have shown antitumor activity, particularly in breast cancer models, the underlying biochemical mechanisms remain incompletely defined, and extract composition is often insufficiently characterized.

In this study, an ethanolic extract of *Lycium barbarum* (LBE) fruit was characterized by ultra-high-performance liquid chromatography coupled with high-resolution mass spectrometry (UHPLC-HRMS/MS)-based metabolomic profiling and evaluated for its biological activity in breast cancer models.

The extract exhibited cytotoxic effects in MCF-7 human breast adenocarcinoma cells, inducing a pro-oxidant shift that triggered pyroptosis, endoplasmic reticulum stress and activation of the phosphorylated inositol-requiring enzyme 1 alpha/X-box binding protein 1/NOD-like receptor family pyrin domain-containing 3 (P-IRE1α/XBP1/NLRP3) signaling axis. Notably, the extract did not exert cytotoxicity in non-tumorigenic mammary epithelial MCF-10A cells, where it instead demonstrated antioxidant activity by reducing reactive oxygen species generated by doxorubicin (Doxo) treatment.

These findings highlight the context-dependent redox behavior of LBE and support its potential as a multifunctional onconutraceutical agent capable of selectively targeting tumor cells while preserving redox balance in non-tumorigenic cells.

2.2 Introduction

Breast cancer remains one of the leading causes of death worldwide, and despite advances in surgery, radiotherapy, and chemotherapy, current therapeutic strategies are often associated with significant adverse effects and, in some cases, irreversible chronic toxicity. For this reason, increasing attention has been directed toward plant-derived bioactive compounds with potential chemopreventive and chemosensitizing properties, including *Lycium barbarum* (Guida *et al.*, 2022; Miranda *et al.*, 2024).

Goji berries are the fruit of *L. barbarum*, a species native to China, Mongolia, and the Himalayan region and widely used in Traditional Chinese Medicine for over 2300 years (Islam *et al.*, 2027; Potterat, 2010). Among the main species of the genus (*L. barbarum*, *L. chinense*, and *L. ruthenicum*), *L. barbarum* is the most extensively cultivated and pharmacopeia-recognized species (Wang *et al.*, 2018; Tian *et al.*, 2019), showing a closer phylogenetic relationship with L. chinense than with *L. ruthenicum* (Zeng *et al.*, 2014; Cui *et al.*, 2019; Yossa Nzeuea *et al.*, 2022). More than 200 bioactive compounds have been identified in goji berries, including carotenoids, flavonoids, polyphenols, phenylpropanoids, and polysaccharides (Li, 2007; Lu *et al.*, 2010; Nardi *et al.*, 2016).

Among these constituents, polysaccharides and phenolic compounds represent the most extensively studied fractions in breast cancer research.

Polysaccharides isolated from *Lycium barbarum* fruits (LBPs) account for approximately 5–8% of the dried fruits and are water-soluble glycoconjugates with molecular weights ranging from 10 to 2300 kDa (Zheng *et al.*, 2022; Knok *et al.*, 2019; Liu *et al.*, 2021). Their antitumor activity has been demonstrated in several experimental models, including breast cancer cells (Gong *et al.*; 2020).

LBPs have also been shown to regulate the phosphoinositide 3-kinase/protein kinase B/mechanistic target of rapamycin (PI3K/Akt/mTOR) signaling cascade by reducing phosphorylated Akt expression (Zhang *et al.*, 2017; Yuan *et al.*, 2021), as well as to modulate extracellular signal-regulated kinase (ERK), p53, and Toll-like receptor 4 (TLR4)/nuclear factor kappa B (NF-κB) signaling pathways (Ahmed *et*

al., 2022). Overall, their antitumor effects are mainly associated with growth inhibition, apoptosis induction, and immune modulation.

Beyond direct cytotoxicity, *L. barbarum* extracts have been investigated in combination with doxorubicin, an anthracycline chemotherapeutic agent, showing synergistic or additive antitumor effects in breast cancer cell lines (Georgiev *et al.*, 2019). *In vivo* studies further suggest cardioprotective and immunoprotective effects of LBPs against Doxo-induced toxicity (Chao *et al.*, 2006; Han *et al.*, 2014; Hvarchanova *et al.*, 2023).

Parallel to polysaccharides, phenolic compounds constitute another major class of bioactive constituents in *L. barbarum*. Approximately 88 phenolic compounds have been identified, with flavonoids representing the predominant group in the berries (Miranda *et al.*, 2024).

Variability in total polyphenol and flavonoid content has been reported depending on geographic origin, extraction solvents, and post-harvest processing methods (Islam *et al.*, 2017), highlighting the importance of extract characterization and standardization. Phenolic compounds are recognized as key contributors to the antioxidant activity of goji berries, with increased polyphenol content correlating with enhanced radical scavenging capacity (Yu *et al.*, 2022; Li *et al.*, 2021).

However, the biological behavior of polyphenols is not limited to antioxidant activity. Under specific conditions, such as high concentrations or in the presence of redox-active transition metals, phenolic compounds may exert pro-oxidant effects (**Figure 2.1**).

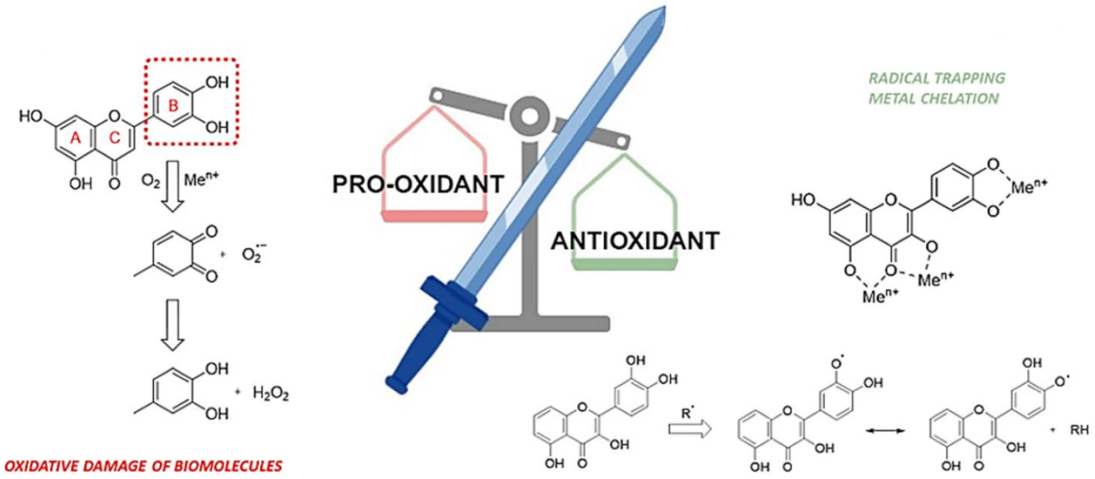

***Figure 2.1**. Polyphenols as a double-edged sword: some pro-oxidant and antioxidant mechanisms.*

Tumor cells are characterized by elevated basal reactive oxygen species (ROS) levels due to metabolic reprogramming and increased nicotinamide adenine dinucleotide phosphate (NADPH) oxidase activity, contributing to carcinogenesis, genomic instability, and resistance to apoptosis (Andrés *et al.*, 2023).

In this context, polyphenols may undergo oxidation to reactive quinones, stimulate intracellular ROS production, or participate in Fenton-type reactions, thereby amplifying oxidative stress selectively within tumor cells (Procházková *et al.*, 2022; Eghbaliferiz *et al.*, 2016).

Despite the extensive literature on LBPs, whose immunomodulatory and proliferative control mechanisms are relatively well characterized, the contribution of the polyphenolic fraction to redox-sensitive signaling and stress-related pathways in breast cancer remains less clearly defined.

Considering the intrinsic oxidative imbalance that characterizes tumor cells and the well-documented dual antioxidant/pro-oxidant behavior of polyphenols, a focused investigation of polyphenol-rich *L. barbarum* extracts is warranted.

In particular, clarifying whether these compounds may selectively amplify oxidative stress in tumor cells while preserving redox homeostasis in non-tumorigenic cells could provide valuable mechanistic insight into their potential onconutraceutical application.

2.2.1 Aim of work

As described above, the polyphenolic fraction, including phenolic acids and flavonoids, of *Lycium barbarum* represents a key component potentially responsible for its redox-modulating activity in breast cancer models. Although the contribution of polyphenols to redox-sensitive stress pathways and regulated cell death mechanisms remains less clearly defined. Given the intrinsic oxidative imbalance that characterizes tumor cells, the context-dependent pro-oxidant activity of polyphenols may represent a selective vulnerability of the cancer compartment.

In addition to polyphenols, goji berries also contain carotenoids, which share antioxidant properties and are characterized by a highly reactive conjugated double-bond system (Ribeiro *et al.*, 2018). Therefore, carotenoids may similarly contribute to redox modulation, particularly under conditions of elevated oxygen tension and oxidative stress.

In this perspective, investigating an extract enriched predominantly in polyphenols, but also containing carotenoid components, may provide a more comprehensive understanding of the redox-dependent effects of the *Lycium barbarum* phytocomplex.

The present study aimed to investigate the biochemical mechanisms underlying the anticancer activity of a polyphenol-rich ethanolic extract of *Lycium barbarum*. After analytical characterization of the extract, its biological effects were evaluated in breast cancer cells to clarify its impact on oxidative stress modulation and stress-related signaling pathways (**Figure 2.2**) (Miranda *et al.*, 2024).

Particular attention was devoted to determining whether LBE could selectively enhance oxidative imbalance in tumor cells while preserving redox homeostasis in non-tumorigenic mammary epithelial cells, thereby supporting its potential role as a bifunctional onconutraceutical agent.

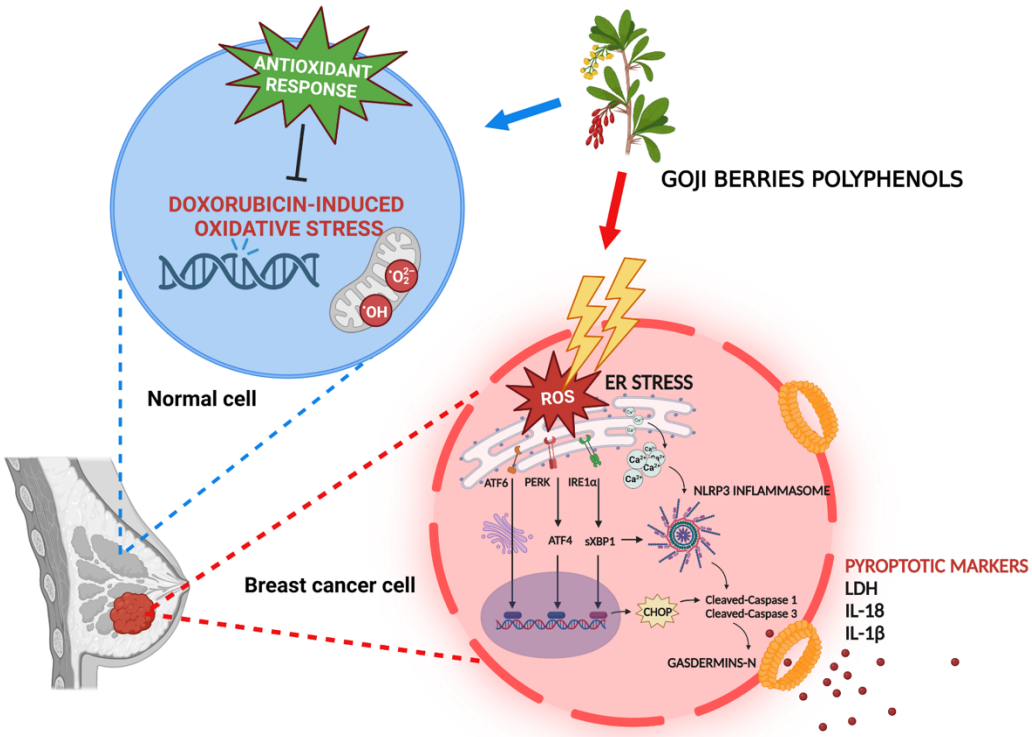

Figure 2.2. *LBE dual mechanism: pro-oxidant action in MCF-7 cells, activating ER stress and pyroptosis. Antioxidant action in MCF-10A cells, reducing doxorubicin-induced ROS.*

2.3 Materials and methods

2.3.1 Sample preparation

Red goji berries were kindly donated by DO.DA.CO. Srl (Scafati, Salerno, Italy).

The fruits were freeze-dried for 24 h (condenser temperature −52 °C; vacuum 0.100 mBar; LyoQuest-55, Telstar Technologies). The resulting powder (1.0 g) was extracted three times with 25 mL of 100% ethanol (EtOH) at 40 °C under magnetic stirring (470 rpm) for 20 min (last extraction overnight).

After centrifugation at 6000 × *g* for 15 min at 4 °C, the supernatant was collected, vacuum-filtered, and the solvent removed by vacuum evaporation (Eppendorf™ Concentrator plus/Vacufuge® plus, 35 °C, V-HV mode).

The dried extract was dissolved in 50 mL of 100% 1-butanol and washed three times with water to remove sugars. The organic phase was collected, filtered through a 0.45 µm nylon membrane (Merck Millipore), evaporated under reduced pressure, and freeze-dried for 24 h.

2.3.2 Determination of total phenolic content (TPC), total flavonoid content (TFC), total chlorophyll (CHLs) and carotenoid (CARs) content

The total phenolic content (TPC) of LBE was determined using the Folin–Ciocalteu (Aquino *et al.*, 2023). Gallic acid was used as standard for the calibration curve (10–500 µg/mL; y = 1779.61x − 2.0811; R^2 = 99.92%). Results were expressed as milligrams of gallic acid equivalents per gram of dry weight (mg GAE/g DW).

Total flavonoid content (TFC) was measured according to Imeneo *et al.* (Imeneo *et al.*, 2022) and expressed as milligrams of rutin equivalents (RE) per gram of dry weight (mg RE/g DW) using a calibration curve (10–500 µg/mL; y = 2239.24x − 5.3342; R^2 = 99.93%).

The chlorophyll content was determined using the methods described by Wang *et al.* and Zhang *et al.*, and the carotenoids content was determined using the method reported by Samec *et al.*, appropriately modified (Šamec *et al.*, 2014; Wang *et al.*, 2022; Zhang *et al.*, 2022).

The content of the pigments was calculated by the measured absorbance value, the solution volume, and the sample mass according to the following equations:

$$Chl\ a\ \left(\frac{mg}{gDW}\right) = \frac{\{[(12.25\times A_{663.2}) - (2.79\times A_{646.8})]\times V\}}{m} \qquad \textit{Equation 2.1}$$

$$Chl\ b\ \left(\frac{mg}{gDW}\right) = \frac{\{[(21.50\times A_{646.8}) - (5.10\times A_{663.2})]\times V\}}{m} \qquad \textit{Equation 2.2}$$

$$Car\ \left(\frac{mg}{gDW}\right) = \frac{\{[(4.75\times A_{452.5}) - (0.226\times (Chl\ a + Chl\ b))]\times V\}}{m} \qquad \textit{Equation 2.3}$$

where V is the extract volume (mL), m is the dry sample weight (mg), and A_663.2, A_646.8, and A_452.5 are the absorbance values.

2.3.3 Determination of antioxidant activity by radical scavenging assays

The antioxidant capacity of LBE was evaluated using two complementary radical scavenging assays: the 1,1-diphenyl-2-picrylhydrazyl (DPPH) assay and the 2,2'-azino-bis(3-ethylbenzothiazoline-6-sulfonic acid) (ABTS) assay.

In both methods, the ability of the extract to neutralize stable free radicals was determined spectrophotometrically.

The results were expressed as half-maximal inhibitory concentration (IC_{50}) values, reported in micrograms per milliliter (µg/mL).

Lower IC_{50} values indicate greater radical scavenging activity.

Trolox (6-hydroxy-2,5,7,8-tetramethylchroman-2-carboxylic acid), a water-soluble vitamin E analogue, was used as a positive antioxidant control.

2.3.4 Metal binding studies

The metal binding studies were performed in this way (Umar *et al.*, 2018): the UV absorption of the LBE (500 µg/mL) alone or in the presence of CuSO4, FeSO4, or FeCl3 (40 µM) for 30 min in 20% (v/v) ethanol/buffer (20 mM HEPES, 150 mM NaCl, pH 7.4) was recorded using a microplate reader (Multiskan Go, Thermo Scientific) with a wavelength ranging from 280 to 400 nm.

2.3.5 LBE LC-MS identification: UHPLC-HRMS/MS

LC-MS/MS analysis was performed on a Thermo Ultimate RS 3000 coupled online to a Q-Exactive hybrid quadrupole Orbitrap mass spectrometer (Thermo Fisher Scientific) equipped with a heated electrospray ionization probe (HESI II).

Separation was performed in reversed-phase mode, with a Kinetex® 2.6 µm EVO C18 100 Å and an LC Column 150 × 2.1 mm (Phenomenex, Bologna, Italy) with a guard cartridge system (SecurityGuard ULTRA cartridges for EVO-C18, sub-2 µm and core–shell columns with 2.1 mm internal diameters).

The column temperature was set at 40 °C and the flow rate was 0.4 mL/min. The mobile phase was (A) H_2O with 0.1% HCOOH (v/v) and (B) ACN with 0.1% HCOOH (v/v). The following gradient was employed: 0.01–3.00 min, isocratic to 0% B; 3.01–10.00 min, 0–10% B; 10.01–25.00 min, 10–20% B; 25.01–30.00 min, 20–50% B; 30.01–33.00 min, 50–95% B; 33.01–36.00 min, isocratic to 95% B; 36.01–38.00 min, 95–0%; then, six minutes were employed for column re-equilibration. The injection volume was 5 µL. All additives and mobile phases were LCMS grade and purchased from Merck.

The ESI was operated in positive and negative mode. The MS was calibrated by Thermo CalMix Pierce™ calibration solutions in both polarities.

Full MS (100–1500 m/z) and data-dependent MS/MS were performed at a resolution of 35,000 and 17,500 FWHM, respectively, and normalized collision energy (NCE) values of 15, 20, and 25 were used. The source parameters were as follows: sheath gas pressure, 50 arbitrary units; auxiliary gas flow, 13 arbitrary units; spray voltage, +3.5 kV, −2.8 kV; capillary temperature, 310 °C; auxiliary gas heater temperature, 300 °C.

Identification of the investigated analytes was carried out by comparing their retention times and MS/MS data with those present in the literature.

The MS spectra were processed using FreeStyle™ 1.8 SP2 and the commercial software Compound Discoverer v. 3.3.1.111 SP1 (Thermo Fisher). Identification was accomplished by activating the Chem Spider and mzCloud nodes. The following online databases were also consulted accessed, on 1 September 2023: Phenol-Explorer (www.phenolexplorer.eu), PubChem (https://pubchem.ncbi.nlm.nih.gov), and SciFinder Scholar (https://scifinder.cas.org).

2.3.6 Quantitative analysis

The quantification of phytochemicals in the LBE extract was performed using LC-MS/MS. For the quantitative analysis of hydroxycinnamic acids, flavonoids, and fatty acids, we used as an external standard caffeic acid (CA), rutin (R), and oleic acid (OA) in negative ionization mode, respectively.

Stock solutions were prepared in methanol (MeOH), and the calibration curves were obtained in a concentration range of 0.03–3.91 µg/mL for caffeic acid, 0.06–15.63 µg/mL for rutin, and 15.63–2000 µg/mL for oleic acid, using six concentration levels with triplicate injections for each level. Linear regression was used to generate the calibration curves with R^2 values ≥ 0.999. Extracted ion chromatogram (XIC) areas of the standard were plotted against corresponding concentrations (µg/mL).

The compound content in the sample was expressed as milligrams of oleic acid (OAE), micrograms of rutin (RE), and micrograms of caffeic acid equivalent (CAE) per gram of dried extract.

The method validation parameters for the quantitative assay included accuracy, linearity, range, limit of detection (LOD), and limit of quantitation (LOQ).

LOD and LOQ were calculated by using the standard deviation (SD) and the slope of the calibration curve, multiplied by 3.3 and 10, respectively.

2.3.7 Cell cultures and drug treatment

The human breast cancer cell lines, MCF-7, SK-BR-3, and MDA-MB-231, were obtained from American Type Culture Collection (ATCC).

Cells were grown in Dulbecco's Modified Eagle Medium (DMEM, 4500 mg/mL glucose) supplemented with 10% (v/v) fetal bovine serum (FBS), 2 mM L-glutamine, 100 U/mL penicillin, and 0.1 mg/mL streptomycin.

The human breast endothelial line (MCF-10A) was purchased from ATCC and maintained in a 1:1 mixture of DMEM and Ham's F12 medium supplemented with 5% horse serum, 2 mM L-glutamine, human recombinant epidermal growth factor (20 ng/mL), insulin (10 mg/mL), cholera toxin (100 ng/mL), and hydrocortisone (5 mg/mL).

Cells were routinely grown in culture dishes in a 95% humidified environment containing 5% CO_2 at 37 °C and split every 2 days.

In each experiment, cells were placed in a fresh medium and cultured in the presence of LBE at different concentrations and times, as reported in subsequent sections. Each treatment and analysis were performed at least in three separate experiments.

2.3.8 Cell viability assay and phase-contrast analysis

Cell viability was established by measuring the mitochondrial metabolic activity with 3-[4,5-dimethylthiazol-2,5-diphenyl-2H-tetrazolium bromide (MTT) assay.

Briefly, MCF-7 (6×10^3 cells/well), MDA-MB-231 (6×10^3 cells/well), SK-BR-3 (6×10^3 cells/well), and MCF-10A (6×10^3 cells/well) were plated into 96-well plates, and then, LBE (3.125-100 µg/mL) was added for 24 h.

Afterward, the MTT reagent was added for 2-4 h depending on the cell line.

Cell lysis was performed with an isopropanol/HCl solution to dissolve blue formazan crystals formed by viable mitochondria.

The absorbance of formazan crystals was measured at 570 nm (Multiskan Go, Thermo Scientific).

Cell viability was expressed as a percentage relative to the untreated cells cultured in medium with 0.1% DMSO and set to 100%, whereas 10% DMSO was used as positive control and set to 0% of viability.

The EC_{50} values were calculated using GraphPad Prism 8.0 software by nonlinear regression of the dose-response inhibition.

Phase-contrast images were captured using a Zeiss Axiocam 208 inverted microscope (Magnification, 40×. N ≥ 10. Scale bar: 50 µm).

2.3.9 Colony formation assay

The clonogenic potential was assessed using a subtoxic dose (6 µg/mL) of LBE.

Cells were plated in 6-well plates at a seeding density of 5×10^2 cells/well.

After incubation for 7 days, the culture was terminated by removing the medium and washing the colonies twice with Phosphate-Buffered Saline (PBS). The cells were fixed and stained with a solution containing 3.7% formaldehyde and 0.5% crystal violet for 30 min, and then washed twice with PBS.

Images were obtained and the clonogenic potential was determined from 1% SDS cell dissolution and measured by spectrophotometer at 570 nm (Multiskan Go, Thermo Scientific).

2.3.10 Wound healing assay

In the wound healing analysis, 3×10^5 cells were seeded in 6-well plates and then incubated at 37 °C for 24 h. After that, a linear scratch was created with a 10 µL sterile pipette tip. Cells were washed with PBS, necessary to remove cell debris, and cultured in a medium containing a subtoxic dose (6 µg/mL) of LBE. To avoid cell proliferation, DMEM with 2% FBS was used.

Different fields were analyzed by contrast-phase microscopy, and each scratch area was photographed at 0 and 24 h.

Images were obtained and the wound size for the different times was calculated with the free image-processing software ImageJ, version 1.47.

2.3.11 Determination of hypodiploid nuclei

Hypodiploid nuclei were analyzed using propidium iodide (PI) staining by flow cytometry (FC). MCF-7 cells (4×10^4 cells/well) were grown in 12-well plates and allowed to adhere for 24 h. Later the medium was replaced, and cells were treated with LBE (6, 12, 25 µg/mL) for 24 h. After treatments, the culture medium was replaced, cells washed twice with PBS and then suspended in 200 µL of a hypotonic staining solution containing 50 µg/mL PI, 0.1% (*w*/*v*) sodium citrate, and 0.1% Triton X-100. Culture medium and PBS were centrifuged, and cell pellets were pooled with cell suspension to retain both dead and living cells for analysis. After incubation at 4 °C for 30 min in the dark, cell nuclei were analyzed with a Becton Dickinson FACScan flow cytometer using the Cell Quest software, version 4.

Cellular debris was excluded from the analysis by raising the forward scatter threshold, then the percentage of cells in the hypodiploid region (sub G0/G1) was calculated.

2.3.12 Propidium iodide (PI)/Hoechst 33342 double staining assay

Cell-permeable DNA dye Hoechst 33342 and PI were used to validate necrosis in cell populations. MCF-7 cells (4×10^4 cells/well) seeded on glass cover slips were grown in 12-well plates and allowed to adhere for 24 h. Next the medium was replaced, and cells were treated with LBE (6, 12, 25 µg/mL) for 24 h.

After treatments the culture medium was replaced, and live cells were stained with a Hoechst 33342/PI solution added to cell culture medium (Hoechst 33342, 5 µM; PI, 30 µg/mL) at 37 °C for 20 min in the dark.

The stained cells were washed two times and then fixed with 3.7 % formaldehyde for 10 min. Images were acquired on a fluorescence microscope (Axioshop 40, Zeiss. Magnification, 20×. Scale bar: 20 µm). Quantitative analyses were performed by the ImageJ program, version 1.47 ($N \geq 10$).

2.3.13 Western blotting analysis

The MCF-7 cell line was seeded in 60 mm culture dishes and treated with LBE (6 µg/mL) at different times (2, 4, 8 h). After 8 h, the cells were washed, detached with a scraper, and centrifuged to remove debris. Full proteins were extracted by using a lysis buffer. Then, cell lysates were centrifuged at 4850 × *g* for 20 min at 4 °C.

A total of 30 µg of total proteins was run on 8-12% SDS-PAGE and transferred to nitrocellulose membranes using a minigel apparatus (Bio-Rad Laboratories).

Blots were blocked in phosphate-buffered saline, containing Tween-20 0.1% and 10% non-fat dry milk or bovine serum albumin (BSA), for 1 h at room temperature and incubated overnight with specific primary antibodies at 4 °C with slight agitation.

α-tubulin or GAPDH was used as the loading control.

The following antibodies were used:

- rabbit monoclonal anti-PERK (Cell Signaling),
- mouse monoclonal anti-ATF6 (Cell Signaling),
- rabbit polyclonal anti-caspase-12 (Abcam),
- mouse monoclonal anti-α-tubulin (Santa Cruz Biotechnology),
- mouse monoclonal anti-GAPDH (Sigma Aldrich),
- rabbit polyclonal anti-phospho-IRE1α (Sigma Aldrich),
- mouse monoclonal anti-NRLP3 (Sigma Aldrich),
- rabbit polyclonal anti-GRP78 (Sigma Aldrich),
- rabbit monoclonal anti-Nrf2 (Santa Cruz Biotechnology),
- rabbit polyclonal anti-CHOP (Sigma Aldrich),
- rabbit polyclonal anti-caspase-3 (Cell Signaling),
- mouse monoclonal anti-caspase-1 (Santa Cruz Biotechnology),
- rabbit monoclonal anti-Gasdermin D (Sigma Aldrich).

After washes in PBS/Tween-20 0.1%, the appropriate anti-rabbit or anti-mouse (Pierce, Thermo Fisher Scientific) peroxidase-linked secondary antibody was added for 1 h at room temperature.

Antigen-antibody complexes were detected by enhanced chemiluminescence (ECL kit, Amersham). Filters were exposed to LAS 4000 (GE Healthcare) and the densitometry analysis of autoradiographs was performed by the ImageJ program, version 1.47.

2.3.14 Measurement of lactate dehydrogenase (LDH)

MCF-7 cells (6×10^3 cells/well) were seeded in 96-well allowing to adhere for 24 h. Next, cells were incubated for 24 h with LBE (6, 12, 25 µg/mL).

To verify the release of lactate dehydrogenase (LDH) into the cell culture medium after plasma membrane disruption, the LDH-Glo™ cytotoxicity assay (Promega) was performed. According to the LDH-Glo™ kit protocol, the LDH detection reagent (containing lactate, NAD^+, reductase, reductase substrate, and rLuciferase Ultra-Glo™) were added to the cell culture medium sample.

The luminescent signal generated was read in end-point mode using a PerkinElmer AlphaScreen multimode plate reader.

2.3.15 Reactive oxygen species (ROS) detection

Reactive oxygen species levels were measured using 10 µM 6-carboxy-2',7'-dichlorodihydrofluorescein diacetate (DCFH-DA, Sigma Aldrich).

To test the effect of LBE to ROS neutralization, MCF-7 cells (6×10^3 cells/well) and MCF-10A (6×10^3 cells/well) were seeded in 96-well allowing to adhere for 24 h. Next, cells were incubated for 1-24 h with LBE (6 or 25 µg/mL).

Doxorubicin (indicated as Doxo, 400 and 200 nM, 4h) was used as positive control.

After treatments, the medium was removed, and the cells were washed twice with PBS. A staining solution containing DCFH-DA in serum-free medium without phenol-red was added for 40 min at 37 °C in the dark. The fluorescence signals (excitation/emission 485 nm/535 nm) were read in end point mode using a PerkinElmer EnSpire multimode plate reader.

2.3.16 RNA extraction, reverse transcription, and real-time PCR

Total RNA was isolated from the treated cells after 24 h using Trizol reagent (Gibco, Thermo Fisher Scientific), according to the manufacturer's instructions.

Aliquots of total RNA for the real-time PCR test were subjected to DNase I digestion (Thermo Fisher Scientific) and were reverse-transcribed using M-MLV

Reverse Transcriptase (Thermo Fisher Scientific) according to the manufacturer's protocol. In the last step, RNAse H was added.

Real-time PCR was performed with the QuantStudio™ 5 Real-Time PCR System (Thermo Fisher Scientific) using SYBR Green detection in a total volume of 20 µL with 1 µL of forward and reverse primers (5 µM) and 10 µL of PowerUp™ SYBR™ Green Master Mix (Thermo Fisher Scientific).

The values were determined from a standard curve generated from serial cDNA dilutions and normalized to GAPDH.

The primers used for the real-time PCR reactions are listed in the table below.

The $2^{-\Delta\Delta CT}$ method was used to analyze the results and relative mRNA expression levels were determined as fold-induction relative to Ctrl cells, set as 1.

Table 2.1. *Forward and Reverse Primer Sequences for Target Genes*

Primer sequence (5'–3')		
Target gene	**Forward**	**Reverse**
ATF4	GTCCCTCCAACAACAGCAAG	CTATACCCAACAGGGCATCC
XBP1	TTACGAGAGAAAACTCATGGC	GGGTCCAAGTTGTCCAGAATGC
SOD1	AAGGCCGTGTGCGTGCTGAA	CAGGTCTCCAACATGCCTCT
Catalase	GCAGATACCTGTGAACTGTC	GTAGAATGTCCGCACCTGAG

2.3.17 XBP1 splicing assay

MCF-7 cells were seeded in 100 mm culture dishes and treated alone with LBE (6 µg/mL). Thapsigargin (TG, 300 nM) was used as the positive control for XBP1 splicing.

After 24 h, the total RNA of MCF-7 cells was extracted. One microgram of DNAse-treated total RNA was retro-transcribed with the M-MLV Reverse Transcriptase (Thermo Fisher Scientific) according to manufacturer instructions.

Semi-quantitative PCR was performed on 3 µL of cDNA with the following primers:

- forward XBP1 5'-TTA CGA GAG AAA ACT CAT GGC-3',
- reverse XBP1 5'-GGG TCC AAG TTG TCC AGA ATG C-3'.

The resulted un-spliced and spliced XBP1 mRNA were separated by gel electrophoresis on 3% agarose gel.

Then, ethidium bromide-stained amplicons were exposed to LAS 4000 (GE Healthcare).

2.3.18 Determination of protein misfolding

Protein misfolding was analyzed by using Thioflavn T (ThT, Sigma Aldrich) staining and flow cytometry.

MCF-7 cells (20×10^3 cells/well) were grown in 24-well plates and allowed to adhere for 24 h. Later, the medium was replaced, and the cells were treated with LBE (25 µg/mL) and also thapsigargin (indicated as TG, 300 nM) as the positive control for 24 h.

After treatments, the culture medium was replaced, and the cells were washed and suspended in 100 µL ThT at 20 µM. After incubation at 4 °C for 30 min in the dark, the cells were analyzed with the same flow cytometer reported above.

A second analysis was performed through fluorescence microscopy.

MCF-7 cells (4×10^4 cells/well) seeded on glass cover slips were grown in 12-well plates and allowed to adhere for 24 h.

After treatments, live cells were stained with a Hoechst 33342/ThT solution added to the cell culture medium (Hoechst 33342, 5 µM; ThT, 20 µM) at 37 °C for 20 min in the dark. The stained cells were washed and fixed with 3.7% formaldehyde for 10 min. Images were acquired using a fluorescence microscope (Axioshop 40, Zeiss. Magnification, 20×. Scale bar 20 µm).

Quantitative analyses were performed by using the ImageJ program, version 1.47 ($N \geq 10$), and expressed as ThT-positive cells (%).

2.3.19 Measurement of intracellular Ca^{2+} signaling

Intracellular Ca^{2+} concentrations were measured using fluorescent Mag Fluo-4 a.m. probe (Molecular Probes, Thermo Fisher Scientific).

MCF-7 cells (20×10^4 cells/well) were grown in 6-well plates and allowed to adhere for 24 h. Later, the medium was replaced, and the cells were treated with LBE (25 µg/mL) for 24 h. After treatments, the cells were trypsinized and incubated with Mag Fluo-4 a.m. at 22 µM in DMEM without serum for 1 h at RT.

Then, the cells were washed through centrifugation and incubated at 37 °C for 20 min in PBS (without calcium and magnesium). Finally, the cells were washed and the fluorescence in each sample was analyzed by flow cytometry.

2.3.20 Statistical analysis

The data are reported as mean ± SD of the results from three independent experiments. Statistical analysis was performed using an analysis of variance test (ANOVA), and multiple comparisons were made with the Bonferroni test using GraphPad Prism 8.0 software (San Diego, CA, USA).

Significance was assumed at $p < 0.05$.

2.4 Results and discussion

2.4.1 Total phenolic, flavonoid, chlorophyll, carotenoid content and antioxidant activity

In order to evaluate the biological properties of the *L. barbarum* extract, several analyses were performed to clarify the phenolic, flavonoid, chlorophyll and carotenoid content.

TPC and TFC assays indicate that LBE possesses values of 31.26 ± 0.01 mg GAE/g DW and 65.51 ± 0.01 mg RE/g DW, respectively.

The values investigated in this study were comparable to those stated by Wang *et al.* (Wang *et al.*, 2018) for TFC and TPC in different goji genotypes.

Furthermore, spectrophotometric analysis revealed the presence of chlorophyll a and chlorophyll b at concentrations of 0.417 ± 0.001 mg/g DW and 0.693 ± 0.019 mg/g DW, respectively. Additionally, in agreement with the results reported by Ilić *et al.*, the total carotenoid content in the ethanolic extract was quantified as 0.508 ± 0.004 mg/g DW (Ilić *et al.*, 2020).

The antioxidant potential of LBE was evaluated through the DPPH and ABTS assays. In the ABTS assay, a blue/green ABTS·+ radical is formed and can be mitigated by antioxidants, while the DPPH assay involves the reduction of purple DPPH to 1,1-diphenyl-2-picryl hydrazine.

The DPPH free radical scavenging activity of LBE yielded an IC_{50} value of 533.17 ± 3.32 µg/mL (Trolox, IC_{50} of 4.57 ± 0.27 µg/mL), which, when compared with values reported by Skenderidis *et al.*, indicated a notable antioxidant activity (Skenderidis *et al.*, 2019).

Furthermore, LBE exhibited good ABTS scavenging potency (IC_{50} 9.05 ± 1.73 µg/mL), showing 20 times less activity than the positive control (Trolox, IC_{50} of 0.45 ± 0.04 µg/mL).

Metal binding studies were performed to further support these results.

The results showed that LBE also exerted its antioxidant activity through chelation with iron and copper ions (**Figure 2.3**), in agreement with the high polyphenolic content and DPPH and ABTS scavenging action determined through previous assays.

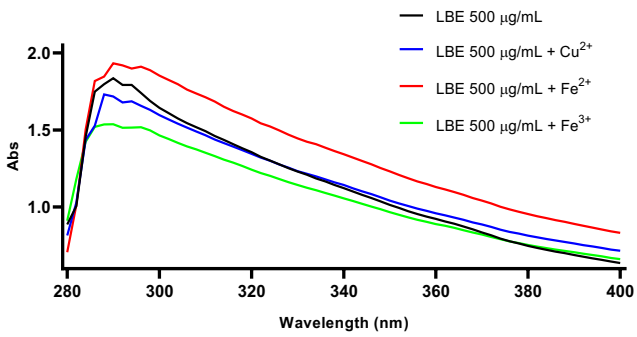

***Figure 2.3**. UV spectra (in range 280 to 400 nm) of LBE (500 µg/mL) alone and in the presence of 40 µM $FeSO_4$, $FeCl_3$ and $CuSO_4$.*

2.4.2 Phytochemical profile of LBE

The metabolomic profile of LBE was investigated by LC-MS/MS operating in both negative and positive ionization modes. The analytical platform allowed the tentative identification of 60 compounds (**Table S2.1**), mainly belonging to polyphenols, including phenolic acids, hydroxycinnamic acids, and flavonoids.

Among hydroxycinnamic derivatives, compounds containing caffeoyl (162 Da), feruloyl (175 Da), coumaroyl (162 Da), spermidine (145 Da), putrescine (90 Da), and tyramine (137 Da) moieties were detected.

Peaks 14 and 15 were tentatively identified as N^1-dihydrocaffeoyl-N^{10}-caffeoyl spermidine (m/z 470, $[C_{25}H_{33}N_3O_6]^-$).

The MS/MS spectra showed fragment ions at m/z 308 and 163, corresponding to the loss of a caffeoyl group (162 Da) and a spermidine amide moiety (145 Da), respectively (Xiao *et al.*, 2019).

Peak 11 exhibited an $[M^+H]^+$ ion at m/z 634 ($C_{31}H_{44}O_{11}N_3$) with fragment ions at m/z 472, 310, 220, and 163, suggesting its identification as N^1-dihydrocaffeoyl-N^{10}-caffeoyl spermidine hexose (**Figure S2.1**) (Yossa Nzeuwa *et al.*, 2017).

Peak 6 was assigned as di-O-caffeoylquinic acid ($[M^-H]^-$ at m/z 515), characterized by fragment ions at m/z 353 and 323 due to the loss of caffeoyl and quinic moieties.

Similarly, peak 9 ($[M^-H]^-$ m/z 515) showed fragments at m/z 191 and 179 and was identified as a di-O-caffeoylquinic acid derivative (7.68 ± 1.98 µg CAE/g DW) (Alcázar Magaña *et al.*, 2021).

Peaks 29 and 37 (53.05 ± 3.07 µg CAE/g DW) exhibited $[M^-H]^-$ at m/z 282 ($C_{17}H_{17}NO_3$) and were identified as isomers of N-p-coumaroyl tyramine. The same compound was confirmed in positive ionization mode (**Figure S2.2**) (Liu *et al.*, 2021).

Additional hydroxycinnamic acids were identified as caffeic acid (peak 7, m/z 179), p-coumaric acid (peak 16, m/z 163), and ferulic acid (peak 23, m/z 193), with characteristic carbon dioxide neutral loss (44 Da) in MS/MS spectra.

Flavonoids were also abundant, including rutin (m/z 609), isorhamnetin (m/z 316), quercetin (m/z 303), and kaempferol (m/z 287) derivatives.

Compound 21 (18.49 ± 7.96 µg RE/g DW) was tentatively identified as rutin hexoside (m/z 771), showing sequential losses of hexose and rhamnose residues.

Rutin (compound 26; 1607 ± 89.85 µg RE/g DW) and compound 27 were also detected (Xiao *et al.*, 2019).

Peaks 31 and 32 were identified as kaempferol O-hexoside-rhamnoside (nictoflorin), with $[M^-H]^-$ at m/z 593 and characteristic fragments at m/z 285/287 corresponding to sugar loss (**Figure S2.3**) (Cerqua *et al.*, 2022).

Peak 35 (182.55 ± 36.32 µg RE/g DW) was tentatively assigned as isorhamnetin-O-rutinoside based on fragment ions at m/z 315 and 300.

Peak 36 was identified as isorhamnetin-O-hexoside (m/z 477), showing sequential loss of sugar and methyl groups.

Hydroxy fatty acids were also detected. Peak 52 ($[M^{-}H]^{-}$ m/z 295) was tentatively identified as hydroxy-octadecadienoic acid (HODE), characterized by fragment ions at m/z 277 and 171 (1737.23 ± 23.17 mg OAE/g DW).

Peaks 47–49 ($[M^{-}H]^{-}$ m/z 311) were assigned as dihydroxy-octadecadienoic acid (DiHODE) isomers, showing a base peak at m/z 293 due to water loss.

Trihydroxy-octadecadienoic acid (TriHODE) isomers (peaks 42, 44, and 45; $[M^{-}H]^{-}$ m/z 327) were identified based on fragments at m/z 309 and 291.

Quantitative analysis yielded 3.22 ± 0.3, 276.61 ± 6.2, and 440.45 ± 10.03 mg OAE/g DW, respectively (Zang *et al.*, 2026; Lu *et al.*, 2014).

LBE showed a complex phytochemical profile characterized by hydroxycinnamic derivatives, flavonoids, and oxidized fatty acids, supporting its multifunctional redox-related biological activity.

2.4.3 LBE induces pyroptosis in MCF-7 cells, saving MCF-10A non-tumorigenic cells

The anticancer activity of LBE has initially been evaluated on MCF-7, MDA-MB-231, and SK-BR-3 human breast cancer cell lines.

The control non-tumorigenic breast cell line MCF-10A was used.

The viability of LBE-treated cells was measured after 24 h of treatment, using the extract in a concentration range of 3.125–100 µg/mL.

The extract exhibited the strongest antiproliferative effects on the MCF-7 cell line (EC_{50} = 45 ± 3 µg/mL) compared to MDA-MB-231 (EC_{50} = 55 ± 2 µg/mL) and SK-BR-3 (EC_{50} = 60 ± 5 µg/mL). Moreover, no toxicity was found on the MCF-10A breast endothelial cell line (EC_{50} > 100 µg/mL), suggesting a selective mechanism of action against cancer cell lines (**Figure 2.4 A**).

The observation of morphological changes using an inverted microscope revealed distinct swelling and membranolysis in MCF-7 cells after treatment with LBE (EC_{50}) for 24 h (**Figure 2.4 B**).

Considering these findings, to acquire further insights into the cytotoxic effect showed by LBE, its clonogenic potential was evaluated on the MCF-7 cell line to assess its long-term interference in colony formation by individual cells.

The results showed a reduction in colony formation after the administration of 6 µg/mL of LBE, with statistically significant differences compared to the control (LBE after 7 days: $p < 0.05$ vs. Ctrl after 7 days) (**Figures 2.4 C, D**).

Subsequently, to examine the effect of LBE extract on tumor cell motility, a wound closure test was carried out on both untreated and LBE-treated MCF-7 cells.

As can be seen in **Figures 2.4 E** and **F**, a larger wound area after 24 h was observed in LBE-treated MCF-7 cells (69% wound area) compared to untreated cells (24% wound area. (LBE after 24 h: $p < 0.05$ vs. Ctrl after 24 h).

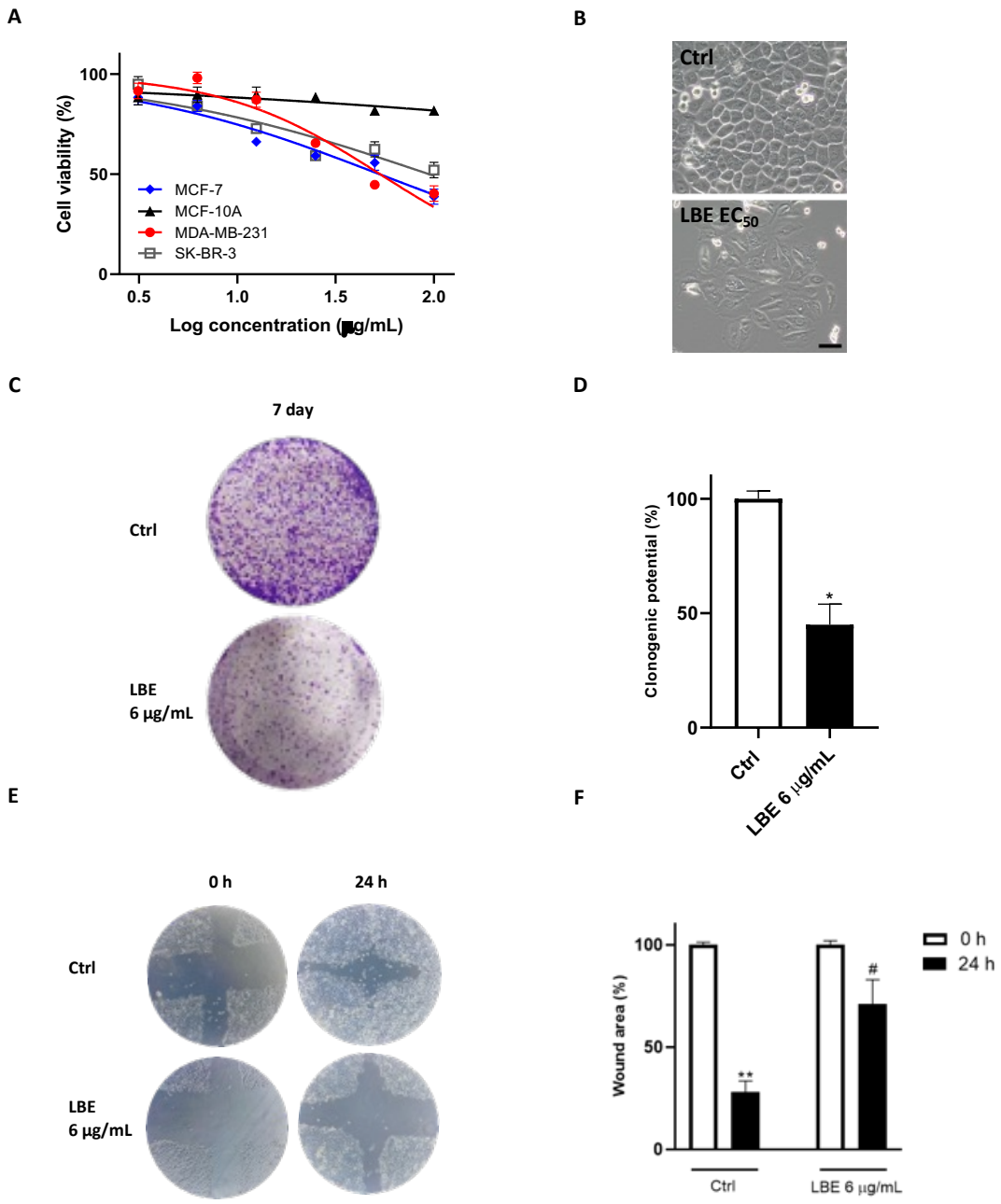

***Figure 2.4**. Cytotoxic effects of LBE on MCF-7 breast cancer cell line. MTT assay after 24 h of treatment of MCF-7, MDA-MB-231, and SK-BR-3 cell lines and MCF-10A healthy epithelial cell line (**A**). Then, EC_{50}s were estimated. (**B**) After 24 h of LBE exposure (EC_{50}), morphological changes were observed using phase-contrast microscope, revealing pyroptotic features of MCF-7 cells treated with LBE (Magnification 40×. N ≥ 10. Scale bar: 50 µm). (**C**) Representative images of clonogenic assay in presence of LBE (6 µg/mL) for 7 days. (**D**) OD quantification from SDS-dissolved colonies. (**E**) Effect of LBE exposure (6 µg/mL) on cell migration of MCF-7 cells through wound healing assay (Magnification 20×). (**F**) Quantitative analysis of wound area of MCF-7 cells at time 0 and 24 h.*

Data are shown as mean ± SD of three different experiments performed in triplicate.

** $p < 0.05$ vs. Ctrl; ** $p < 0.01$ vs. Ctrl; $^{\#}$ $p < 0.05$ vs. Ctrl after 24 h.*

To assess if the reduction in cell metabolization, observed through MTT assays, and the morphological changes were attributed to cell death induction, a PI staining was performed. Flow cytometry analysis was then conducted to assess the formation of hypodiploid nuclei, which represent a hallmark of cell death.

The results demonstrated a significant increase in the number of hypodiploid nuclei induced by LBE in a concentration-dependent manner (6-25 µg/mL) (**Figures 2.5 A, B**).

Interestingly, an accumulation of cellular debris resembling necrosis rather than an apoptosis event was observed, prompting a more detailed investigation into this phenomenon.

Thus, to investigate necrosis of MCF-7 due to LBE extract, PI/Hoechst 33342 double staining was carried out. Hoechst 33342 is a cell-permeable nuclear counterstain that emits blue fluorescence in combination with the minor groove of dsDNA. On the other hand, PI is a membrane-impermeable dye that labels dead cells which have lost their membrane integrity, emitting strong red fluorescence (Carolina *et al.*, 2011).

The results indicated that LBE significantly influenced necrotic events, consistent with the flow cytometry data (LBE 25 µg/mL: $p < 0.01$ vs. Ctrl) (**Figures 2.5 C, D**).

Therefore, based on the morphological analysis, has been hypothesized that LBE treatment induces pyroptosis in breast cancer cells. This inference stems from the observation of cell permeability to PI, facilitated by the low molecular weight and pore formation associated with this regulated cell death form (Yu *et al.*, 2001).

To confirm this hypothesis, western blotting was used to measure the expression of some pyroptosis markers. The results revealed the generation of cleaved caspase-1, cleaved caspase-3, and gasdermin D (GSDMD) and its N-terminal proteolytic fragment of GSDMD (GSDMD-N, active monomeric form), consistent with the activation of pyroptosis (**Figures 2.5 E, F**) (Suchiya *et al.*, 2021).

Caspase-1 causes the production of GSDMD-N, which is responsible for the formation of pores on the cell membrane. Following damage to the plasma membrane, lactate dehydrogenase is released.

In line with our results, LDH production was evaluated, revealing a significant increase in LDH levels following LBE administration compared to the control (LBE 6-25 µg/mL: $p < 0.05$ vs. Ctrl) (**Figure 2.5 G**).

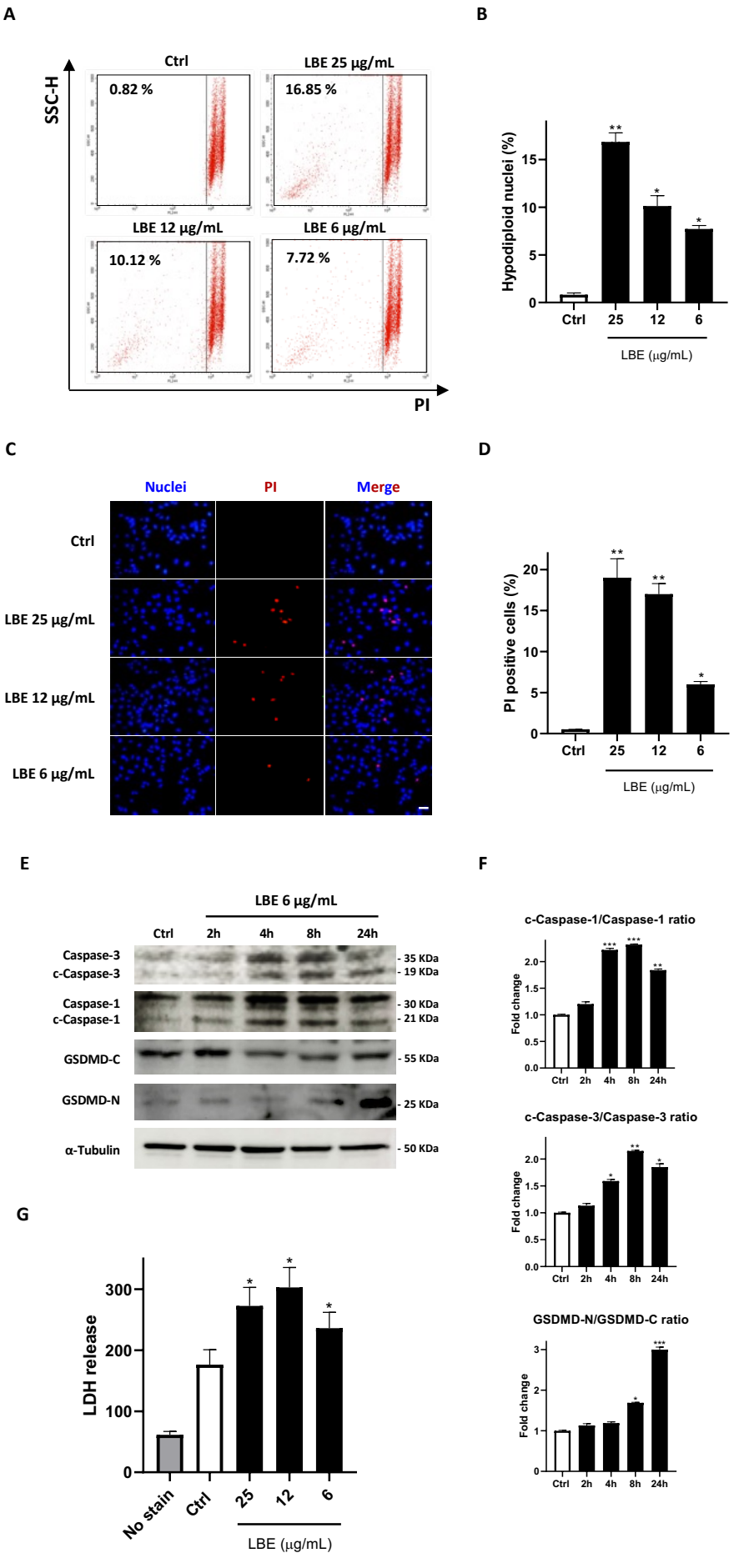
A
Ctrl
LBE 25 µg/mL
0.82 %
16.85 %
LBE 12 µg/mL
LBE 6 µg/mL
10.12 %
7.72 %
SSC-H
PI
B
Hypodiploid nuclei (%)
Ctrl
25
12
6
LBE (µg/mL)
C
Nuclei
PI
Merge
Ctrl
LBE 25 µg/mL
LBE 12 µg/mL
LBE 6 µg/mL
D
PI positive cells (%)
Ctrl
25
12
6
LBE (µg/mL)
E
LBE 6 µg/mL
Ctrl
2h
4h
8h
24h
Caspase-3
c-Caspase-3
35 KDa
19 KDa
Caspase-1
c-Caspase-1
30 KDa
21 KDa
GSDMD-C
55 KDa
GSDMD-N
25 KDa
α-Tubulin
50 KDa
F
c-Caspase-1/Caspase-1 ratio
Fold change
c-Caspase-3/Caspase-3 ratio
GSDMD-N/GSDMD-C ratio
G
LDH release
No stain
Ctrl
25
12
6
LBE (µg/mL)

***Figure 2.5**. LBE selectively induces pyroptosis of MCF-7 breast cancer cell line. (**A**) After 24 h of LBE exposure (25, 12, 6 µg/mL), MCF-7 cells were stained with PI and fluorescence of hypodiploid nuclei (sub G0/G1) was measured by flow cytometry. (**B**) Quantitative analysis of hypodiploid nuclei was performed. (**C**) Hoechst 33342/PI double staining was performed to analyze dead and living cell distributions after exposure to LBE (25, 12, 6 µg/mL). (**D**) Quantitative analysis of PI-positive cells was performed (Magnification 20x. N ≥ 10. Scale bar: 20 µm) (**E**) Western blots of pyroptosis markers after exposure to LBE (6 µg/mL) at 2, 4, 8, and 24 h. (**F**) Densitometric analysis of Western blots. (**G**) LDH levels after exposure to LBE (25, 12, 6 µg/mL) at 24 h revealed by luminescence assay.*
Data are shown as mean ± SD of three different experiments performed in triplicate.
** p < 0.05 vs. Ctrl; ** p < 0.01 vs. Ctrl; *** p < 0.001 vs. Ctrl.*

2.4.4 Differential modulation of redox status by LBE in MCF-7 cancer and MCF-10A non-tumorigenic cells

Reactive oxygen species participate in physiological processes such as immune defense and programmed cell death; however, when their production exceeds the cellular antioxidant capacity, a pro-oxidant imbalance occurs, leading to oxidative stress, a key feature of tumor initiation and progression.

Cancer cells, due to hyperproliferative metabolism and oncogenic signaling, exhibit elevated basal ROS levels and an adaptive increase in antioxidant defenses. Therapeutic strategies based on oxidative damage aim to overwhelm this redox adaptation by pushing ROS levels beyond the cytotoxic threshold, thereby selectively targeting cancer cells while sparing healthy compartments (Shin et al., 2020; D'angelo *et al.*, 2017).

In this context, was investigated whether LBE could exert a pro-oxidant action capable of disrupting redox homeostasis in MCF-7.

LBE (6 µg/mL) induced a significant increase in intracellular ROS production within 1-8 h of treatment, indicating an early oxidative insult (**Figure 2.6 A**).

Co-administration with doxorubicin further amplified ROS production compared to each treatment alone (LBE + Doxo: $p < 0.01$ vs. Doxo) (**Figure 2.6 A**), suggesting a potential synergistic redox effect.

This early oxidative burst was followed, at 24 h, by a compensatory increase in catalase and superoxide dismutase 1 (SOD1), key enzymes involved in cellular antioxidant defense mechanisms, mRNA expression ($p < 0.001$ vs. Ctrl) (**Figure 2.6 C**) (Irazabal *et al.*, 2020).

The functional relevance of ROS in LBE-induced cytotoxicity was confirmed by co-treatment with N-acetylcysteine (NAC), a ROS scavenger, which completely restored cell viability (NAC + LBE: $p < 0.001$ vs. LBE alone) (**Figure 2.6 D**).

These findings demonstrate that ROS accumulation could be a primary driver of LBE-mediated cancer cell death.

Moreover, the elevated ROS levels may also be explained by the metal-rich tumor microenvironment. Cancer cells display increased intracellular iron and copper concentrations, which can catalyze Fenton and Fenton-like reactions, amplifying hydroxyl radical generation (Courage *et al.*, 2024). Given the metal-chelating and redox-active properties of LBE, which we have previously observed in cell-free assays, the interaction between LBE constituents and transition metals likely contributes to the observed pro-oxidant shift.

Interestingly, this redox effect was context dependent. In non-tumorigenic mammary epithelial cells (MCF-10A), LBE did not induce oxidative stress, significantly attenuated doxorubicin-induced ROS accumulation (Doxo + LBE: $p < 0.001$ vs LBE alone) (**Figure 2.6 B**). Considering that doxorubicin exerts cardiotoxicity and endothelial toxicity through oxidative mechanisms, this dual redox behavior supports a bifunctional profile of LBE: pro-oxidant in cancer cells and antioxidant in healthy cells.

Given the well-established interplay between oxidative stress and ER stress (Martucciello *et al.*, 2020), was next evaluated whether LBE-induced ROS disrupted endoplasmic reticulum homeostasis.

ThT staining revealed increased protein misfolding in LBE-treated MCF-7 cells, comparable to the positive control thapsigargin (FC analysis, LBE: $p < 0.001$ vs Ctrl; TG: $p < 0.001$ vs Ctrl.) (**Figures 2.5 E–H**), confirming activation of the ER stress.

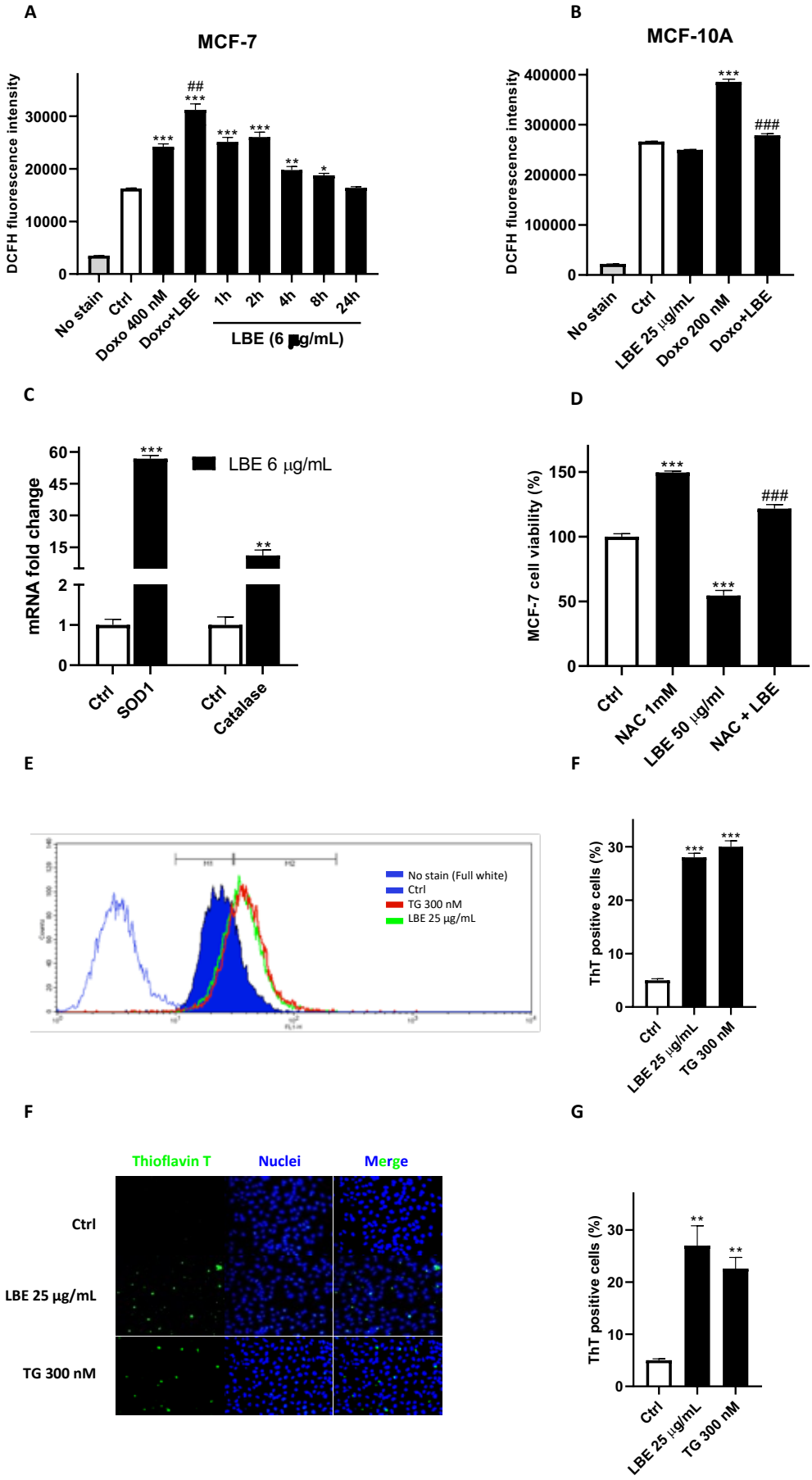
A
MCF-7
DCFH fluorescence intensity
No stain
Ctrl
Doxo 400 nM
Doxo+LBE
1h
2h
4h
8h
24h
LBE (6 µg/mL)
B
MCF-10A
DCFH fluorescence intensity
No stain
Ctrl
LBE 25 µg/mL
Doxo 200 nM
Doxo+LBE
C
mRNA fold change
LBE 6 µg/mL
Ctrl
SOD1
Ctrl
Catalase
D
MCF-7 cell viability (%)
Ctrl
NAC 1mM
LBE 50 µg/ml
NAC + LBE
E
No stain (Full white)
Ctrl
TG 300 nM
LBE 25 µg/mL
F
ThT positive cells (%)
Ctrl
LBE 25 µg/mL
TG 300 nM
F
Thioflavin T
Nuclei
Merge
Ctrl
LBE 25 µg/mL
TG 300 nM
G
ThT positive cells (%)
Ctrl
LBE 25 µg/mL
TG 300 nM

***Figure 2.6**. LBE selectively triggers oxidative stress in MCF-7 breast cancer cell line while protecting MCF-10A cell line from doxorubicin-induced ROS. DCFH-DA assay was conducted on MCF-7 (**A**) and MCF-10A cells (**B**) to reveal ROS production. Doxorubicin was used as positive control (400 and 200 nM for 4 h). (**C**) Total RNA samples extracted from MCF-7 cells exposed for 24 h to LBE (6 µg/mL) were analyzed by q-PCR to detect catalase and SOD1 mRNA levels. (**D**) MCF-7 cell viability using NAC as antioxidant corroborates pro-oxidant mechanism of LBE. ThT assay was performed for both flow cytometry (**E**) and fluorescence microscopy (**G**) (Magnification 20×. N ≥ 10. Scale bar: 20 µm). TG 300 nM was used as positive control. (**F, H**) Quantitative analysis of ThT-positive cells was reported.*
Data are shown as mean ± SD of three different experiments performed in triplicate.
** $p < 0.05$ vs. Ctrl; ** $p < 0.01$ vs. Ctrl; *** $p < 0.001$ vs. Ctrl. $^{\#\#}$ $p < 0.01$ vs. Doxo.*
$^{\#\#\#}$ $p < 0.001$ vs. doxorubicin.

Western blot analysis was performed to evaluate the increase of the three principal UPR transducers: PKR-like ER kinase Ser/Thr protein kinase (PERK) expression, inositol-requiring Ser/Thr protein kinase 1α and RNA endonuclease (IRE1α) phosphorylation, as well as activating transcription factor 6 (ATF6) cleavage (**Figure 2.7 A**). Short times were specifically selected for the investigation, aligning with the functional timeframe of LBE concerning oxidative stress. This choice was also based on the role of the UPR, which typically aids cellular adaptation to such stress within a period of a few hours post-activation.

Figure 2.7 A shows that a concentration of 6 µg/mL of LBE led to a significant activation of all three transducers, indicative of a general cellular stress condition.

As expected, the chaperone glucose regulatory protein 78 (GRP78), the master regulator of the UPR, was found to be overexpressed compared to the control.

This overexpression is consistent with its role in regulating the binding release of the ER stress transducers, which also appear to be activated.

Moreover, considering that the ER stress response ultimately leads to caspase-12 activation (Morishima *et al.*, 2004), its activation following LBE administration was evaluated. A notable reduction in its non-cleaved form was observed after LBE administration (**Figures 2.7 A, B**).

Considering the strong increase in P-IRE1α, the activation of its target NLPR3 inflammasome was determined. Additionally, considering the endoribonuclease activity of IRE1α, to confirm its activation, a semiquantitative PCR and q-PCR analysis was performed to evaluate the levels of unconventional mRNA splicing of XBP1 ($p <$

0.001 vs Ctrl) (**Figures 2.7 C, D**), a specific transcription factor that undergoes excision of a 26-nucleotide unconventional intron from IRE1α.

The activation of PERK was also assessed through its downstream activation product, ATF4 (activating transcription factor 4), and was obtained significantly high levels of ATF4 compared to the control ($p < 0.001$ vs Ctrl) (**Figure 2.7 D**).

The remarkable activation of the ATF4 transcript, together with c-ATF6 and s-XBP1 activation, is fully compatible with the increased expression of their transcription factor CHOP (C/EBP Homologous Protein), as highlighted in **Figure 2.7 A**.

The CHOP protein, also known as GADD153 (growth arrest- and DNA damage-inducible gene 153), is activated as part of the UPR when ER stress is severe or prolonged. It plays a role in triggering pyroptosis through NLRP3 activation (Li *et al.*, 2020).

The expression of the antioxidant protein Nrf2, activated in a critical adaptive response to oxidative stress, was evaluated, revealing a time-dependent increase in its expression (**Figure 2.7 A**). Nrf2 was also activated, inter alia, from PERK phosphorylation.

Elevated levels of ROS prompt the opening of the ER calcium channels IP3Rs and the ryanodine receptor, resulting in the augmented release of Ca^{2+} from the ER. This process further disrupts proper protein folding within the ER, further leading to NLRP3 inflammasome activation (Gomez-Suaga *et al.*, 2018).

In this regard, the cytoplasmic calcium level was assessed. The effects are illustrated in a representative graph and the quantitative analysis result is depicted in **Figures 2.7 E** and **F**, executed in a calcium-depleted buffer.

Notably, a substantial alteration in Ca^{2+} concentrations was observed following LBE (25 µg/mL) administration, affirming its capacity to induce ER stress (LBE: $p < 0.05$ vs. Ctrl). Ionomycin was employed as a positive control.

Collectively, these results support a model in which LBE disrupts redox homeostasis in breast cancer cells, triggers endoplasmic reticulum stress, activates the NLRP3 inflammasome, and induces pyroptosis, while exerting antioxidant protection in epithelial cells.

This bifunctional redox behavior reinforces the potential of LBE as a candidate onconutraceutical agent targeting oxidative vulnerabilities in breast cancer.

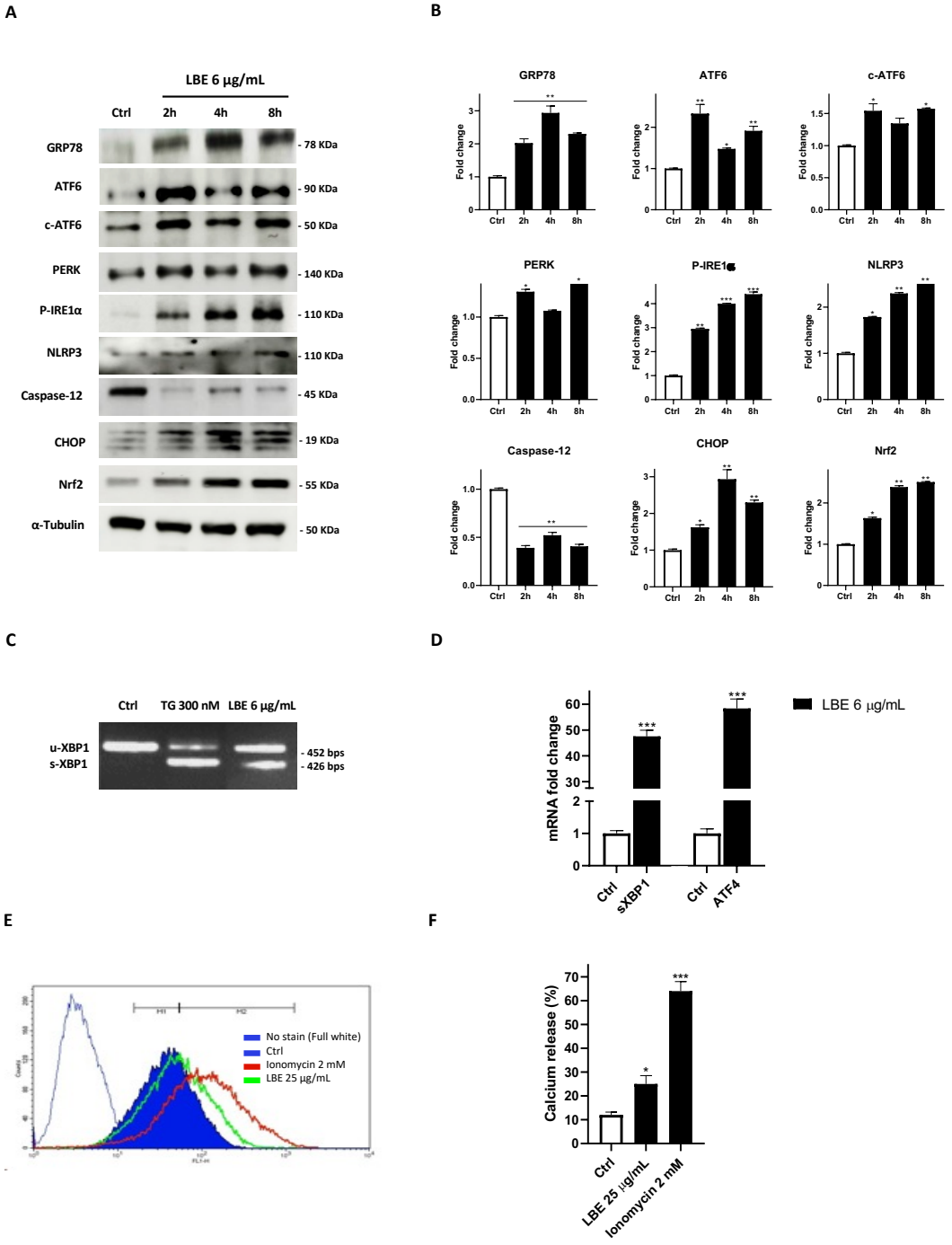

Figure 2.7. *Biochemical effects of LBE on ER stress pathways. (**A**) Representative Western blot images showing increased expression of ER stress markers GRP78, ATF6, PERK, and P-IRE1α and some of their downstream targets (NLRP3, CHOP, Nrf2). Levels of cleaved proteins involved in UPR (c-caspase-12 and c-ATF6) were also evaluated. α-tubulin was used to check equal loading of protein extracts. (**B**) Densitometric analysis of Western blots. (**C**) Total RNA samples extracted from MCF-7 cells exposed for 8 h to LBE were analyzed by RT-PCR to detect*

*XBP1 mRNA splicing forms. (**D**) s-XBP1 and ATF4 mRNA ER stress hallmarks were assessed through q-PCR. GAPDH was used as housekeeping control. (**E**) Calcium mobilization analysis was performed with Mag fluo4-AM by flow cytometry. Ionomycin 2 mM was used as positive control. (**F**) Quantitative analysis of calcium-releasing cells was performed.*
Data are shown as mean ± SD of three different experiments performed in triplicate.
** p < 0.05 vs. Ctrl; ** p < 0.01 vs. Ctrl; *** p < 0.001 vs. Ctrl.*

2.5 Conclusions

Nutraceuticals have garnered significant attention in cancer research owing to their multifaceted effects and low toxicity profile.

They play a crucial role in anticancer treatments by enhancing therapy efficacy, reducing drug concentrations to alleviate adverse effects, and delaying the development of therapy resistance. Despite their promising role in cancer treatment, the specific mechanisms underlying their actions remain largely unclear.

This lack of mechanistic understanding can hinder their optimization and integration into clinical practice.

The present study aimed to conduct a comprehensive analysis of the onconutraceutical mechanism of the ethanolic extract derived from *Lycium barbarum* fruits. Was demonstrated for the first time the inhibitory effects of LBE on cell proliferation through the induction of inflammatory programmed cell death in breast cancer cells. This effect could be mediated by the pro-oxidant action of the extract, leading to the activation of ER stress.

The results obtained showed that goji berry extract selectively triggers pyroptosis of tumor cells without having a significant toxic effect on healthy cells.

However, further studies are needed to elucidate the mechanism and the crucial role of ER stress in the activation of pyroptosis, as well as preclinical studies to corroborate these data. Furthermore, the current findings on the antitumor actions of LBE suggest that its bioactive compounds could be used as part of adjuvant therapeutic approaches in the potential treatment of cancer with anthracyclines, contributing to chemoprevention and tumor cell growth control.

Taken together, these findings highlight that *Lycium barbarum* may be a very promising natural extract in cancer therapy.

2.6 Supporting information

Table S2.1. *Metabolomic profiling of LBE.*

Peak	Compound	Rt (min)	$[M-H]^-$	$[M+H]^+$	MS/MS	Molecular Formula	Error (ppm)	Classification
1	Gallic acid	2.37	169.0136	-	125.0233	$C_7H_5O_5$	1.55	Phenolic acids
2	*p*-coumaric acid-hexoside	3.41	325.0934	-	119.0491 163.0392	$C_{15}H_{18}O_8$	0.76	Hydroxycinnamic acid derivates
3	Hydroxybenzoic acid	5.15	137.0235	-	93.0333	$C_7H_6O_3$	0.74	Phenolic acids
4	Benzoic acid	6.68	121.0285	-	/	$C_7H_6O_2$	−0.33	Organic acids
5	Blechnic acid	7.37	371.0988	-	119.0491 163.0392	$C_{16}H_{20}O_{10}$	2.69	Flavonoids
6	di-*O*-caffeoylquinic acid	8.60	515.1413	-	353.0885 323.0759	$C_{22}H_{28}O_{14}$	1.77	Hydroxycinnamic acid derivates
7	Caffeic acid	9.06	179.0344	-	135.0441	$C_9H_8O_4$	1.13	Hydroxycinnamic acids
8	*p*-coumaric acid-hexoside (*isomer I*)	9.35	325.0934	-	145.0285 163.0391	$C_{15}H_{18}O_8$	4.42	Hydroxycinnamic acid derivates
9	di-*O*-caffeoylquinic acid	10.10	515.1415	-	191.0554 179.0333	$C_{22}H_{28}O_{14}$	3.78	Hydroxycinnamic acid derivates
10	*N*-Caffeoyl, *N'*-dihydrocaffeoyl spermidine dihexose	10.46	-	796.3496	163.0388 220.0966 310.2125 472.2498	$C_{37}H_{53}N_3O_{16}$	−1.31	Hydroxycinnamic acid amides
11	N^1-dihydrocaffeoyl, N^{10}-caffeoyl spermidine hexose	11.25	-	634.2977	163.0389 220.0967 165.0546 472.2523 310.2133	$C_{31}H_{43}N_3O_{11}$	−0.54	Hydroxycinnamic acid amides
12	Ferulic acid hexoside	11.26	355.1041	-	175.0392 160.0157	$C_{16}H_{20}O_9$	6.70	Hydroxycinnamic acid derivates
13	*p*-coumaric acid-hexoside (*isomer II*)	11.40	325.0933	-	145.0285 163.0390	$C_{15}H_{18}O_8$	2.26	Hydroxycinnamic acid derivates

					119.0491			
14	N^1-dihydrocaffeoyl, N^{10}-caffeoyl spermidine	11.76	470.2301	-	135.0442 308.1985 163.0402 291.1843	$C_{25}H_{33}N_3O_6$	−4.32	Hydroxycinnamic acid amides
15	N^1-dihydrocaffeoyl, N^{10}-caffeoyl spermidine (*isomer I*)	11.77	-	472.2445	163.0389 220.0967 310.2130 293.1865 236.1276	$C_{25}H_{33}N_3O_6$	1.08	Hydroxycinnamic acid amides
16	*p*-coumaric acid	11.88	163.0392	-	119.0490	$C_9H_8O_3$	0.94	Hydroxycinnamic acids
17	*p*-coumaric acid (*isomer I*)	11.97	-	165.0547	147.0439 119.0492	$C_9H_8O_3$	−0.96	Hydroxycinnamic acids
18	N^1,N^{10}-bis-(caffeoyl) spermidine dihexose	12.07	-	794.3350	163.0389 220.0969 308.1956 632.3118 470.2307	$C_{40}H_{49}N_4O_{13}$	−0.28	Hydroxycinnamic acid amides
19	*p*-coumaroyl-quinic acid	12.76	337.0935	-	191.0553 93.0333	$C_{16}H_{18}O_8$	3.09	Hydroxycinnamic acid derivates
20	*O-trans*-feruloyl-*O*-*β*-d-glucopyranosyl-*α*-d-glucopyranoside	12.80	517.1569	-	193.0500 175.0392	$C_{22}H_{30}O_{14}$	2.32	Hydroxycinnamic acid derivates
21	Rutin hexose	13.35	771.2005	-	609.1435 462.0828 301.0348	$C_{33}H_{40}O_{21}$	2.72	Flavonoids
22	Scopoletin	13.70	191.0343	-	176.0107 148.0156 134.0363	$C_{10}H_8O_4$	2.18	Coumarins
23	Ferulic acid	14.11	193.0501	-	178.0264 149.0598	$C_{10}H_{10}O_4$	2.42	Hydroxycinnamic acids

24	*N*-acetyl-DL-tryptophan	14.23	245.0931	-	203.0820 74.0235 116.0493	$C_{13}H_{14}N_2O_3$	3.93	Tryptophan derivates
25	Azelaic acid	17.44	187.0968	-	125.0961 97.0646	$C_9H_{16}O_4$	2.02	Fatty acids
26	Rutin	18.05	609.1463	-	300.0275 301.0356	$C_{27}H_{30}O_{16}$	0.41	Flavonoids
27	Rutin (*isomer I*)	18.07	-	611.1603	303.0497 465.1002	$C_{27}H_{30}O_{16}$	−0.63	Flavonoids
28	Quercetin-*O*-hexoside	18.24	463.0886	-	300.0275 301.0358	$C_{21}H_{20}O_{12}$	2.69	Flavonoids
29	*N-p-cis/trans*-coumaroyl-tyramine	18.81	282.1139	-	119.0491 243.0793	$C_{17}H_{17}NO_3$	4.28	Hydroxycinnamic acid amides
30	Naringenin-*O*-hexoside (Prunin)	18.99	433.1145	-	271.0610	$C_{21}H_{22}O_{10}$	2.38	Flavonoids
31	Kaempferol *O*-hexoside-rhamnoside (Nictoflorin)	19.90	593.1516	-	285.0405 255.0298	$C_{27}H_{30}O_{15}$	2.04	Flavonoids
32	Kaempferol *O*-hexoside-rhamnoside (Nictoflorin) (*isomer I*)	19.96	-	595.1658	287.0550 258.2194	$C_{27}H_{30}O_{15}$	−0.37	Flavonoids
33	*N-cis/trans*-feruloyltyramine	20.05	312.1245	-	148.0520 297.1012	$C_{18}H_{19}NO_4$	3.75	Hydroxycinnamic acid amides
34	Kaempferol-*O*-hexoside	20.06	447.0939	-	284.0340 285.0403 255.0299	$C_{21}H_{20}O_{11}$	−0.87	Flavonoids
35	Isorhamnetin-*O*-rutinoside	20.45	623.1626	-	315.0511 300.0198	$C_{28}H_{32}O_{16}$	2.13	Flavonoids
36	Isorhamnetin-*O*-hexoside	20.68	477.1046	-	314.0432 243.0302 271.0262	$C_{22}H_{22}O_{12}$	1.09	Flavonoids

37	*N-p-cis/trans*-coumaroyl-tyramine (*isomer I*)	21.60	282.1139	-	119.0491	$C_{17}H_{17}NO_3$	4.28	Hydroxycinnamic acid amides
38	*N-p-cis/trans*-coumaroyl-tyramine (*isomer II*)	21.63	-	284.1280	147.0439 121.0649 164.0692	$C_{17}H_{17}NO_3$	−0.88	Hydroxycinnamic acid amides
39	*N-cis/trans*-feruloyltyramine	22.62	312.1245	-	148.0520 297.1007	$C_{18}H_{19}NO_4$	4.15	Hydroxycinnamic acid amides
40	Quercetin	23.36	301.2023	-	151.0028 178.9983	$C_{15}H_{10}O_7$	4.13	Flavonoids
41	Naringenin	23.82	271.0615	-	119.0491 151.0028	$C_{15}H_{12}O_5$	5.03	Flavonoids
42	Trihydroxy-octadecadienoic acid (TriHODE)	24.46	327.2179	-	171.1019 211.1336 291.2002	$C_{18}H_{32}O_5$	4.33	Fatty acids
43	Trihydroxy-octadecenoic acid	24.84	329.2334	-	171.1018 139.1117 211.1336	$C_{18}H_{34}O_5$	3.76	Fatty acids
44	Trihydroxy-octadecadienoic acid (TriHODE) (*isomer I*)	25.48	327.2180	-	201.1126 213.1127 291.1967	$C_{18}H_{32}O_5$	3.68	Fatty acids
45	Trihydroxy-octadecadienoic acid (TriHODE) (*isomer II*)	26.11	327.2180	-	171.1019 201.1127 291.1961	$C_{18}H_{32}O_5$	4.05	Fatty acids
46	13-Oxo-octadecadienoic acid (13-Oxo-ODE)	26.61	-	295.2268	277.2162 179.1434	$C_{18}H_{30}O_3$	0.95	Fatty acids
47	Dihydroxy octadecadienoic acid (DiHODE)	26.63	311.2230	-	293.2125 275.2019	$C_{18}H_{32}O_4$	4.29	Fatty acids
48	Dihydroxy octadecadienoic acid (DiHODE) (*isomer I*)	26.76	311.2230	-	293.2125 275.2019	$C_{18}H_{32}O_4$	4.69	Fatty acids

49	Dihydroxy octadecadienoic acid (DiHODE) (*isomer II*)	26.94	311.2231	-	293.2123 275.2020	$C_{18}H_{32}O_4$	4.49	Fatty acids
50	13-Oxo-octadecadienoic acid (13-Oxo-ODE) (*isomer I*)	27.40	293.2126	-	275.2016 171.1017	$C_{18}H_{30}O_3$	4.79	Fatty acids
51	*tris*-(Dihydrocaffeoyl) spermine	27.41	-	693.3461	293.0565	$C_{37}H_{48}N_4O_9$	−5.43	Hydroxycinnamic acid amides
52	Hydroxy-octadecadienoic acid (HODE)	27.86	295.2279	-	171.1018 277.2176	$C_{18}H_{32}O_3$	4.05	Fatty acids
53	13-Oxo-octadecadienoic acid (13-Oxo-ODE) (*isomer II*)	28.24	293.2124	-	275.2015	$C_{18}H_{30}O_3$	4.37	Fatty acids
54	Palmitic acid	28.91	255.2330	-	-	$C_{16}H_{31}O_2$	4.07	Fatty acids
55	Linoleamide	29.36	-	280.2636	263.2368	$C_{18}H_{33}NO$	−0.34	Fatty acids
56	Palmitic amide	29.84	-	256.2636	88.0761 102.0913 172.1689	$C_{16}H_{33}NO$	0.47	Fatty acids
57	Oleamide	30.06	-	282.2789	265.2529 247.2418	$C_{18}H_{36}NO$	0.66	Fatty acids
58	Oleic acid	30.86	281.2487	-	-	$C_{18}H_{34}O_2$	4.09	Fatty acids
59	Protocatechuate	31.01	153.0184	-	109.0283	$C_7H_5O_4^-$	0.89	Phenolic acids
60	Violaxanthin	34.24	-	601.4229	-	$C_{40}H_{56}O_4$	−4.10	Xanthophylls

Table S2.2. *Quantitative analysis of the major compounds identified in LBE.*

Peak	Compounds	µg CAE/g DW
2	*p*-Coumaric acid-hexoside (*isomer I*)	27.98 ± 1.38
6	3,4-di-*O*-caffeoylquinic acid	6.20 ± 0.18
7	Caffeic acid	1.07 ± 0.12
8	*p*-coumaric acid-hexoside (*isomer II*)	35.55 ± 2.84
9	3,5-di-*O*-caffeoylquinic acid	7.68 ± 1.98
12	Ferulic acid hexoside	<LOQ
13	*p*-coumaric acid-hexoside (*isomer III*)	<LOQ
14	N^1-dihydrocaffeoyl, N^{10}-caffeoyl spermidine	<LOQ
16	*p*-coumaric acid	214.43 ± 1.42
19	*p*-coumaroyl-quinic acid	2.38 ± 0.076
23	Ferulic acid	0.99 ± 0.18
29	*N-p-cis/trans*-coumaroyl-tyramine	<LOQ
33	*N-cis/trans*-feruloyltyramine	407.24 ± 20.86
37	*N-p-cis/trans*-coumaroyl-tyramine (*isomer I*)	53.05 ± 3.07
39	*N-cis/trans*-feruloyltyramine	522.52 ± 24.10
	Total Hydroxycinnamic Acids	1279.10 ± 0.05
		µg RE/g DW
21	Rutin hexose	18.49 ± 7.96
26	Rutin	1607.36 ± 89.85
28	Quercetin-3-*O*-hexoside	<LOQ
30	Naringenin-7-*O*-hexoside (Prunin)	1.15 ± 1.58
31	Kaempferol 3-*O*-hexoside-7-*O*-rhamnoside (Nictoflorin) (*isomer I*)	298.88 ± 17.93
34	Kaempferol-3-*O*-hexoside	<LOQ
35	Isorhamnetin-3-*O*-rutinoside	182.55 ± 36.32
36	Isorhamnetin-3-*O*-hexoside	<LOQ
40	Quercetin	<LOQ
41	Naringenin	14.91 ± 8.61
	Total Flavonoids	2123.34 ± 0.06
		mg OAE/g DW
42	Trihydroxy-octadecadienoic acid (TriHODE)	3.22 ± 0.30

43	Trihydroxy-octadecenoic acid	1201.76 ± 30.44
44	Trihydroxy-octadecadienoic acid (TriHODE) (*isomer I*)	276.61 ± 6.20
45	Trihydroxy-octadecadienoic acid (TriHODE) (*isomer II*)	440.45 ± 10.03
47	Dihydroxy octadecadienoic acid (DiHODE)	538.99 ± 6.96
48	Dihydroxy octadecadienoic acid (DiHODE) (*isomer I*)	435.75 ± 2.64
49	Dihydroxy octadecadienoic acid (DiHODE) (*isomer II*)	433.99 ± 7.60
50	13-Oxo-octadecadienoic acid (13-Oxo-ODE) (*isomer I*)	472.07 ± 18.54
52	Hydroxy-octadecadienoic acid (HODE)	1737.23 ± 23.17
53	13-Oxo-octadecadienoic acid (13-Oxo-ODE) (*isomer II*)	220.76 ± 9.00
54	Palmitic acid	<LOQ
58	Oleic acid	26.25 ± 0.33
	Total Fatty Acids	5787.08 ± 24.83

Data expressed as mean ± deviation standard (n = 3). CAE: caffeic acid equivalents; RE: rutin equivalents; OAE: oleic acid equivalents

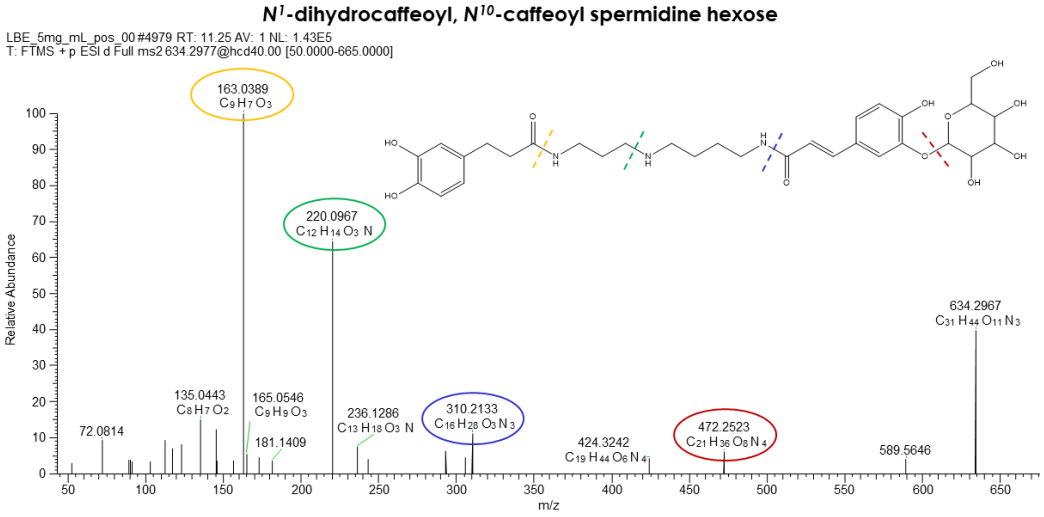

Figure S2.1. *UHPLC-ESI(+)-Orbitrap-MS/MS spectra and proposed fragmentation pathway of N^1-Dihydrocaffeoyl, N^{10}-caffeoyl spermidine hexose.*

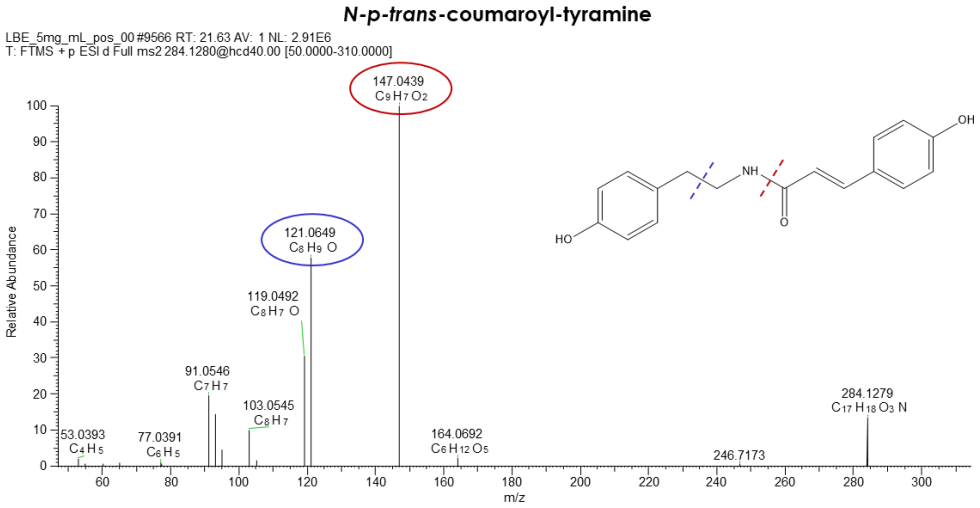

Figure S2.2. *UHPLC-ESI(+)-Orbitrap-MS/MS spectra and proposed fragmentation pathway of N-p-trans-coumaroyltyramine.*

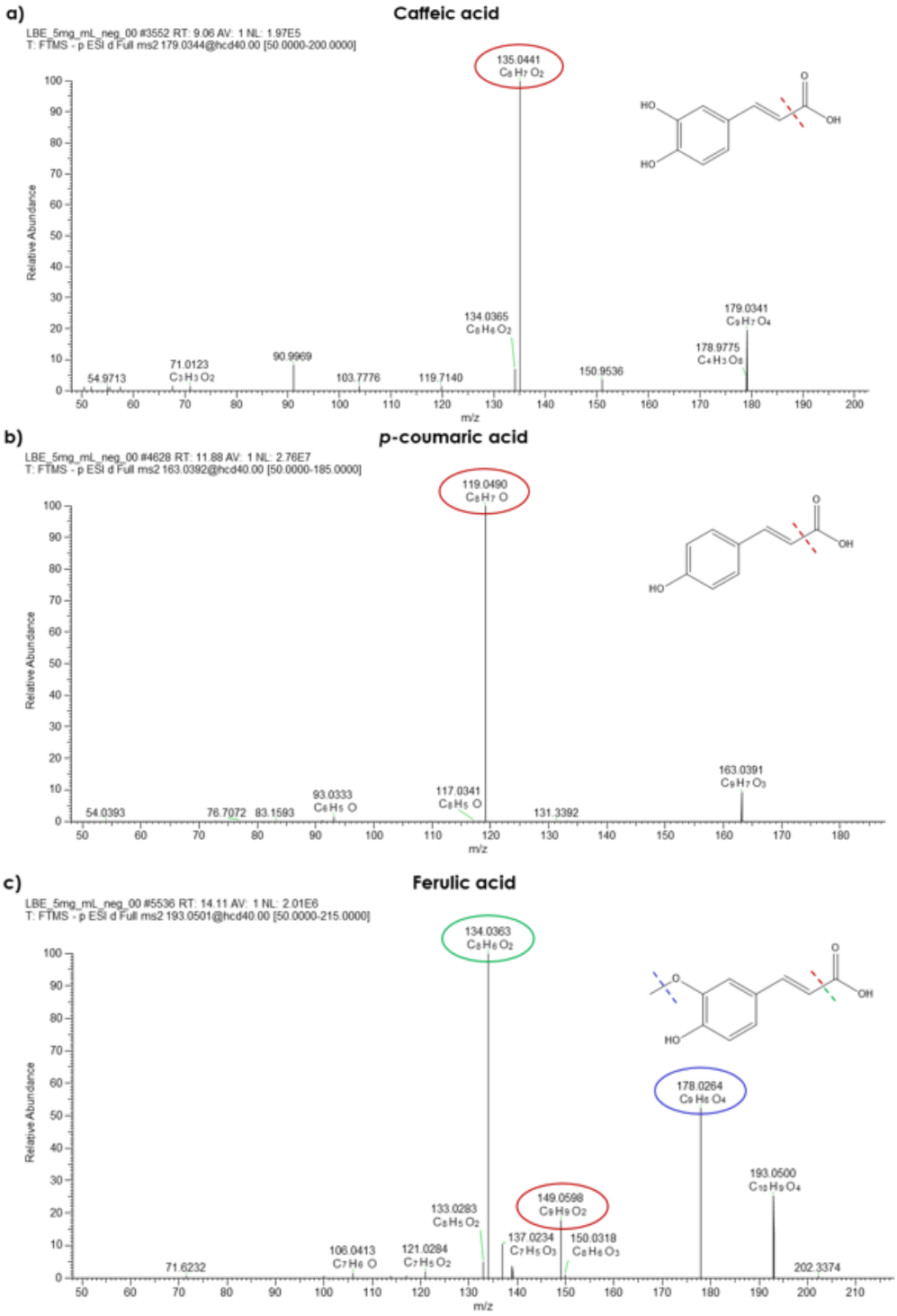

Figure S2.3. *UHPLC-ESI(–)-Orbitrap-MS/MS spectra and proposed fragmentation pathway of a) Caffeic acid, b) p-coumaric acid, c) ferulic acid.*

2.7 References

Ahmed, M.S., Uddin, M.J., Hossen, M.J., Rahman, M.A., Mohibbullah, M., Hannan, M.A. and Choi, J.-S. (2022). Dendritic Cells (DCs)-Based Cancer Immunotherapy: A Review on the Prospects of Medicinal Plants and Their Phytochemicals as Potential Pharmacological Modulators. *Applied Sciences*, 12, 9452.

Alcázar Magaña, A., Kamimura, N., Soumyanath, A., Stevens, J.F. and Maier, C.S. (2021). Caffeoylquinic acids: Chemistry, biosynthesis, occurrence, analytical challenges, and bioactivity. *The Plant Journal*, 107, 1299–1319.

Andrés, C.M.C., Pérez de la Lastra, J.M., Juan, C.A., Plou, F.J. and Pérez-Lebeña, E. (2023). Polyphenols as Antioxidant/Pro-Oxidant Compounds and Donors of Reducing Species: Relationship with Human Antioxidant Metabolism. *Processes*, 11, 2771.

Aquino, G., Basilicata, M.G., Crescenzi, C., Vestuto, V., Salviati, E., Cerrato, M., Ciaglia, T., Sansone, F., Pepe, G. and Campiglia, P. (2023). Optimization of microwave-assisted extraction of antioxidant compounds from spring onion leaves using Box–Behnken design. *Scientific Reports*, 13, 14923.

Carolina, L., Ramirez, A. and Aguilera, R.J. (2011). Differential nuclear staining assay for high-throughput screening to identify cytotoxic compounds. *Current Cell Biochemistry*, 1, 1.

Cerqua, I., Musella, S., Peltner, L.K., D'Avino, D., Di Sarno, V., Granato, E., Vestuto, V., Di Matteo, R., Pace, S., Ciaglia, T., et al. (2022). Discovery and Optimization of Indoline-Based Compounds as Dual 5-LOX/sEH Inhibitors: In Vitro and In Vivo Anti-Inflammatory Characterization. *Journal of Medicinal Chemistry*, 65, 14456–14480.

Chao, J.C., Chiang, S.W., Wang, C.C., Tsai, Y.H. and Wu, M.S. (2006). Hot water-extracted *Lycium barbarum* and *Rehmannia glutinosa* inhibit proliferation and induce apoptosis of hepatocellular carcinoma cells. *World Journal of Gastroenterology*, 12, 4478–4484.

Courage, S.D., Haihui, Z., Vera, G., David, A.-D. and Yuqing, D. (2024). Anti- and pro-oxidant properties of polyphenols and their role in modulating glutathione synthesis, activity and cellular redox potential: Potential synergies for disease management. *Advances in Redox Research*, 11, 100099.

Cui, Y., Zhou, J., Chen, X., Xu, Z., Wang, Y., Sun, W., Song, J. and Yao, H. (2019). Complete chloroplast genome and comparative analysis of three *Lycium* (Solanaceae) species with medicinal and edible properties. *Gene Reports*, 17, 100464.

D'Angelo, S., Martino, E., Ilisso, C.P., Bagarolo, M.L., Porcelli, M. and Cacciapuoti, G. (2017). Pro-oxidant and pro-apoptotic activity of polyphenol extract from Annurca apple and its underlying mechanisms in human breast cancer cells. *International Journal of Oncology*, 51, 939–948.

Eghbaliferiz, S. and Iranshahi, M. (2016). Prooxidant Activity of Polyphenols, Flavonoids, Anthocyanins and Carotenoids: Updated Review of Mechanisms and Catalyzing Metals. *Phytotherapy Research*, 30, 1379–1391.

Gan, L., Zhang, S.H., Yang, X.L. and Xu, H.B. (2014). Immunomodulation and antitumor activity by a polysaccharide-protein complex from *Lycium barbarum*. *International Immunopharmacology*, 4, 563–569.

Georgiev, K.D., Slavov, I.J. and Iliev, I.A. (2019). Synergistic Growth Inhibitory Effects of *Lycium barbarum* (Goji berry) Extract with Doxorubicin against Human Breast Cancer Cells. *Journal of Pharmaceutical Pharmacology Research*, 3, 051–058.

Gomez-Suaga, P., Bravo-San Pedro, J.M., Gonzalez-Polo, R.A., Fuentes, J.M. and Niso-Santano, M. (2018). ER-mitochondria signaling in Parkinson's disease. *Cell Death & Disease*, 9, 337.

Gong, G., Liu,Q., Deng, Y., Dang, T., Dai, W., Liu, T., Liu, Y., Sun, J., Wang, L., Liu, Y., et al. (2020). Arabinogalactan derived from *Lycium barbarum* fruit inhibits cancer cell growth via cell cycle arrest and apoptosis. *International Journal of Biological Macromolecules*, 149, 639–650.

Guida, F., Kidman, R., Ferlay, J., Schüz, J., Soerjomataram, I., Kithaka, B., Ginsburg, O., Mailhot Vega, R.B., Galukande, M., Parham, G., et al. (2022). Global and regional estimates of orphans attributed to maternal cancer mortality in 2020. *Nature Medicine*, 28, 2563–2572.

Hvarchanova, N., Stoeva, S., Radeva-Ilieva, M., Zhelev, I., Georgieva, M., Dzhenkov, D. and Georgiev, K.D. (2023). Cardio- and nephroprotective effects of fractions isolated from *Lycium barbarum* (goji berry) in models of cardio- and nephrotoxicity in rats. *Biotechnology & Biotechnological Equipment*, 37, 64–73.

Ilić, T., Dodevska, M., Marčetić, M., Božić, D., Kodranov, I. and Vidović, B. (2020). Chemical Characterization, Antioxidant and Antimicrobial Properties of Goji Berries Cultivated in Serbia. *Foods*, 6, 1614.

Imeneo, V., De Bruno, A., Piscopo, A., Romeo, R. and Poiana, M. (2022). Valorization of 'Rossa di Tropea' Onion Waste through Green Recovery Techniques of Antioxidant Compounds. *Sustainability*, 14, 4387.

Irazabal, M.V. and Torres, V.E. (2020). Reactive Oxygen Species and Redox Signaling in Chronic Kidney Disease. *Cells*, 9, 1342.

Islam, T., Yu, X., Badwal, T.S. and Xu, B. (2017). Comparative studies on phenolic profiles, antioxidant capacities and carotenoid contents of red goji berry (*Lycium barbarum*) and black goji berry (*Lycium ruthenicum*). *Chemical Central Journal*, 11, 59.

Kang, J., Price, W.E., Ashton, J., Tapsell, L.C. and Johnson, S. (2016). Identification and characterization of phenolic compounds in hydromethanolic extracts of sorghum wholegrains by LC-ESI-MS(n). *Food Chemistry*, 211, 215–226.

Kwok, S.S., Bu, Y., Lo, A.C., Chan, T.C., So, K.F., Lai, J.S. and Shih, K.C. (2019). A Systematic Review of Potential Therapeutic Use of *Lycium barbarum* Polysaccharides in Disease. *BioMed Research International*, 2019, 4615745.

Li, W., Cao, T., Luo, C., Cai, J., Zhou, X., Xiao, X. and Liu, S. (2020). Crosstalk between ER stress, NLRP3 inflammasome, and inflammation. *Applied Microbiology and Biotechnology*, 104, 6129–6140.

Li, W.S., Lin, S.C., Chu, C.H., Chang, Y.K., Zhang, X., Lin, C.C. and Tung, Y.T. (2021). The Gastroprotective Effect of Naringenin against Ethanol-Induced Gastric Ulcers in Mice through Inhibiting Oxidative and Inflammatory Responses. *International Journal of Molecular Sciences*, 22, 11985.

Li, X.M. (2007). Protective effect of *Lycium barbarum* polysaccharides on streptozotocin-induced oxidative stress in rats. *International Journal of Biological Macromolecules*, 40, 461–465.

Liu, J., Pu, Q., Qiu, P. and Di, D. (2021). Polysaccharides isolated from *Lycium barbarum* L. by integrated tandem hybrid membrane technology exert antioxidant activities in mitochondria. *Industrial Crops and Products*, 168, 113547.

Liu, W., Xia, M., Bai, J., Yang, L., Wang, Z., Wang, R. and Shi, Y. (2021). Chemical characterization and 5α-reductase inhibitory activity of phenolic compounds in goji berries. *Journal of Pharmaceutical and Biomedical Analysis*, 201, 114119.

Lu, S.-P. and Zhao, P.-T. (2010). Chemical characterization of *Lycium barbarum* polysaccharides and their reducing myocardial injury in ischemia/reperfusion of rat heart. *International Journal of Biological Macromolecules*, 47, 681–684.

Lu, W., Jiang, Q., Shi, H., Niu, Y., Gao, B. and Yu, L.L. (2014). Partial least-squares-discriminant analysis differentiating Chinese wolfberries by UPLC-MS and flow injection mass spectrometric (FIMS) fingerprints. *Journal of Agricultural and Food Chemistry*, 62, 9073–9080.

Martucciello, S., Masullo, M., Cerulli, A. and Piacente, S. (2020). Natural Products Targeting ER Stress, and the Functional Link to Mitochondria. *International Journal of Molecular Sciences*, 21, 1905.

Miranda, M.R., Basilicata, M.G., Vestuto, V., Aquino, G., Marino, P., Salviati, E., Ciaglia, T., Domínguez-Rodríguez, G., Moltedo, O., Campiglia, P., Pepe, G. and Manfra, M. (2024). Anticancer Therapies Based on Oxidative Damage: *Lycium barbarum* Inhibits the Proliferation of MCF-7 Cells by Activating Pyroptosis through Endoplasmic Reticulum Stress. *Antioxidants*, 13(6), 708.

Miranda, M.R., Vestuto, V., Amodio, G., Manfra, M., Pepe, G. and Campiglia, P. (2024). Antitumor Mechanisms of *Lycium barbarum* Fruit: An Overview of In Vitro and In Vivo Potential. *Life*, 14(3), 420.

Morishima, N., Nakanishi, K., Tsuchiya, K., Shibata, T. and Seiwa, E. (2004). Translocation of Bim to the endoplasmic reticulum (ER) mediates ER stress signaling for activation of caspase-12 during ER stress-induced apoptosis. *Journal of Biological Chemistry*, 279, 50375–50381.

Nardi, G.M., Farias Januario, A.G., Freire, C.G., Megiolaro, F., Schneider, K., Perazzoli, M.R., Do Nascimento, S.R., Gon, A.C., Mariano, L.N., Wagner, G., et al. (2016). Anti-inflammatory activity of berry fruits in mice model of inflammation is based on oxidative stress modulation. *Pharmacognosy Research*, 8, S42–S49.

Potterat, O. (2010). Goji (*Lycium barbarum* and *L. chinense*): Phytochemistry, Pharmacology and Safety in the Perspective of Traditional Uses and Recent Popularity. *Planta Medica*, 76, 7–19.

Procházková, D., Boušová, I. and Wilhelmová, N. (2011). Antioxidant and prooxidant properties of flavonoids. *Fitoterapia*, 82, 513–523.

Ribeiro, D., Freitas, M., Silva, A.M.S., Carvalho, F. and Fernandes, E. (2018). Antioxidant and pro-oxidant activities of carotenoids and their oxidation products. *Food and Chemical Toxicology*, 120, 681–699.

Šamec, D., Bogović, M., Vincek, D., Martinčić, J. and Salopek-Sondi, B. (2014). Assessing the authenticity of the white cabbage (*Brassica oleracea* var. *capitata* f. *alba*) cv. 'Varaždinski' by molecular and phytochemical markers. *Food Research International*, 60, 266–272.

Shin, J., Song, M.H., Oh, J.W., Keum, Y.S. and Saini, R.K. (2020). Pro-Oxidant Actions of Carotenoids in Triggering Apoptosis of Cancer Cells: A Review of Emerging Evidence. *Antioxidants*, 9, 532.

Skenderidis, P., Lampakis, D., Giavasis, I., Leontopoulos, S., Petrotos, K., Hadjichristodoulou, C. and Tsakalof, A. (2019). Chemical Properties, Fatty-Acid Composition, and Antioxidant Activity of Goji Berry (*Lycium barbarum* L. and *Lycium chinense* Mill.) Fruits. *Antioxidants*, 8, 60.

Tian, X., Liang, T., Liu, Y., Ding, G., Zhang, F. and Ma, Z. (2019). Extraction, Structural Characterization, and Biological Functions of *Lycium barbarum* Polysaccharides: A Review. *Biomolecules*, 9, 389.

Tsuchiya, K. (2021). Switching from Apoptosis to Pyroptosis: Gasdermin-Elicited Inflammation and Antitumor Immunity. *International Journal of Molecular Sciences*, 22, 426.

Umar, T., Shalini, S., Raza, M.K., Gusain, S., Kumar, J., Ahmed, W., Tiwari, M. and Hoda, N. (2018). New amyloid beta-disaggregating agents: Synthesis, pharmacological evaluation, crystal structure and molecular docking of N-(4-((7-chloroquinolin-4-yl)oxy)-3-ethoxybenzyl)amines. *MedChemComm*, 9, 1891–1904.

Wang, H., Li, J., Tao, W., Zhang, X., Gao, X., Yong, J., Zhao, J., Zhang, L., Li, Y. and Duan, J.-A. (2018). *Lycium ruthenicum* studies: Molecular biology, phytochemistry and pharmacology. *Food Chemistry*, 240, 759–766.

Wang, H., Zhu, Y., Xie, D., Zhang, H., Zhang, Y., Jin, P. and Du, Q. (2022). The Effect of Microwave Radiation on the Green Color Loss of Green Tea Powder. *Foods*, 11, 2540.

Xiao, X., Ren, W., Zhang, N., Bing, T., Liu, X., Zhao, Z. and Shangguan, D. (2019). Comparative study of the chemical constituents and bioactivities of the extracts from fruits, leaves and root barks of *Lycium barbarum*. *Molecules*, 24, 1585.

Yossa Nzeuwa, I.B., Nea, F., Makemteu, J., Ngandeu Neubi, G.M., Mabou, F.D., Noumedem Kenfack, J.A., Djeussi, D.E. and Sun, G. (2022). Comparative study of polyphenols quantification, total phenolic content, and antioxidant activities of the fruits of three plants of the family of Solanaceae: *Lycium ruthenicum*, *Lycium barbarum*, and *Lycium chinense*. *Investigational Medicinal Chemistry and Pharmacology*, 5, 2.

Yossa Nzeuwa, I.B., Xia, Y., Qiao, Z., Feng, F., Bian, J., Liu, W. and Qu, W. (2017). Comparison of the origin and phenolic contents of *Lycium ruthenicum* Murr. by high-performance liquid chromatography fingerprinting combined with quadrupole time-of-flight mass spectrometry and chemometrics. *Journal of Separation Science*, 40, 1234–1243.

Yu, C., Wang, D., Yang, Z. and Wang, T. (2022). Pharmacological Effects of Polyphenol Phytochemicals on the Intestinal Inflammation via Targeting TLR4/NF-κB Signaling Pathway. *International Journal of Molecular Sciences*, 23, 6939.

Yuan, Q., Yuan, Y., Zheng, Y., Sheng, R., Liu, L., Xie, F. and Tan, J. (2021). Anti-cerebral ischemia reperfusion injury of polysaccharides: A review of the mechanisms. *Biomedicine & Pharmacotherapy*, 137, 111303.

Zeng, S., Liu, Y., Wu, M., Liu, X., Shen, X., Liu, C. and Wang, Y. (2014). Identification and validation of reference genes for quantitative real-time PCR normalization and its applications in lyceum. *PLOS ONE*, 9, e97039.

Zhang, M., Choe, J., Bu, T., Liu, S. and Kim, S. (2022). Comparison of Antioxidant Properties and Metabolite Profiling of *Acer pseudoplatanus* Leaves of Different Colors. *Antioxidants*, 12, 65.

Zhang, X.J., Yu, H.Y., Cai, Y.J. and Ke, M. (2017). *Lycium barbarum* polysaccharides inhibit proliferation and migration of bladder cancer cell lines BIU87 by suppressing PI3K/AKT pathway. *Oncotarget*, 8, 5936–5942.

Zheng, Z., Pan, X., Luo, L., Zhang, Q., Huang, X., Liu, Y., Wang, K. and Zhang, Y. (2022). Advances in oral absorption of polysaccharides: Mechanism, affecting factors, and improvement strategies. *Carbohydrate Polymers*, 282, 119110.

3. Chapter III: *Olea europaea* L. leaves extract

Olea europea L. leaves extract (OE) ameliorates non-alcoholic lipid accumulation in hepatic cells

3.1 Abstract

Olive leaves (*Olea europaea* L.), traditionally considered an agricultural by-product, are emerging as a rich source of BACs with antioxidant properties relevant to metabolic disorders. MAFLD are characterized by excessive lipid accumulation in liver and are closely associated with oxidative stress and disrupted cellular homeostasis. Identifying natural compounds able to modulate lipid metabolism and limit lipotoxic damage represents a promising strategy for their prevention and early management.

Therefore, was evaluated the protective effects of an olive leaves extract (OE) obtained from Olevano sul Tusciano in an *in vitro* model of fatty acid-induced steatosis. HepG2 cells were exposed to a mixture of oleic and palmitic acids (OA/PA) to mimic non-alcoholic lipid accumulation.

OE treatment reduced fatty acids accumulation, restored redox balance and attenuated stress markers associated with lipid overload.

Furthermore, the activation of Sirtuin 1 (SIRT1), a nicotinamide adenine dinucleotide (NAD^+)-dependent deacetylase that acts as a key metabolic sensor, was partially implicated in the observed protective effects.

Taken together, the results demonstrate that this specific phytocomplex derived from olive leaves grown in the Mediterranean region of Southern Italy effectively counteracts fatty acid–induced lipotoxicity in hepatic cells. These findings provide the first evidence of its activity in a cellular model of MAFLD and support its potential application as a nutraceutical for the prevention and modulation of hepatic alterations.

3.2 Introduction

MAFLD is characterized by the accumulation of lipids in the liver (hepatic steatosis) in association with metabolic dysfunction and is therefore considered the hepatic manifestation of a systemic disturbance of metabolic homeostasis (Carli *et al.*, 2024; Eslam *et al.*, 2020).

Unlike the previous definition of non-alcoholic fatty liver disease (NAFLD), which was based on exclusion criteria, MAFLD relies on positive diagnostic criteria, requiring the presence of steatosis together with at least one metabolic condition, such as overweight/obesity, type 2 diabetes mellitus, or evidence of metabolic dysregulation in normal-weight individuals (Eslam *et al.*, 2020).

This conceptual shift reflects the recognition of MAFLD as an expression of metabolic imbalance, commonly associated with insulin resistance, dyslipidemia, and chronic low-grade inflammation.

From a biological perspective, MAFLD encompasses a disease spectrum ranging from simple steatosis to inflammatory and fibrotic stages (historically defined as non-alcoholic steatohepatitis, NASH), with potential progression to advanced fibrosis, cirrhosis, and hepatocellular carcinoma (Gofton *et al.*, 2022; Eslam *et al.*, 2020).

Its pathogenesis is multifactorial and involves a complex interplay of metabolic alterations and intracellular signaling pathways. Increased hepatic influx of free fatty acids, together with activation of *de novo* lipogenesis, leads to excessive intracellular lipid availability. When mitochondrial oxidative capacity becomes insufficient or impaired, triglycerides and bioactive lipid intermediates accumulate, promoting lipotoxicity (Buzzetti *et al.*, 2016).

These alterations are accompanied by impaired beta-oxidation, mitochondrial dysfunction, increased production of ROS, activation of ER stress, and engagement of pro-inflammatory pathways, including NF-κB activation. The interaction among these processes results in redox imbalance and contributes to the progression of hepatic injury (Tauil *et al.*, 2024; Iturbe-Rey *et al.*, 2025; Li *et al.*, 2025).

MAFLD should therefore be regarded as a dynamic condition in which lipid metabolism, oxidative stress, and inflammation are tightly interconnected,

supporting the rationale for interventions capable of targeting multiple molecular pathways simultaneously.

Among the intracellular regulators extensively studied in metabolic disorders, Sirtuin 1 has emerged as a key modulator of energy homeostasis.

SIRT1 is a nicotinamide adenine dinucleotide (NAD^+)-dependent deacetylase whose activity is closely linked to the cellular NAD^+/NADH ratio, positioning it at the interface between energy sensing and adaptive metabolic responses (Meng *et al.*, 2023).

SIRT1 regulates several transcription factors and co-regulators involved in lipid and glucose metabolism. Deacetylation of Forkhead box O (FOXO1 and FOXO3) enhances the expression of genes involved in antioxidant defense and metabolic control. Moreover, SIRT1 operates in close functional interaction with Adenosine Monophosphate-Activated Protein Kinase (AMPK) through a bidirectional regulatory circuit. Activation of AMPK increases the NAD^+/NADH ratio, thereby promoting SIRT1 activity, while SIRT1 deacetylates Liver Kinase B1 (LKB1), contributing to AMPK activation. This coordinated interaction suppresses lipogenesis and promotes fatty acid oxidation, representing a central mechanism in the regulation of hepatic lipid accumulation (Meng *et al.*, 2023; Ding *et al.*, 2017; Anggreini *et al.*, 2022; Ruderman *et al.*, 2010).

Through modulation of FOXO proteins and Nrf2, SIRT1 also enhances the expression of antioxidant systems, including superoxide dismutase (SOD), catalase, and glutathione peroxidase (GPx). In experimental models of steatosis, reduced SIRT1 activity has been associated with increased susceptibility to oxidative stress and worsening hepatic injury.

In parallel, SIRT1 exerts anti-inflammatory effects by modulating the NF-kB signaling pathway and reducing the expression of pro-inflammatory cytokines. Down-regulation of SIRT1 therefore contributes to a pro-inflammatory environment that may accelerate disease progression (Elsayed *et al.*, 2025; Zhang *et al.*, 2025) (**Figure 3.1**).

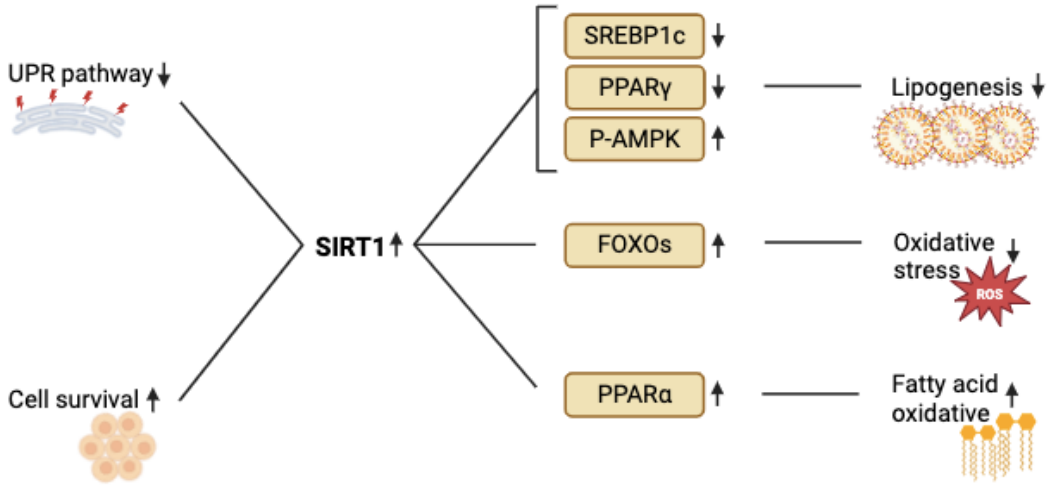

Figure 3.1. *Principal biochemical processes regulated by SIRT1 signaling.*

Several polyphenolic compounds, including resveratrol, quercetin, curcumin, and catechins from green tea, have been described as modulators of the SIRT1–AMPK axis. In experimental settings, these compounds have been shown to enhance SIRT1 activity, promote beta-oxidation, and improve cellular antioxidant responses, acting simultaneously on key metabolic and inflammatory nodes implicated in MAFLD (Kitada *et al.*, 2019; Anggreini *et al.*, 2022; Chung *et al.*, 2010; Domi and Hoxha, 2025).

Leaves of *Olea europaea* represent a plant matrix particularly rich in polyphenols, including oleuropein, hydroxytyrosol, and related phenolic derivatives (De Oliveira *et al.*, 2024; Omagari *et al.*, 2021). Although the precise molecular mechanisms are not yet fully elucidated, preclinical evidence suggests that these compounds may influence hepatic lipid metabolism and redox balance. These findings provide a strong biological foundation to further investigate the potential role of this specific and original phytocomplex derived from olive leaves in modulating the molecular mechanisms involved in non-alcoholic fatty liver disease.

3.2.1 Aim of work

Olive leaves extract (OE) was obtained by hydroalcoholic maceration of olive leaves cultivated in Southern Italy and subsequently characterized by liquid chromatography–tandem mass spectrometry (LC–MS/MS), which identified 30 compounds, mainly free phenolic acids, flavonoids, and terpenes.

Given the established ability of polyphenolic nutraceuticals to modulate metabolic and redox-sensitive pathways, as previously described, this study was designed to investigate the mechanistic basis of OE activity in a cellular model of steatosis.

Specifically, was aimed to evaluate the protective effects of OE in HepG2 hepatocarcinoma cells exposed to a mixture of free fatty acids (OA/PA), a well-established *in vitro* model that recapitulates key features of metabolic dysfunction-associated fatty liver disease, including intracellular lipid accumulation, oxidative imbalance and activation of stress-related pathways.

Particular attention was devoted to determining whether OE could modulate pathways involved in hepatic lipid metabolism and redox regulation, with a focus on the SIRT1–AMPK axis (**Figure 3.2**).

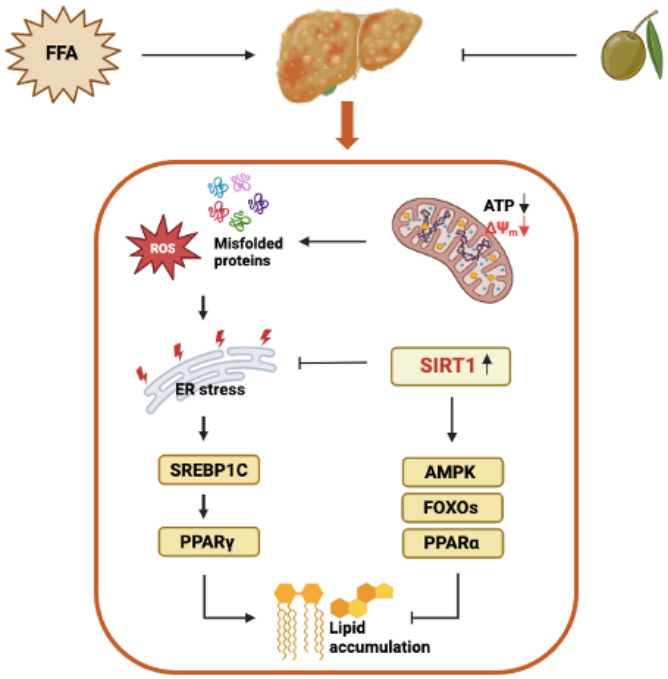

Figure 3.2. *OE exerts protective effects against FFA-induced lipotoxic damage, potentially through activation of Sirtuin 1 signaling and modulation of metabolic and redox pathways.*

3.3 Materials and methods

3.3.1 Sample preparation

50 mL of OE were diluted with H_2O + 0.1% HCOOH (1:1 *v/v*) and loaded on a Strata^{TM}-X 33 µm Polymeric Reversed Phase 500 mg 6 mL^{-1} cartridge.

After activation (MeOH) and conditioning (H_2O) of the resin, the sample was loaded and washed (H_2O) to remove the sugar. Later, the polyphenolic components were eluted with MeOH + 2% HCOOH.

The elution fraction was collected, the solvent removed by evaporation under vacuum, and then injected in a concentration of 10 mg/mL in EtOH/H_2O (50:50 *v/v*).

3.3.2 UHPLC-PDA-ESI-Orbitrap-MS/MS conditions

UHPLC-HRMS/MS analysis was performed on a Thermo Scientific™ Vanquish™ UHPLC system, equipped with a VF-P10-A binary solvent delivery system, a VC-D11-A photodiode array detector, a VH-C10-A column compartment and VF-A10-A autosampler. The UHPLC system was coupled online to a Orbitrap Exploris 120 mass spectrometer (Thermo Fisher Scientific) equipped with a heated electrospray ionization probe (HESI II) operating in positive mode.

The chromatographic separation was performed on a Kinetex® 2.6µm EVO C18 100 Å, LC Column 150 x 2.1 mm (Phenomenex).

The column temperature and the flow rate were set at 40°C and 0.4 mL/min, respectively. The mobile phases were: H_2O (A) and ACN (B) both acidified with 0.5 % HCOOH (*v/v*) with the following gradient: 0.01–3.00 min, isocratic to 2%: 3.01-20.00 min, 2-30% B; 20.01–30.00 min, 30-95% B; 30.01–33.00 min, isocratic to 95% B; 33.01-35.00 min, 95-2% B; then eight minutes for column re-equilibration.

The following PDA parameters were applied: sampling rate, 20.0 Hz; detector response time, 0.200 s; and detector peak width, 0.020 min. Data acquisition was set in the range 190-800 nm, and chromatograms were monitored at 280 and 330 nm at maximum absorbance of the compounds of interest.

The MS was calibrated by Thermo Pierce™ FlexMix™ Calibration Solutions in both polarities. Full MS (100-1400 m/z) and data-dependent MS/MS were performed at a resolution of 60,000 and 15,000 FWHM respectively; Normalized Collision Energy

(NCE) value of 15, 20, 30 were used. Source parameters: Sheath gas pressure, 40 arbitrary units; auxiliary gas flow, 15 arbitrary units; spray voltage, +3.4 kV, -2.0 kV; capillary temperature, 320°C; auxiliary gas heater temperature, 300°C.

Peaks annotations were carried out by comparing their retention times and MS/MS data with those present in the literature. The identification level was established according to Metabolomics Standards Initiative (MSI): level 1, unambiguous identification with reference standards; level 2, putative identification by matching MS2 data to literature data or spectral databases; level 3, putative identification established by spectral similarity to chemical class of compounds and chemotaxonomic.

For HRMS data analysis and processing, FreeStyle™ 1.8 SP2 and Compound Discoverer™ 3.1 software (Thermo Scientific) were used for raw data processing (baseline correction, noise filtering, spectral alignment, and peak detection) and for putative identification of metabolites based on molecular formula (matched), exact mass (mass tolerance <5 ppm) and MS2 fragmentation pattern [Fragment Ion Search (FISh)], with a global database search (mzCloud, MassList and ChemSpider).

Other databases, containing fragmentation spectrum information of natural product molecules from different sources, mainly include MassBank (https://massbank.eu/MassBank/), GNPS (https://gnps.ucsd.edu/ProteoSAFe/static/gnps-splash.jsp/), PubChem (https://pubchem.ncbi.nlm.nih.gov/), LipidMAPS (http://www.lipidmaps.org/), FooDB (http://foodb.ca/), Phenol-Explorer (http://phenol-explorer.eu/), PlantaeDB (https://plantaedb.com/), PMhub (https://pmhub.org.cn/#/) and LOTUS (https://lotus.naturalproducts.net/).

3.3.3 Quantitative analysis

For the quantification of the main compound in *Olea europea L.* leaves extract the chromatographic separation was conducted under the same conditions as previously described. For the quantitative analysis of phenolic acids and flavonoids were used as an external standard, hesperidin, in negative ionization mode, and rutin, in positive ionization mode, respectively.

Stock solutions (1 mg/mL) were prepared in MeOH, and the calibration curves were obtained in a concentration range of 1-500 µg/mL for rutin (Ru), 1-250 µg/mL for hesperidin (Hesp), using six concentration levels with triplicate injections for each level. Linear regression was used to generate the calibration curves with R^2 values ≥ 0.999. UV peak areas of the standard were plotted against corresponding concentrations (µg/mL).

The compounds content in the sample was expressed as milligram per gram of dried extract mean ± deviation standard (n=3). Limits of detection (LOD) and quantification (LOQ) were calculated by using the standard deviation (SD) and the slope of the calibration curve, multiplied by 3.3 and 10, respectively.

3.3.4 *Determination of total phenolic content (TPC) and total flavonoid content (TFC).*

The total phenolic content (TPC) of OE was determined using the Folin–Ciocalteu. Gallic acid was used as standard for the calibration curve (10–500 µg/mL; y = 1779.61x − 2.0811; R^2 = 99.92%). Results were expressed as milligrams of gallic acid equivalents per gram of dry weight (mg GAE/g DW).

Total flavonoid content (TFC) was expressed as milligrams of rutin equivalents per gram of dry weight (mg RE/g DW) using a calibration curve (10–500 µg/mL; y = 2239.24x − 5.3342; R^2 = 99.93%).

3.3.5 FRAP (Ferric Reducing Antioxidant Power) antioxidant activity test

The antioxidant capacity of OE was evaluated using FRAP assay. Trolox was used as reference (1–200 µg/mL; y = 0.0202x + 0.1323; R^2 = 99.99%).

All the samples were prepared in triplicate, shaked and incubated in dark for 30 min at 37 °C. The assay is based on the reduction of ferric-tripyridyltriazine (Fe^{3+}-TPTZ) to an intense blue color ferrous-tripyridyltriazine complex (Fe^{2+}-TPTZ).

Changes in the absorbance of the samples were measured against blank at 593 nm using a microplate reader (Multiskan Go, Thermo Scientific).

FRAP activity was calculated as milligrams of trolox equivalents per gram of dry weight (mg TEX/g DW).

3.3.6 Cell cultures and drug treatment

The human hepatocellular carcinoma cell line HepG2 was obtained from ATCC. Cells were grown in Minimum Essential Medium (MEM, 4500 mg/mL glucose) supplemented with 10% (*v*/*v*) fetal bovine serum, 2 mM L-glutamine, 100 U/mL penicillin, 0.1 mg/mL streptomycin and 5% non-essential amino acid.

Cells were routinely grown in culture dishes in a 95% humidified environment containing 5% CO_2 at 37 °C and split every 2 days.

In each experiment, cells were placed in a fresh medium and treated with OE in the presence of a mix of oleic and palmitic acids (OA/PA), in a 2:1 ratio, for different experimental times. Each treatment and analysis were performed at least in three separate experiments.

3.3.7 Preparation of free fatty acids (FFA) treatments

OA and PA were purchased from Sigma Aldrich. Stock solutions of 100 mM OA and PA were first prepared in 100% ethanol.

In particular, PA was solubilized by heating at 70 °C for approximately 30 min, while OA was dissolved at room temperature. To prepare the FFA–BSA conjugates, a 5% bovine serum albumin (BSA) solution was obtained by diluting a 20% BSA stock (Sigma Aldrich) with complete MEM culture medium.

OA and PA were then added to the 5% BSA solution at final concentrations of 2.5 mM and 1.25 mM, respectively, to obtain an OA:PA molar ratio of 2:1.

The mixture was incubated under gentle agitation for 1 h at 37 °C to allow conjugation. For cell treatments, the conjugated FFA solution was diluted 1:5 in complete MEM medium, yielding final concentrations of 500 µM OA and 250 µM PA. A 5% BSA solution prepared under the same conditions was used as the control and added to the cells at the same dilution as the FFA–BSA conjugates.

3.3.8 Growth and maturation of spheroids in culture

HepG2 spheroids were generated by seeding 3,000 cells in 20 µL of medium as hanging drops on the inner side of 60 mm Petri dish lids.

The cells aggregated by gravity at the bottom of each drop, forming a single spheroid per drop (Vestuto *et al.*, 2024). After 3 days of incubation, the spheroids were carefully collected and transferred into 24-well plates previously coated with 1% agarose to prevent cell adhesion. Once transferred, the spheroids were treated for 24 h with OE at a concentration of 25 µg/mL and a mixture of OA/PA.

3.3.9 Cell viability assays

Cell viability was established by measuring the mitochondrial metabolic activity with MTT assay and double staining with Calcein-AM/PI (propidium iodide).

Briefly, HepG2 (30×10^3 cells/well) cells were plated into 96-well plates, and then, OE (6.25-100 µg/mL) was added for 24 h (with and without OA/PA).

Afterward, the MTT reagent was added for 2 h. Cell lysis was performed with an isopropanol/HCl solution to dissolve blue formazan crystals formed by viable mitochondria. The absorbance of formazan crystals was measured at 570 nm (Multiskan Go, Thermo Scientific).

Cell viability was expressed as a percentage relative to the untreated cells cultured in medium with 0.1% DMSO and set to 100%, whereas 10% DMSO was used as positive control and set to 0% of viability.

For the Calcein-AM/Propidium Iodide double staining assay, 2D and 3D cells were seeded under the same experimental conditions described above.

After 24 h of treatment, the culture medium was removed, and cells were washed twice with PBS. Cells were then incubated in phenol red–free medium containing Calcein-AM and PI at final concentrations of 3 µM and 2.5 µg/mL, respectively.

Calcein-AM was used to label viable cells, while PI was employed to identify membrane-compromised cells.

Fluorescence representative images were acquired using a ZOE Fluorescence Imager (Bio-Rad. Magnification, 20×. N ≥ 10. Scale bar: 100 µm).

3.3.10 Oil Red O staining

Oil Red O staining was used to assess lipid droplet formation in cells.

The HepG2 cells were seeded (60×10^3 cells/well) in 24-well plates and cultivated overnight. The cells were treated with OE (25 µg/mL) and OA/PA for 24 h.

The treated cells were washed twice with PBS and fixed with 10% paraformaldehyde for 15 min at room temperature, followed by 60% isopropanol incubation for 5 min. Then, the staining with ORO solution was performed for 20 min.

The images were acquired on a fluorescence microscope (Axioshop 40, Zeiss. Magnification, 40×. N ≥ 10. Scale bar: 10 µm).

Quantitative analyses were conduced dissolving droplets in 100% isopropanol and measuring the absorbance at 510 nm. Results were expressed as percentage of lipid accumulation, normalized to the control condition.

3.3.11 Lipidomic analysis

HepG2 cells were cultured and treated as described above. At the end of treatment, culture medium was removed, and cells were rapidly washed twice with ice-cold phosphate-buffered saline (PBS). Cells were collected by scraping in ice-cold PBS, transferred into pre-chilled tubes, and pelleted by centrifugation (1.000 × g, 5 min, 4 °C). Supernatants were discarded and pellets were immediately processed or stored at −80 °C until extraction.

Lipid extracts were analyzed by reversed-phase ultra-high-performance liquid chromatography coupled to high-resolution tandem mass spectrometry (RP-UHPLC-HRMS/MS). A C18/CSH reversed-phase column was used to separate major lipid classes using a water/acetonitrile phase and an organic phase enriched in isopropanol (typical lipidomics gradients). Data were acquired in electrospray ionization (ESI) mode, operating both positive and negative ionization (separate runs or polarity switching depending on instrument capability), to enhance coverage across glycerolipids, phospholipids, sphingolipids, and free fatty acids. MS1 full-scan spectra were acquired at high resolution, followed by data-dependent MS/MS (DDA) to support structural annotation.

Lipid annotation was based on accurate mass, isotopic pattern, retention time behavior, and MS/MS spectral matching when available. Features detected in extraction blanks were filtered out to reduce background contamination. Peak areas

were normalized to internal standards (when used) and/or to total protein content/cell number, and QC-based filtering was applied (e.g., removing features with high QC variability). Multivariate analyses (principal component analysis, PCA) were used to visualize group separation, while univariate statistics were applied to identify significantly modulated lipids (ANOVA or t-test with multiple-testing correction). Heat maps was generated from normalized data (Merciai *et al.*, 2022).

3.3.12 Quantitative real time-PCR for molecular pathway analysis

HepG2 cells were seeded in in 100 mm culture dishes at 80% confluence and treated with OE (25 µg/mL) and OA/PA for 24 h. After 24 h from treatments, cells were washed twice with PBS and detached with a scraper.

Total RNA was isolated using a modified procedure with the Quick-RNA™ Miniprep Kit (Zymo Research). Genomic DNA was eliminated by treatment with DNase I provided in the kit. The resulting purified RNA was then reverse transcribed into cDNA using the SensiFAST™ cDNA Synthesis Kit (Meridian Bioscience).

Real-time PCR was performed with LightCycler® 480 System (La Roche Ltd) using SYBR Green detection in a total volume of 20 µL with 1 µL of forward and reverse primers (5 µM) and 10 µL of SensiFAST™ SYBR No-ROX Kit (Meridian Bioscience). Values were determined from standard curve generated from serial cDNA dilutions and normalized to GAPDH.

The primers used for the real-time PCR reactions are listed in the table below.

The $2^{-\Delta\Delta CT}$ method was used to analyze the results and relative mRNA expression levels were determined as fold-induction relative to Ctrl cells, set as 1.

Table 3.1. *Forward and Reverse Primer Sequences for Target Genes*

Primer sequence (5'–3')		
Target gene	**Forward**	**Reverse**
SREBP1c	CGGAACCATCTTGGCAACA	GCCGGTTGATAGGCAGCTT
PPAR-α	AACATCCAAGAGATTTCGCAATC	CCGTAAAGCCAAAGCTTCCA
PPAR-γ	TGCAGGTGATCAAGAAGACG	AGTGCAACTGGAAGAAGGGA
DGAT1	AACTGGTGTGTGGTGATGCT	CCTTCAGGAACAGAGAAACC

SIRT1	GCAACATCTTATGATTGGCACA	AAATACCATCCCTTGACCTGAA
FOXO1	GAGATAAGCAATCCCGAAAACA	TGGCGCAAACGAGTAGCA
PERK	TCATCCAGCCTTAGCAAACC	ATGCTTTCACGGTCTTGGTC
CHOP	ACCAAGGGAGAACCAGGAAAC	TCACCATTCGGTCAATCAGAGC
BIP	CGGGCAAAGATGTCAGGAAAG	TTCTGGACGGGCTTCATAGTAGAC
IRE1α	CTCTGTCCGTACCGCCC	GAAGCGTCACTGTGCTGGT
ATF4	GTCCCTCCAACAACAGCAAG	CTATACCCAACAGGGCATCC

3.3.13 Western blotting analysis

HepG2 cells were seeded in in 60 mm culture dishes at 80% confluence and treated with OE (25 µg/mL) and OA/PA for 24 h. After 24 h from treatments, cells were washed twice with PBS and detached with a scraper and centrifuged to remove debris. Full proteins were extracted by using a lysis buffer. Then, cell lysates were centrifuged at 4850 × *g* for 20 min at 4 °C.

A total of 30 µg of total proteins was run on 10% SDS-PAGE and transferred to nitrocellulose membranes using a minigel apparatus (Bio-Rad Laboratories).

Blots were blocked in phosphate-buffered saline, containing Tween-20 0.1% and 10% BSA, for 1 h at room temperature and incubated overnight with specific primary antibodies at 4 °C with slight agitation.

α-tubulin was used as the loading control.

The following antibodies were used:

- rabbit polyclonal anti-AMPK (Sigma Aldrich),
- rabbit polyclonal anti-phospho-AMPK (Sigma Aldrich),
- mouse monoclonal anti-α-tubulin (Santa Cruz Biotechnology),

After washes in PBS/Tween-20 0.1%, the appropriate anti-rabbit or anti-mouse (Pierce, Thermo Fisher Scientific) peroxidase-linked secondary antibody was added for 1 h at room temperature.

Antigen-antibody complexes were detected by enhanced chemiluminescence (ECL kit, Amersham). Filters were exposed to LAS 4000 (GE Healthcare) and the densitometry analysis of autoradiographs was performed by the ImageJ program, version 1.47.

3.3.14 Flow cytometry analysis of SIRT1

The HepG2 cells were seeded (50 × 10^3 cells/well) in 24-well plates and cultivated overnight. The cells were treated with OE (25 µg/mL) and OA/PA for 24 h.

After treatment, the collected cells were resuspended in 50 µL FACS buffer (2% BSA, 1% formaldehyde in PBS) for 20 min.

Then cells were centrifuged at 600 g for 10 minutes, and the resulting pellet was resuspended in a permeabilization buffer consisting of 2% BSA, 1% formaldehyde, and 0.1% Triton X-100 in PBS, containing the primary anti-SIRT1 antibody (*Anti-Mouse Monoclonal Antibody*, Thermo Fisher Scientific) and the Alexa Fluor 488-conjugated secondary antibody (*Anti-Mouse Secondary Antibody*, Thermo Fisher Scientific). After 30 minutes of incubation, the cells were centrifuged again and washed with PBS.

The final pellet was resuspended in 200 µL of FACS buffer. Samples were analyzed by flow cytometry using a Becton Dickinson FACScan equipped with CellQuest software, version 4.

3.3.15 SIRT1 activity assay

HepG2 cells were seeded in in 100 mm culture dishes at 80% confluence and treated with OE (25 µg/mL) and OA/PA for 24 h.

After 24 h of treatment, cells were detached and lysed according to the manufacturer's instructions using the SIRT1 Activity Assay Kit (Fluorometric, ab156065, Abcam). The assay was performed as recommended by the supplier, and fluorescence was measured using a PerkinElmer EnSpire multimode plate reader.

Results were expressed as relative SIRT1 activity, normalized to the control condition.

3.3.16 Reactive oxygen and nitrogen species (ROS/RNS) detection

Reactive oxygen species levels were measured using 10 µM 6-carboxy-2',7'-dichlorodihydrofluorescein diacetate (DCFH-DA, Sigma Aldrich). While reactive

nitrogen species (RNS) were evaluated using 5 µM 4-amino-5-methylamino-2',7'-difluorofluorescein diacetate (DAF-FM-DA, Thermo Fisher Scientific)

HepG2 cells (30 × 10^3/well) were seeded in 96-well plates and allowed to adhere for 24 h, then treated for 24 h with OE (25 µg/mL) co-administered with OA/PA. After treatment, cells were washed with PBS and incubated for 20 min at 37 °C in the dark with DCFH-DA or DAF-FM-DA diluted in serum-free, phenol-red-free medium. The fluorescence signals (DCFH-DA: excitation/emission 485 nm/535 nm; DAF-FM-DA excitation/emission 495 nm/515 nm) were read in end point mode using a PerkinElmer EnSpire multimode plate reader.

3.3.17 Mitochondrial membrane potential determination

Mitochondrial membrane potential was measured using tetramethlyrhodamine ethyl ester (TMRE, Invitrogen). HepG2 cells (30 × 10^3/well) were seeded in 96-well plates and allowed to adhere for 24 h, then treated for 24 h with OE (25 µg/mL) co-administered with OA/PA. After treatment, cells were washed with PBS and incubated for 20 min at 37 °C in the dark with TMRE diluted in serum-free, phenol-red-free medium. The fluorescence signals (excitation/emission 549 nm/574 nm) were read in end point mode using a PerkinElmer EnSpire multimode plate reader.

The fluorescence representative images of live cells were captured using a ZOE Fluorescence Imager (Bio-Rad. Magnification, 20×. N ≥ 10. Scale bar: 100 µm).

3.3.18 Determination of protein misfolding

Protein misfolding was analyzed by using Thioflavn T (ThT, Sigma Aldrich) staining. HepG2 cells (30 × 10^3/well) were seeded in 96-well plates and allowed to adhere for 24 h, then treated for 24 h with OE (25 µg/mL) co-administered with OA/PA.

After treatment, cells were washed with PBS and incubated for 20 min at 37 °C in the dark with 20 µM ThT diluted in serum-free, phenol-red-free medium.

The fluorescence signals (excitation/emission 450 nm/482 nm) were read in end point mode using a PerkinElmer EnSpire multimode plate reader.

The fluorescence representative images of live cells were captured using a ZOE Fluorescence Imager (Bio-Rad. Magnification, 20×. N ≥ 10. Scale bar: 100 µm).

3.3.19 Indirect immunofluorescence analysis of CHOP

HepG2 spheroids were generated as previously described. After formation and stabilization, spheroids were treated for 24 h under the same experimental conditions applied to the 2D cell cultures.

After treatments, cells were washed in PBS, fixed in PBS-4% paraformaldehyde and permeabilized 10 min in PBS containing 0.25% triton. A blocking solution containing PBS-1% BSA and 50 mM NH_4Cl for 30 min was added to each well. Thereafter, cells were stained with CHOP (Sigma Aldrich) for 1 h.

Alexa fluor 568 antibody (Molecular Probes, Invitrogen) was used as secondary antibody and incubated for 45 min. Nuclei were counterstained with 1.5 µM Hoechst 33,342 (Sigma Aldrich) for 10 min. Images were acquired on a laser scanning confocal microscope (TCS SP8; Leica MicroSystems) equipped with a plan Apo 63X, NA 1.4 oil immersion objective lens. Quantitative analyses were performed by the ImageJ program, version 1.47 ($N \geq 10$).

3.3.20 Statistical analysis

The data are reported as mean ± SD of the results from three independent experiments. Statistical analysis was performed using an analysis of variance test (ANOVA), and multiple comparisons were made with the Bonferroni test using GraphPad Prism 8.0 software (San Diego, CA, USA).

Significance was assumed at $p < 0.05$.

3.4 Results and discussion

3.4.1 LC-MS/MS identification and quantification

Olea europea L. leaves extract was analyzed by UHPLC-PDA-ESI-MS/MS for the tentative identification of the investigated analytes.

The assignments were based on combined evaluation of UV−Vis absorbance, MS/MS fragmentation patterns, and retention times (**Table S3.1**), while quantitative date, expressed as mg/g DW ± SD, are reported in **Tables 3.2** and **3.3**.

Table 3.2. *Quantitative analysis of the major compounds identified in OE*

Peak	Name	mg/g DW
10	Vicenin II	2.07 ± 0.05 [b]
11	Rutin	3.53 ± 0.01 [a]
12	Luteolin-7-*O*-glucoside	7.53 ± 0.02 [b]
13	Vicenin II (*isomer*)	1.35 ± 0.01 [b]
14	Naringin	10.42 ± 0.08 [b]
17	Neohesperidin	17.1 ± 0.09 [b]
20	Diosmin	1.02 ± 0.01 [a]
22	Luteolin	0.96 ± 0.03 [b]
28	trans-3,3′,4′,5,5′,7-Hexahydroxyflavanone	0.51 ± 0.01 [b]
29	Tangeritin	0.21 ± 0.02 [a]
31	Sinensetin	0.88 ± 0.01 [a]

** Data expressed as mean (mg/g dried extracts) ± deviation standard (n=3)*

[a] *RuE: Rutin Equivalents*

[b] *HespE: Hesperidin Equivalents*

Table 3.3. *Quantitative parameters*

Parameters	Rutin	Hesperidin
Slope	7.12E-05	6.71E-05
Intercept	-3.35E+00	-1.56E+00
Correlation coefficient (R^2)	0.99902	0.99976
LOD (µg mL^{-1})	0.197	0.202
LOQ (µg mL^{-1})	0.596	0.611

The chromatographic profile acquired by UHPLC couplet to Photodiode Array Detector (PDA) (**Figure 3.3**) was recorded at 280 and 330 nm, corresponding to the maximum absorbance wavelength of phenolic acids and flavonoids, respectively.

Peak **12** was tentatively identified as luteolin-7-*O*-glucoside based on the deprotonated molecular ion $[M-H]^-$ at *m/z* 447 ($C_{21}H_{19}O_{11}$). MS2 fragmentation yielded a product ion at *m/z* 285, consistent with the loss of a glucoside moiety and formation of the luteolin aglycone. The identification was confirmed by co-injection of the reference standard (MSI level 1). The compound was among the most abundant constituents of the extract (7.53 ± 0.02 mg/g DW).

Rutin was also identified as compound **11**, showing a protonated molecular ion $[M+H]^+$ at *m/z* 611 ($C_{27}H_{30}O_{16}$) and a characteristic fragment at *m/z* 303

corresponding to the quercetin aglycon after loss of the rutinose disaccharide. The compound was quantified at 3.53 ± 0.01 mg/g DW.

Compound **14** was tentatively identified as naringin, characterized by a precursor ion $[M–H]^-$ *m/z* at 579 and a major fragment at m/z 271, attributable to the naringenin aglycone following rutinose cleavage. This compound was also detected as one of the most abundant (10.89 ± 0.08 mg/g DW) in the extract and was confirmed as MSI level 1.

Peaks **17** was identified as neohesperidin (MSI level 1), with a deprotonated ion $[M-H]^-$ at *m/z* 609 and an MS2 fragment at *m/z* 301, resulting from the loss of neohesperidoside moiety $[M-H-308]^-$, and corresponding to hesperetin residue. Quantitative analysis indicated a significant presence in the extract (17.10 ± 0.09 mg/g DW).

UHPLC-MS/MS analysis in negative ionization mode also enabled the detection of oleuropein (peak **19**), which exhibited a $[M–H]^-$ ion at *m/z* 447 and a characteristic fragmentation pattern leading to the formation of the oleuropein aglycone at *m/z* 377 after hexose loss.

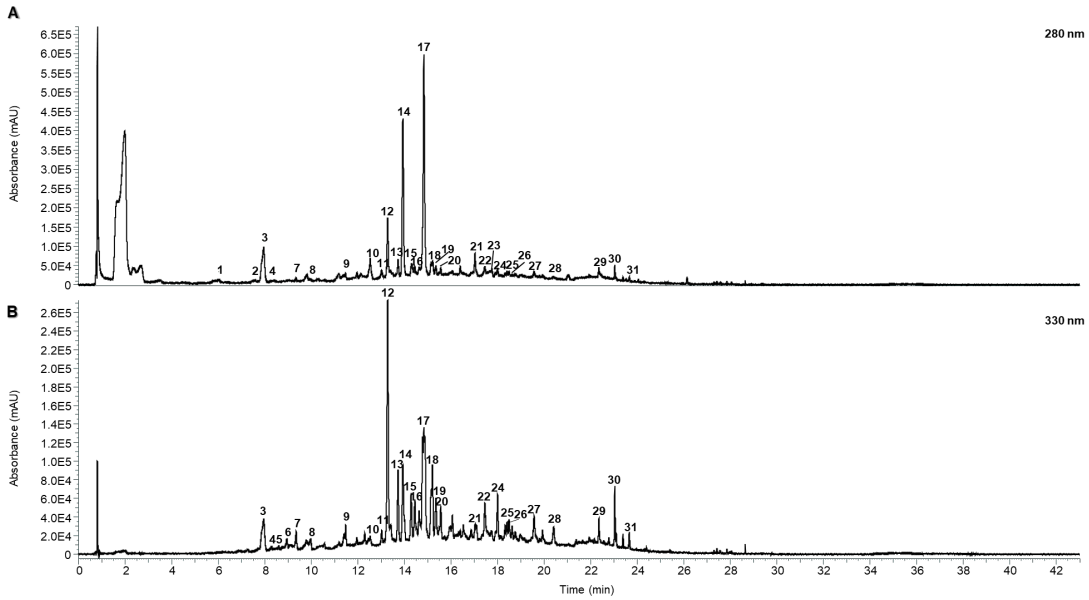

Figure 3.3. *RP-UHPLC-PDA chromatogram of OE at λ = 280 nm (**A**) and 330 nm (**B**).*

3.4.2 *Evaluation of polyphenol, flavonoid content and antioxidant effect of OE in cell-free assay*

The extract was first analyzed using the Folin–Ciocalteu method to estimate its total phenolic content, and the aluminum chloride method was employed to evaluate flavonoid levels, both tested at a final concentration of 100 µg/mL.

The TPC was calculated from the regression equation of the gallic acid calibration curve and expressed as gallic acid equivalents, giving a value of 149.44 ± 0.02 mg GAE/g for the OE.

Similarly, the TFC was obtained from the regression equation of the rutin calibration curve and reported in rutin equivalents (RE), resulting in a concentration of 41.91 ± 0.03 mg RE/g for the CN extract.

The antioxidant capacity of the CN extract was evaluated through FRAP assays.

This method relies on the reduction of Fe^{3+} to Fe^{2+} by antioxidants in the presence of TPTZ, generating a blue Fe^{2+}–TPTZ complex. The OE extract, tested at 25–100 µg/mL, showed a scavenging capacity equivalent to 57.48 ± 0.02 mg TXE/g DW at 100 µg/mL.

3.4.3 OE attenuates FFA-induced steatosis in HepG2 cells

To determine the intrinsic cytotoxicity of olive leaf extract, HepG2 cells were first exposed to increasing concentrations of the extract (6.25-100 µg/mL), and cell viability was assessed by the mitochondrial activity assay (MTT) (**Figure 3.4 A**).

OE did not induce any significant reduction in mitochondrial metabolic activity at concentrations under to 25 µg/mL, indicating the absence of intrinsic cytotoxic effects in this cellular model. Based on these findings, the non-toxic concentrations (6.25, 12.5 and 25 µg/mL) were selected for co-treatment experiments with a mixture of oleic acid and palmitic acid (OA/PA) to induce steatogenic stress. As expected, OA/PA exposure significantly reduced cell viability compared to untreated controls ($p < 0.001$ vs Ctrl). Notably, co-administration of OE at all tested concentrations significantly counteracted the reduction in viability induced by OA/PA ($p < 0.001$ vs OA/PA), restoring mitochondrial activity toward control levels (**Figure 3.4 B**).

Among the tested concentrations, 25 µg/mL was selected for subsequent experiments, given its consistent protective effect.

These findings were further supported by Calcein-AM/PI double staining.

While OA/PA treatment increased the proportion of PI-positive cells, indicating membrane damage and reduced viability, co-treatment with OE markedly decreased PI staining, consistent with the MTT results (**Figure 3.4 C**).

To further investigate the cytoprotective action of OE, intracellular lipid accumulation was evaluated by Oil Red O staining, followed by quantitative spectrophotometric analysis. OA/PA treatment induced a robust increase in lipid droplet formation ($p < 0.01$ vs Ctrl), confirming the establishment of a steatotic phenotype. Co-treatment with OE reduced lipid droplet accumulation compared to OA/PA-treated cells ($p < 0.05$ vs OA/PA), indicating that the extract effectively attenuates FFA-induced steatosis (**Figure 3.4 D, E**).

Taken together, these results demonstrate that OE exerts a dual effect under steatogenic conditions: it preserves cell viability and significantly reduces lipid accumulation, supporting the hypothesis that OE modulates metabolic and stress-related pathways.

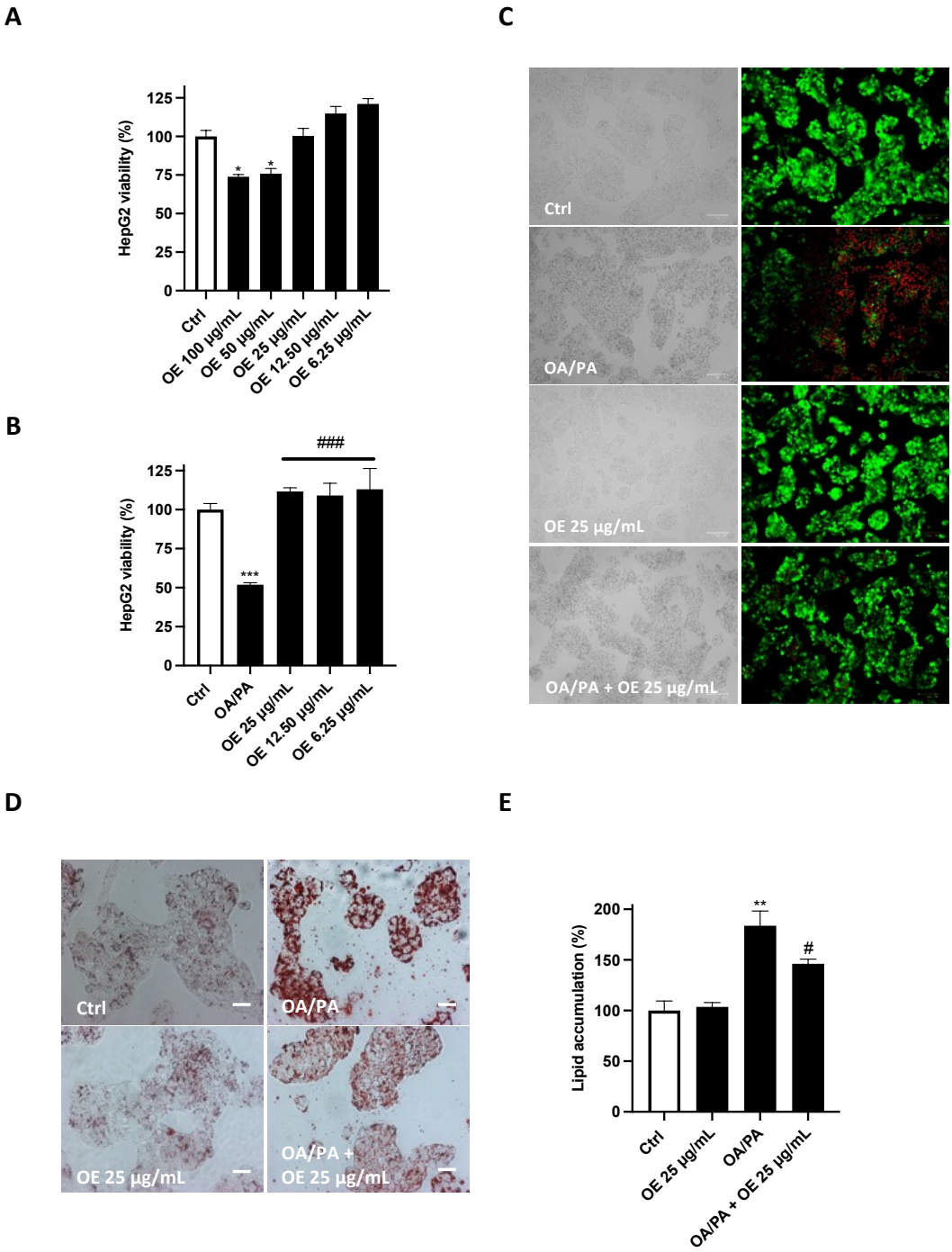

Figure 3.4. *Cytoprotective effect of OE against fatty acids in HepG2 cells. (**A**) HepG2 cells were exposed to OE in the range of 6.25–100 µg/mL. (**B**) Hepatoprotective effect of OE against OA/PA-induced cytotoxicity. The viability variations were calculated as percentage of viable cells in treated cultures compared to untreated ones. After 24h of treatment with OA/PA and OE (25 µg/mL), (**C**) HepG2 cells were stained by propidium iodide (red) and calcein AM (green). The fluorescence was observed by fluorescence microscope (Magnification, 20x. N ≥ 10. Scale bar: 100 µm).*
Data are shown as the mean ± SD of three different experiments performed in triplicate.
** p < 0.05 vs. Ctrl; *** p < 0.001 vs. Ctrl. ### p < 0.001 vs. OA/PA.*

To analyze in greater detail the reduction in neutral lipid storage, an untargeted lipidomic analysis was performed. Multivariate principal component analysis (PCA) revealed a clear separation among experimental groups, indicating distinct lipidomic fingerprints across conditions (**Figure 3.5 A**).

Consistent with the steatotic phenotype, the OA/PA group showed a marked enrichment in neutral lipid classes. Notably, triglycerides (TG) and diacylglycerols (DG), lipid species widely reported as central features of metabolic dysfunction–associated steatotic liver disease and linked to disease severity and lipotoxic signaling, were prominently modulated in this dataset (Carli *et al.*, 2024; Syed-Abdul *et al.*, 2023).

The heat map (**Figure 3.5 B**) highlights a significant reduction ($p < 0.001$ vs. OA/PA) in lipid biomarkers, specifically triglycerides and diacylglycerols, in the OE co-treatment group: two DG species and five TG species were downregulated in the OA/PA+OE group (**Figures 3.5 C, D**).

This decrease in TG and DG levels aligns with the reduction in lipid accumulation observed in the ORO staining.

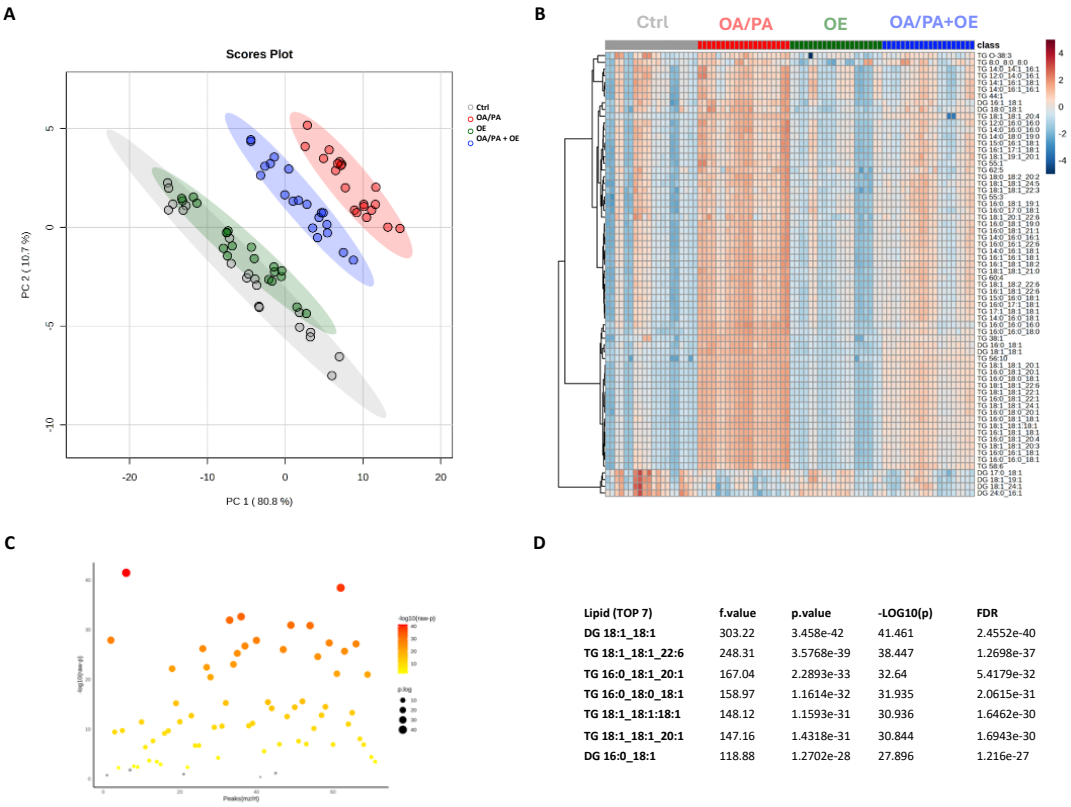

Lipid (TOP 7)	f.value	p.value	-LOG10(p)	FDR
DG 18:1_18:1	303.22	3.458e-42	41.461	2.4552e-40
TG 18:1_18:1_22:6	248.31	3.5768e-39	38.447	1.2698e-37
TG 16:0_18:1_20:1	167.04	2.2893e-33	32.64	5.4179e-32
TG 16:0_18:0_18:1	158.97	1.1614e-32	31.935	2.0615e-31
TG 18:1_18:1:18:1	148.12	1.1593e-31	30.936	1.6462e-30
TG 18:1_18:1_20:1	147.16	1.4318e-31	30.844	1.6943e-30
DG 16:0_18:1	118.88	1.2702e-28	27.896	1.216e-27

Figure 3.5. *OE reduces the levels of lipid accumulation. (**A**) PCA Scores Plot showing the pattern of distribution of lipids in HepG2 cells, after the exposure of OE and OA/PA (25 µg/mL) for 24 h (Grey: Ctrl; Green: OE; Red: OA/PA; Blue: OA/PA + OE). (**B**) HeatMap of targeted lipidomic analysis of HepG2 cells. Heatmap scales presented red for higher, and blue for lower abundance of lipids, detected according to ANOVA test. Scale is used for each of the top 66 lipids listed on the y-axis. (**C, D**) Main lipids biomarkers with statistical analysis by ANOVA test.*

3.4.4 OE modulates SIRT1 signaling and lipogenic pathways under steatogenic stress

Subsequently, was sought to elucidate the molecular mechanisms underlying the reduction in lipid droplets induced by OE, focusing on the activation of Sirtuin 1 and its downstream signaling pathways.

Co-treatment with OE markedly increased SIRT1 mRNA levels after 24 h, as demonstrated by quantitative PCR ($p < 0.01$ vs. OA/PA) (**Figure 3.6 A**). This transcriptional upregulation was confirmed at the protein level by flow cytometric analysis, which revealed a significant increase in SIRT1 expression in the OE co-treatment group compared with OA/PA alone ($p < 0.01$ vs. OA/PA) (**Figure 3.6 D**).

Consistent with SIRT1 activation, OE co-treatment led to a significant downregulation of key lipogenic markers.

In particular, sterol regulatory element-binding protein 1c (SREBP1c) expression was significantly reduced ($p < 0.01$ vs. OA/PA), together with peroxisome proliferator-activated receptor gamma (PPARγ) ($p < 0.05$ vs. OA/PA) and diacylglycerol O-acyltransferase 1 (DGAT1) ($p < 0.05$ vs. OA/PA) (**Figure 3.6 A**).

DGAT1 catalyzes the final step of triglyceride synthesis by converting diacylglycerol into triglycerides, and its upregulation has been linked to hepatic lipid accumulation and steatotic progression (Wilfling et al., 2013; Scoditti *et al.*, 2024). Coherent with the increase in DG and TG species observed in lipidomic analysis under OA/PA treatment.

Concomitantly, OE increased the expression of peroxisome proliferator-activated receptor alpha (PPARα) ($p < 0.01$ vs. OA/PA) and FOXO1 ($p < 0.01$ vs. OA/PA), two regulators involved in fatty acid oxidation and metabolic adaptation. These changes suggest a metabolic shift from lipid storage toward lipid catabolism (**Figure 3.6 A**).

OE also enhanced the phosphorylation of AMPK ($p < 0.001$ vs. OA/PA) (**Figures 3.6 B, C**), a central energy sensor that suppresses lipogenesis and promotes fatty acid oxidation. Given the well-established functional interplay between SIRT1 and AMPK, the increase in phospho-AMPK further supports activation of the SIRT1–AMPK axis under co-treatment conditions.

To confirm that SIRT1 enzymatic function was effectively stimulated, SIRT1 deacetylase activity was directly measured using a specific activity assay kit. OE co-treatment increased SIRT1 enzymatic activity compared with OA/PA alone ($p < 0.05$ vs. OA/PA), demonstrating that the phytocomplex not only upregulates SIRT1 expression but also enhances its functional activity (**Figure 3.6 E**).

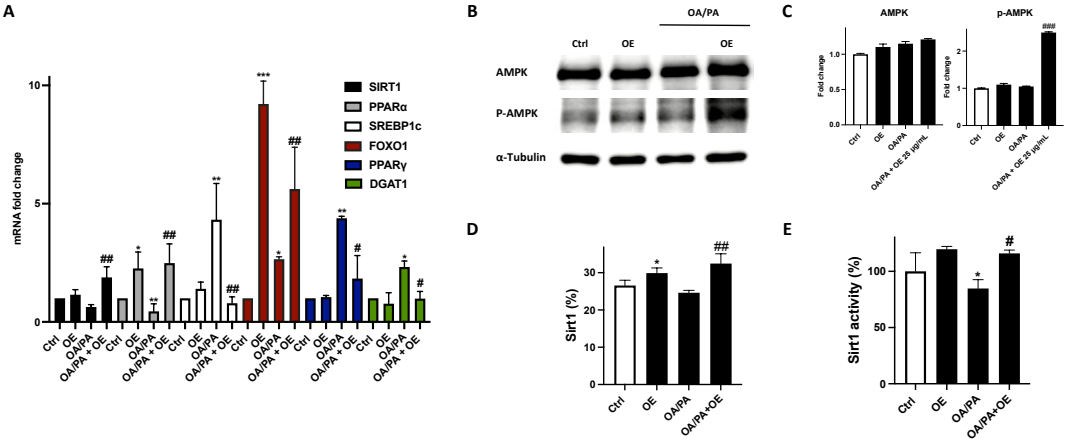

Figure 3.6. Biochemical effects of OE. *(**A**) Real-time PCR of lipid metabolism genes and (**B, C**) western blots. (**D**) Quantitative determination of SIRT1 expression through flow cytometry analysis. (**D**) Sirtuin enzymatic activity tested on HepG2 cells lysates. OE co-treatment (25 µg/mL) with OA/PA for 24 h.*
Data are shown as mean ± SD of three different experiments performed in triplicate.
** p < 0.05 vs. Ctrl; ** p < 0.01 vs. Ctrl; *** p < 0.001 vs. Ctrl.*
 # p < 0.05 vs. OA/PA; ## p < 0.01 vs. OA/PA; ### p < 0.001 vs. OA/PA.

3.4.5 OE reduces lipotoxic oxidative stress and ER stress activation

It is well established that exposure of hepatocytes to a mixture of oleic and palmitic acids induces oxidative and nitrosative stress, characterized by increased production of reactive oxygen species and nitric oxide, which contribute to lipotoxic damage (Moravcová *et al*., 2015).

In line with this evidence, OA/PA-treated HepG2 cells displayed significantly elevated intracellular ROS and NO levels compared with untreated controls ($p <$

0.01 vs. Ctrl). Co-treatment with OE markedly attenuated both ROS and NO production (p < 0.001 vs. OA/PA), indicating a robust antioxidant effect after exposure (**Figures 3.7 A, B**). These findings suggest that OE could counteract the redox imbalance associated with FFA-induced steatogenic stress.

Oxidative and nitrosative stress are tightly linked to mitochondrial dysfunction, a central event in the progression of non-alcoholic fatty liver disease (Karkucinska-Wieckowska *et al.*, 2022). Excess ROS impairs mitochondrial integrity, disrupts membrane potential, and compromises fatty acid oxidation, thereby establishing a vicious cycle that sustains lipid accumulation and further oxidative injury.

To evaluate mitochondrial functionality, mitochondrial membrane potential (ΔΨm) was assessed using TMRE, a fluorescent probe that selectively accumulates in active mitochondria in a membrane potential–dependent manner.

OA/PA treatment significantly reduced ΔΨm compared with control cells (p < 0.01 vs. Ctrl), confirming mitochondrial impairment. In contrast, OE co-treatment significantly restored mitochondrial membrane potential (p < 0.01 vs. OA/PA) (**Figures 3.7 C, D**), indicating preservation of mitochondrial function under lipotoxic conditions.

In addition to mitochondrial alterations, excessive lipid accumulation is associated with ER proteostasis disruption in hepatic cells (Wang *et al.*, 2025; Yuan *et al.*, 2025). To assess ER stress, misfolded protein accumulation was evaluated using a thioflavin assay. OA/PA exposure increased the accumulation of misfolded proteins (p < 0.01 vs. Ctrl), whereas OE significantly mitigated this effect (p < 0.01 vs. OA/PA) (**Figures 3.7 E, F**), suggesting attenuation of ER stress.

To further characterize UPR signaling, key markers were analyzed by qPCR (**Figure 3.7 G**). OE significantly reduced activation of PERK (p < 0.001 vs. OA/PA), as evidenced by decreased expression of ATF4 (p < 0.001 vs. OA/PA) and CHOP (p < 0.05 vs. OA/PA). Moreover, IRE1α expression was also significantly reduced (p < 0.001 vs. OA/PA).

Overall, OE not only reduces oxidative stress but also preserves mitochondrial integrity and limits ER stress activation.

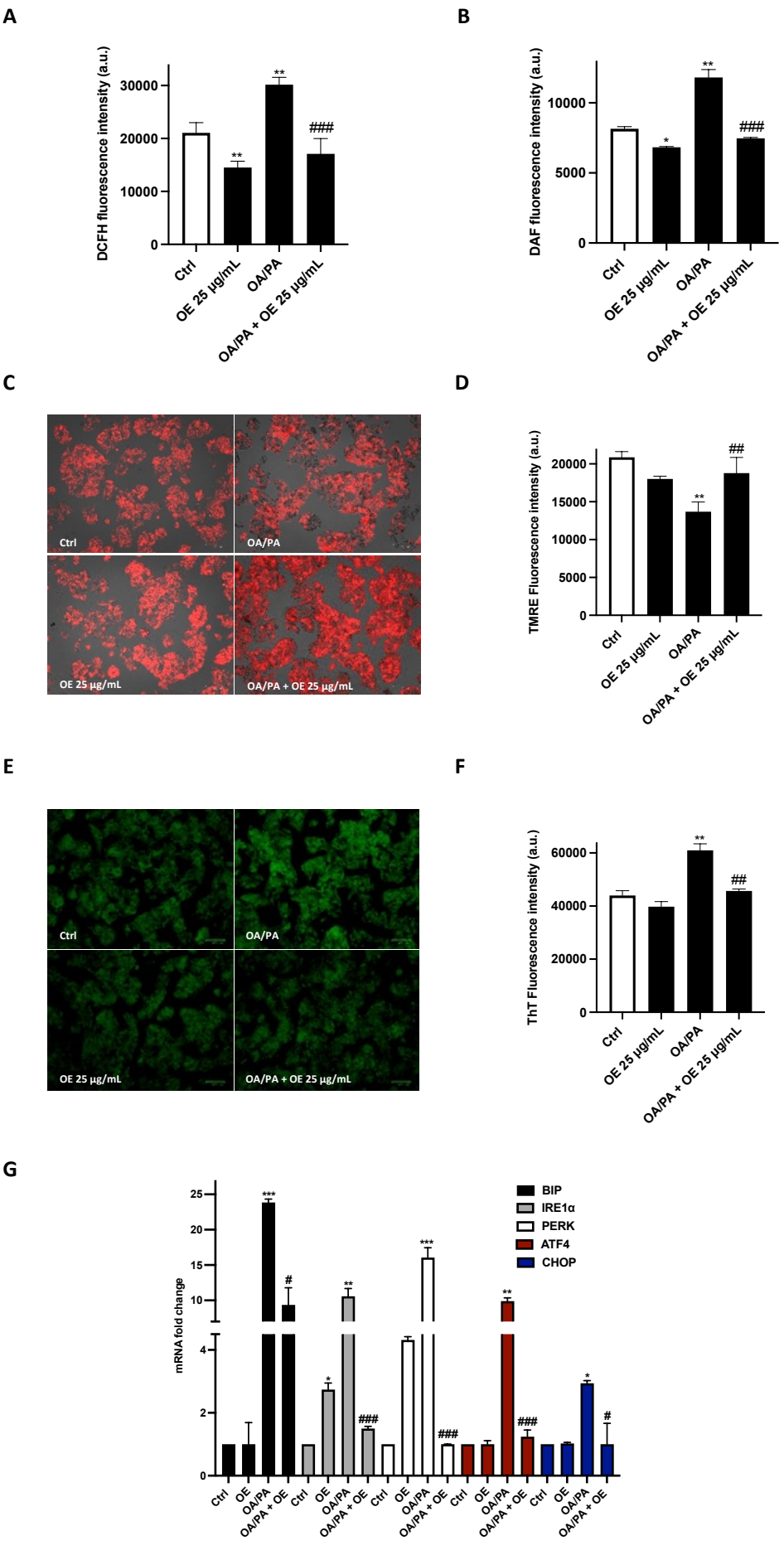
A
DCFH fluorescence intensity (a.u.)
30000
20000
10000
0
**
**
###
Ctrl
OE 25 µg/mL
OA/PA
OA/PA + OE 25 µg/mL
B
DAF fluorescence intensity (a.u.)
10000
5000
0
*
**
###
Ctrl
OE 25 µg/mL
OA/PA
OA/PA + OE 25 µg/mL
C
Ctrl
OA/PA
OE 25 µg/mL
OA/PA + OE 25 µg/mL
D
TMRE Fluorescence intensity (a.u.)
20000
15000
10000
5000
0
**
##
Ctrl
OE 25 µg/mL
OA/PA
OA/PA + OE 25 µg/mL
E
Ctrl
OA/PA
OE 25 µg/mL
OA/PA + OE 25 µg/mL
F
ThT Fluorescence intensity (a.u.)
60000
40000
20000
0
**
##
Ctrl
OE 25 µg/mL
OA/PA
OA/PA + OE 25 µg/mL
G
mRNA fold change
25
20
15
10
4
2
0
BIP
IRE1α
PERK
ATF4
CHOP
Ctrl
OE
OA/PA
OA/PA + OE

Figure 3.7. *OE decreases oxidative stress and protects the mitochondrial membrane and ER of HepG2 cells from OA/PA steatosis. (**A**) Quantitative analysis of ROS and NO (**B**) production. (**C**) Representative images for comparison of mitochondrial permeability based on TMRE staining (Magnification, 20x. N ≥ 10. Scale bar: 100 µm). (**D**) Quantitative analysis was reported. OE co-treatment (25 µg/mL) with OA/PA for 24 h. (**E**) Representative images of ThT staining (Magnification, 20x. N ≥ 10. Scale bar: 100 µm). (**F**) Quantitative analysis was reported. (**G**) Real-time PCR of ER stress genes. OE co-treatment (25 µg/mL) with OA/PA for 24 h. Data are shown as mean ± SD of three different experiments performed in triplicate.*
** p < 0.05 vs. Ctrl; ** p < 0.01 vs. Ctrl; *** p < 0.001 vs. Ctrl.*
 # p < 0.05 vs. OA/PA; ## p < 0.01 vs. OA/PA; ### p < 0.001 vs. OA/PA.

Finally, it was sought to determine whether the protective effects of OE observed in monolayer cultures could be reproduced in a 3D spheroid model, which more closely mimics the structural and metabolic features of hepatic tissue.

HepG2 spheroids were subjected to the same steatogenic conditions, and cell viability was assessed by Calcein-AM/Propidium Iodide double staining, as previously performed in the 2D system. Consistent with the monolayer data, OA/PA treatment increased the proportion of PI-positive cells within the spheroids, indicating reduced viability. In contrast, OE co-treatment markedly decreased PI staining and preserved calcein-positive viable cells (**Figure 3.8 A, second column**), confirming a cytoprotective effect under MAFLD-like conditions.

To validate the modulation of endoplasmic reticulum stress in the 3D model, CHOP, a pro-death marker associated with prolonged unfolded protein response activation, was analyzed by immunofluorescence. OA/PA-treated spheroids exhibited enhanced CHOP expression ($p < 0.01$ vs. Ctrl), whereas OE co-treatment significantly reduced CHOP signal intensity ($p < 0.001$ vs. OA/PA) (**Figures 3.8 A, third column, B**). These findings demonstrate that the protective effects of OE extend to a more physiologically relevant 3D model, supporting its ability to attenuate ER stress and promote cell survival under lipotoxic conditions

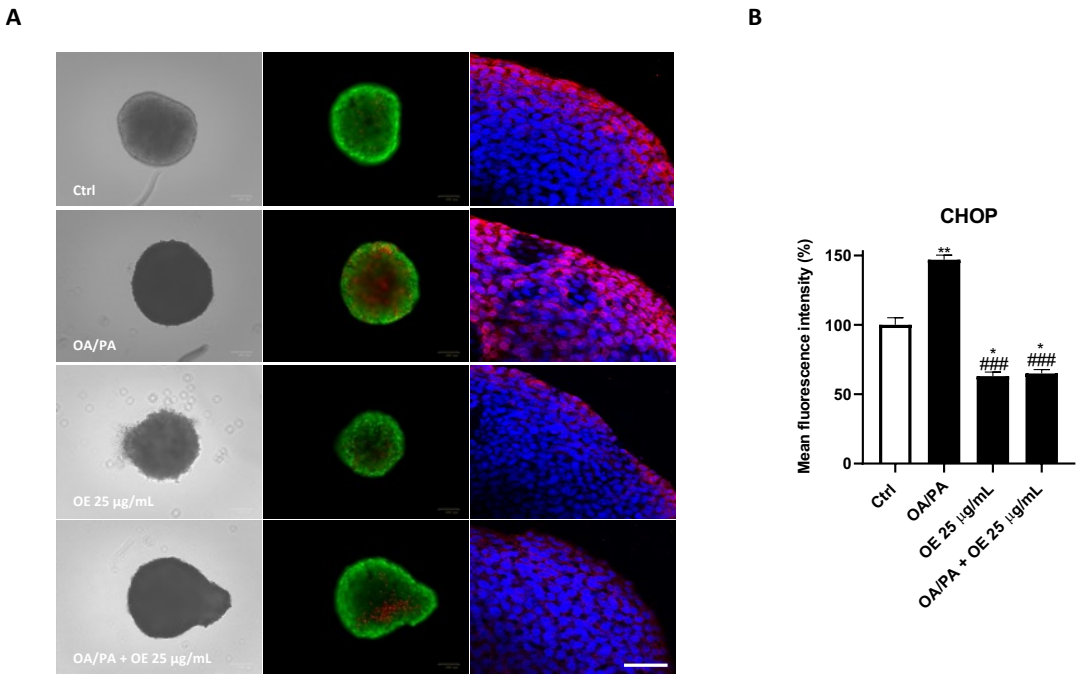

Figure 3.8. *OE protects against OA/PA in a 3D model. (**A**) 3D HepG2 cells were stained by propidium iodide (red) and calcein AM (green) (Magnification, 20x. N ≥ 10. Scale bar: 100 µm). (**B**) Confocal microscopy analysis of CHOP expression in HepG2 spheroids (red signal: CHOP; blue signal: nuclei) (Magnification, 63x. N ≥ 10. Scale bar: 25 µm). (**C**) Quantitative analysis was reported. OE co-treatment (25 µg/mL) with OA/PA for 24 h.*
Data are shown as mean ± SD of three different experiments performed in triplicate.
** p < 0.05 vs. Ctrl, ** p < 0.01 vs. Ctrl; ### p < 0.001 vs. OA/PA.*

3.5 Conclusions

This study demonstrates that a hydroalcoholic olive leaves extract attenuates free fatty acid–induced lipid accumulation and preserves cell viability in an *in vitro* model of fatty liver disease.

Lipidomic analysis confirmed a reduction in triglyceride and diacylglycerol species, while molecular investigations revealed activation of the Sirtuin 1–AMPK axis, suppression of lipogenic markers, and enhancement of lipid catabolism.

OE also reduced oxidative and nitrosative stress, preserved mitochondrial membrane potential, and mitigated endoplasmic reticulum stress, effects that were confirmed in a three-dimensional spheroid model.

Although these findings support a role for Sirtuin 1 in mediating the protective effects of OE, further mechanistic studies are necessary to definitively clarify its causal involvement.

Overall, the data highlight the potential of this olive leaf–derived phytocomplex as a modulator of metabolic and redox pathways relevant to MAFLD.

3.6 Supporting information

Table S3.1. *Tentatively identified compounds from Olea europea L. leaves extract by PDA-ESI-Orbitrap-MS/MS analysis, including the UV retention time (min), molecular formula, experimental molecular ions, calculated mass error (Δm/z, ppm), MS/MS product ions, MSI level.*

Peak	RT (min)	Name	Formula	m/z	MS2	Error (ppm)	Class	MSI Level	Adduct
1	6.04	Vanillin	$C_8H_8O_3$	153.0545	125.0597; 111.0440; 93.0334	-0.96	Phenylpropanoid	2	$[M+H]^+$
2	7.58	Norisoprenoid glucoside derivative	$C_{19}H_{34}O_9$	451.2185	405.2132; 179.0561; 167.1078; 89.0245	-3.63	Isoprenoid	2	$[M-H+FA]^-$
3	7.97	Vanillin	$C_8H_8O_3$	151.0401	123.0452; 105.0355; 63.1465	0.42	Phenylpropanoid	2	$[M-H]^-$
4	8.29	Calceolarioside	$C_{23}H_{26}O_{11}$	447.1507	401.1455; 269.1031; 161.0456	-3.36	Phenylpropanoid	2	[M-H]-1
5	8.60	Feruloyl hexoside	$C_{17}H_{21}O_{11}$	401.1089	355.1035; 269.1031; 193.0517; 179.0562; 89.0245;	2.69	Phenylpropanoid	2	$[M-H+FA]^-$
6	8.86	Vomifoliol 9-hexoside	$C_{19}H_{30}O_8$	431.1921	385.1871; 223.133; 153.0922	-0.40	Isoprenoid	2	$[M-H+FA]^-$
7	9.36	Didehydro-chebulic acid triethyl ester	$C_{20}H_{22}O_{11}$	437.1089	275.0562; 317.0667; 196.7854	2.61	Other	2	$[M-H-H_2O]^-$
8	9.99	Verbascoside	$C_{20}H_{30}O_{12}$	461.1665	415.1613; 149.0457; 89.0245	2.43	Phenylpropanoid	2	$[M-H]^-$
9	11.49	Unknown	-				-	4	
10	12.55	Vicenin II	$C_{27}H_{30}O_{15}$	593.1514	285.0404; 327.0490; 547.2759	2.25	Flavonoid	2	$[M-H]^-$
11	13.29	Rutin	$C_{27}H_{30}O_{16}$	611.1962	303.0865; 465.1384; 345.0971; 129.0546	-1.44	Flavonoid	1	$[M+H]^+$
12	13.53	Luteolin-7-*O*-glucoside	$C_{21}H_{19}O_{11}$	447.0933	285.0407; 327.0503; 88.8040	2.40	Flavonoid	1	$[M-H]^-$
13	13.74	Vicenin II (*isomer*)	$C_{27}H_{30}O_{15}$	593.1514	547.2750; 285.0404; 139.7659	2.14	Flavonoid	2	$[M-H+FA]^-$
14	13.95	Naringin	$C_{27}H_{32}O_{14}$	579.1718	459.1158; 271.0613; 151.0039	1.59	Flavonoid	1	$[M-H]^-$
15	14.32	Unknown	-				-	4	
16	14.46	Cichorioside	$C_{21}H_{28}O_{10}$	485.1664	407.1353; 227.0719; 89.0247	-3.13	Sesquiterpene	2	$[M-H+FA]^-$
17	14.85	Neohesperidin	$C_{28}H_{34}O_{15}$	609.1824	301.0719; 343.0834; 447.1274	-0.10	Flavonoid	1	$[M-H]^-$
18	15.22	Deoxylactucin (8-)	$C_{15}H_{16}O_4$	261.1119	189.0546; 243.1015; 201.0541	-0.87	Sesquiterpene	2	$[M+H]^+$
19	15.37	Oleuropein	$C_{25}H_{32}O_{13}$	539.1768	377.1244; 307.0825; 275.0924	1.67	Secoiridoid	1	$[M-H]^-$
20	15.58	Diosmin	$C_{28}H_{32}O_{15}$	609.1808	301.0705; 463.1247; 129.0545	-1.00	Flavonoid	2	$[M+H]^+$
21	17.04	2"'-O-Rhamnosyl-2"-O-glucosylcytisoside	$C_{34}H_{42}O_{19}$	753.2249	609.1826; 651.1931; 691.2242	0.13	Flavonoid	2	$[M-H]^-$
22	17.46	Luteolin	$C_{15}H_{10}O_6$	285.0404	228.9089; 147.3670; 133.0338	0.02	Flavonoid	2	$[M-H]^-$

23	17.76	Luteolin (*isomer*)	$C_{15}H_{10}O_6$	287.0548	195.3084; 176.6797; 137.6104	-0.71	Flavonoid	2	$[M+H]^+$
24	18.01	Unknown	-				-	4	
25	18.50	Citrubuntin	$C_{15}H_{15}O_3$	243.1013	189.0547; 201.0548; 187.0391; 159.040	-0.91	Flavonoid	2	$[M+H]^+$
26	18.78	Dimethyl hydroxy octenoyloxy secologanoside	$C_{26}H_{37}O_{13}$	557.224	513.2344; 227.1289; 345.1185	2.03	Secoiridoid	2	$[M-H]^-$
27	19.58	3-(3,4-Methylenedioxyphenyl)propenal	$C_{10}H_8O_3$	177.0545	145.0285; 117.0335; 135.0448	-0.48	Phenylpropanoid	2	$[M+H]^+$
28	20.42	trans-3,3',4',5,5',7-Hexahydroxyflavanone	$C_{15}H_{12}O_8$	319.0462	301.0354; 275.0547; 34.6907	0.81	Flavonoid	2	$[M-H]^-$
29	22.36	Tangeritin	$C_{20}H_{21}O_7$	373.1281	358.1054; 285.7596; 86.0289	-0.34	Flavonoid	2	$[M+H]^+$
30	23.04	Glycyrrhizin	$C_{42}H_{62}O_{16}$	821.3965	351.0570; 193.0351; 113.0243	-0.04	Terpene Glycosides	2	$[M-H]^-$
31	23.67	Sinensetin	$C_{20}H_{20}O_7$	373.1278	358.1045; 312.1012; 343.0812;312.5631; 212.4986	-0.91	Flavonoid	2	$[M+H]^+$

*according to metabolomics standard initiative (MSI).

3.7 References

Anggreini, P., Kuncoro, H., Sumiwi, S.A. and Levita, J. (2023). Role of the AMPK/SIRT1 pathway in non alcoholic fatty liver disease (Review). *Molecular Medicine Reports*, 27(2), 35.

Buzzetti, E., Pinzani, M. and Tsochatzis, E.A. (2016). The multiple-hit pathogenesis of non-alcoholic fatty liver disease (NAFLD). *Metabolism*, 65(8), 1038–1048.

Carli, F., Della Pepa, G., Sabatini, S., Vidal Puig, A. and Gastaldelli, A. (2024). Lipid metabolism in MASLD and MASH: From mechanism to the clinic. *JHEP Reports*, 6, 101185.

Chung, S., Yao, H., Caito, S., Hwang, J.W., Arunachalam, G. and Rahman, I. (2010). Regulation of SIRT1 in cellular functions: role of polyphenols. *Archives of Biochemistry and Biophysics*, 501(1), 79–90.

de Oliveira, N.M., Machado, J., Chéu, M.H., Lopes, L., Barroso, M.F., Silva, A., Sousa, S., Domingues, V.F. and Grosso, C. (2024). Potential Therapeutic Properties of *Olea europaea* Leaves from Selected Cultivars Based on Their Mineral and Organic Profiles. *Pharmaceuticals*, 17(3), 274.

Ding, R.B., Bao, J. and Deng, C.X. (2017). Emerging roles of SIRT1 in fatty liver diseases. *International Journal of Biological Sciences*, 13(7), 852–867.

Domi, E. and Hoxha, M. (2025). Natural Compounds Targeting SIRT1 and Beyond: Promising Nutraceutical Strategies Against Atherosclerosis. *Nutrients*, 17(21), 3316.

Elmorsy, A.E., Elsisi, H.A., Alkhamiss, A.S., Alsoqih, N.S., Khodeir, M.M., Alsalloom, A.A., Almeman, A.A., Elghandour, S.R., Nadwa, E.H., Khalifa, A.K., Khaled, B.E.A., Ramadan, A., Kamal, M.M., Alsaeed, T.S., Alharbi, M.S., Abdel-Moneim, A.H., Ellethy, A.T. and Saber, S. (2025). Activation of SIRT1 by SRT1720 alleviates dyslipidemia, improves insulin sensitivity and exhibits liver-protective effects in diabetic rats on a high-fat diet: New insights into the SIRT1/Nrf2/NFκB signaling pathway. *European Journal of Pharmaceutical Sciences*, 206, 107002.

Eslam, M., Newsome, P.N., Sarin, S.K., Anstee, Q.M., Targher, G., Romero-Gomez, M., Zelber-Sagi, S., Wai-Sun Wong, V., Dufour, J.F., Schattenberg, J.M., Kawaguchi, T., Arrese, M., Valenti, L., Shiha, G., Tiribelli, C., Yki-Järvinen, H., Fan, J.G., Grønbæk, H., Yilmaz, Y., Cortez-Pinto, H., Oliveira, C.P., Bedossa, P., Adams, L.A., Zheng, M.H., Fouad, Y., Chan, W.K., Mendez-Sanchez, N., Ahn, S.H., Castera, L., Bugianesi, E., Ratziu, V. and George, J. (2020). A new definition for metabolic dysfunction-associated fatty liver disease: An international expert consensus statement. *Journal of Hepatology*, 73(1), 202–209.

Eslam, M., Sanyal, A.J. and George, J. (2020). MAFLD: A Consensus-Driven Proposed Nomenclature for Metabolic Associated Fatty Liver Disease. *Gastroenterology*, 158(7), 1999–2014.e1.

Gofton, C., Upendran, Y., Zheng, M.H. and George, J. (2023). MAFLD: How is it different from NAFLD? *Clinical and Molecular Hepatology*, 29(Suppl), S17–S31.

Karkucinska-Wieckowska, A., Simoes, I.C.M., Kalinowski, P., Lebiedzinska-Arciszewska, M., Zieniewicz, K., Milkiewicz, P., Górska-Ponikowska, M., Pinton, P., Malik, A.N., Krawczyk, M., Oliveira, P.J. and Wieckowski, M.R. (2022). Mitochondria, oxidative stress and nonalcoholic fatty liver disease: A complex relationship. *European Journal of Clinical Investigation*, 52(3), e13622.

Kitada, M., Ogura, Y., Monno, I. and Koya, D. (2019). Sirtuins and type 2 diabetes: role in inflammation, oxidative stress, and mitochondrial function. *Frontiers in Endocrinology*, 10.

Li, X., Chen, W., Jia, Z., Xiao, Y., Shi, A. and Ma, X. (2025). Mitochondrial Dysfunction as a Pathogenesis and Therapeutic Strategy for Metabolic-Dysfunction-Associated Steatotic Liver Disease. *International Journal of Molecular Sciences*, 26(9), 4256.

Meng, D., Zhang, F., Yu, W., Zhang, X., Yin, G., Liang, P., Feng, Y., Chen, S. and Liu, H. (2023). Biological Role and Related Natural Products of SIRT1 in Nonalcoholic Fatty Liver. *Diabetes, Metabolic Syndrome and Obesity*, 16, 4043–4064.

Merciai, F., Musella, S., Sommella, E., Bertamino, A., D'Ursi, A.M. and Campiglia, P. (2022). Development and application of a fast ultra-high performance liquid chromatography-trapped ion mobility mass spectrometry method for untargeted lipidomics. *Journal of Chromatography A*, 1673, 463124.

Moravcová, A., Červinková, Z., Kučera, O., Mezera, V., Rychtrmoc, D. and Lotková, H. (2015). The effect of oleic and palmitic acid on induction of steatosis and cytotoxicity on rat hepatocytes in primary culture. *Physiological Research*, 64(Suppl 5), S627–S636.

Omagari, K., Koba, C., Nagata, A., Ngo, L.C.T., Yamasaki, M., Fukuda, A., Yuasa, M., Suruga, K., Inada, N., Ichimura-Shimizu, M. and Tsuneyama, K. (2021). Olive leaf powder prevents nonalcoholic steatohepatitis in Sprague–Dawley rats fed a high-fat and high-cholesterol diet. *Clinical Nutrition Open Science*, 37, 47–59.

Ruderman, N.B., Xu, X.J., Nelson, L., Cacicedo, J.M., Saha, A.K., Lan, F. and Ido, Y. (2010). AMPK and SIRT1: A long-standing partnership? *American Journal of Physiology-Endocrinology and Metabolism*, 298, E751–E760.

Scoditti, E., Sabatini, S., Carli, F., et al. (2024). Hepatic glucose metabolism in the steatotic liver. *Nature Reviews Gastroenterology & Hepatology*, 21, 319–334.

Syed-Abdul, M.M. (2023). Lipid Metabolism in Metabolic-Associated Steatotic Liver Disease (MASLD). *Metabolites*, 14(1), 12.

Tauil, R.B., Golono, P.T., de Lima, E.P., de Alvares Goulart, R., Guiguer, E.L., Bechara, M.D., Nicolau, C.C.T., Yanaguizawa Junior, J.L., Fiorini, A.M.R., Méndez-Sánchez, N., Abenavoli, L., Direito, R., Valente, V.E., Laurindo, L.F. and Barbalho, S.M. (2024). Metabolic-Associated Fatty Liver Disease: The Influence of Oxidative Stress, Inflammation, Mitochondrial Dysfunctions, and the Role of Polyphenols. *Pharmaceuticals*, 17(10), 1354.

Vestuto, V., Ciaglia, T., Musella, S., Di Sarno, V., Smaldone, G., Di Matteo, F., Scala, M.C., Napolitano, V., Miranda, M.R., Amodio, G., Novi, S., Pepe, G., Basilicata, M.G., Gazzillo, E., Pace, S., Gomez-Monterrey, I.M., Sala, M., Bifulco, G., Tecce, M.F., et al. (2024). A comprehensive in vitro characterization of a new class of indole-based compounds developed as selective haspin inhibitors. *Journal of Medicinal Chemistry*, 8, 12711–12734.

Wang, G., Sun, B., Liu, H., Hu, M., Xu, H., Li, H., Wang, X. and Tong, M. (2025). Interactions between lipid droplets and mitochondria in metabolic diseases. *Lipids in Health and Disease*, 24(1), 357.

Wilfling, F., Wang, H., Haas, J.T., et al. (2013). Triacylglycerol synthesis enzymes mediate lipid droplet growth by relocalizing from the ER to lipid droplets. *Developmental Cell*, 24, 384–399.

Yuan, X., Sun, W., Xu, Y., Xiang, M., Gao, Y., Feng, W., Xiao, H., Zhang, L., Tang, Q., Lu, J. and Zhang, Y. (2025). Altered mitochondrial unfolded protein response and FGF21 secretion in MASLD progression and the effect of exercise intervention. *Scientific Reports*, 15, 3686.

Zhao, K., Zhang, H. and Yang, D. (2024). SIRT1 exerts protective effects by inhibiting endoplasmic reticulum stress and NF-κB signaling pathways. *Frontiers in Cell and Developmental Biology*, 12.

4. Chapter IV: *Allium cepa* L. (Cipollotto Nocerino) leaves extract

Cipollotto Nocerino (CN) leaves extract ameliorates non-alcoholic lipid accumulation in hepatic cells

4.1 Abstract

Cipollotto Nocerino leaves (*Allium cepa L.*), traditionally cultivated in the Campania region (Southern Italy) and typically consumed at an early developmental stage, represent an underexplored agricultural matrix rich in bioactive compounds.

Therefore, this study evaluated the hepatoprotective activity of a CN leaves alcoholic extract in HepG2 cells exposed to oleic and palmitic acids (OA/PA) to induce steatosis, in both two- and three-dimensional culture systems.

UHPLC-HRMS/MS analysis revealed a complex phytochemical profile comprising polar and apolar lipids, chlorophylls, carotenoids, and flavonoids. These metabolites, known to regulate oxidative stress, inflammation, and lipid metabolism, likely mediate CN's protective effects against lipotoxicity.

In HepG2 cells, CN markedly improved cell viability, attenuated lipid droplet accumulation, restored redox balance, alleviated ER stress, preserved mitochondrial membrane potential, and reduced some inflammation markers.

Sirtuin 1 expression and activity were enhanced by CN in the presence of OA/PA, and the pharmacological modulation confirmed its partial involvement in the protective effects.

These findings demonstrate that CN counteracts free fatty acid-induced lipotoxicity through an integrated mechanism targeting lipid metabolism, oxidative and ER stress, mitochondrial function, and inflammation, with SIRT1 activation acting as a central, though not exclusive, mediator supporting its potential as a promising, sustainable nutraceutical for the prevention or adjunct management of non-alcoholic steatosis.

4.2 Introduction

Onion (*Allium cepa* L.) is one of the most widely consumed vegetables worldwide and contributes significantly to municipal and industrial waste streams.

Onion processing generates large quantities of solid by-products, including skins, outer fleshy scales, roots, leaves, and apical and basal trimmings of bulbs, collectively referred to as onion solid wastes (OSW) (Nile *et al.*, 2018; Črnivec *et al.*, 2021).

A substantial amount of OSW is generated globally; for example, approximately 100,000 tons are produced annually in California, USA, and about 500,000 tons each year in the European Union, particularly in Spain, Holland, and the UK (Nile *et al.*, 2017). Despite being traditionally regarded as waste, OSW have attracted increasing interest for the recovery of bioactive compounds (González-de-Peredo *et al.*, 2021; González-de-Peredo *et al.*, 2022; Bordin Viera *et al.*, 2023).

In particular, fresh onion leaves contain high levels of bioactive compounds such as polyphenols, flavonoids, carotenoids, vitamins, and chlorophylls (El-Hadidy, Mossa and Habashy, 2014; Yuasa *et al.*, 2018). However, despite their significant nutraceutical potential, onion leaves remain comparatively underexplored.

Cipollotto Nocerino (CN) is a traditional Italian spring onion cultivated for over 2000 years in the Campania region, particularly in the Pompeii–Nocera area.

It has been granted Protected Designation of Origin (PDO) status (Reg. CE n. 656/2008). While bulbs and dry skins have been extensively investigated, CN leaves remain largely unexplored, representing a clear gap in the literature and a potential target for nutraceutical valorization (Bedir *et al.*, 2025; Lee *et al.*, 2025).

Leaves of *Allium* species are rich in phenolic compounds, flavonoids, and other secondary metabolites, often at levels comparable to or higher than those found in bulbs. Several studies report high levels of quercetin derivatives and strong antioxidant activity in onion leaves, supporting their potential role in preventing oxidative stress–related disorders (Kurnia *et al.*, 2021; Lee *et al.*, 2025).

Previous investigations demonstrated for the first time that microwave-assisted extraction of CN leaves yields extracts with high total phenolic content and strong antioxidant capacity. Two-dimensional LC–MS analyses identified diverse bioactive

compounds, including flavonoids, saponins, and fatty acids, supporting their potential as functional ingredients (Aquino *et al.*, 2025; Aquino *et al.*, 2023).

The valorization of onion leaves aligns with circular economy principles, transforming agricultural by-products into high-value nutraceutical resources (Augimeri *et al.*, 2021; Abderrezag *et al.*, 2021; Aquino *et al.*, 2023).

In this context, the antioxidant potential previously observed in CN leaf extracts raises the question of whether such redox-modulating properties could translate into functional benefits in a steatogenic environment.

Specifically, it remains to be clarified whether the bioactive constituents of CN leaves can influence lipid accumulation and stress-responsive pathways in hepatocytes exposed to fatty acid overload.

Exploring this possibility would provide further insight into the nutraceutical value of CN leaves and their potential role in mitigating metabolic liver alterations.

4.2.1 Aim of work

Oxidative stress, ER stress, and inflammation play central roles in MAFLD pathogenesis, suggesting that natural products able to counteract these events may offer significant benefits.

Among the molecular targets of interest, Sirtuin 1, as previously explored, is particularly relevant. Its activation has been associated with reduced triglyceride deposition, improved antioxidant defenses, and suppression of NF-κB-mediated inflammation. Therefore, compounds that enhance SIRT1 activity are being investigated as potential strategies to limit hepatic fat accumulation and its downstream complications (Meng *et al.*, 2023; Lewis Lujian *et al.*, 2024).

The valorization of onion leaves aligns with circular economy and biodiversity, because CN leaves remain a geographically and culturally specific residue that is still poorly investigated despite their rich phytochemical profile.

To gain insight into the phytochemical composition of the CN extract and to identify potential classes of bioactive compounds that may contribute to its protective effects against lipid accumulation, a comprehensive UHPLC-HRMS/MS analysis was performed. This approach enabled an in-depth characterization of

the alcoholic extract, providing detailed information on its major constituents and molecular diversity.

The extract was tested in HepG2 cells exposed to oleic and palmitic acids to induce diet-related steatosis, both in two-dimensional and three-dimensional culture systems. Was assessed the ability of CN to attenuate lipid droplet accumulation, to regulate genes involved in lipid metabolism and SIRT1 signaling, and to enhance SIRT1 activity in the presence of fatty acids. In addition, we evaluated CN effects on oxidative stress, ER stress markers, mitochondrial membrane potential, and inflammatory mediators (**Figure 4.1**).

Finally, the contribution of SIRT1 was examined by pharmacological modulation with inhibitors and activators of SIRT1, confirming its central role in mediating CN-induced hepatoprotection. These findings highlight the capacity of CN to mitigate steatosis and related oxidative damage, supporting its development as a sustainable nutraceutical for the prevention of MAFLD.

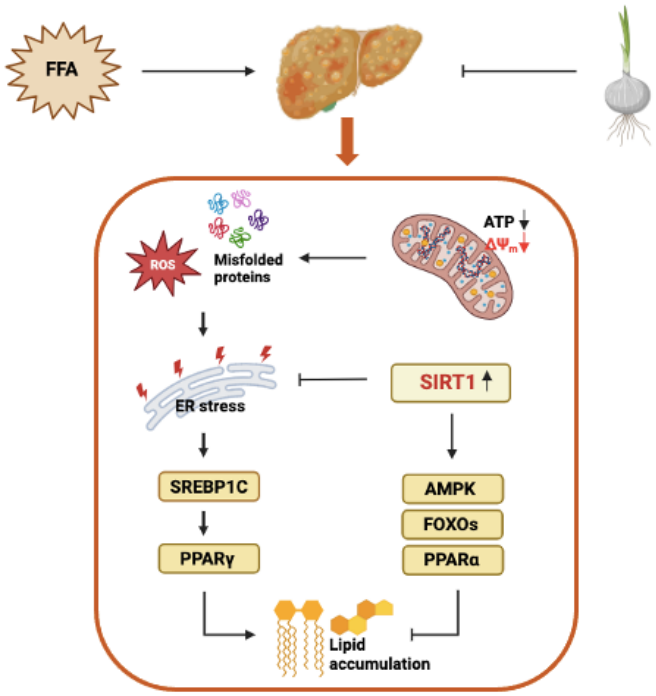

Figure 4.1. *CN exerts protective effects against FFA-induced lipotoxic damage, potentially through activation of Sirtuin 1 signaling and modulation of metabolic and redox pathways.*

4.3 Materials and Methods

4.3.1 Sample preparation

CN leaves were lyophilized for 24 h (Manifold Freeze Dryer MFDQ 2002, Laboquest), using condenser temperature at − 80 °C and 1 Pa as vacuum pressure. Briefly, 2.5 g of dry CN leaves were extracted with 50 mL of EtOH two times at 40 °C under magnetic stirring at 550 rpm for 60 min. Then, the solutions were centrifuged at 6000 rpm for 15 minutes at 4°C (Mikro 220R centrifuge), and the supernatant were filtered under vacuum, polled, and concentrated by vacuum evaporation. Finally, the extracts were freeze-dried, reconstituted in 1 mL of the corresponding extraction solvent, and subjected to further analysis.

4.3.2 UHPLC-HRMS/MS conditions

UHPLC-HRMS/MS analysis were performed on a Thermo Scientific™ Vanquish™ UHPLC system coupled online to a Orbitrap Exploris 120 mass spectrometer (Thermo Fisher Scientific) equipped either with a heated electrospray ionization (HESI II) or an atmospheric pressure chemical ionization (APCI) source.

Chromatographic separation was carried out in reversed-phase mode using a Kinetex® 2.6 µm EVO C18 100 Å, 150 × 2.1 mm analytical column (Phenomenex), thermostated at 40 °C for HESI analysis and at 45 °C for APCI analysis.

For HESI analysis, the mobile phases consisted of H_2O (A) and ACN (B) both acidified with 0.1 (v/v %) HCOOH and delivered at a constant flow rate of 0.4 mL/min. The elution gradient was: 0.01-15.00 min, 5-20% B; 15.01-24.00 min, 20-95% B; 24.01-30.00 min, 95-100% B; 30.01-32.00 min, isocratic to 100% B; 32.01-34.00 min, 100-5% B; then four minutes for column re-equilibration.

For APCI analysis, the aqueous mobile phase was H_2O containing10 mM ammonium acetate (A) and the organic phase (B) was ACN/MeOH/IPA (70:20:10 v/v) (B) The elution gradient was as follows: 0.01-25.00 min, 50-100% B; 25.01-30.00 min, isocratic to 100% B; 30.01-31.00 min, 100-50% B; followed by 4 minre-equilibration.

Both ionization sources were operated in positive and negative mode, with calibration performed using Thermo calmix Pierce™ calibration solutions in both polarities.

For HESI, Full MS (150–1500 m/z) and data-dependent MS/MS were acquired at 35,000 and 17,500 FWHM resolution, respectively, with NCE values of 15, 20, and 25. Source parameters were: sheath gas 50 arbitrary units (a.u.), auxiliary gas 13 a.u., spray voltage +3.5/–2.8 kV, capillary temperature 310 °C, auxiliary gas heater 300 °C.

For APCI, Full MS (100–1500 m/z) and data-dependent MS/MS were acquired at 60,000 and 15,000 FWHM resolution, respectively, with an NCE of 30. Source parameters were: sheath gas 45 a.u., auxiliary gas 5 a.u., sweep gas 1 a.u., discharge current +4/–10 µA, capillary temperature 300 °C, auxiliary gas heater 350 °C.

4.3.3 Data analysis

For data analysis and processing, FreeStyle™ 1.8 SP2 and Compound Discoverer™ 3.1 software (Thermo Scientific,) were used for raw data processing (baseline correction, noise filtering, spectral alignment, and peak detection) and for putative identification of metabolites based on molecular formula (matched), exact mass (mass tolerance <5 ppm) and MS2 fragmentation pattern [Fragment Ion Search (FISh)], with a global database search (mzCloud, MassList and ChemSpider).

To obtain more information about the chemical profile of the investigated extract, further processing was carried out using MZmine (version 4.4.3). An untargeted LC-MS/MS workflow was applied by performing a processing mzwizard by selected UHPLC system and MS Orbitrap type. After the final aligned feature list, spectral library search was performed to annotate compounds by matching features with spectral libraries such as MoNA (https://mona.fiehnlab.ucdavis.edu/), GNPS (https://gnps.ucsd.edu/ProteoSAFe/static/gnps-splash.jsp/) and the freely available MSnLib Mass spectral libraries (.mgf) on Zenodo (https://zenodo.org/records/11163381).

4.3.4 Determination of total phenolic content (TPC), total flavonoids content (TFC), chlorophylls (CHLs) and carotenoids (CARs) content

TPC of the CN extract was assessed using a modified version of the Folin–Ciocalteu method. A standard calibration curve was generated using gallic acid dissolved in methanol (1 mg/mL stock), with concentrations ranging from 30 to 500 µg/mL (y =

0.0014x − 0.1549; R^2 = 99.62%). All measurements were performed in triplicate. Results were expressed as milligrams of gallic acid equivalents per gram of dry weight (mg GAE/g DW).

The total flavonoid content of the extract was quantified according to the method described previously. Quantification was carried out using a standard curve prepared with rutin (30–500 µg/mL; y = 0.0004x – 0.0567; R^2 = 99.78%). All assays were performed in triplicate. TFC was expressed as milligrams of rutin equivalents per gram of dry weight (mg RU/g DW).

The chlorophyll content was determined using the methods described by Wang *et al.* and Zhang *et al.*, and the carotenoids content was determined using the method reported by Samec *et al.*, appropriately modified (Šamec *et al.*, 2014; Wang *et al.*, 2022; Zhang *et al.*, 2022).

The content of the pigments was calculated by the measured absorbance value, the solution volume, and the sample mass according to the following equations:

$$Chl\ a\ \left(\frac{mg}{gDW}\right) = \frac{\{[(12.25\times A_{663.2}) - (2.79\times A_{646.8})]\times V\}}{m} \qquad \textit{Equation 4.1}$$

$$Chl\ b\ \left(\frac{mg}{gDW}\right) = \frac{\{[(21.50\times A_{646.8}) - (5.10\times A_{663.2})]\times V\}}{m} \qquad \textit{Equation 4.2}$$

$$Car\ \left(\frac{mg}{gDW}\right) = \frac{\{[(4.75\times A_{452.5}) - (0.226\times (Chl\ a + Chl\ b))]\times V\}}{m} \qquad \textit{Equation 4.3}$$

where V is the extract volume (mL), m is the dry sample weight (mg), and A_663.2, A_646.8, and A_452.5 are the absorbance values.

All analyses were carried out in triplicate, and CHL and CAR contents were expressed in micrograms per gram of dry weight (µg/g DW).

4.3.5 DPPH (2,2-diphenyl-1-picrylhydrazyl) assay

The free radical scavenging ability of the CN was tested using DPPH radical scavenging assay (Aquino *et al.*, 2023). The DPPH radical scavenging activity of the sample was expressed as Trolox equivalent antioxidant capacity (TEAC, mg TXE/g) calculated as follows: TEAC = $IC50Trolox\ /AIC50sample$. The higher TEAC value means a higher DPPH radical scavenging activity.

4.3.6 FRAP (Ferric Reducing Antioxidant Power) assay

The assay was conducted under the conditions previously described (Aquino *et al.*, 2023). Trolox was used as reference (1–200 µg/mL; y = 0.0202x + 0.1323; R^2 = 99.99%). FRAP activity was calculated as milligrams of trolox equivalents per gram of dry weight (mg TXE/g DW).

4.3.7 Cell cultures and drug treatment

Human hepatocellular carcinoma cell line HepG2 was obtained from ATCC.

These cells were grown in Minimum Essential Medium (MEM, 4500 mg/mL glucose) supplemented with 10% (*v*/*v*) fetal bovine serum, 2 mM L-glutamine, 100 U/mL penicillin, 0.1 mg/mL streptomycin and 5% non-essential amino acid.

Cells were routinely grown in culture dishes in a 95% humidified environment containing 5% CO_2 at 37 °C and split every 2 days.

In each experiment, cells were placed in a fresh medium and and treated with CN in the presence of a mix of OA/PA, in a 2:1 ratio, for different experimental times.

As additional controls, cells were also exposed to the Sirtuin 1 inhibitor EX527 (Sigma-Aldrich; 10 µM) and the Sirtuin 1 activator SRT2104 (MedChemExpress; 10 µM). Each treatment and analysis were performed in at least three independent experiments carried out in triplicate.

4.3.8 Preparation of free fatty acids (FFA) treatments

OA and PA were purchased from Sigma Aldrich. Stock solutions of 100 mM OA and PA were first prepared in 100% ethanol.

PA was solubilized by heating at 70 °C for approximately 30 min, while OA was dissolved at room temperature. To prepare the FFA–BSA conjugates, a 5% bovine serum albumin solution was obtained by diluting a 20% BSA stock (Sigma Aldrich) with complete MEM culture medium. OA and PA were then added to the 5% BSA solution at final concentrations of 2.5 mM and 1.25 mM, respectively, to obtain an OA:PA molar ratio of 2:1. The mixture was incubated under gentle agitation for 1 h at 37 °C to allow conjugation. For cell treatments, the conjugated FFA solution was

diluted 1:5 in complete MEM medium, yielding final concentrations of 500 µM OA and 250 µM PA. A 5% BSA solution prepared under the same conditions was used as the control and added to the cells at the same dilution as the FFA–BSA conjugates.

4.3.9 Growth and maturation of spheroids in culture

HepG2 spheroids were generated by seeding 3,000 cells in 20 µL of medium as hanging drops on the inner side of 60 mm Petri dish lids. The cells aggregated by gravity at the bottom of each drop, forming a single spheroid per drop.

After 3 days of incubation, the spheroids were carefully collected and transferred into 24-well plates previously coated with 1% agarose to prevent cell adhesion. Once transferred, the spheroids were treated for 24 h with CN at a concentration of 50 µg/mL and a mixture of OA/PA.

4.3.10 Cell viability assay

Cell viability was established by measuring mitochondrial metabolic activity with MTT. Briefly, HepG2 (20×10^3 cells/well) was plated into 96-well plates, then the CN (12.5–50 µg/mL) was added in co-administration with OA/PA for 24 h to assess cytoprotective effects in the hepatic steatotic model.

Afterward, MTT reagent at 0.5 mg/mL final concentration for 2 h was added.

Then, 100 µL per well of 0.1 M isopropanol/HCl solution was added to dissolve the formazan crystals. The absorbance was measured at 570 nm, using a microplate reader (Multiskan Go, Thermo Scientific).

Cell viability was expressed as a percentage relative to the untreated cells cultured in medium with 0.1% DMSO and set to 100%, whereas 10% DMSO was used as positive control and set to 0% of viability.

4.3.11 Reactive oxygen species (ROS) detection

Reactive oxygen species were quantified using 10 µM DCFH-DA (Sigma Aldrich). HepG2 cells (20×10^3/well) were seeded in 96-well plates and allowed to adhere for 24 h, then treated for 24 h with CN (50 µg/mL) co-administered with OA/PA.

After treatments, the medium was removed, and the cells were washed twice with PBS. A staining solution containing DCFH-DA in serum-free medium without phenol-red was added for 40 min at 37 °C in the dark. The fluorescence signals (excitation/emission 485 nm/535 nm) were read in end point mode using a PerkinElmer EnSpire multimode plate reader.

The fluorescence representative images of live cells were captured using a ZOE Fluorescence Imager (Bio-Rad. Magnification, 20×. N ≥ 10. Scale bar: 10 µm).

4.3.12 Nitrite determination

HepG2 cells (20 × 10^3/well) were seeded in 96-well plates and allowed to adhere for 24 h, then treated for 24 h with CN (50 µg/mL) co-administered with OA/PA.
NO generation was measured as nitrite, indicating NO_2 release by cells in the culture medium. NO_2 amounts were measured by Griess reaction.
Briefly, 100 µL of cell culture medium were mixed with 100 µL of Griess reagent-equal volumes of 1% (w:v) sulphanilamide in 5% (v:v) phosphoric acid and 0.1% (w:v) naphtylethylenediamine-HCl and incubated at room temperature for 10 min, then the absorbance was measured at 550 nm in a microplate reader (Multiskan Go, Thermo Scientific). The amount of NO_2, as µM concentration, in the samples was calculated by a sodium nitrite standard curve.

4.3.13 Quantification of cellular glutathione (GSH) levels

A colorimetric assay using Ellman's reagent was used for this test.

The assay based on the oxidation of GSH by 5,5'-dithiobis(2-nitrobenzoic acid) (DTNB) to measure the total glutathione (tGSH) content of biological samples (Isaac *et al.*, 2021). HepG2 cell line (1.5 × 10^6 cells/well) was seeded in 60 mm culture dishes, treated with CN extract (50 µg/mL) and OA/PA.

After 24 h from treatments, cells were washed twice with PBS and detached with a scraper, centrifuged at 655*g* × 10 min at 4 °C. Then, 100 µL of 5% (v/v) trichloroacetic acid (TCA), previously cooled to 4 °C, was added to the cell pellet. Samples were incubated on ice for 15 minutes to promote protein precipitation. Subsequently, the samples were centrifuged at 13,000 × g for 10 minutes at 4 °C.

The supernatant was supplemented with 1 M NaOH to neutralize the TCA for subsequent analysis with Ellman's reagent, while the pellet was used for protein quantification. Next, in a 96-well plate were added: 70 µg (in 50 µL) of total protein in reaction buffer (100 mM Na_2HPO_4 $7H_2O$, 1 mM EDTA pH 8); 30 µL (9 mM) of DTNB in reaction buffer and 20 µL of reaction buffer. The resulting mixture was incubated for 30 min at 37 °C. Absorbance was measured at 405 nm with a microplate reader (Multiskan Go, Thermo Fisher Scientific). GSH (1 mM) was used as a negative control.

4.3.14 Glutathione S Transferase (GST) activity

A colorimetric assay using 1-chloro-2,4-dinitrobenzene (CDNB) was performed to measure the GST activity (Moore *et al.*, 2010). HepG2 cell line was treated and lysed.

The reaction mixture was first prepared: 20 µL of phosphate buffer pH 7.5; 20 µL of 1 mM reduced GSH; 20 µL of 10 mM CDNB; 30 µL of cell lysate.

After conjugation of the thiol group of glutathione to the CDNB substrate, CDNB-GSH conjugation (formation of DNP-glutathione conjugate by nucleophilic displacement of Cl with GSH-thiol) was measured spectrophotometrically at 340 nm. The values were expressed as the percentage of enzyme activity (U/mg protein).

4.3.15 Lipid peroxidation

Lipid rancidity measurements were performed using thiobarbituric acid reactive substances (TBAR). For these analyses, a lipid peroxidation assay kit (MDA, Malondialdehyde) (Sigma-Aldrich) was used for the colorimetric determination at λ = 532 nm. HepG2 cells were seeded in 60 mm dishes at approximately 80% confluence. The following day, the cells were treated as previously described with 50 µg/mL of CN and OA/PA. After 24 hours of incubation, the cells were detached and centrifuged at 655 × g for 10 minutes at 4 °C. The resulting cell pellet was used to determine the malondialdehyde content in the samples, following the instructions provided with the kit.

4.3.16 Measurement of lactate dehydrogenase (LDH)

HepG2 cells (20 × 10^3 cells/well) were seeded in 96-well plates and treated with CN (50 µg/mL) and OA/PA for 24 h.

To verify the release of lactate dehydrogenase (LDH) into the cell culture medium after plasma membrane disruption, the LDH-Glo™ cytotoxicity assay (Promega) was performed. According to the LDH-Glo™ kit protocol, the LDH detection reagent (containing lactate, NAD^+, reductase, reductase substrate, and rLuciferase Ultra-Glo™) were added to the cell culture medium sample.

The luminescent signal generated was read in end-point mode using a PerkinElmer AlphaScreen multimode plate reader.

4.3.17 Mitochondrial membrane potential determination

Mitochondrial membrane potential was measured using TMRE (Invitrogen).

After growing hepatocytes at 20 × 10^3 per well, the cells were treated with CN (50 µg/mL) and OA/PA for 24 h. The cells were then washed with PBS and incubated with 100 nM TMRE in in serum-free medium without phenol-red for 30 min at 37 °C in the dark. Excess dye was then removed by washing with PBS and fluorescence was measured using a PerkinElmer EnSpire multimode plate reader (excitation/emission 549 nm/574 nm). The quantitative analysis is reported as fluorescence intensity and compared to the relative controls. The fluorescence representative images of live cells were captured using a ZOE Fluorescence Imager (Bio-Rad. Magnification, 20×. N ≥ 10. Scale bar: 10 µm).

4.3.18 Endoplasmatic reticulum (ER) expansion evaluation

To assess the expansion of the endoplasmic reticulum, a hallmark of activated ER stress, the ER-ID Red analysis kit (Enzo Life Science) was used to quantify ER-specific fluorescence.

HepG2 cells (20 × 10^3 cells/well) were seeded in 96-well plates and allowed to adhere for 24 hours. Following this, cells were treated for 24 hours with a combination of OA/PA and CN (50 µg/mL). After treatment, 100 µL of 1X assay buffer containing 1 µL of the ER-ID Red detection reagent was added to each well. The plate was then incubated for 20 minutes at 37 °C. Subsequently, cells were washed and

imaged using a ZOE Fluorescent Cell Imaging System (Bio-Rad. Magnification, 20×. N ≥ 10. Scale bar: 10 µm). ER-specific fluorescence (excitation/emission: 560 nm/630 nm) was measured using a PerkinElmer EnSpire multimode plate reader.

4.3.19 Indirect immunofluorescence analysis of NF-κB localization

HepG2 were seeded (50×10^4 cells/well) in 24-well plates containing glass cover slips allowing them to adhere for 24 h. Then, cells were treated with CN (50 ug/mL) and OA/PA for 24h. After treatments, cells were washed in PBS, fixed in PBS-4% paraformaldehyde and permeabilized 10 min in PBS containing 0.25% triton. A blocking solution containing PBS-1% BSA and 50 mM NH_4Cl for 30 min was added to each well.

Thereafter, cells were stained with NF-kB (Cell Signaling Technology) for 1 h.

Alexa fluor 568 antibody (Molecular Probes, Invitrogen) was used as secondary antibody and incubated for 45 min.

Nuclei were counterstained with 1.5 µM Hoechst 33,342 (Sigma Aldrich) for 10 min. Images were acquired on a laser scanning confocal microscope (TCS SP8; Leica MicroSystems) equipped with a plan Apo 63X, NA 1.4 oil immersion objective lens. Quantitative analyses were performed by the ImageJ program, version 1.47 (N ≥ 10).

4.3.20 Oil Red O (ORO) staining

Oil Red O staining was used to assess lipid droplet formation in cells. The HepG2 cells were seeded (50×10^3 cells/well) in 24-well plates and cultivated overnight.

The 2D cells and spheroids, formed as previously described, were treated with CN (50 µg/mL) and OA/PA for 24 h.

The treated cells were washed twice with PBS and fixed with 10% paraformaldehyde for 15 min at room temperature, followed by 60% isopropanol incubation for 5 min. Then, the staining with Oil red O staining solution was performed for 20 min. Images in 2D were acquired on a fluorescence microscope (Axioshop 40, Zeiss. N ≥ 10. Magnification, 20×), while the 3D images were acquired on a laser scanning confocal microscope (TCS SP8; Leica MicroSystems.

N ≥ 5. Magnification, 20×). Quantitative analyses were conduced dissolving droplets in 100% isopropanol and measuring the absorbance at 510 nm.

4.3.21 Quantitative real time-PCR for molecular pathway analysis

HepG2 cells were seeded in in 100 mm culture dishes at 80% confluence and treated with CN (50 µg/mL) and OA/PA for 24 h. After 24 h from treatments, cells were washed twice with PBS and detached with a scraper. Total RNA was isolated using a modified procedure with the Quick-RNA™ Miniprep Kit (Zymo Research). Genomic DNA was eliminated by treatment with DNase I provided in the kit. The resulting purified RNA was then reverse transcribed into cDNA using the SensiFAST™ cDNA Synthesis Kit (Meridian Bioscience).

Real-time PCR was performed with LightCycler® 480 System (La Roche Ltd) using SYBR Green detection in a total volume of 20 µL with 1 µL of forward and reverse primers (5 µM) and 10 µL of SensiFAST™ SYBR No-ROX Kit (Meridian Bioscience, EU). Values were determined from standard curve generated from serial cDNA dilutions and normalized to GAPDH.

The primers used for the real-time PCR reactions are listed in the table below.

The $2^{-\Delta\Delta CT}$ method was used to analyze the results and relative mRNA expression levels were determined as fold-induction relative to Ctrl cells.

Table 4.1. Forward and Reverse Primer Sequences for Target Genes

Primer sequence (5'–3')		
Target gene	**Forward**	**Reverse**
SREBP1c	CGGAACCATCTTGGCAACA	GCCGGTTGATAGGCAGCTT
PPAR-α	AACATCCAAGAGATTTCGCAATC	CCGTAAAGCCAAAGCTTCCA
PPAR-γ	TGCAGGTGATCAAGAAGACG	AGTGCAACTGGAAGAAGGGA
FASN	TATGCTTCTTCGTGCAGCAGTT	GCTGCCACACGCTCCTCTAG
SIRT1	GCAACATCTTATGATTGGCACA	AAATACCATCCCTTGACCTGAA
FOXO1	GAGATAAGCAATCCCGAAAACA	TGGCGCAAACGAGTAGCA
NF-κB	CCCCACGAGCTTGTAGGAAAG	CCAGGTTCTGGAAACTGTGGAT
iNOS	ATGTCCGAAGCAAACATCAC	TAATGTCCAGGAAGTAGGTG

COX2	CAGCAAATCCTTGCTGTTCC	TGGGCAAAGAATGCAAACATC
GCS	CCTTCTGGCACAGCACGTTG	TAAGACGGCATCTCGCTCCT
GPx	CCTCAAGTACGTCCGACCTG	CAATGTCGTTGCGGCACACC
SOD2	AGGGAACCATCCACTTCGAG	TGCGCAATCCCAATCACTCC
Catalase	GCAGATACCTGTGAACTGTC	GTAGAATGTCCGCACCTGAG
BIP	CGGGCAAAGATGTCAGGAAAG	TTCTGGACGGGCTTCATAGTAGAC
IRE1α	CTCTGTCCGTACCGCCC	GAAGCGTCACTGTGCTGGT
ATF6	TTGACATTTTTGGTCTTGTGG	GCAGAAGGGGAGACACATTT

4.3.22 Flow cytometry analysis of SIRT1

HepG2 cells (50×10^3) were seeded into 24-well plates and incubated for 24 h with CN (50 µg/mL) and OA/PA. After treatment, the collected cells were resuspended in 50 µL FACS buffer (2% BSA, 1% formaldehyde in PBS) for 20 min.

Then cells were centrifuged at 600 g for 10 minutes, and the resulting pellet was resuspended in a permeabilization buffer consisting of 2% BSA, 1% formaldehyde, and 0.1% Triton X-100 in PBS, containing the primary anti-SIRT1 antibody (*Anti-Mouse Monoclonal Antibody*, Thermo Fisher Scientific) and the Alexa Fluor 488-conjugated secondary antibody (*Anti-Mouse Secondary Antibody*, Thermo Fisher Scientific). After 30 minutes of incubation, the cells were centrifuged again and washed with PBS. The final pellet was resuspended in 200 µL of FACS buffer. Samples were analyzed by flow cytometry using a Becton Dickinson FACScan equipped with CellQuest software, version 4.

4.3.23 SIRT1 activity assay

HepG2 cells were seeded in 60-mm culture dishes at 80% confluence and allowed to adhere overnight. Cells were then treated with CN (50 µg/mL) and in the presence of the mixture of oleic and palmitic acid. After 24 h of treatment, cells were detached and lysed according to the manufacturer's instructions using the SIRT1 Activity Assay Kit (Fluorometric, ab156065; Abcam).

The assay was performed as recommended by the supplier, and fluorescence was measured using a PerkinElmer EnSpire multimode plate reader. Results were expressed as relative SIRT1 activity, normalized to the control condition.

4.3.24 Statistical analysis

Data are reported as mean ± SD of results from three independent experiments. Statistical analysis was performed using an analysis of variance test (ANOVA), and multiple comparisons were made with the Bonferroni's test with GraphPad Prism 8.0 software (San Diego, CA, USA). Significance was assumed at $p < 0.05$.

4.4 Results and Discussion

4.4.1 *LC-MS/MS characterization*

RP-UHPLC-Orbitrap-HRMS/MS analysis was carried out to comprehensively characterize the chemical profile of the alcoholic extract of CN leaves.

Previous LC×LC-based investigations on this species identified several major phytochemical classes, including flavonoids, phenolic acids, phenylpropanoids, isoprenoids, and saponins. Those studies, however, focused on extracts prepared with an EtOH/H_2O solvent mixture (Aquino *et al.*, 2023; Aquino *et al.*, 2025).

In contrast, the present work employed absolute ethanol as the extraction solvent, with the purpose of obtaining a compositionally distinct extract potentially enriched in less polar constituents. This approach was designed to explore whether the different solvent polarity could influence the phytochemical composition and, consequently, the biological properties of this agri-food by-product. To achieve a broader coverage of compounds, both electrospray ionization ($ESI^{+/-}$) and atmospheric pressure chemical ionization ($APCI^{+/-}$) were employed. As summarized in **Table S4.1**, this complementary approach enabled the putative identification of 53 compounds using ESI and 58 compounds using APCI.

The analyses confirmed the flavonoids represented the predominant class of compounds, primarily occurring as glycosides, with kaempferol and quercetin identified as the main aglycones. Furthermore, the analysis revealed compound classes not previously reported, including chlorophylls and carotenoids, and provided a more comprehensive characterization of lipids, which had only been partially detected in earlier investigations.

Carotenoids were predominantly detected in the ESI$^+$ mode. Based on their characteristic positive ion fragmentation patterns, peaks **45E** and **49E** were tentatively identified as lutein isomers, showing precursor ion $[M+H]^+$ at *m/z* 569 and diagnostic product ions at *m/z* 551 (loss of H_2O) (Wojdyło *et al.*, 2021).

In the ESI$^+$ spectra, several chlorophyll derivatives were also observed, including pheophytin a (peaks **46E** and **52E**, *m/z* 871), pheophytin b (peak **48E**, *m/z* 885), hydroxypheophytin a (peaks **47E** and **51E**, *m/z* 887), pheophorbide a (peaks **42E** and **53E**, *m/z* 593).

Two dominant fragment ions were observed at $[M + H - 278]^+$, corresponding to the neutral loss of the phytil chain (as the phytadiene, $C_{20}H_{38}$), and at $[M + H - COOCH_3 - C_{20}H_{39}]^+$, resulting from the subsequent loss of the carboxymethoxy-group (**Figure 4.2**) (Chen *et al.*, 2017).

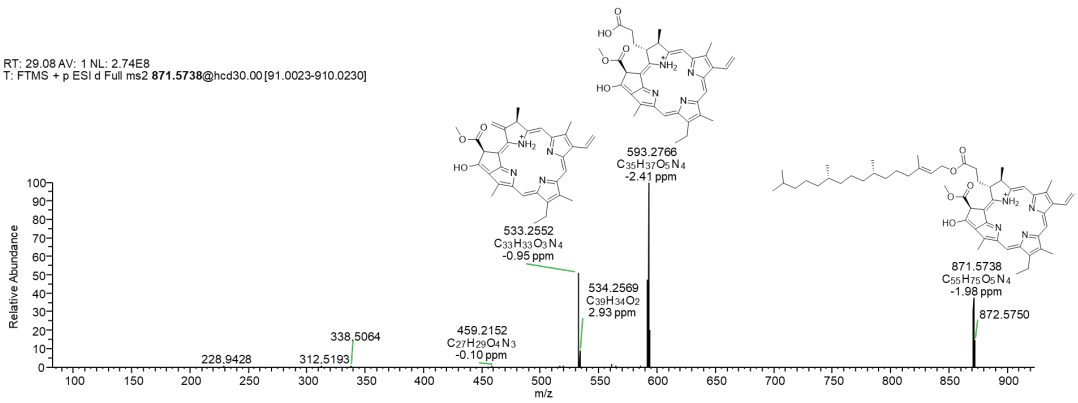

***Figure 4.2**. Representative ESI+ fragmentation pattern of pheophytin a.*

The APCI approach provide a more in-depth characterization of the pigments and lipidic components in the CN extract.

As in ESI, APCI enabled the detection of carotenoids including zeaxanthin (compound **18A**, $[M+H]^+$, *m/z* 569) and β-cryptoxanthin (compound **51A**, $[M+H]^+$, *m/z* 553). Both compounds exhibited a predominant fragment ion due to dehydration, at m/z 551 and m/z 535, respectively, similar to the fragmentation behavior of lutein.

Additionally, several lipid subclasses were tentatively identified, including fatty acids (FA), digalactosyldiacylglycerols (DGDG), monogalactosyldiacylglycerols (MGDG), phosphatidylethanolamines (PE), and phosphatidic acids (PA). The

compounds were mainly detected as $[M–H]^-$ and $[M+H]^+$ ions, but also as adducts such as $[M–H+HAc]^-$ and $[M+NH_4]^+$, in agreement with their expected ionization behavior and consistent with previously reported data (Liebisch *et al.*, 2020).

MGDG 36:4 (compound **39A**, $C_{45}H_{76}O_{10}$) was detected as the $[M+NH_4]^+$ adduct at *m/z* 796. The subclass was tentatively assigned based on the observed neutral loss of $C_6H_{11}O_6$ (179 Da), corresponding to the galactosyl moiety as well as the loss of the ammonium adduct (18 Da), which generated a fragment ion at *m/z* 599 ($C_{39}H_{67}O_4^+$). Additionally, the fragmentation pattern suggested the presence of an 18:2 fatty acyl chain, indicated by the diagnostic ion at *m/z* 337 ($C_{21}H_{37}O_3^+$) (**Figure 4.3**). Similarly, MGDG 36:5 (compound **30A**, $C_{45}H_{76}O_{10}$) was detected as the $[M+NH_4]^+$ adduct at *m/z* 794 with main fragment ion at *m/z* 597, and MGDG 36:6 (compound **26A**, $C_{45}H_{74}O_{10}$) was detected as the $[M+NH_4]^+$ adduct at *m/z* 792 with main fragment ion at *m/z* 595.

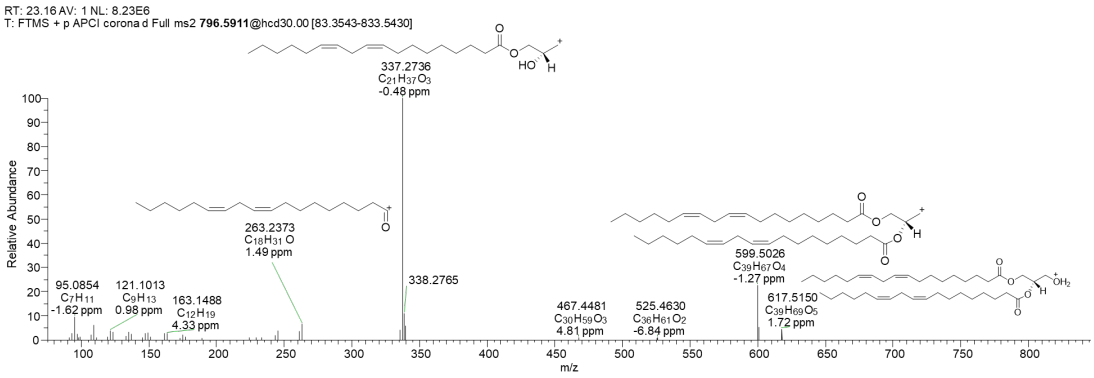

Figure 4.3. *Representative APCI⁺ fragmentation pattern of monogalactosyldiacylglycerols (MGDG) 36:4.*

4.4.2 Evaluation of polyphenol and flavonoid content and antioxidant effect of CN in cell-free assays

The extract was first analyzed using the Folin–Ciocalteu method to estimate its total phenolic content, and the aluminum chloride method was employed to evaluate flavonoid levels, both tested at a final concentration of 100 µg/mL.

The total phenolic content was calculated from the regression equation of the gallic acid calibration curve and expressed as gallic acid equivalents, giving a value of 78.04 ± 0.03 mg GAE/g for the CN extract.

Similarly, the total flavonoid content was obtained from the regression equation of the rutin calibration curve and reported in rutin equivalents, resulting in a concentration of 59.36 ± 0.02 mg RE/g for the CN extract.

Figure S4.1 illustrates the results of the spectrophotometric analysis: total chlorophyll (CHLs) content was 380.92 ± 10.08 μg/g DW, with chlorophyll a (Chl a) and chlorophyll b (Chl b) contributing 252.24 ± 6.93 and 128.68 ± 3.77 μg/g DW, respectively. Total carotenoids (CARs) content was 151.41 ± 4.38 μg/g DW. Compared to reference values reported in the literature (CHLs: 156.05 ± 9.26 μg/g DW; Chl a: 79.73 ± 5.94 μg/g DW; Chl b: 54.16 ± 2.19 μg/g DW), CN extract exhibited significantly higher pigment concentrations. Approaching values were reported for particularly pigment-rich specimens (Ozgur *et al.*, 2011; Huh *et al.*, 2022).

The antioxidant capacity of the CN extract was evaluated through DPPH and FRAP assays.

As regards DPPH assay, the results were expressed as Trolox equivalent antioxidant capacity (TEAC, mg TXE/g), based on a Trolox calibration curve within the range of 0.025–0.2 mg.

The extract was tested at concentrations between 25 and 100 μg/mL, and radical scavenging activity was determined using the equations described in the experimental section. The data revealed a concentration-dependent increase in radical-scavenging activity in the DPPH assay, with a TEAC value of 153.86 ± 1.07 mg TXE/g for CN, indicating a strong antioxidant effect of the extract when compared with Trolox, employed as the reference standard.

The FRAP assay was also carried out to support these findings. This method relies on the reduction of Fe^{3+} to Fe^{2+} by antioxidants in the presence of TPTZ, generating a blue Fe^{2+}–TPTZ complex. The CN extract, tested at 25–100 μg/mL, showed a scavenging capacity equivalent to 6.49 ± 0.04 mg TXE/g DW at 100 μg/mL.

4.4.3 Antisteatotic effects of CN extract

First, the MTT cell viability assay was conducted to evaluate the potential cytotoxic effects of different concentrations of CN extract.

HepG2 cells were exposed to increasing concentrations of CN extract ranging between 12.5–50 µg/mL.

After 24h of exposure, the results showed that none of the tested concentrations caused a significant decrease in cell viability (**Figure S4.2**). Therefore, 50 µg/mL CN was used for drug treatment in all the subsequent experiments.

Was evaluated the lipid-lowering potential of CN extract to reduce lipid accumulation in HepG2 cells treated with free fatty acids mix of OA/PA.

Intracellular lipid accumulation was visualized using ORO staining after 24h of treatment. As shown in **Figures 4.4 A, B**, while the extract alone did not induce steatotic effects ($p < 0.05$ vs Ctrl), OA/PA treatment led to a marked increase in size and intensity of lipid droplets accumulation within HepG2 cells compared to the control group, indicating a pronounced induction of MAFLD-like conditions ($p < 0.001$ vs. Ctrl). Conversely, the addition of CN extract in the steatosis model significantly reduced lipid buildup ($p < 0.01$ vs. OA/PA) showing a potential relieve effect on lipid accumulation.

In addition, the ability of CN extract in reducing HepG2 lipid droplet accumulation has been also assessed in 3D cell culture systems (**Figure 4.4 C**). As showed in **Figure 4.4 D**, the treatment with 50 µg/mL CN resulted in a reduction in the intracellular lipid content compared to OA/PA cells (OA/PA: $p < 0.001$ vs. Ctrl; OA/PA + CN: $p < 0.01$ vs. OA/PA). Thus, consistent with the results in 2D model, the extract showed protective effects to spheroids as well.

To clarify the effects of CN on lipid metabolism, the mRNA expression levels were analysed after 24 h of treatments. Lipogenic markers involved in promoting *de novo* fatty acid synthesis and lipid storage in hepatocytes, contributing to steatosis markers, such as SREBP-1c, FASN, and PPARγ, were significantly increased in OA/PA group compared to untreated cells (SREBP-1c, FASN, PPARγ: $p < 0.001$ vs. Ctrl) (**Figure 4.4 E**). On the other hand, their expression significantly decreased in the coadministration with CN treatment (SREBP-1c, FASN, PPARγ: $p < 0.001$ vs. Ctrl).

This effect may be attributed to the presence of compounds such as α-tocopherol, which has been shown to decreasing SREBP-1c processing and lipogenic gene expression (Podszun *et al.*, 2019).

Polyunsaturated fatty acids (PUFAs), particularly α-linolenic acid, are potent modulators of hepatic lipid metabolism. Omega-3s inhibit SREBP-1c, thereby reducing *de novo* lipogenesis, promoting fatty acid β-oxidation, and decreasing triglyceride synthesis and secretion. They also upregulate PPARs and enhance the production of anti-inflammatory resolvins (Wal *et al.*, 2025; Howell *et al.*, 2009).

On the contrary, the expression level of FOXO1 and PPARα, two key transcriptional regulators involved in promoting fatty acid oxidation and lipid catabolism, are increased in coadministration compared to FFA mix OA/PA, demonstrating the ability of the extract to activate genes involved in lipid catabolism, reducing the steatotic phenotype (FOXO1, PPARα: $p < 0.01$ vs. OA/PA) (**Figure 4.4 E**).

Moreover, SIRT1, that can be activated by natural compounds and functions upstream of these genes, was also affected by the treatment (Sirt1: $p < 0.01$ vs. Ctrl, $p < 0.001$ vs. OA/PA), suggesting a potential role in orchestrating the overall modulation of lipid metabolic pathways (**Figure 4.4 E**). To further confirm this hypothesis, the protein level of SIRT1 was evaluated through flow cytometry, highlighting an increase in SIRT1 expression after the coadministration with CN in OA/PA treated cells in accordance with the gene expression (OA/PA + CN: $p < 0.01$ vs OA/PA) (**Figure 4.4 F**).

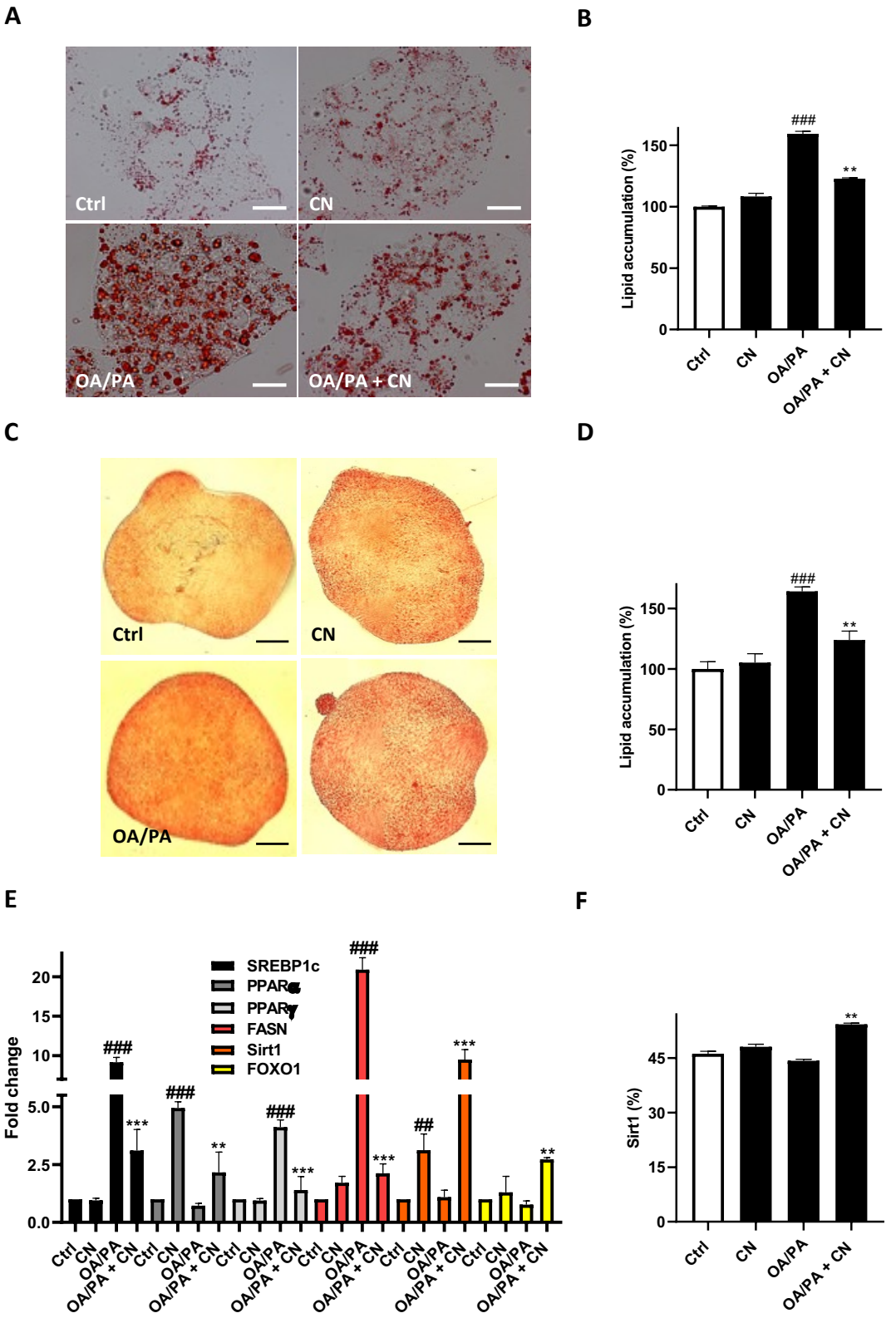

Figure 4.4. *Antisteatotic effects exerted by CN extract. (**A**) Representative images for comparison of lipid accumulation in HepG2 cells (Magnification, 20x. N ≥ 10. Scale bar: 100 µm). (**B**) Quantitative determination of lipid accumulation in 2D cells. (**C**) Representative images of ORO-stained HepG2 spheroids (Magnification, 20x. N ≥ 5. Scale bar: 100 µm). (**D**) Quantitative determination of lipid accumulation in 3D cells. (**E**) mRNA expression of lipid*

*metabolism markers. (**F**) Quantitative determination of SIRT1 expression through flow cytometry analysis. Data are shown as mean ± SD of three different experiments performed in triplicate. ## p < 0.01 vs. Ctrl; ### p < 0.001 vs. Ctrl.*
*** p < 0.01 vs. OA/PA; *** p < 0.001 vs. OA/PA.*

4.4.4 Antioxidant activity of CN extract

Treatment with oleic acid and palmitic acid proved is strong inducers of ROS and RNS, which play a key role in worsening the cellular microenvironment by amplifying oxidative stress caused by the intracellular accumulation of fatty acids (Kim *et al.*, 2023; Guerra *et al.*, 2011).

For these reasons, the antioxidant activity of the CN extract was evaluated. Experiments performed using DCFHDA (**Figures 4.5 A, B**) showed a significant reduction in intracellular ROS levels compared to OA/PA treatment group (p < 0.001 vs. OA/PA), confirming that the decrease in intracellular lipid droplets contributes to restoring cellular redox balance. Furthermore, quantification of intracellular nitrite levels (**Figure 4.5 G**) also showed a significant decrease compared to the fatty acid mixture (p < 0.001 vs OA/PA).

Concurrently, levels of key antioxidant defenses, reduced glutathione and glutathione S-transferase (**Figures 4.5 C, D**), were increased following CN treatment (GSH: p < 0.05 vs. OA/PA; GST: p < 0.05 vs. OA/PA), likely due to its combined antioxidant and antisteatotic effects, which help restore the cellular capacity to neutralize free radicals. By contrast, exposure to the fatty acid mixture alone reduced GSH (p < 0.01 vs Ctrl) and GST (p < 0.01 vs Ctrl) levels, reflecting an overwhelmed and impaired antioxidant defense system under excessive oxidative stress.

Moreover, the CN extract significantly lowered malondialdehyde (CN: p < 0.001 vs OA/PA; OA/PA: p < 0.001 vs Ctrl) concentrations (**Figure 4.5 E**), which reflects diminished lipid peroxidation and oxidative injury.

Real-time PCR analyses (**Figure 4.5 F**) were performed to assess the expression of important antioxidant-related genes, including γ-glutamylcysteine synthetase (GCS), glutathione peroxidase (GPx) and superoxide dismutase 2 (SOD2).

In all cases, the gene expression trends mirrored those observed for GSH and GST levels: treatment with the fatty acid mixture caused a modest downregulation

compared to the CN-treated groups (GCS: $p < 0.05$ vs OA/PA; GPx: $p < 0.01$ vs OA/PA; SOD2: $p < 0.01$ vs OA/PA).

These results suggest that CN extract helps preserve and enhance the antioxidant defense pathways, counteracting the suppressive effect induced by OA/PA and supporting cellular redox homeostasis.

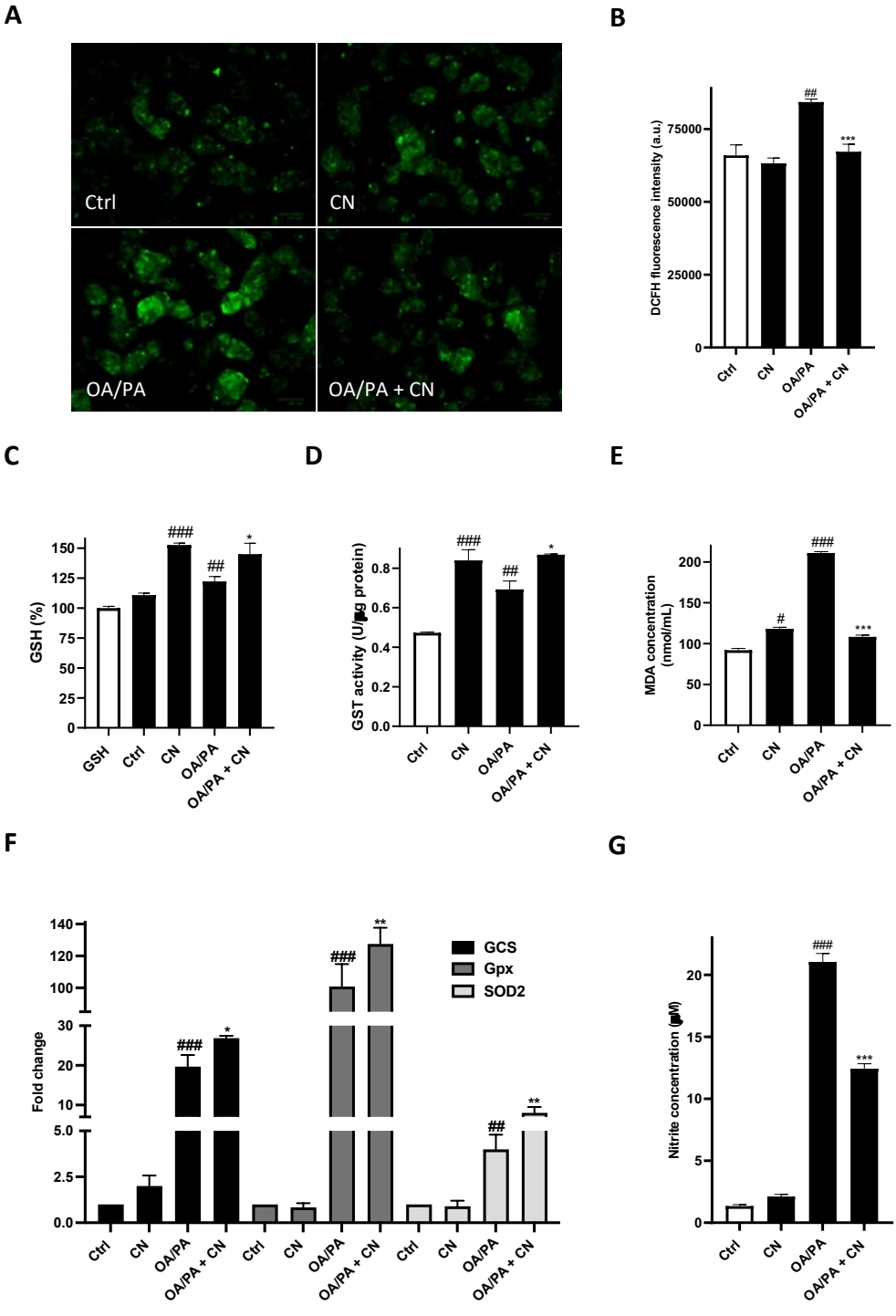

Figure 4.5. *Antioxidant properties showed by CN extract. (**A**) Representative images for comparison of ROS accumulation in HepG2 cells based on DCFHDA staining (Magnification, 20×. Scale bar: 100 µm). (**B**) Quantitative determination of intracellular ROS through spectrofluorometric analysis. (**C**) Quantitative analysis of intracellular GSH determination through spectrophotometric analysis. (**D**) Quantitative analysis of GST activity through spectrophotometric analysis. (**E**) Malondialdehyde quantification through spectrophotometric analysis. (**F**) Quantitative determination of Sirtuin1 expression through flow cytometry analysis.*
Data are shown as mean ± SD of three different experiments performed in triplicate.
#, ## and ### denote respectively $p < 0.05$, $p < 0.01$ and $p < 0.001$ vs. Ctrl.
, ** and * denote respectively $p < 0.05$, $p < 0.01$ and $p < 0.001$ vs. OA/PA.*

4.4.5 Protective effects of CN extract on ER stress and mitochondrial disfunction

The accumulation of intracellular lipids not only generates oxidative stress but also triggers ER stress, a key contributor to the development and progression of hepatic steatosis. Excessive lipid overload disrupts ER homeostasis by promoting protein misfolding and activating the unfolded protein response, which, if unresolved, exacerbates cellular injury and lipotoxicity (Han *et al.*, 2016; Lebeaupin *et al.*, 2018).

Moreover, ER stress can propagate mitochondrial dysfunction, amplifying oxidative damage and energy imbalance.

To assess mitochondrial membrane potential, TMRE staining was performed: the results showed that fluorescence intensity was markedly decreased in cells treated with the fatty acid mixture ($p < 0.01$ vs Ctrl), indicating mitochondrial dysfunction and depolarization. Conversely, co-treatment with the CN extract effectively restored TMRE fluorescence levels ($p < 0.01$ vs OA/PA), demonstrating a protective effect on mitochondrial integrity (**Figures 4.6 A, B**).

This data was further confirmed by the MTT assay (**Figure 4.6 C**), which showed that cellular mitochondrial activity was significantly reduced following OA/PA treatment ($p < 0.001$ vs Ctrl). Notably, treatment with the CN extract increased mitochondrial activity ($p < 0.01$ vs. OA/PA), supporting its protective effect in maintaining mitochondrial function under lipotoxic stress.

The endoplasmic reticulum stress level was assessed using ER-ID staining (**Figure 4.6 D, E**), which measures ER expansion and integrity.

Co-treatment with the CN significantly reduced ER-ID fluorescence compared to OA/PA-treated group ($p < 0.001$ vs OA/PA). This reduction suggests that the extract helps alleviate the excessive protein-folding burden and misfolded protein accumulation.

In addition, the expression of key ER stress-related genes, including BiP ($p < 0.01$ vs OA/PA), ATF6, ($p < 0.05$ vs OA/PA) and IRE1α ($p < 0.001$ vs OA/PA), was evaluated by real-time PCR (**Figure 4.6 F**).

The results revealed that treatment with the extract markedly downregulated the transcription of these genes, further confirming its ability to mitigate ER stress and restore ER homeostasis under lipotoxic conditions.

Given the abundance of flavonoids identified in the CN extract, their contribution to the observed protective effects appears highly plausible.

Among them, quercetin stands out for its well-documented hepatoprotective activities. Previous studies have shown that quercetin reduces hepatic triglyceride accumulation and upregulates the spliced form of XBP1s, thereby enhancing very low-density lipoprotein (VLDL) assembly and promoting lipophagy through activation of the IRE1α/XBP1s signaling axis.

This dual regulation of lipid metabolism and ER homeostasis highlights the potential role of quercetin, and the flavonoid-rich fraction of the CN extract, in restoring hepatic metabolic balance under steatotic conditions (Zhu *et al.*, 2018; Sotiropoulou *et al.*, 2021).

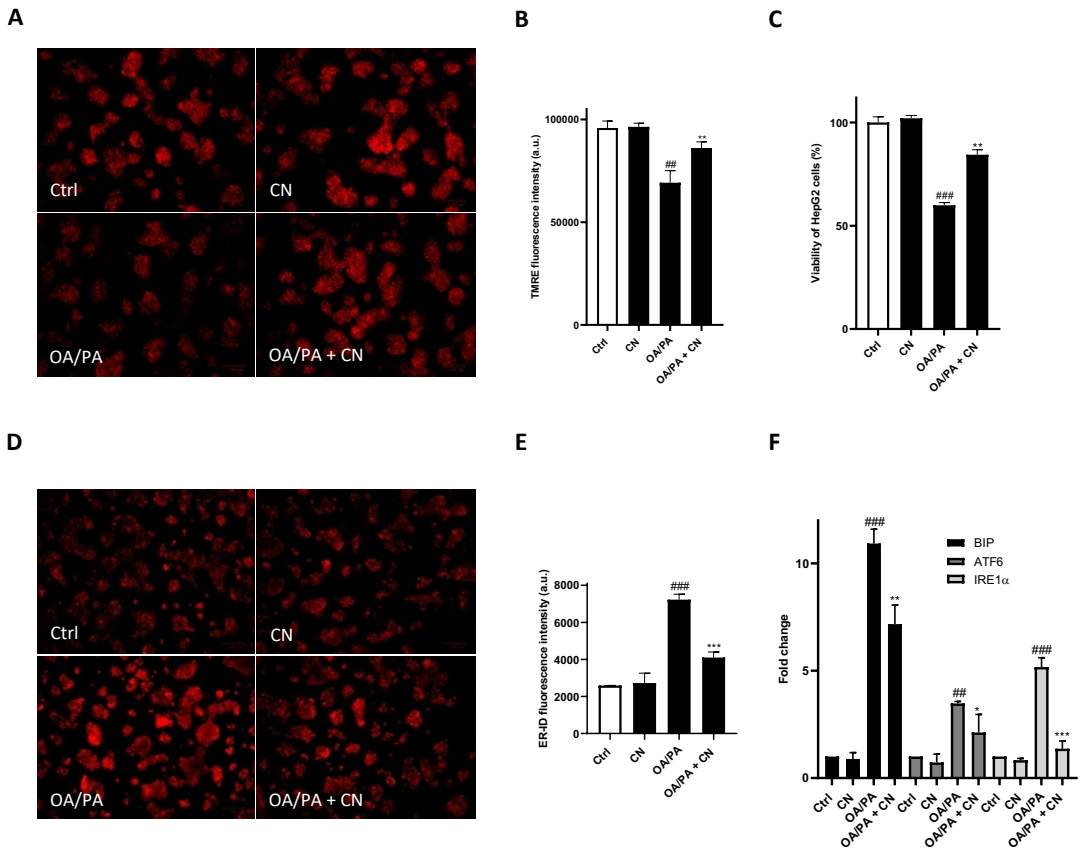

Figure 4.6. *Protective effects exerted by CN extract against ER stress and mitochondrial disfunction. (**A**) Representative images for comparison of mitochondrial permeability in HepG2 cells based on TMRE staining (Magnification, 20×. Scale bar: 100 µm). (**B**) Quantitative analysis of TMRE fluorescence intensity related to mitochondrial permeability. (**C**) Mitochondrial metabolic activity tested by MTT assay. (**D**) Representative images for comparison of ER expansion in HepG2 cells based on ER-ID staining (Magnification, 20×. Scale bar: 100 µm). (**E**) Quantitative analysis of ER-ID fluorescence intensity related to ER expansion. (**F**) mRNA expression of ER stress markers.*
Data are shown as mean ± SD of three different experiments performed in triplicate.
and ### denote respectively $p < 0.01$ and $p < 0.001$ vs. Ctrl.
, ** and * denote respectively $p < 0.05$, $p < 0.01$ and $p < 0.001$ vs. OA/PA.*

4.4.6 Anti-inflammatory properties of CN extract

When steatosis occurs in hepatocytes, various inflammatory markers are activated and released. Therefore, we performed q-PCR to monitor the mRNA expression of some inflammatory factors in OA/PA-induced HepG2 cells.

Upon the treatments, the mRNA expression levels of NF-κB, INOS, and COX-2 were significantly increased (NF-κB: $p < 0.01$ vs. Ctrl; INOS, COX-2: $p < 0.001$ vs. Ctrl); however, these levels were markedly decreased following CN treatment (NF-κB, INOS: $p < 0.01$ vs. OA/PA; COX-2: $p < 0.001$ vs. OA/PA) (**Figure 4.7 A**).

Several classes of bioactive compounds identified in the CN extract are known to influence the NF-κB signaling pathway, suggesting a potential contribution to its observed anti-inflammatory effects (Lewis Lujan *et al.*, 2024). Among these, lutein has been shown to reduce lipid accumulation and modulate oxidative stress by lowering TNF-α, LPS, and NF-κB levels (Chang *et al.*, 2024).

In addition, to corroborate the transcriptional modulation of pro-inflammatory genes observed by q-PCR, we assessed LDH release as an indicator of cellular inflammation and injury. Consistently, OA/PA exposure led to a significant increase in LDH release compared to control cells ($p < 0.01$ vs. Ctrl), reflecting lipid-induced cytotoxicity and inflammation. Notably, CN treatment markedly reduced LDH levels ($p < 0.01$ vs. OA/PA) (**Figure 4.7 B**). Furthermore, confocal microscopy confirmed a reduced nuclear translocation of NF-κB in CN-treated cells ($p < 0.01$ vs OA/PA) compared to OA/PA ($p < 0.001$ vs. Ctrl), supporting its role in mitigating inflammatory signaling at both transcriptional and functional levels (**Figure 4.7 C**).

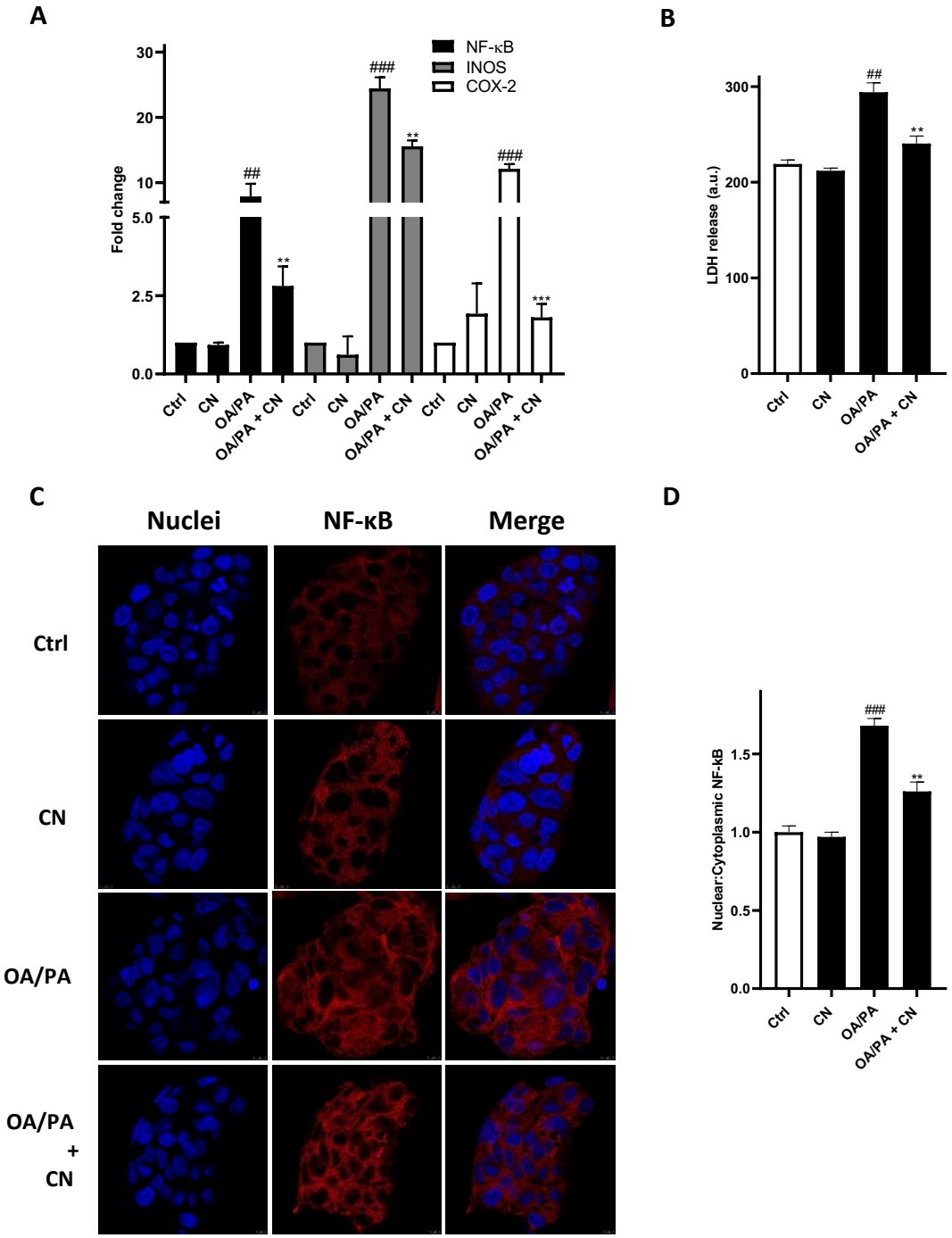

Figure 4.7. *Anti-inflammatory effects exerted by CN extract. (**A**) mRNA expression of inflammatory markers. (**B**) Quantitative analysis of LDH release through luminescence assay. (**C**) Representative images of immunofluorescence staining of NF-κB. (Magnification, 63×. N ≥ 10. Scale bar: 10 μm). (**D**) Quantification of nuclear/cytoplasmic ratios of NF-κB staining. Data are shown as mean ± SD of three different experiments performed in triplicate.*
and ### denote respectively $p < 0.01$ and $p < 0.001$ vs. Ctrl.
*** and *** denote respectively $p < 0.01$ and $p < 0.001$ vs. OA/PA.*

4.4.7 Role of SIRT1 in hepatoprotective properties of CN

To elucidate the contribution of SIRT1 to the protective effects of CN against fatty acid-induced lipotoxicity, we performed a set of experiments using the selective SIRT1 inhibitor EX527 and the activator SRT2104 (**Figure 4.8**).

Treatment of HepG2 cells with OA/PA markedly decreased cell viability ($p < 0.001$ vs Ctrl), whereas co-incubation with CN extract restored survival to near-control levels ($p < 0.01$ vs OA/PA).

The selective SIRT1 activator SRT2104 reproduced this effect ($p < 0.01$ vs OA/PA), while the inhibitor EX527 prevented the CN-mediated improvement, maintaining low viability ($p < 0.001$ vs Ctrl). When OA/PA were administered together with CN and EX527, cell viability was significantly reduced compared with OA/PA + CN alone ($p < 0.01$ vs OA/PA + CN), whereas SRT2104 further enhanced the protective action of CN ($p < 0.05$ vs OA/PA + CN), indicating a probable additive interaction between the extract and SIRT1 activation, and confirming that SIRT1 is at least partially involved in the hepatoprotective mechanism elicited by CN (**Figure 4.8 A**).

Consistently, the assessment of SIRT1 enzymatic activity revealed that its levels, while not markedly suppressed by OA/PA alone, were further increased when CN was co-administered ($p < 0.01$ vs OA/PA), following a trend comparable to that observed for SIRT1 protein expression (**Figure 4.8 B**).

This finding provides additional confirmation that the protective effects observed in the cell viability assay are supported by a direct enhancement of SIRT1 activity under lipotoxic conditions.

ORO staining further substantiated the findings obtained from the cell viability assay (**Figures 4.8 C, D**). As expected, exposure to OA/PA led to marked intracellular lipid accumulation ($p < 0.001$ vs Ctrl), whereas treatment with CN partially reduced the number and size of lipid droplets ($p < 0.01$ vs OA/PA). A similar attenuation of steatosis was observed with SRT2104 ($p < 0.05$ vs OA/PA), while EX527 largely retained the steatotic effect of fatty acids ($p < 0.01$ vs Ctrl). When OA/PA were co-administered with CN and EX527, lipid accumulation increased compared with OA/PA + CN ($p < 0.01$ vs OA/PA + CN), restoring the lipid burden to levels close to those induced by OA/PA alone. On the other hand, SRT2104 produced a reduction in lipid droplets comparable to that achieved by CN, and their combination did not further

enhance the effect, suggesting a mainly additive contribution of SIRT1 activation to the action of CN, possibly reflecting a ceiling effect once SIRT1 is sufficiently stimulated. Interestingly, unlike the MTT results where the combination of CN and SRT2104 slightly outperformed OA/PA + CN, lipid droplet content did not decrease further, suggesting that while SIRT1 activation may still support cell viability, its contribution to CN-mediated lipid clearance reaches a plateau beyond which additional stimulation does not translate into greater antisteatotic benefit.

Overall, these results mirror the pattern observed in the MTT assay and provide further confirmation that SIRT1 plays at least a partial role in mediating the antisteatotic action of CN. Spectrophotometric quantification of extracted ORO dye corroborated the microscopic observations, confirming that CN significantly lowers lipid content through a mechanism that involves SIRT1-dependent modulation of lipid storage in hepatocytes challenged with free fatty acids (**Figure 4.8 D**).

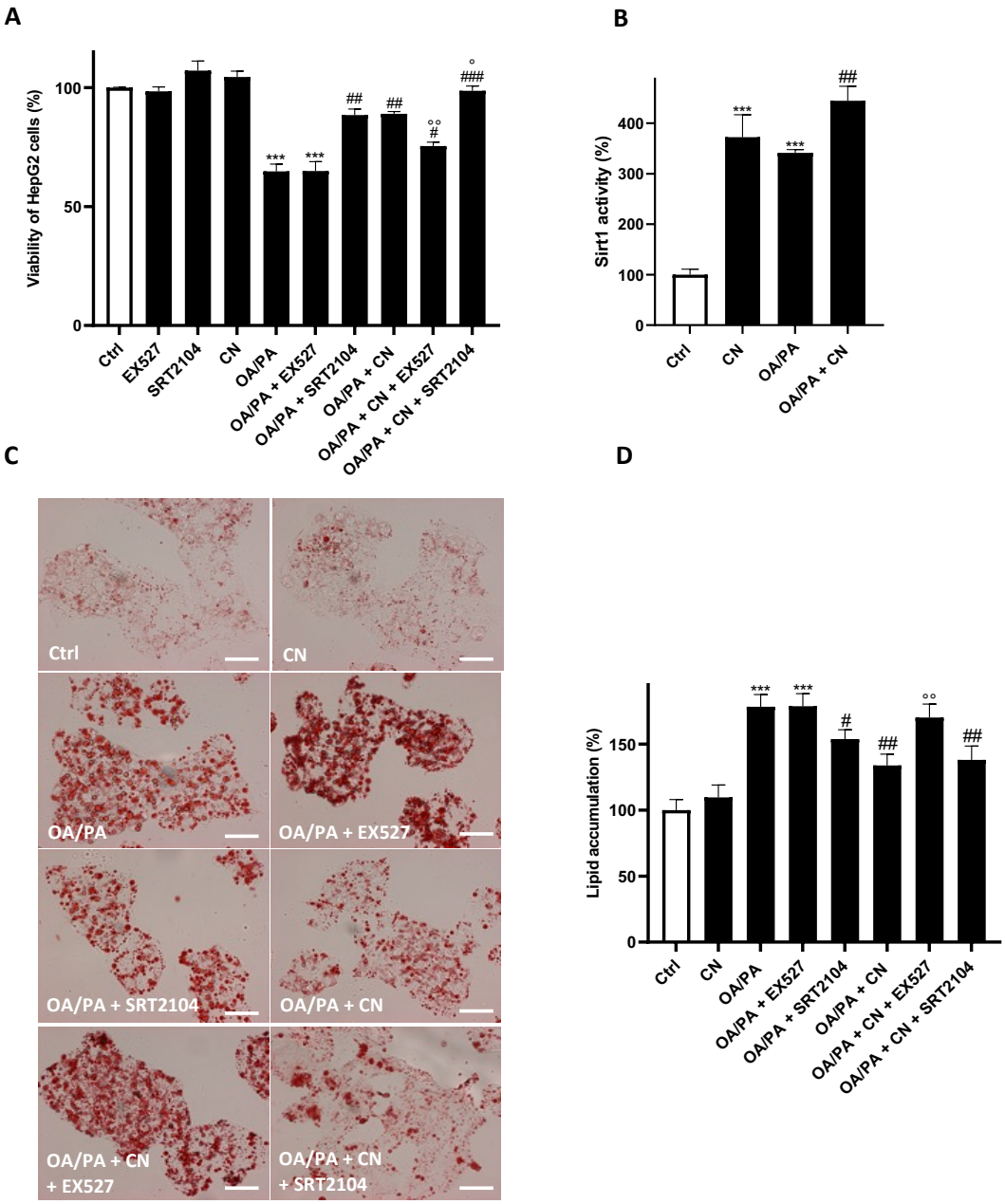

Figure 4.8. *Anti-steatotic effects exerted by CN extract are mediated by SIRT-1. (**A**) Mitochondrial metabolic activity tested by MTT assay. (**B**) Sirtuin enzymatic activity tested on HepG2 cells lysates. (**C**) Representative images for comparison of lipid accumulation in HepG2 cells based on ORO staining (Magnification, 20×. Scale bar: 100 µm). (**D**) Quantitative determination of lipid accumulation in HepG2 cells through spectrophotometric analysis. Data are shown as mean ± SD of three different experiments performed in triplicate.*
#, ## and ### denote respectively $p < 0.05$, $p < 0.01$ and $p < 0.001$ vs. Ctrl.
**** denotes $p < 0.001$ vs. OA/PA.*
°, °° denote respectively $p < 0.05$ and $p < 0.01$ vs. OA/PA + CN.

4.5 Conclusions

These findings demonstrate that the CN extract exerts a potent protective effect against lipotoxicity-induced cellular dysfunction in MAFLD HepG2 model.

CN treatment effectively mitigated intracellular lipid accumulation, both in 2D and 3D culture systems, by downregulating lipogenic genes and upregulating lipid catabolism markers. In parallel, the extract restored redox homeostasis, as evidenced by reduced ROS and RNS levels, enhanced antioxidant defenses, and increased the expression of key antioxidant enzymes, highlighting its ability to counteract oxidative stress.

Moreover, CN extract alleviated ER stress and preserved mitochondrial integrity, as shown by reduced ER-ID fluorescence, decreased expression of ER stress markers, and restoration of mitochondrial membrane potential and activity. A key element underlying these effects appears to be the activation of Sirtuin 1, a master regulator of lipid metabolism, mitochondrial function, and oxidative/ER stress responses. CN markedly increased SIRT1 expression and activity, and pharmacological modulation with the selective inhibitor EX527 and the activator SRT2104 confirmed the pivotal contribution of SIRT1 to the antisteatotic and cytoprotective actions of CN.

Finally, CN demonstrated anti-inflammatory properties by reducing the expression of pro-inflammatory genes, limiting NF-κB nuclear translocation, and attenuating LDH release.

Collectively, these results suggest that CN extract counteracts the deleterious effects of FFA-induced lipotoxicity through a multi-target mechanism in which SIRT1 activation plays a pivotal role, integrating the modulation of lipid metabolism, oxidative and ER stress, mitochondrial dysfunction, and inflammation. This highlights its potential as a promising candidate for further investigation as a sustainable nutraceutical in the prevention or adjunct treatment of MAFLD and related metabolic disorders.

4.6 Supporting information

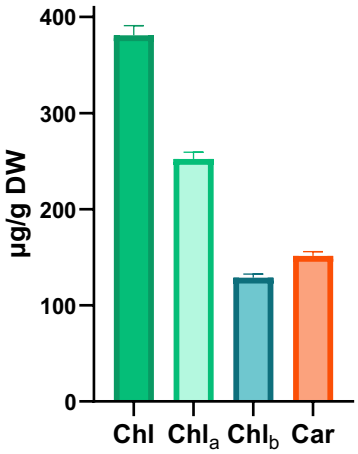

Figure S4.1. *Chlorophyll and carotenoid contents in CN extract expressed as µg/g dry weight (DW). Chl: total chlorophylls; Chl_a: chlorophyll a; Chl_b: chlorophyll b; Car: total carotenoids. Data are shown as mean ± SD of three different experiments performed in triplicate.*

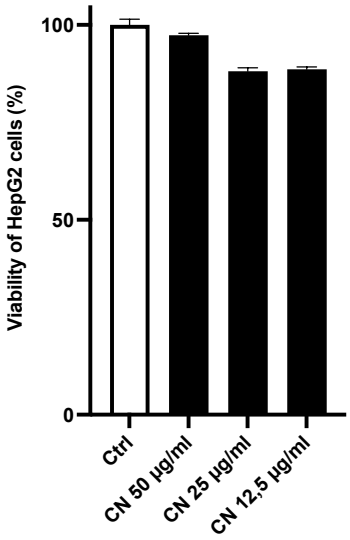

Figure S4.2. *Cell viability was examined by the MTT assay. HepG2 cells were exposed to CN in the range of 12.5-50 µg/mL. Data are shown as mean ± SD of three different experiments performed in triplicate.*

Table S4.1. *Putatively identified compounds from CN extract by UHPLC-Orbitrap-MS/MS analysis.*

Peak*	Rt (min)	Compounds	m/z	MS2	Chemical Formula	Error (ppm)	Reference Ion	Class
1E	8.48	Quercetin 3-sophorotrioside	787.1949	300.0281; 271.0256; 255.0309; 151.0029	$C_{33}H_{40}O_{22}$	-4.96	$[M-H]^-$	Flavonoids
2E	9.05	Ferulic acid	193.0501	178.0264; 149.0599; 134.0363	$C_{10}H_{10}O_4$	1.95	$[M-H]^-$	Phenylpropanoids
3E	10.62	Kaempferol 3,7-*O*-diglucoside (Allivicin)	609.1466	489.1031; 401.1822; 285.0405; 175.1357	$C_{27}H_{30}O_{16}$	2.42	$[M-H]^-$	Flavonoids
4E	10.52	Quercetin 3,4'-di-*O*-beta-D-glucopyranoside	625.1412	463.0887; 301.0355	$C_{27}H_{30}O_{17}$	2.58	$[M-H]^-$	Flavonoids
5E	10.57	Quercetin 3-*O*-glucoside	465.1035	303.0503	$C_{21}H_{20}O_{12}$	1.71	$[M+H]^+$	Flavonoids
6E	10.68	6-Hydroxyluteolin 7-*O*-rhamnoside (*isomer I*)	449.1084	287.0555; 329.0522	$C_{21}H_{20}O_{11}$	3.29	$[M+H]^+$	Flavonoids
7E	10.7	Cyanidin 3,5-*O*-diglucoside	611.1616	449.1082; 287.0552; 145.0495; 85.029	$C_{27}H_{31}O_{16}$	0.66	$[M+H]^+$	Flavonoids
8E	12.08	Kaempferol 3,7-*O*-diglucoside	609.1463	485.2004; 285.0405; 151.0029; 178.998	$C_{27}H_{30}O_{16}$	2.42	$[M-H]^-$	Flavonoids
9E	12.77	Quercetin 3,4'-di-*O*-beta-D-glucopyranoside	625.1417	463.089; 301.0354	$C_{27}H_{30}O_{17}$	2.49	$[M-H]^-$	Flavonoids
10E	12.91	Quercetin-3-*O*-βD-glucopyranoside (Isoquercetin)	463.0884	301.0352; 178.9974; 151.0024	$C_{21}H_{20}O_{12}$	2.69	$[M-H]^-$	Flavonoids
11E	14.82	Kaempferol hexoside (*isomer I*)	447.0936	327.0511; 284.0328; 447.1080; 255.0312	$C_{21}H_{20}O_{11}$	2.81	$[M-H]^-$	Flavonoids
12E	15.25	Kaempferol hexoside (*isomer II*)	447.0937	327.0508; 285.0406; 255.0308; 284.0327; 447.0936	$C_{21}H_{20}O_{11}$	2.95	$[M-H]^-$	Flavonoids
13E	14.87	Quercetin-3-*O*-βD-glucopyranoside (Isoquercetin)	463.0886	301.0354; 178.9983; 151.0025	$C_{21}H_{20}O_{12}$	3.42	$[M-H]^-$	Flavonoids
14E	14.89	Quercetin (*isomer I*)	301.0349	178.9979; 151.0027	$C_{15}H_{10}O_7$	3.93	$[M-H]^-$	Flavonoids
15E	14.92	Quercetin 3-*O*-glucoside	465.103	303.0502	$C_{21}H_{20}O_{12}$	0.85	$[M+H]^+$	Flavonoids
16E	14.95	6-Hydroxyluteolin 7-*O*-rhamnoside (*isomer II*)	449.1079	287.0554	$C_{21}H_{20}O_{11}$	1.79	$[M+H]^+$	Flavonoids
17E	15.39	Isorhamnetin hexoside (*isomer I*)	477.1045	357.0596; 314.0435; 178.9977; 151.0026	$C_{22}H_{22}O_{12}$	2.81	$[M-H]^-$	Flavonoids
18E	16.44	Isorhamnetin hexoside (*isomer II*)	477.1045	357.0612; 314.0435; 153.0191	$C_{22}H_{22}O_{12}$	2.43	$[M-H]^-$	Flavonoids
19E	15.53	Quercetin 3-[2'''-(E)-caffeylsophoroside]-7-glucoside	963.2431	787.1949; 301.035; 178.998	$C_{43}H_{48}O_{25}$	2.93	$[M-H]^-$	Flavonoids

20E	16.11	Quercetin-3-*O*-feruloyl-sophoroside-7-*O*-D-glucoside	963.2433	787.1962; 301.035; 178.9981	$C_{43}H_{48}O_{25}$	2.43	$[M-H]^-$	Flavonoids
21E	16.15	Kaempferol-3-*O*-coumaroyldiglucoside-7-*O*-glucoside	917.2375	771.1992; 591.139; 285.0405	$C_{42}H_{46}O_{23}$	2.2	$[M-H]^-$	Flavonoids
22E	16.57	Kaempferol-3-*O*-feruloyldiglucoside-7-*O*-glucoside (*isomer I*)	947.2477	771.201; 609.1489; 489.1191; 285.0405	$C_{43}H_{48}O_{24}$	3.09	$[M-H]^-$	Flavonoids
23E	17.79	Kaempferol-3-*O*-feruloyldiglucoside-7-*O*-glucoside (*isomer II*)	947.2484	771.1993; 285.0411	$C_{43}H_{48}O_{24}$	2.45	$[M-H]^-$	Flavonoids
24E	17.81	Neohecogenin-3- Oβ-Dglucopyranosyl (1→2)-β-Dglucopyranosyl (1→4)-β-Dgalactopy-ranoside	901.4795	269.1900; 287.2009; 413.3049; 595.3123	$C_{45}H_{72}O_{18}$	0.32	$[M+H]^+$	Steroidal glycosides
25E	18.06	Pennogenin-3-*O*-α-L-arabinofuranosyl(1→4)[α-L-rhamnopyranosyl(1→2)]-β-D-Glucopyranoside	871.4682	709.4157; 413.3049; 269.1901; 287.2009	$C_{44}H_{70}O_{17}$	1.88	$[M+H]^+$	Steroidal glycosides
26E	18.12	Quercetin (*isomer II*)	301.0353	178.9978; 151.0027	$C_{15}H_{10}O_7$	3.52	$[M-H]^-$	Flavonoids
27E	18.94	Kampferol 3-*O*-feruloylsophoroside	785.1951	285.0403; 284.0327; 609.1461	$C_{33}H_{38}O_{22}$	18.92	$[M-H]^-$	Flavonoids
28E	19.4	Palmitoylglycine (*isomer I*)	314.2693	240.2319; 296.2588; 60.0443; 90.0548; 72.0443	$C_{18}H_{35}O_3N$	-0.06	$[M+H]^+$	Lipids
29E	19.45	Isorhamnetin	317.066	285.0496; 151.0038	$C_{16}H_{12}O_7$	0.68	$[M+H]^+$	Flavonoids
30E	19.65	Dehydrophytosphingosine	316.2846	298.2747; 280.2637; 262.2536; 60.0443; 250.2529	$C_{18}H_{37}O_3N$	0.44	$[M+H]^+$	Lipids
31E	19.79	α-Linolenic acid	279.2326	261.2217; 247.0990; 95.0859	$C_{18}H_{30}O_2$	0.82	$[M+H]^+$	Lipids
32E	19.81	Palmitoylglycine (*isomer II*)	314.2693	296.2588; 279.2321; 72.045	$C_{18}H_{35}O_3N$	0.33	$[M+H]^+$	Lipids
34E	20.12	Phytosphingosine	318.3004	60.0451; 300.2899; 282.2794	$C_{18}H_{39}O_3N$	0.45	$[M+H]^+$	Lipids
35E	20.67	N-acetylsphinganine	344.3159	300.2899; 282.2792; 326.3059; 88.0761; 60.0451	$C_{20}H_{41}O_3N$	-0.19	$[M+H]^+$	Lipids
36E	22.02	LPC 18:2	520.3395	184.0735; 104.1074	$C_{26}H_{50}O_7NP$	0.5	$[M+H]^+$	Lipids
37E	22.36	LPC 16:0	496.3401	184.0736; 104.1074; 478.3296	$C_{24}H_{50}O_7NP$	0.34	$[M+H]^+$	Lipids
38E	22.77	α-Linolenoyl ethanolamide	322.2743	62.0607; 234.9611; 305.2466	$C_{20}H_{35}O_2N$	-0.5	$[M+H]^+$	Lipids
39E	23.4	Linoleoyl ethanolamide	324.2899	62.0607; 307.2635; 263.2375; 245.2273; 179.1798	$C_{20}H_{37}O_2N$	0.46	$[M+H]^+$	Lipids

40E	23.93	α-Linolenic acid	279.2322	95.086; 109.1015; 81.0705; 123.117	$C_{18}H_{30}O_2$	1.37	$[M+H]^+$	Lipids
41E	24.42	Oleamide	282.2794	247.2423; 265.2524; 97.1017	$C_{18}H_{35}ON$	1.09	$[M+H]^+$	Lipids
42E	24.92	Pheophorbide a (*isomer I*)	593.2764	533.2548; 565.2811	$C_{35}H_{36}O_5N_4$	0.47	$[M+H]^+$	Chlorophylls
43E	25.76	DG 36:6	613.4821	595.473; 335.2584	$C_{39}H_{64}O_5$	1.12	$[M+H]^+$	Lipids
44E	26.08	Echinenone	551.425	175.144; 119.0858; 145.1015	$C_{40}H_{54}O$	0.89	$[M+H]^+$	Carotenoids
45E	27.36	Lutein (*isomer I*)	569.4351	551.4253	$C_{40}H_{56}O_2$	2.03	$[M+H]^+$	Carotenoids
46E	29.08	Pheophytin a (*isomer I*)	871.5738	539.2766; 533.2552	$C_{55}H_{74}O_5N_4$	0.96	$[M+H]^+$	Chlorophylls
47E	30.11	Hydroxypheophytin a (*isomer I*)	887.5682	609.2692; 549.2486	$C_{55}H_{74}O_6N_4$	-0.07	$[M+H]^+$	Chlorophylls
48E	31.37	Pheophytin b	885.552	607.2556; 547.2344	$C_{55}H_{72}O_6N_4$	0.51	$[M+H]^+$	Chlorophylls
49E	31.47	Lutein (*isomer II*)	569.4350	551.4255	$C_{40}H_{56}O_2$	-1.29	$[M+H]^+$	Carotenoids
50E	32.06	15^1-Hydroxy-lactone-pheophytin a	903.5627	625.2659	$C_{55}H_{74}O_7N_4$	0.29	$[M+H]^+$	Chlorophylls
51E	32.22	Hydroxypheophytin a (*isomer II*)	887.5682	609.2717; 591.2609; 549.2483	$C_{55}H_{74}O_6N_4$	0.07	$[M+H]^+$	Chlorophylls
52E	32.97	Pheophytin a (*isomer II*)	871.5704	593.2761; 533.2553	$C_{55}H_{74}O_5N_4$	-0.79	$[M+H]^+$	Chlorophylls
53E	33.38	Pheophorbide a (*isomer II*)	593.2759	533.2514; 565.2777; 251.3165	$C_{35}H_{36}O_5N_4$	0.98	$[M+H]^+$	Chlorophylls
1A	0.67	Alliin	178.0529	88.0392; 42.0338; 91.0212; 114.0371	$C_6H_{11}NO_3S$	-2.16	$[M+H]^+$	Amino acids, peptides, and analogues
2A	6.40	Monolinolenin (2-Linolenoylglycerol)	353.2678	335.2592; 261.2210; 243.2102; 279.2318	$C_{21}H_{36}O_4$	0.28	$[M+H]^+$	Lipids
3A	6.61	MGMG 18:3	532.3467	353.2686; 335.2573; 261.2209; 243.2104	$C_{27}H_{46}O_9$	0.13	$[M+NH_4]^+$	Lipids
4A	7.26	α-Linolenic acid	277.2170	59.0140; 233.2271; 259.2068	$C_{18}H_{30}O_2$	-1.16	$[M-H]^-$	Lipids
5A	8.08	α-Linolenoyl ethanolamide	322.2733	62.0599; 261.2207; 304.2634	$C_{20}H_{35}NO_2$	0.39	$[M+H]^+$	Lipids
6A	9.27	Linoleic acid	279.2325	261.2229; 71.4639; 112.0822; 149.8636; 194.0919	$C_{18}H_{32}O_2$	-1.24	$[M-H]^-$	Lipids
7A	9.97	Linoleoyl ethanolamide	324.2890	62.0599; 245.2264; 263.2369; 306.2789	$C_{20}H_{37}NO_2$	0.45	$[M+H]^+$	Lipids
8A	10.64	Palmitic acid	255.2325	237.8235; 97.6534; 138.4916; 147.5438; 199.9075	$C_{16}H_{32}O_2$	-1.66	$[M-H]^-$	Lipids
9A	11.25	Palmitoyl ethanolamide	300.289	283.2620; 239.2364; 62.0599	$C_{18}H_{37}NO_2$	-1.04	$[M+H]^+$	Lipids
10A	11.85	N-acetylsphinganine	344.3150	60.0443; 88.0755; 300.2894; 282.2787	$C_{20}H_{41}NO_3$	-2.76	$[M+H]^+$	Lipids
11A	12.18	N-Oleoylethanolamine	326.3047	309.2779; 247.2418; 62.0599; 265.2531	$C_{20}H_{39}NO_2$	-0.71	$[M+H]^+$	Lipids

12A	14.52	Stearic acid	283.2639	265.2500; 177.7347; 194.8538; 239.2507; 258.1577	$C_{18}H_{36}O_2$	-1.19	$[M-H]^-$	Lipids
13A	16.13	FA 24:0;O	383.3525	337.3477; 69.0347; 83.0502; 106.0661; 113.0248; 186.0627; 195.3139	$C_{24}H_{48}O_3$	-1.54	$[M-H]^-$	Lipids
14A	17.94	ST 29:2;O;Hex	633.4367	89.0244; 71.0138; 101.0245; 119.0350; 113.0245; 179.0560; 573.4161	$C_{35}H_{58}O_6$	0.59	$[M-H+HAc]^-$	Lipids
15A	18.20	PE 34:4	712.4895	571.4891; 597.4867; 81.0699; 95.0854; 261.2208; 335.2566;	$C_{39}H_{70}NO_8P$	-2.36	$[M+H]^+$	Lipids
16A	18.31	PE 36:5	738.5049	597.4874; 548.4667; 417.2924; 263.2385; 337.2721	$C_{41}H_{72}NO_8P$	-1.23	$[M+H]^+$	Lipids
17A	19.01	PA 36:4	695.4656	279.2329; 152.9959; 78.9591; 415.2254; 96.9696	$C_{39}H_{69}O_8P$	1.36	$[M-H]^-$	Lipids
18A	19.05	Zeaxanthin	569.4339	551.4288; 534.4861; 431.3326	$C_{40}H_{56}O_2$	-0.64	$[M+H]^+$	Carotenoids
19A	19.10	PE 34:3	714.5046	599.5027; 573.4865; 263.2366; 81.0697; 109.1010; 337.2740; 155.0099	$C_{39}H_{72}NO_8P$	1.36	$[M+H]^+$	Lipids
20A	19.69	DGDG 36:6	954.6124	335.2578; 261.2213; 595.4689	$C_{51}H_{88}NO_{15}$	-2.54	$[M+NH_4]^+$	Lipids
21A	19.70	Di-γ-linolenin	613.4816	595.4727; 521.4341; 261.2213; 335.2577	$C_{39}H_{64}O_5$	1.28	$[M+H]^+$	Lipids
22A	19.75	Ginsenoside Rh2	621.4371	308.3076; 134.0761; 390.3336; 530.3862; 170.5041; 98.9521	$C_{36}H_{62}O_8$	-0.19	$[M-H]^-$	Terpene glycosides
23A	19.91	PE 34:2 (*isomer I*)	716.5208	575.5030; 263.2367; 239.2368;	$C_{39}H_{74}NO_8P$	0.59	$[M+H]^+$	Lipids
24A	20.13	PE 36:6	736.4896	595.4716; 696.2568; 500.4456; 261.2222; 335.2562	$C_{41}H_{70}NO_8P$	-1.03	$[M+H]^+$	Lipids
25A	20.78	FA 22:0	339.3265	61.6178; 106.9795; 114.4943; 138.9756; 145.4787; 182.5089; 191.7177; 192.5654; 228.9366	$C_{22}H_{44}O_2$	-1.38	$[M-H]^-$	Lipids
26A	21.21	MGDG 36:6	792.5597	595.4697; 335.2580; 261.2213; 95.0855; 121.1011; 173.1325; 317.2475	$C_{45}H_{74}O_{10}$	-3.25	$[M+NH_4]^+$	Lipids
27A	21.70	DGDG 34:3 (*isomer I*)	959.5943	277.2173; 255.2328; 397.1349; 415.1453; 101.0244; 913.5890	$C_{49}H_{86}O_{15}$	0.69	$[M-H+HAc]^-$	Lipids
28A	21.76	DGDG 34:3 (*isomer II*)	932.6279	313.2737; 335.2579; 261.2211; 573.4869; 109.1014; 145.0496	$C_{49}H_{86}O_{15}$	-2.75	$[M+NH_4]^+$	Lipids
29A	22.01	FA 23:0	353.3422	52.0230; 66,3141; 146.7255; 164.4188; 224.1623; 254.9975; 271.2473	$C_{23}H_{46}O_2$	-0.87	$[M-H]^-$	Lipids
30A	22.21	MGDG 36:5	794.5753	337.2738; 597.4882; 261.2213; 109.1012; 95.0854	$C_{45}H_{76}O_{10}$	1.71	$[M+NH_4]^+$	Lipids
31A	22.34	PE 36:4 (*isomer I*)	738.5079	279.2329; 280.2364; 140.0118; 476.2786; 196.0379	$C_{41}H_{74}NO_8P$	1.16	$[M-H]^-$	Lipids
32A	22.36	PE 36:4 (*isomer II*)	740.5206	599.5027; 81.0698; 109.1011; 263.2365	$C_{41}H_{74}NO_8P$	-2.44	$[M+H]^+$	Lipids
34A	22.55	PE 33:2	702.5057	561.4868; 263.2357; 337.2741; 225.2211	$C_{38}H_{72}NO_8P$	-0.26	$[M+H]^+$	Lipids

35A	22.69	DGDG 34:2 (*isomer I*)	961.6101	279.2328; 255.2328; 397.1349; 415.1454; 101.0244;	$C_{49}H_{88}O_{15}$	0.76	$[M-H+HAc]^-$	Lipids
36A	22.74	DGDG 34:2 (*isomer II*)	934.6438	313.2736; 337.2736; 575.5029; 239.2376	$C_{49}H_{88}O_{15}$	-2.58	$[M+NH_4]^+$	Lipids
37A	22.88	Stigmasterol	395.3667	81.0700; 159.1177; 95.0854; 109.1014; 177.1645; 255.2109	$C_{29}H_{48}O$	-0.33	$[M+H-H_2O]^+$	Steroids
38A	23.06	FA 24:0;O	367.3575	51.2549; 63.2523; 228.9508; 266.9189	$C_{24}H_{48}O_2$	-1.31	$[M-H]^-$	Lipids
39A	23.13	MGDG 36:4	796.5910	337.2736; 599.5026; 617.5150; 95.0854; 263.2373	$C_{45}H_{78}O_{10}$	0.53	$[M+NH_4]^+$	Lipids
40A	23.22	Monoelaidin	339.2895	308.8995; 265.2529; 214.1314; 279.6796; 69.0698; 83.0854; 95.0853	$C_{21}H_{40}O_4$	1.28	$[M+H-H_2O]^+$	Lipids
41A	23.32	PE 34:2 (*isomer I*)	714.5079	279.2328; 255.2328; 140.0119; 196.0379; 452.2777	$C_{39}H_{74}NO_8P$	-0.08	$[M-H]^-$	Lipids
42A	23.38	PE 34:2 (*isomer II*)	716.5206	575.5026; 95.0854; 239.2367; 81.0697; 109.1011	$C_{39}H_{74}NO_8P$	-2.50	$[M+H]^+$	Lipids
43A	23.42	PE 36:3	742.5361	601.5184; 575.5033; 265.2530; 337.2748	$C_{41}H_{66}NO_8P$	-1.44	$[M+H]^+$	Lipids
44A	24.13	DG (36:5)	632.5237	337.2732; 261.2210; 597.4878; 469.3490	$C_{39}H_{66}O_5$	-0.82	$[M+NH_4]^+$	Lipids
45A	24.18	Ornithine lipid derivative	665.5812	115.0865; 351.3004; 552.3362; 369.3107	$C_{40}H_{76}N_2O_5$	1.02	$[M+H]^+$	Lipids
46A	24.80	Monopalmitolein	311.2577	275.2000; 241.0395; 225.0433	$C_{19}H_{36}O_4$	1.9	$[M+H-H_2O]^+$	Lipids
47A	24.91	FA 26:0	395.3891	61.1764; 134.4456; 228.9383	$C_{26}H_{52}O_2$	2.57	$[M-H]^-$	Lipids
48A	24.93	DG 36:4	634.5393	599.5026; 337.2734; 263.2372	$C_{39}H_{68}O_5$	-0.24	$[M+NH_4]^+$	Lipids
49A	25.44	α-Tocopherol (Vitamin E)	430.3783	165.0908; 360.0287; 289.2167; 205.1223	$C_{29}H_{50}O_2$	-0.05	$[M+H]^+$	Tocopherols
50A	25.72	Chlorophyll a	893.5409	615.2418; 555.2231, 614.2365; 833.5206	$C_{55}H_{72}N_4O_5Mg$	-1.58	$[M+H]^+$	Chlorophylls
51A	25.99	β-Cryptoxanthin	553.4403	535.4289; 335.2736; 497.2682	$C_{40}H_{56}O$	-0.78	$[M+H]^+$	Carotenoids
52A	26.50	1-Palmitoyl-2-oleoyl-sn-glycerol	577.5186	418.9932; 355.0693; 265.2528	$C_{37}H_{70}O_5$	1.72	$[M+H-H_2O]^+$	Lipids
53A	26.65	DG 36:6	613.4815	595.4726; 335.2584; 261.2209; 109.1011	$C_{39}H_{64}O_5$	-1.97	$[M+H]^+$	Lipids
54A	26.66	Monoolein (2-Oleoylglycerol)	339.2889	83.0854; 95.0854; 135.1167; 149.1323; 247.2415; 265.2518; 322.2477	$C_{21}H_{40}O_4$	-2.01	$[M+H-H_2O]^+$	Lipids
55A	27.56	Cer 42:1;O3	682.6332	280.2632; 262.2527; 298.2737; 316.3838; 646.6121; 133.1010; 384.3831	$C_{42}H_{83}NO_5$	-1.66	$[M+H]^+$	Lipids
56A	28.32	Pyropheophytin a	813.5657	535.2694; 461.2354	$C_{53}H_{72}N_4O_3$	-0.49	$[M+H]^+$	Chlorophylls
57A	28.35	Pheophytin a (*isomer I*)	870.5649	515.2452; 559.2347; 461.2338; 315.9254	$C_{55}H_{74}N_4O_5$	-0.57	$[M-H]^-$	Chlorophylls
58A	28.73	Pheophytin a (*isomer II*)	871.5714	539.2766; 533.2552	$C_{55}H_{74}N_4O_5$	0.28	$[M]^+$	Chlorophylls

4.7 References

Abderrrezag, N., Domínguez-Rodríguez, G., Montero, L. and Mendiola, J.A. (2025). Nutraceutical potential of Mediterranean agri-food waste and wild plants: Green extraction and bioactive characterization. In: Toldrá, F. (ed.) *Advances in Food and Nutrition Research*, 114, 1–95.

Aquino, G., Basilicata, M.G., Crescenzi, C., Vestuto, V., Salviati, E., Cerrato, M., Ciaglia, T., Sansone, F., Pepe, G. and Campiglia, P. (2023). Optimization of microwave-assisted extraction of antioxidant compounds from spring onion leaves using Box–Behnken design. *Scientific Reports*, 13, 14923.

Aquino, G., Sommella, E.M., Salviati, E., Manfra, M., Auriemma, G., Campiglia, P., Pepe, G. and Basilicata, M.G. (2025). Advancing profiling of secondary antioxidant metabolites in *Allium cepa* PDO leaf extract: Online 2D-LC–HRMS with pre-column DPPH assay. *Journal of Chromatography A*, 1749, 465877.

Augimeri, G., Montalto, F.I., Giordano, C., Barone, I., Lanzino, M., Catalano, S., Andò, S., De Amicis, F. and Bonofiglio, D. (2021). Nutraceuticals in the Mediterranean diet: Potential avenues for breast cancer treatment. *Nutrients*, 13, 2557.

Bedir, A.S., Almasri, R.S., Azar, Y.O., Elnady, R.E. and Al Raish, S.M. (2025). Exploring the Therapeutic Potential of *Allium cepa* and *Allium sativum* Extracts: Current Strategies, Emerging Applications, and Sustainability Utilization. *Biology*, 14(8), 1088.

Bordin Viera, V., Piovesan, N., Mello, R.D.O., Barin, J.S., Fogaça, A.D.O., Bizzi, C.A., De Moraes Flores, É.M., Dos Santos Costa, A.C., Pereira, D.E. and Soares, J.K.B. (2023). Ultrasonic-assisted extraction of phenolic compounds with evaluation of red onion skin (*Allium cepa* L.) antioxidant capacity. *Journal of Culinary Science & Technology*, 21(1), 156–172.

Chang, N., Li, J., Lin, S., Zhang, J., Zeng, W., Ma, G. and Wang, Y. (2024). Emerging roles of the SIRT1 activator SRT2104 in disease treatment. *Scientific Reports*, 14, 5521.

Chen, K., Ríos, J.J., Pérez-Gálvez, A. and Roca, M. (2017). Comprehensive chlorophyll composition in the main edible seaweeds. *Food Chemistry*, 228, 625–633.

Črnivec, I.G.O., Skrt, M., Šeremet, D., Sterniša, M., Farčnik, D., Štrumbelj, E., Poljanšek, A., Cebin, N., Pogačnik, L. and Možina, S.S. (2021). Waste streams in onion production: bioactive compounds, quercetin and use of antimicrobial and antioxidative properties. *Waste Management*, 126, 476–486.

González-de-Peredo, A.V., Vázquez-Espinosa, M., Espada-Bellido, E., Ferreiro-González, M., Carrera, C., Barbero, G.F. and Palma, M. (2021). Development of optimized ultrasound-assisted extraction methods for the recovery of total phenolic compounds and anthocyanins from onion bulbs. *Antioxidants*, 10(11), 1755.

González-de-Peredo, A.V., Vázquez-Espinosa, M., Espada-Bellido, E., Ferreiro-González, M., Carrera, C., Barbero, G.F. and Palma, M. (2022). Extraction of antioxidant compounds from onion bulb (*Allium cepa* L.) using individual and simultaneous microwave-assisted extraction methods. *Antioxidants*, 11(5), 846.

Guerra, B.A. and Otton, R. (2011). Impact of astaxanthin on phagocytic capacity and ROS/RNS production in neutrophils treated with fatty acids and high glucose. *International Immunopharmacology*, 11, 2220–2226.

Han, J. and Kaufman, R.J. (2016). The role of ER stress in lipid metabolism and lipotoxicity. *Journal of Lipid Research*, 57(8), 1329–1338.

Howell, G. 3rd, Deng, X., Yellaturu, C., Park, E.A., Wilcox, H.G., Raghow, R. and Elam, M.B. (2009). N-3 polyunsaturated fatty acids suppress insulin-induced SREBP-1c transcription via reduced trans-activating capacity of LXRα. *Biochimica et Biophysica Acta*, 1791, 1190–1196.

Huh, M.K. (2022). Effect of chlorophyll content in garlic chives (*Allium tuberosum*) leaves under drought and pH stress. *European Journal of Agriculture and Food Sciences*, 4, 66–69.

Issac, P.K., Guru, A., Velayutham, M., Pachaiappan, R., Arasu, M.V., Al-Dhabi, N.A., Choi, K.C., Harikrishnan, R. and Arockiaraj, J. (2021). Oxidative stress induced antioxidant and neurotoxicity demonstrated in in vivo zebrafish embryo or larval model and their normalization due to morin showing therapeutic implications. *Life Sciences*, 283, 119864.

Kim, S.H., Yun, C., Kwon, D., Lee, Y.H., Kwak, J.H. and Jung, Y.S. (2023). Effect of isoquercitrin on free fatty acid-induced lipid accumulation in HepG2 cells. *Molecules*, 28, 1476.

Kurnia, D., Ajiati, D., Heliawati, L. and Sumiarsa, D. (2021). Antioxidant Properties and Structure-Antioxidant Activity Relationship of *Allium* Species Leaves. *Molecules*, 26(23), 7175.

Lebeaupin, C., Vallée, D., Hazari, Y., Hetz, C., Chevet, E. and Bailly-Maitre, B. (2018). Endoplasmic reticulum stress signalling and NAFLD pathogenesis. *Journal of Hepatology*, 69, 927–947.

Lee, H.J., Lee, I.Y., Park, J.H. and Joo, N. (2025). Comparison of phytochemicals and antioxidant activities of onion (*Allium cepa* L.) bulbs, onion leaves, and green onion (*Allium fistulosum* L.) leaves. *Journal of Food Science and Nutrition*.

Lewis Lujan, L.M., McCarty, M.F., Galvez Ruiz, J.C., Trujillo Lopez, S. and Iloki-Assanga, S.B. (2024). Nutraceutical and dietary measures with potential for preventing/controlling non-alcoholic fatty liver disease and its complications. *Human Nutrition & Metabolism*, 37, 200281.

Liebisch, G., Fahy, E., Aoki, J., Dennis, E.A., Durand, T., Ejsing, C.S., Fedorova, M., Feussner, I., Griffiths, W.J., Köfeler, H., Merrill, A.H. Jr., Murphy, R.C., O'Donnell, V.B., Oskolkova, O., Subramaniam, S., Wakelam, M.J.O. and Spener, F. (2020). Update on LIPID MAPS classification, nomenclature, and shorthand notation for MS-derived lipid structures. *Journal of Lipid Research*, 61, 1539–1555.

Meng, D., Zhang, F., Yu, W., Zhang, X., Yin, G., Liang, P., Feng, Y., Chen, S. and Liu, H. (2023). Biological role and related natural products of SIRT1 in nonalcoholic fatty liver. *Diabetes, Metabolic Syndrome and Obesity*, 16, 4043–4064.

Moore, P.D., Yedjou, C.G. and Tchounwou, P.B. (2010). Malathion-induced oxidative stress, cytotoxicity, and genotoxicity in human liver carcinoma (HepG2) cells. *Environmental Toxicology*, 25, 221–226.

Nile, A., Nile, S.H., Kim, D.H., Keum, Y.S., Seok, P.G. and Sharma, K. (2018). Valorization of onion solid waste and their flavonols for assessment of cytotoxicity, enzyme inhibitory and antioxidant activities. *Food and Chemical Toxicology*, 119, 281–289.

Ozgur, M., Akpinar Bayizit, A., Ozcan, T. and Yilmaz-Ersan, L. (2011). Effect of dehydration on physicochemical properties and antioxidant activity of leeks (*Allium porrum* L.). *Notulae Botanicae Horti Agrobotanici Cluj-Napoca*, 39, 144–151.

Podszun, M.C., Alawad, A.S., Lingala, S., Morris, N., Huang, W.A., Yang, S., Schoenfeld, M., Rolt, A., Ouwerkerk, R., Valdez, K., Umarova, R., Ma, Y., Fatima, S.Z., Lin, D.D., Mahajan, L.S., Samala, N., et al. (2020). Vitamin E treatment in NAFLD patients demonstrates that oxidative stress drives steatosis through upregulation of de novo lipogenesis. *Redox Biology*, 37, 101710.

Šamec, D., Bogović, M., Vincek, D., Martinčić, J. and Salopek-Sondi, B. (2014). Assessing the authenticity of the white cabbage (*Brassica oleracea* var. *capitata* f. *alba*) cv. 'Varaždinski' by molecular and phytochemical markers. *Food Research International*, 60, 266–272.

Sotiropoulou, M., Katsaros, I., Vailas, M., Lidoriki, I., Papatheodoridis, G.V., Kostomitsopoulos, N.G., Valsami, G., Tsaroucha, A. and Schizas, D. (2021). Nonalcoholic fatty liver disease: The role of quercetin and its therapeutic implications. *Saudi Journal of Gastroenterology*, 27, 319–330.

Wal, P., Yadav, S., Jha, S.K., Singh, A., Bhargavi, B., Shivaram, R., Imran, M. and Aziz, N. (2025). Role of natural compounds in NAFLD: A mechanistic approach. *Egyptian Liver Journal*, 15, 50.

Wang, H., Zhu, Y., Xie, D., Zhang, H., Zhang, Y., Jin, P. and Du, Q. (2022). The Effect of Microwave Radiation on the Green Color Loss of Green Tea Powder. *Foods*, 11, 2540.

Wojdyło, A., Nowicka, P., Tkacz, K. and Turkiewicz, I.P. (2021). Fruit tree leaves as unconventional and valuable source of chlorophyll and carotenoid compounds determined by LC-PDA-qTOF-ESI-MS. *Food Chemistry*, 349, 129156.

Yuasa, M., Akao, Y., Kawabeta, K. and Tominaga, M. (2018). Antioxidant activity and characterization of taste in early fresh onions and their leaves produced in Minamishimabara, Nagasaki, Japan. *J Home Econ Jpn*, 69(9), 676–681.

Zhang, M., Choe, J., Bu, T., Liu, S. and Kim, S. (2022). Comparison of Antioxidant Properties and Metabolite Profiling of *Acer pseudoplatanus* Leaves of Different Colors. *Antioxidants*, 12, 65.

Zhu, X., Xiong, T., Liu, P., Guo, X., Xiao, L., Zhou, F., Tang, Y. and Yao, P. (2018). Quercetin ameliorates HFD-induced NAFLD by promoting VLDL assembly and lipophagy via IRE1α/XBP1s pathway. *Food and Chemical Toxicology*, 114, 52–60.

5. Chapter V: Coffee silverskin extracts

Coffee silverskin (CSS) protects keratinocytes from UVA-induced damage in *in vitro* and *in vivo* models

5.1 Abstract

Coffee silverskin (CSS), a major by-product of the coffee roasting process, represents a sustainable and underexplored source of bioactive compounds.

Eco-friendly microwave-assisted extraction enables the recovery of green CSS extracts enriched in phenolic compounds and melanoidins, both known for their antioxidant and functional properties.

Despite growing interest in their application in skin health, the molecular mechanisms underlying their protective effects remain incompletely defined.

In this study, was investigated the cytoprotective and antioxidant effects of two green CSS extracts, a phenols-rich fraction and a melanoidins-rich fraction, in UVA-stressed HaCaT cells and *in vivo* zebrafish models.

CSS extracts significantly attenuated ROS and NO production, which underlies maladaptive ER stress, while confocal analysis showed enhanced nuclear accumulation of Nrf2, indicating activation of the antioxidant pathway.

Notably, pharmacological inhibition of PERK, a central mediator of ER stress signaling, abolished these protective effects, highlighting the role of controlled ER stress in mediating Nrf2-dependent antioxidant responses.

Moreover, the extracts inhibited tyrosinase activity and melanin synthesis, and reduced ferroptosis both *in vitro* and *in vivo*.

Collectively, these findings demonstrate that CSS extracts exert multifunctional protective effects against UVA-induced skin damage, supporting their potential as sustainable dermaceutical ingredients.

5.2 Introduction

The global coffee industry is one of the most significant agricultural sectors, with millions of tons of coffee beans processed annually to meet the demand for one of the world's most popular beverages (Grabs, 2018; Borrella *et al.*, 2015).

Coffee consumption has long been celebrated for its health benefits, primarily due to the antioxidant properties of its key components, such as caffeine, chlorogenic acid, hydroxycinnamic acids, and melanoidins (Yashin *et al.*, 2013).

These compounds not only contribute to coffee's unique flavor and aroma but also exhibit a range of biological activities, including anti-inflammatory, antimicrobial, and photoprotective effects (Surma *et al.*, 2023; Yosboonruang *et al.*, 2022; Elias *et al.*, 2023).

However, during the production of coffee, a staggering 90% of the raw material is discarded as waste, generating an enormous quantity of by-products. Among these, coffee silverskin (CSS), a thin protective layer surrounding the coffee bean, is the most abundant solid by-product, produced in vast quantities during the roasting process. Traditionally, CSS has been used in low-value applications, such as fuel or soil fertilization, but its rich composition of bioactive compounds presents an opportunity for innovative and sustainable uses in health and as cosmetic sectors (Bessada *et al.*, 2018; Del Pozo *et al.*, 2021).

Emerging research has revealed the significant antioxidant potential of CSS, suggesting its applicability in various fields, including antiaging cosmetics and dermaceutics. Natural plant-derived compounds are highly valued today for their versatile benefits and bioactive properties (Restivo *et al.*, 2022; Pojero *et al.*, 2023), also for their ability to protect the skin from damage caused by UV radiation and environmental stressors (Milutinov *et al.*, 2024). Examples include well-known matrices such as algae, aloe, citrus, rosemary, chestnut extracts and inorganic matrices, such as clays (Pangestuti *et al.*, 2018; Minh *et al.*, 2010). Coffee-derived products, including CSS, are also showing promise as effective protectors against photoaging and oxidative damage induced by UV radiation (Chianget *al.*, 2011; Herman and Herman, 2013; Fukushima *et al.*, 2015). While some studies have highlighted the antioxidant, antimicrobial, and cytoprotective effects of CSS extracts,

their potential to mitigate sun damage or serve as depigmenting agents has not yet been fully explored (Juan-García *et al.*, 2021).

Once extracted, CSS exhibits remarkable nutritional and functional properties. Notably, it is rich in dietary fiber, which constitutes approximately 50% of its composition, with a predominance of insoluble fiber.

Special attention is paid to melanoidins, high molecular weight brown polymeric compounds formed in the final stage of the Maillard reaction hese compounds not only contribute to the color, taste, and texture of heat-treated foods but also exhibit various biological properties. Often referred to as "Maillardized dietary fiber" (Tores de la Cruz et al., 2019), coffee melanoidins demonstrate antioxidant, antimicrobial, anti-inflammatory, antihypertensive, anticarcinogenic, prebiotic, and antiglycative activities (Iriondo-DeHond *et al.*, 2021).

Furthermore, CSS contains significant amounts of phenolic compounds such as chlorogenic acid, caffeic acid, and caffeine, all of which contribute to its potent antioxidant properties. These bioactives are widely recognized for their potential health benefits, including anti-inflammatory, anti-aging and protection against skin UV damage (Rojas-González *et al.*, 2022; Metro *et al.*, 2017; Bessada *et al.*, 2018).

Melanin, the primary pigment responsible for skin color, plays a crucial role in shielding the skin from UV-induced damage and maintaining cutaneous homeostasis (Solano, 2020).

The process of melanogenesis relies on the activity of the enzyme tyrosinase, which catalyzes the oxidation of L-tyrosine to L-DOPA and subsequently to L-dopaquinone (D'Mello *et al.*, 2016).

However, excessive melanin production can lead to hyperpigmentation disorders such as melasma, freckles, solar lentigo, post-inflammatory hyperpigmentation and melanoma (Briganti *et al.*, 2016).

In this context, finding effective and safe tyrosinase inhibitors is a critical focus in dermatological and cosmetic research.

While *in vitro* models using human-derived keratinocyte cultures provide valuable insights into the effects of bioactive compounds on the skin, these systems often lack the complexity of *in vivo* microenvironments (Seo *et al.*, 2012). Traditional animal models, such as mice and guinea pigs, have been instrumental in studying depigmenting agents (Hong *et al.*, 2014; Kumar *et al.*, 2013) but come with ethical concerns and practical limitations.

The use of zebrafish (*Danio rerio*) as an alternative model has gained significant attention in recent years due to its unique advantages. Zebrafish embryos are highly transparent, enabling real-time visualization of melanogenesis, and their genetic, physiological, and biochemical pathways related to pigmentation are remarkably similar to those in humans. Moreover, zebrafish offer ethical and economic benefits over traditional mammalian models, aligning with the principles of the 3Rs (replacement, reduction, refinement) in animal research (Agalou *et al.*, 2018; Lajis, 2018; Saleem and Kannan, 2018).

As illustrated in the developmental timeline (**Figure 5.1**), embryogenesis is rapid and well defined: within 24–48 hours post-fertilization, embryos progress from cleavage and gastrulation to segmentation and hatching stages. This accelerated and externally developing process allows precise temporal exposure to test compounds during critical windows of melanocyte differentiation and pigment formation.

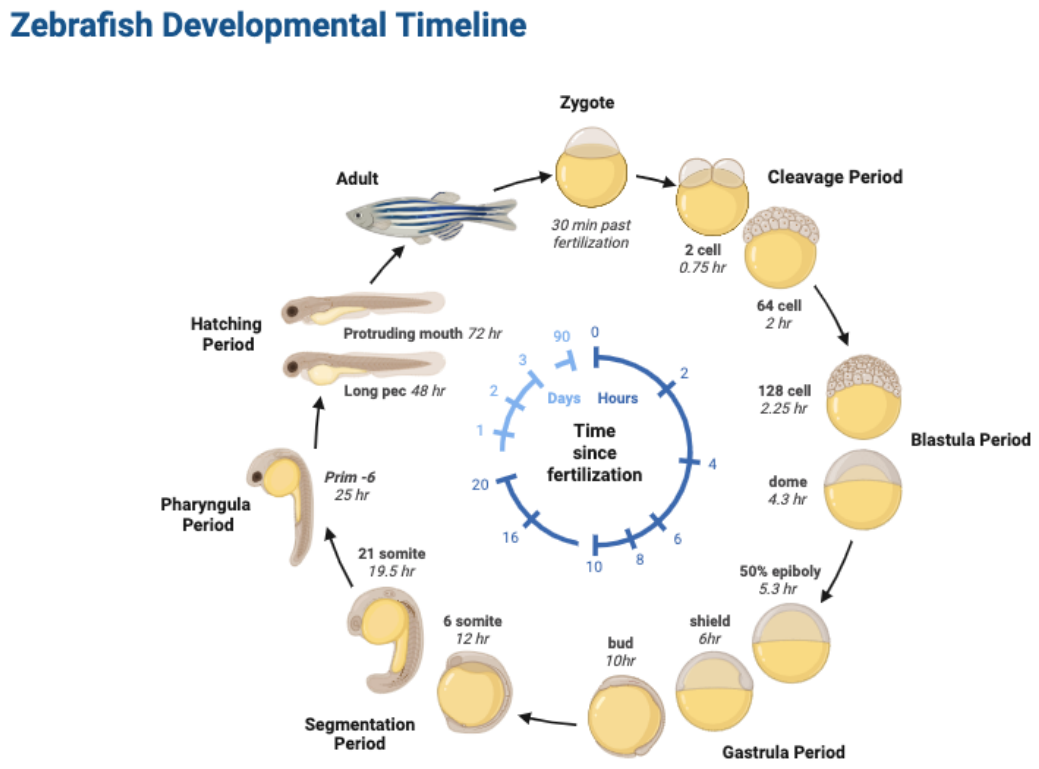

Figure 5.1. *Zebrafish developmental timeline from fertilization to hatching, highlighting the rapid embryonic progression within the first 72 hours post-fertilization.*

In addition, zebrafish represent an efficient platform for screening natural compounds with photoprotective and antioxidant potential (Arteaga *et al.*, 2021; Wang *et al.*, 2025). Their small size, high fecundity, and rapid development support high-throughput approaches to assess tyrosinase activity, pigmentation, oxidative stress, and overall skin-related endpoints. The ability of embryos to absorb water-soluble compounds directly from the surrounding medium further simplifies experimental design and enhances reproducibility.

5.2.1 Aim of work

In this study, was explored the biochemical potential of two CSS extracts, a phenols-rich fraction and a melanoidins-rich fraction, focusing on their antioxidant and cytoprotective properties through both *in vitro* and *in vivo* zebrafish models.

This investigation assessed their efficacy as antioxidants and tyrosinase inhibitors, targeting the modulation of melanogenesis and the protection of HaCaT cells from oxidative stress and ferroptosis.

Notably, the protective effects of the extracts involved a reduction of ER stress, which is closely linked to UVA-induced ROS accumulation and ferroptosis. Mechanistically, ER stress plays a dual role in cellular homeostasis: while moderate activation of the PERK pathway can trigger adaptive responses that activates Nrf2 and its downstream antioxidant genes, excessive or prolonged ER stress can lead to cell death (Spencer and Finnie, 2020; Valerio *et al.*, 2021).

It has been observed that CSS extracts were found to bias the ER stress response towards the protective side by sustaining PERK signaling, which enhanced Nrf2 activation and the expression of downstream antioxidant genes.

This modulation enabled cells to cope more effectively with UVA-induced ROS and limited ferroptotic cell death. Importantly, pharmacological inhibition of PERK abolished these protective effects, confirming that the cytoprotective action of CSS extracts depends, at least in part, from the functional ER stress signaling.

Moreover, our findings demonstrate that the extracts inhibit tyrosinase activity and melanin synthesis, while simultaneously exerting antioxidant and anti-ferroptotic effects *in vivo*, providing direct evidence of their protective action and highlighting the innovative potential of CSS for dermaceutical applications (**Figure 5.2**).

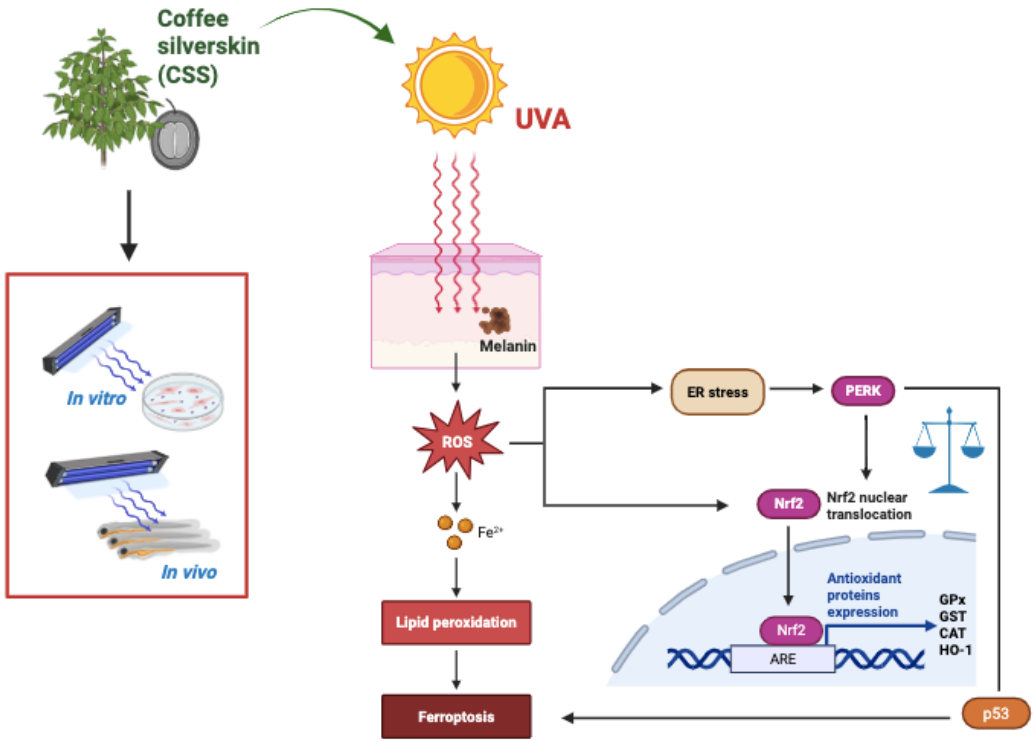

Figure 5.2. *CSS protects against UVA-induced photodamage via a multifunctional action.*

5.3 Materials and Methods

5.3.1 Sample preparation

Coffee silver skin (CSS) from green Ugandan Robusta coffee (*Coffea canephora* Pierre ex A.Froehne) was kindly donated by Resi S.r.l (Naples, Italy).

CSS was milled into powder and stored at room temperature in a cool and dry place, away from direct light. CSS extract was obtained performing a microwave-assisted extraction using a CEM Discover SP (CEM Corporation) apparatus operating in dynamic mode using 35 mL closed vessels to perform the extraction at elevated temperatures.

The mixture was then centrifuged at 6000 rpm for 15 minutes at 4°C. The resulting supernatants were freeze-dried and stored at -20°C until further analysis.

The extract was subjected to ultracentrifugation to obtain a melanoidins-rich fraction. Briefly, ten milliliters of water extract (5 mg/mL) was subjected to ultrafiltration using an Amicon Ultra-15, regenerated cellulose 10 kDa (Millipore) at 6000 rpm for 25 min at 25 °C. The retentate was refilled with 10 mL of water and washed three times to separate the low molecular weight compounds from

the retentate. The content of melanoidins fraction was determined by weighing the freeze dried retentate obtained after ultracentrifugation. The results were expressed as mg/g CSS DW.

5.3.2 UHPLC-PDA-ESI-Orbitrap-MS/MS conditions

UHPLC-HRMS/MS analysis was performed on a Thermo Scientific™ Vanquish™ UHPLC system, equipped with a VF-P10-A binary solvent delivery system, a VC-D11-A photodiode array detector, a VH-C10-A column compartment and VF-A10-A autosampler. The UHPLC system was coupled online to a Orbitrap Exploris 120 mass spectrometer (Thermo Fisher Scientific) equipped with a heated electrospray ionization probe (HESI II) operating in positive mode.

The chromatographic separation was performed on a Kinetex® EVO C18 100 Å, 150 × 2.1 mm × 2.6µm (Phenomenex). The column temperature and the flow rate were set at 40°C and 0.4 mL/min, respectively. The mobile phases were H_2O (A) and ACN (B) both acidified with 0.1 % HCOOH (*v/v*) with the following gradient: 0.01-2.00 min, isocratic to 2% B; 2.01-14.00 min, 2-98% B; 14.01-16.00 min, isocratic to 98% B; 16.01-17.00 min, 98-2% B; then five minutes for column re-equilibration.

The following PDA parameters were applied: sampling rate, 20.0 Hz; detector response time, 0.200 s; and detector peak width, 0.020 min. Data acquisition was set in the range 190-800 nm, and chromatograms were monitored at 280 and 330 nm at maximum absorbance of the compounds of interest.

The MS was calibrated by Thermo Pierce™ FlexMix™ Calibration Solutions in both polarities. Full MS (100-1400 m/z) and data-dependent MS/MS were performed at a resolution of 60,000 and 15,000 FWHM respectively; Normalized Collision Energy (NCE) value of 30 was used. Source parameters: Sheath gas pressure, 30 arbitrary units; auxiliary gas flow, 10 arbitrary units; spray voltage, +3.4 kV, -2.8 kV; capillary temperature, 320°C; auxiliary gas heater temperature, 320°C.

Peaks annotations were carried out by comparing their MS/MS fragmentation pattern with libraries as well as with reported data in literature. The identification level was established according to Metabolomics Standards Initiative (MSI): level 1, unambiguous identification with reference standards; level 2, putative identification

by matching MS2 data to literature data or spectral databases; level 3, putative identification established by spectral similarity to chemical class of compounds and chemotaxonomic (Sumner *et al.*, 2007).

For HRMS data analysis and processing, FreeStyle™ 1.8 SP2 and Compound Discoverer™ 3.1 software (Thermo Scientific, SanJose, CA, U.S.A.) were used for raw data processing (baseline correction, noise filtering, spectral alignment, and peak detection) and for putative identification of metabolites based on molecular formula (matched), exact mass (mass tolerance < 5 ppm) and MS2 fragmentation pattern [Fragment Ion Search (FISh)], with a global database search (mzCloud, MassList and ChemSpider).

Other databases, containing fragmentation spectrum information of natural product molecules from different sources, mainly include MassBank (https://massbank.eu/MassBank/), GNPS (https://gnps.ucsd.edu/ProteoSAFe/static/gnps-splash.jsp/), PubChem (https://pubchem.ncbi.nlm.nih.gov/), LipidMAPS (http://www.lipidmaps.org/), FooDB (http://foodb.ca/), Phenol-Explorer (http://phenol-explorer.eu/), PlantaeDB (https://plantaedb.com/), PMhub (https://pmhub.org.cn/#/) and LOTUS (https://lotus.naturalproducts.net/).

5.3.3 MALDI-MS analysis

MALDI-MS experiments were performed on a rapifleX® Tissuetyper MALDI mass spectrometer (Bruker Daltonics) equipped with a Smartbeam 3D laser and with a digitizer frequency of 5 GHz. The analyzer was operated in the reflector mode, and the laser was fired with a repetition rate of 10 kHz. Melanoidins measurement was performed in a positive mode across the m/z range of 700–3500. A total of 1000 laser shots were fired at each sampling position and the laser power was optimized at the start of each run and then held constant during the experiments. The external calibration was performed using red phosphorous dissolved in 50% ACN. α-cyano-hydroxycinnamic acid (HCCA) was used as the matrix for the positive ionization mode at a concentration of 10 mg/mL in a solution of 0.1% TFA in ACN/H_2O 50:50 (*v/v*).

The mixture of HCCA-matrix and melanoidins was prepared (1:1, *v/v*), and then 1 µL of this mixture was spotted onto ground steel microtiter plates for subsequent measurements.

5.3.4 Determination of total phenolic content (TPC) and total flavonoids content (TFC)

The TPC of the CSS extracts was determined using the Folin–Ciocalteau method. Gallic acid was selected as the standard, the stock solution (1 mg/mL) was prepared in MeOH, and the calibration curve was obtained in a concentration range of 30–500 µg/mL (y = 0,0014x − 0.1549; R^2 = 99.62%).

The analysis was performed in triplicate. The total phenolic content was expressed as milligrams of gallic acid equivalents per gram of dry weight (mg GAE/g DW).

For, TFC the absorbance values were then compared to a rutin calibration standard curve (30–500 µg/mL; y = 0,0004x – 0,0567; R^2 = 99.78%).

The analysis was performed in triplicate. The TFC was expressed as milligrams of rutin equivalents per gram of dry weight (mg RU/g DW).

5.3.5 DPPH (2,2-diphenyl-1-picrylhydrazyl) and FRAP (Ferric Reducing Antioxidant Power) antioxidant activity assays

The free radical scavenging ability of the CSS extracts was tested using DPPH radical scavenging assay. The DPPH radical scavenging activity of the sample was expressed as Trolox equivalent antioxidant capacity (TEAC, mg TXE/g) calculated as follows: TEAC = $IC50Trolox\ /AIC50sample$. The higher TEAC value means a higher DPPH radical scavenging activity.

The FRAP assay was conducted under the conditions previously described. Trolox was used as reference (1–200 µg/mL; y = 0.0202x + 0.1323; R^2 = 99.99%). FRAP activity was calculated as milligrams of trolox equivalents per gram of dry weight (mg TEX/g DW).

5.3.6 Metal binding studies

The metal binding studies were performed in this way (Umar *et al.*, 2018): the UV absorption of the CSS extracts (100 µg/mL) alone or in the presence of CuSO4, FeSO4, or FeCl3 (40 µM) for 30 min in 20% (v/v) ethanol/buffer (20 mM HEPES, 150 mM NaCl, pH 7.4) was recorded using a microplate reader (Multiskan Go, Thermo Scientific) with a wavelength ranging from 280 to 400 nm.

5.3.7 Determination of copper-chelating activity

The copper chelation activity was assessed using pyrocatechol violet.

In brief, a 4 mM solution of the chromogenic reagent pyrocatechol violet was prepared in 50 mM sodium acetate buffer (pH 6.0).

In a 96-well plate, 10 µL of the compounds (100 µg/mL), 70 µL of sodium acetate buffer, 10 µL of CuSO4 (1 mM), and 4 µL of pyrocatechol violet were added.

The mixture was thoroughly mixed, and the absorbance of the pyrocatechol–Cu^{2+} complex was measured at 632 nm using a Multiskan Go spectrophotometer (Thermo Scientific). Ethylenediaminetetraacetic acid (EDTA, final concentration 1 mM) was used as a positive control.

The results are expressed as the chelating activity of compounds.

5.3.8 Inhibition of tyrosinase activity assay

The tyrosinase inhibitory activity of CSS extracts was analysed using L-tyrosine and 3,4-dihydroxy-L-phenylalanine (L-DOPA) as substrates in order to investigate the monophenolase and diphenolase inhibitory activity, respectively (Wang et al., 2018). Tyrosinase inhibitory activity was evaluated using a method reported by Widelski *et al.* with some modifications (Widelski *et al.*, 2023). The following were added to a 96-well plate: 100 µL of L-tyrosine or L-DOPA (1 mM or 3 mM, in PBS; as a substrate of tyrosinase); 20 µL of mushroom tyrosinase (12.5 µg/mL, in K_3PO_4 50 mM; T3824, Sigma); 80 µL of samples (25 µg/mL, in PBS). Kojic acid (1 mM) was used as a control. The resulting mixture was incubated for 2 h at room temperature. Absorbance was measured at 492 nm with a microplate reader (Multiskan Go, Thermo Fisher Scientific). The values were corrected by the absorbance of CSS extracts without tyrosinase, L-tyrosine, and L-DOPA. A control sample (100% tyrosinase activity)

contained tyrosinase, an equal volume of the buffer, and the appropriate dose of each substrate. The monophenolase or diphenolase inhibitory activity was calculated based on the equation:

$$\% \text{ inhibition: } \left(\frac{Abs\ Ctrl - Abs\ S}{Abs\ Ctrl}\right) \times 100 \qquad \textit{Equation 5.1}$$

where Abs S is the absorbance of the sample (extract + tyrosinase + substrate), and Abs Ctrl is the absorbance of the control sample (buffer + tyrosinase + substrate).

5.3.9 Cell cultures and photoprotective treatment

HaCaT cells were obtained from ATCC. These cells, derived from the human keratinocyte line, were grown in Dulbecco's Modified Eagle Medium (DMEM, 4500 mg/mL glucose) supplemented with 10% (*v*/*v*) fetal bovine serum, 2 mM L-glutamine, 100 U/mL penicillin and 0.1 mg/mL streptomycin.

Cells were routinely grown in culture dishes in a 95% humidified environment containing 5% CO_2 at 37 °C and split every 2 days.

Before each experiment, the medium was removed, and the cells were washed twice with PBS. Next, a serum-free medium without phenol red was added, supplemented with 2 mM L-glutamine, 100 U/mL penicillin and 0.1 mg/mL streptomycin.

Then cells were irradiated with a UV lamp (VL-6.LC; Vilber Lourmat) (366 mJ/cm^2, 10 min, 365 nm) and treated, simultaneously with UVA irradiation, with total CSS extract (Tl) and melanoidin extract of CSS (Ml) for different experimental times.

Each treatment and analysis were performed at least in triplicate separate experiments.

5.3.10 Cell viability assay

Cell viability was established by measuring mitochondrial metabolic activity with MTT. Briefly, HaCaT cells (10×10^3 cells/well) were plated in 96-well plates, after 24 h were treated with CSS extracts (6-50 µg/mL) and UVA irradiation for 10 min.

The PERK inhibitor GSK2606414 was subsequently used as a positive control at a concentration of 0.5 µM, in co-administration with CSS extracts and UV treatment. After 4 h, MTT reagent at 0.5 mg/mL final concentration for 1 h was added.

Then, 100 µL per well of 0.1 M isopropanol/HCl solution was added to dissolve the formazan crystals. The absorbance was measured at 570 nm, using a microplate reader (Multiskan Go, Thermo Scientific).

Cell viability was expressed as a percentage relative to the untreated cells cultured in medium with 0.1% DMSO and set to 100%, whereas 10% DMSO was used as positive control and set to 0% of viability.

5.3.11 Annexin V-FITC/Propidium iodide (PI) staining

Cell apoptosis was assessed using Annexin V-FITC/PI reagents. HaCaT cells (60 × 10^3 cells/well) were seeded in 24-well plates, then treated with CSS extracts (25 µg/mL) and irradiated with UVA for 10 min. After 4 h after treatment, the harvested cells were resuspended in 100 µL of assay buffer containing 5 µL of Annexin V-FITC and 1 µL of PI reagents. After 20 min incubation at RT according to the manufacturer's protocol (Dead Cell Apoptosis Kits with Annexin V for Flow Cytometry, Thermo Fisher Scientific), the cells were analyzed with a Becton Dickinson FACScan flow cytometer using Cell Quest software, version 4.

5.3.12 Measurement of lactate dehydrogenase (LDH)

HaCaT cells (10 × 10^3 cells/well) were grown in 96-well plates and allowed to adhere for 24 h. Later the medium was replaced, and cells were treated with UVA irradiation and CSS extracts (25 µg/mL).

The PERK inhibitor GSK2606414 was subsequently used as a positive control at a concentration of 0.5 µM, in co-administration with CSS extracts and UV treatment. After 4 h from treatments, the release of LDH in the cell culture medium was verified with LDH-GloTM cytotoxicity test (Promega).

According to the LDH-Glo™ kit protocol, the LDH detection reagent (containing lactate, NAD^+, reductase, reductase substrate, and rLuciferase Ultra-Glo™) were added to the cell culture medium sample.

The luminescent signal generated was read in end-point mode using a PerkinElmer AlphaScreen multimode plate reader.

5.3.13 Reactive oxygen and nitrogen species (ROS/RNS) determination

Reactive oxygen species levels were measured using 10 µM 6-carboxy-2',7'-dichlorodihydrofluorescein diacetate (DCFH-DA, Sigma Aldrich). While reactive nitrogen species (RNS) were evaluated using 5 µM 4-amino-5-methylamino-2',7'-difluorofluorescein diacetate (DAF-FM-DA, Thermo Fisher Scientific)

HaCaT cells were seeded at a density of 10×10^3 cells per well in a 96-well and allowed to adhere for 24 h.

Subsequently, cells were treated with CSS extracts (25 µg/mL) and irradiated with UVA for 10 min. After washing, the cells were incubated with DCFH-DA or DAF-FM-DA in serum-free medium without phenol red for 30 min at 37 °C in the dark. The stained cells were washed, and representative images were acquired using a ZOE Fluorescent Cell Imaging System (Bio-Rad. Magnification, 20×. N ≥ 10. Scale bar: 100 µm). Fluorescence signals (DCFH-DA: excitation/emission 485 nm/535 nm; DAF-FM-DA excitation/emission 495 nm/515 nm) were measured using a PerkinElmer EnSpire multimode plate reader and expressed as the DCFH/ DAF-FM fluorescence intensity.

5.3.14 Quantification of cellular glutathione (GSH) levels

A colorimetric assay using Ellman's reagent was used for this test.

The assay based on the oxidation of GSH by 5,5'-dithiobis(2-nitrobenzoic acid) [DTNB] to measure the total glutathione (tGSH) content of biological samples.

HaCaT cell line (2×10^6 cells/well) was seeded in 100 mm culture dishes, treated with CSS extracts (25 µg/mL) and UVA irradiation for 10 min.

After 4 h from treatments, cells were washed twice with PBS and detached with a scraper, centrifuged at 655 g × 10 min at 4 °C. Full proteins were extracted as follows: 100 µL of 5% (v/v) trichloroacetic acid (TCA), previously cooled to 4 °C, was added to the cell pellet; samples were incubated on ice for 15 minutes to promote protein precipitation.

Subsequently, the samples were centrifuged at 13,000 g for 10 minutes at 4 °C. The supernatant was supplemented with 1 M NaOH to neutralize the TCA for subsequent analysis with Ellman's reagent, while the pellet was used for protein quantification. In a 96-well plate, the following were sequentially added: 70 µg of

total protein (in 50 µL) in reaction buffer (100 mM $Na_2HPO_4 \cdot 7H_2O$, 1 mM EDTA, pH 8), 30 µL of DTNB (9 mM) prepared in the same buffer and an additional 20 µL of reaction buffer. The resulting mixture was incubated at 37 °C for 30 minutes. Absorbance was then measured at 405 nm using a microplate reader (Multiskan Go, Thermo Fisher Scientific). GSH (1 mM) served as negative control.

5.3.15 Glutathione S Transferase (GST) activity

A colorimetric assay using 1-chloro-2,4-dinitrobenzene (CDNB) was performed to measure the GST activity. HaCaT cell line was treated as previously described and lysed in 100 mM sodium phosphate buffer (pH 6.5) containing 1 mM EDTA and 0.1% Triton X-100. The reaction mixture was first prepared, consisting of 10 µl of phosphate buffer pH 7.5; 30 µl of 1 mM reduced GSH; 30 µl of 1 mM CDNB and 30 µl of cell lysate (70 µg of total protein). After conjugation of the thiol group of glutathione to the CDNB substrate, CDNB-GSH conjugation (formation of DNP-glutathione conjugate by nucleophilic displacement of Cl with GSH-thiol) was measured spectrophotometrically at 340 nm. The values were expressed as the percentage of enzyme activity (U/mg protein).

5.3.16 Glutathione peroxidase (GPx) activity

Glutathione peroxidase (GSH-px) activity was based upon the reaction of reduced glutathione (GSH) transformation to oxidized glutathione (GSSG). GSH-px was determined by spectrophotometric measurement at 340 nm of the conversion of NADPH to NADP+ at pH 7.4. HaCaT cell line was treated and lysed as previously described. The reaction mixture was prepared with 20 µL of 5 mM NADPH, 20 µL of 5 mM sodium azide, 20 µL of 1 mM reduced GSH, 20 µL of 50 mM H_2O_2 and 20 µL of lysate (70 µg of total protein). The values were expressed as the percentage of enzyme activity (U/mg protein).

5.3.17 Determination of protein misfolding

Protein misfolding was analyzed using Thioflavn T (ThT, Sigma Aldrich, St. Louis, MO, USA) staining. HaCaT cells (10×10^3 cells/well) were grown in 96-well plates and

allowed to adhere for 24 h. Later the medium was replaced, cells were treated with CSS extracts (25 µg/mL) under UVA irradiation.

After 24 h, the culture medium was replaced, cells washed twice with PBS and a staining solution containing 20 µM ThT in PBS was added for 30 min at 37 °C in the dark. The stained cells were washed, and representative images were acquired using ZOE Fluorescent Cell Imaging System (Bio-Rad. Magnification, 20×. N ≥ 10. Scale bar: 100 µm). Quantitative analyses were performed reading the fluorescence signals (excitation/emission 450 nm/482 nm) using a PerkinElmer EnSpire multimode plate reader.

5.3.18 Western blotting analysis

HaCaT cell line (2 × 10^6 cells/well) was seeded in 100 mm culture dishes and treated with CSS extracts (25 µg/mL) under UVA irradiation. After 4 or 24 h from treatments,the cells were washed, detached with a scraper, and centrifuged to remove debris. Full proteins were extracted by using a lysis buffer. Then, cell lysates were centrifuged at 4850 × *g* for 20 min at 4 °C.

A total of 50 µg of total proteins was run on 8-12% SDS-PAGE and transferred to nitrocellulose membranes using a minigel apparatus (Bio-Rad Laboratories).

Blots were blocked in phosphate-buffered saline, containing Tween-20 0.1% and 10% non-fat dry milk or bovine serum albumin (BSA), for 1 h at room temperature and incubated overnight with specific primary antibodies at 4 °C with slight agitation.

α-tubulin was used as the loading control.

The following antibodies were used:

- mouse monoclonal anti-α-tubulin (Santa Cruz Biotechnology),
- mouse polyclonal anti-Nrf2 (Santa Cruz Biotechnology),
- rabbit polyclonal anti-P53 (Elabscience),
- mouse monoclonal anti-Heme Oxygenase 1 (Santa Cruz Biotechnology),
- rabbit monoclonal anti-PARP (Cell Signaling Technology).

After washes in PBS/Tween-20 0.1%, the appropriate anti-rabbit or anti-mouse (Pierce, Thermo Fisher Scientific) peroxidase-linked secondary antibody was added for 1 h at room temperature.

Antigen-antibody complexes were detected by enhanced chemiluminescence (ECL kit, Amersham). Filters were exposed to LAS 4000 (GE Healthcare) and the densitometry analysis of autoradiographs was performed by the ImageJ program, version 1.47.

5.3.19 Indirect immunofluorescence of Nrf2 localization

HaCaT cell line (60×10^3 cells/well) was seeded in 24-well plates allowing to adhere for 24 h. Cells were treated with CSS extracts (25 µg/mL) and UVA irradiation for 10 min. The PERK inhibitor GSK2606414 was subsequently used as a positive control at a concentration of 0.5 µM, in co-administration with CSS extracts and UV treatment. Cells seeded on glass coverslips were washed in PBS, fixed in PBS-4% paraformaldehyde and permeabilized 15 min in PBS containing 0.25% triton. Then, cells were incubated with a blocking solution containing PBS-0.5% BSA and 50 mM NH_4Cl for 30 min. The cells were immunostained with the following primary antibody for 1 h at RT: mouse polyclonal anti-Nrf2 (Santa Cruz Biotechnology, Dallas, TX, USA). Primary antibody was revealed with Alexa 488-conjugated secondary antibodies (Molecular Probes, Invitrogen). Nuclei were counterstained with 1.5 µM Hoechst 33,342 (Sigma Aldrich, St. Louis, MO, USA) for 10 min. Images were acquired on a laser scanning confocal microscope (TCS SP8; Leica MicroSystems) equipped with a plan Apo 63X, NA 1.4 oil immersion objective lens. Co-localization analysis was conducted on 30 cells per sample using a Leica SP5 confocal microscope, following the method previously described.

The co-localization rates shown in the figures were obtained using the proprietary co-localization algorithm included in the Leica Software (LAS-AF 2.7.3.9723). This value represents the percentage of co-localization, calculated as the ratio between the number of pixels showing overlapping fluorescence and the total number of fluorescent pixels from both fluorophores in the image. Specifically, the Nrf2 vs. DAPI co-localization rate was determined by dividing the number of Nrf2–DAPI overlapping pixels by the sum of Nrf2 and DAPI pixels (number of Nrf2–DAPI co-localizing pixels / total number of Nrf2 + DAPI pixels).

5.3.20 Quantitative real time-PCR for molecular pathway analysis

HaCaT cell line (2 × 10^6 cells/well) was seeded in 100 mm culture dishes and treated with CSS extracts (25 µg/mL) under UVA irradiation.

The PERK inhibitor GSK2606414 was subsequently used as a positive control at a concentration of 0.5 µM, in co-administration with CSS extracts and UV treatment. After 4 and 24 h from treatments, cells were washed twice with PBS and detached with a scraper. Total RNA was isolated using a modified procedure with the Quick-RNA™ Miniprep Kit (Zymo Research).

Genomic DNA was eliminated by treatment with DNase I provided in the kit. The resulting purified RNA was then reverse transcribed into cDNA using the SensiFAST™ cDNA Synthesis Kit (Meridian Bioscience).

Real-time PCR was performed with LightCycler® 480 System (La Roche Ltd) using SYBR Green detection in a total volume of 20 µL with 1 µL of forward and reverse primers (5 µM) and 10 µL of SensiFAST™ SYBR No-ROX Kit (Meridian Bioscience). Values were determined from standard curve generated from serial cDNA dilutions and normalized to GAPDH.

The primers used for the real-time PCR reactions are listed in the table below.

The $2^{-\Delta\Delta CT}$ method was used to analyze the results and relative mRNA expression levels were determined as fold-induction relative to Ctrl cells.

Table 5.1. *Forward and Reverse Primer Sequences for Target Genes*

Primer sequence (5'–3')		
Target gene	**Forward**	**Reverse**
GPx	CCTCAAGTACGTCCGACCTG	CAATGTCGTTGCGGCACACC
Catalase	GCAGATACCTGTGAACTGTC	GTAGAATGTCCGCACCTGAG
BIP	CGGGCAAAGATGTCAGGAAAG	TTCTGGACGGGCTTCATAGTAGAC
PERK	TCATCCAGCCTTAGCAAACC	ATGCTTTCACGGTCTTGGTC
ATF4	GTCCCTCCAACAACAGCAAG	CTATACCCAACAGGGCATCC

5.3.21 Lipid peroxidation

Lipid rancidity was assessed by measuring thiobarbituric acid reactive substances (TBARs). For this purpose, a lipid peroxidation assay kit for malondialdehyde (MDA) (Sigma-Aldrich) was used to perform a colorimetric quantification at λ = 532 nm.

HaCaT cells were seeded in 60 mm dishes at approximately 80% confluence and, on the following day, treated as previously described with 25 µg/mL CSS extracts under UVA irradiation.

The PERK inhibitor GSK2606414 (0.5 µM) and ferrostatin-1 (1 µM) were applied as positive controls in co-treatment with CSS extracts and/or UV exposure.

After 24 hours of incubation, cells were harvested by detachment and centrifuged at 655 × g for 10 minutes at 4 °C. The resulting pellets were then used to determine malondialdehyde levels, following the manufacturer's instructions provided with the kit.

5.3.22 Detection of labile iron ions (Fe^{2+}) using FerroOrange

Labile iron ions (Fe^{2+}) were detected using BioTracker™ FerroOrange Live Cell Dye (1 µM, Sigma Aldrich). HaCaT cells were seeded (10×10^3 cells/well) in 96-well plates and allowed to adhere for 24 h.

Subsequently, cells were treated with CSS extracts (25 µg/mL) and irradiated with UVA for 10 min. The PERK inhibitor GSK2606414 (0.5 µM) and Ferrostatin-1 (1 µM) were applied as positive controls in co-treatment with CSS extracts and/or UV exposure. After 4 h, the cells were incubated with FerroOrange in serum-free medium without phenol red for 30 min at 37 °C in the dark.

The stained cells were washed, and representative images were acquired using a ZOE Fluorescent Cell Imaging System (Magnification, 20×. N ≥ 10. Scale bar: 100 µm).

Fluorescence signals (excitation/emission 542 nm/572 nm) were measured using a PerkinElmer EnSpire multimode plate reader and expressed as the FerroOrange fluorescence intensity.

5.3.23 Lipid ROS detection

A C11 BODIPY 581/591 (5 µM, MedChemExpress) dye was used to measure lipid ROS. This probe detects lipid peroxidation and ferroptosis via reaction with

hydroxyl radicals, showing emission at 591 nm in the reduced form and at 510 nm in the oxidized form, with excitation at 581 nm and 500 nm, respectively.

HaCaT cells were seeded (10×10^3 cells/well) in 96-well plates and allowed to adhere for 24 h. Subsequently, cells were treated with CSS extracts (25 µg/mL) and irradiated with UVA for 10 min.

The PERK inhibitor GSK2606414 (0.5 µM) and Ferrostatin-1 (1 µM) were applied as positive controls in co-treatment with CSS extracts and/or UV exposure.

After 4 h, the cells were incubated with C11 BODIPY in serum-free medium without phenol red for 40 min at 37 °C in the dark.

The stained cells were washed, and representative images were acquired using a ZOE Fluorescent Cell Imaging System (Magnification, 20×. N ≥ 10. Scale bar: 100 µm).

Fluorescence signals were measured using a PerkinElmer EnSpire multimode plate reader. The fluorescence intensity values were calculated as the ratio between oxidized and reduced lipid signals, thus reflecting the extent of lipid peroxidation.

5.3.24 Origin and maintenance of parental zebrafish

Wild-type adult zebrafish were maintained as breeding stocks in a recirculating aquatic system under standard husbandry conditions (28–28.5 °C; 14 h light/10 h dark photoperiod) and managed according to established zebrafish housing recommendations. Spawning was set up using adult pairs (or groups) in breeding tanks, and fertilized eggs were collected shortly after light onset. Embryos/larvae were rinsed, staged, and reared at 28.5 °C in E3 medium (or equivalent “egg water”) in Petri dishes, with regular removal of unfertilized/dead embryos and routine medium changes as needed until the experimental endpoint. All experiments were performed exclusively on zebrafish embryos/larvae up to 5 days post-fertilization (≤120 hpf), prior to the independently feeding larval stage, which is commonly used as the boundary for protected life stages in zebrafish under European regulatory guidance.

For imaging and experimental procedures requiring immobilization, larvae were anesthetized with buffered tricaine methanesulfonate (MS-222; ethyl 3-aminobenzoate methanesulfonate salt) at a working concentration of 0.016% (w/v)

until loss of response to tactile stimulation. At the experimental endpoint, euthanasia was performed by immersion in an overdose of buffered tricaine solution (≥0.2% w/v) for an appropriate exposure time to ensure irreversible cessation of opercular movement and cardiac activity, in accordance with established zebrafish welfare guidelines and international recommendations for the use of laboratory animals.

5.3.25 UVA radiation of zebrafish embryos

Zebrafish embryos were exposed to UVA radiation at a dose of 366 mJ/cm^2 for 10 minutes. Briefly, the incubation medium was removed, and the zebrafish embryos were rinsed with fresh embryo medium. Then, the zebrafish embryos were plated in different multiwells according to the type of assay, covered with sufficient embryo medium with CSS extracts (50 µg/mL) and exposed to UVA.

5.3.26 Morphology of zebrafish embryos after exposure to treatment

Embryos were placed in 96-well culture plates (one embryo/well, 10 wells/group) at 3 dpf. Embryos were exposed to CSS extracts (50 µg/mL) and UVA irradiation. Embryo morphology and survival rates were observed 24 h after treatment using a miscroscope (SZX7, Olympus).

Microscopic images were used to determine the yolk area (in mm^2) of each group. Ten zebrafish from each group were measured, and the experiment was repeated three times.

5.3.27 Estimation of intracellular ROS generation and imaging

Generation of ROS production in zebrafish embryos was assessed using an oxidation-sensitive fluorescent probe dye, DCFH-DA.

At 3 dpf, embryos were plated in a 96-well multiwell (one embryo/well, 10 wells/group) and treated with CSS extracts (50 µg/mL), and 1 h later, the plate was irradiated with UVA.

After irradiation with UVA, the embryos were treated with DCFH-DA (10 µM), after which the plates were incubated for 30 min in the dark at 28.5 °C.

After incubation, embryos were rinsed in embryo medium and anesthetized with tricaine (1/20 dilution; 5 min) before visualization.

The fluorescence intensity (excitation/emission 485 nm/535 nm) of individual embryos was quantified with a Perkin-Elmer LS-5B spectrofluorometer.

The stained embryos were observed under a fluorescence microscope to determine representative images (N ≥ 5).

5.3.28 Determination of melanin content and tyrosinase activity

For the determination of melanin content, 90 zebrafish embryos, at 3 dpf, were plated in 6-well plates per group. The embryos were treated with CSS extracts (50 µg/mL) and 1 h later, were irradiated with UVA irradiation for 10 min. After 24 h from the treatment, embryos were sonicated in cold lysis buffer (20 mM sodium phosphate pH 6.8, 1% Triton X-100, 1 mM PMSF, 1 mM EDTA) containing protease inhibitors cocktail. An aliquot of the lysate was used to determine the protein content with a BCA assay. The lysate was clarified by centrifugation at 10,000 × g for 10 min.

After protein quantification, 250 µg of total protein was transferred into a 96-well plate, and 5 mM L-DOPA was added. The control contained lysis buffer and 5 mM L-DOPA. After incubation for 1 h at 37°C, absorbance was measured at 490 nm. The absorbance of the blank sample was subtracted from each absorbance value, and the final activity was expressed as a percentage of that of the water-exposed control group. Instead, the melanin precipitation was then resuspended with 1 mL of 1 N NaOH/20% DMSO at 95 °C for 1 h.

Spectrophotometric absorbance of intracellular melanin content was measured at 490 nm. The data were normalized to the total protein content of the embryo lysates.

5.3.29 Labile iron, lipid ROS detection and imaging

To detect ferroptosis in zebrafish larvae, labile iron (II) ions and lipid ROS were assessed using FerroOrange (1 µM) and C11 BODIPY 581/591 (10 µM), as previously described.

At 3 dpf, embryos were plated in a 96-well multiwell (one embryo/well, 10 wells/group) and treated with CSS extracts (50 µg/mL), and 1 h later, the plate was

irradiated with UVA. After irradiation with UVA, the embryos were treated with probes, after which the plates were incubated for 30 min in the dark at 28.5 °C. After incubation, embryos were rinsed in embryo medium and anesthetized with tricaine (1/20 dilution; 5 min) before visualization.

The representative images were acquired using a ZOE Fluorescent Cell Imaging System (Magnification, 20×. N ≥ 5. Scale bar: 100 µm). The fluorescence intensity of individual embryos was quantified with PerkinElmer EnSpire multimode plate reader.

5.3.30 Hematoxylin and eosin (H&E) staining

Larvae were euthanized and subsequently fixed in 4% paraformaldehyde, dehydrated, cleared, embedded in paraffin wax and sectioned down completely into serial 4 mm thick sagittal sections and stained with Haematoxylin and Eosin for morphology. Approximately 10 slides were produced from each larva for microscopic analysis. After staining with hematoxylin and eosin (H&E), all sections were scanned and analysed using a Pannoramic ScanScope (3DHistech),

Histopathological changes such as skeletal deformities, muscle cell degeneration, swelling and edematous changes in pericardium and yolk sac, eye lesions and impaired differentiation and other possible morphological changes in treatment groups were determined, evaluated and compared to the control group.

5.3.31 In vivo thioflavin staining

Larvae were euthanized and subsequently fixed in 4% paraformaldehyde, dehydrated, cleared, embedded in paraffin wax and sectioned down completely into serial 4 mm thick sagittal sections and stained with Thioflavn T (20 µM).

Approximately 10 slides were produced from each larva for microscopic analysis. Quantitative analyses were performed reading the fluorescence signals (excitation/emission 450 nm/482 nm) using a PerkinElmer EnSpire multimode plate reader. Images were acquired on a laser scanning confocal microscope (TCS SP8; Leica MicroSystems) equipped with a plan Apo 20X, NA 1.4 air objective lens (N ≥ 5).

5.3.32 Statistical analysis

The data are reported as mean ± SD of results from three independent experiments. Statistical analysis was performed using an analysis of variance test (ANOVA), and multiple comparisons were made with the Bonferroni's test with GraphPad Prism 8.0 software (San Diego, CA, USA).

Significance was assumed at $p < 0.05$.

5.4 Results and discussion

5.4.1 Qualitative profiles of CSS extracts

The melanoidin content obtained through the ultrafiltration technique was 1338.33 ± 52.99 mg/g CSS DW, while the permeate fraction contained 4236.67 ± 75.22 mg/g CSS DW.

A total of 45 peaks were annotated as belonging to various metabolite classes, including hydroxycinnamic acids, diterpenoids, fatty acids, alkaloids, and phenolic acids glucosides, along with other tentatively identified compounds. **Table S5.1** presents the complete spectral data for the identified peaks in the coffee silver skin total water extract.

Four alkaloids were identified: trigonelline (**1**), theophylline (**5**), theobromine (**6** and **8**), and caffeine (**10**). Caffeine was detected in positive ion mode at *m/z* 195 for $[M + H]^+$, generating a fragment ion at *m/z* 138 due to the loss of methyl isocyanate (*m/z* 57). Trigonelline was detected at *m/z* 138 for $[M + H]^+$, with a fragment ion at *m/z* 93 corresponding to a methyl pyridinium ion. Both theophylline and theobromine were detected at *m/z* 181 for $[M + H]^+$, with MS/MS fragment ions at *m/z* 163, 138, and 137.

Among phenolic acid the most representative class involved was hydroxycinnamic acid derivatives.

The main identified compounds was 3-*O*-feruloylquinic acid (*m/z* 367, $[M-H]^-$). The MS/MS fragmentation typically results in a loss of quinic acid (*m/z* 191), yielding a predominant fragment at *m/z* 193, corresponding to the ferulic acid moiety. Further

fragmentation leads to a product ion at *m/z* 134 associated with the cleavage of the feruloyl residue (Panuesa *et al.*, 2017).

Also, 5-*O*-caffeoylquinic acid (*m/z* 353, $[M-H]^-$) was tentatively identified. This compound undergoes a characteristic loss of 162 Da, forming a fragment ion at *m/z* 191, which is a marker of quinic acid-containing derivatives. Further fragmentation results in ions at *m/z* 179, corresponding to caffeic acid, and at *m/z* 135, derived from the cleavage of the catechol moiety (Yulianti *et al.,* 2023).

Caffeic acid (*m/z* 179, $[M-H]^-$) and *p*-coumaric acid (*m/z* 164, $[M-H]^-$) showed a similar fragmentation pattern, mainly driven by the loss of CO_2 (-44 Da), generating a fragment ion at *m/z* 135, which corresponds to the catechol cation, and at *m/z* 119, which corresponds to the styrene-like cation, respectively.

3,5-di-*O*-caffeoylquinic acid was identified at *m/z* 515, $[M-H]^-$. The fragmentation of dicaffeoylquinic acid typically proceeds via the sequential loss of one or both caffeoyl groups (-162 Da each), generating fragment ions at *m/z* 353 (mono-caffeoylquinic acid) and *m/z* 191 (quinic acid). Additional fragmentation results in ions at *m/z* 179 (caffeic acid) and *m/z* 135 (catechol-derived ion) (Yulianti *et al.*, 2023).

3-*O*-feruloyl-4-*O*-caffeoylquinic acid was identified as peak **29**, with a precursor ion at *m/z* 529 $[M-H]^-$. The fragmentation pattern is more complex due to its two ester linkages: one between ferulic acid and quinic acid, and the other between caffeic acid and quinic acid. Upon ionization, the molecule may first undergo the loss of ferulic acid (-178 Da), forming a fragment ion at m/z 351, which corresponds to a caffeoyl-quinic acid derivative. Another major fragmentation pathway involves the loss of caffeic acid (-180 Da), generating a fragment ion at m/z 349, which was tentatively identified as 3-*O*-feruloylquinic acid residue. Further fragmentation produced ions at *m/z* 191, corresponding to quinic acid, and additional fragments at *m/z* 179 and *m/z* 135, both of which represent forms of caffeic acid or other minor cleavage products. These fragmentation patterns help confirm the presence of both caffeoyl and feruloyl groups attached to the quinic acid backbone (El-Hawary *et al.*, 2022).

The fragmentation of caffeoyl tyrosine (*m/z* 342, $[M-H]^-$) primarily occurs through the breaking of the ester bond between caffeic acid and tyrosine. The most significant fragmentation ion is produced by the loss of caffeic acid (-178 Da), leading to the formation of a fragment ion at *m/z* 164 (Clifford and Knight, 2004).

Matrix-assisted laser desorption/ionization (MALDI) was carried out to determine the degree of ionization of high molecular weight (HMW) compounds and time of flight mass spectrometry (ToF-MS) allows for the determination of their exact molecular masses. The mass spectra of the CSS extracts are shown in (**Figure 5.3**). CSS melanoidins-rich fraction exhibit polymer pattern in *m/z* regions between m/z 1200–2000 (**Figure 5.3 B**), not registered in <10kDa fraction (polyphenols-rich fraction) (**Figure 5.3 A**). Additionally, the average mass differences between the adjacent peaks were *m/z* 58, characteristic of polymers with the repeated units (or isomers) (**Figure 5.3 C**).

As previously described by Mohsin *et al.* (Mohsin *et al.,* 2018) melanoidins exhibited polymer patterns with different m/z 58, and the intermediate was presumed to be glyoxal.

The intensity of peak signal reached its maximum at 1528 *m/z* and showed an apparent Gaussian distribution with reduced peak signals on both sides.

A

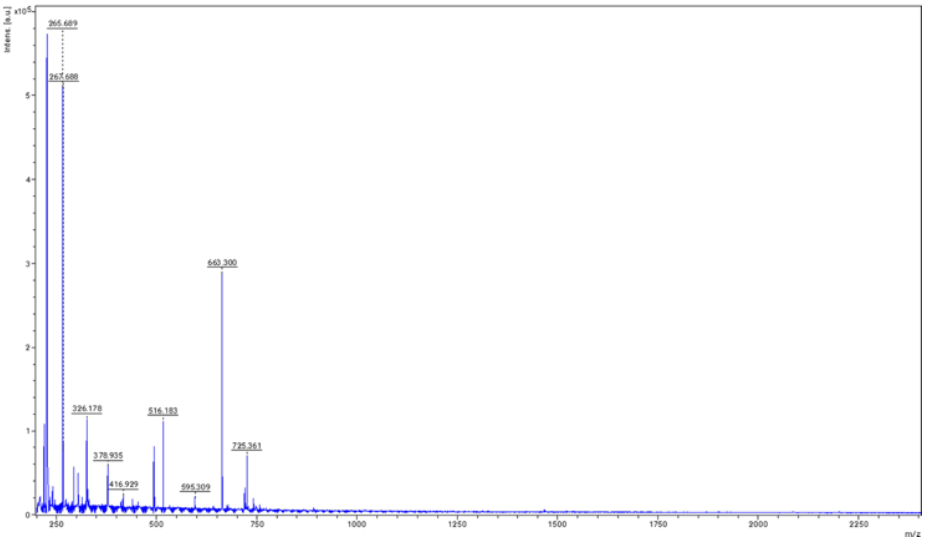
265.689
267.688
660.300
326.178
516.183
725.361
378.935
416.929
695.309
m/z

B

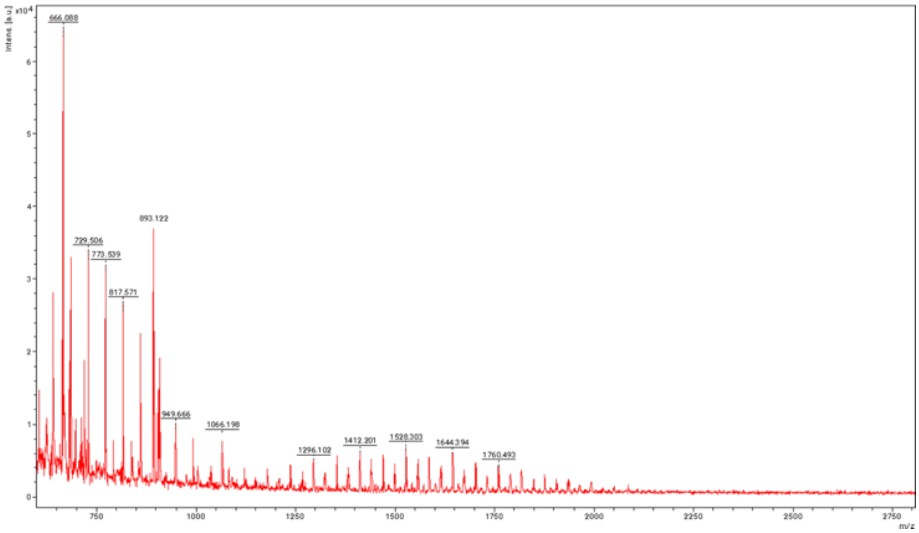
666.088
893.122
729.506
773.539
817.571
969.666
1066.198
1296.102
1412.201
1528.303
1644.394
1760.493
m/z

C

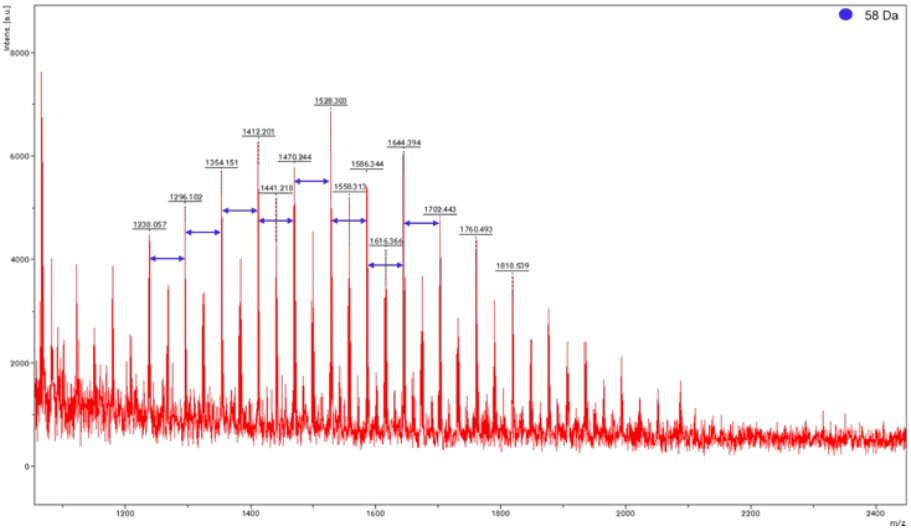
58 Da
1528.303
1412.201
1644.394
1354.151
1470.244
1586.344
1441.218
1558.313
1296.102
1702.443
1238.057
1760.493
1616.366
1818.539
m/z

***Figure 5.3**. MALDI-TOF mass spectrum of CSS phenols-rich (**A**) and melanoidins-rich (**B**) fractions using HCCA as matrix. The mass difference of 58 Da between neighboring peaks is observed in melanoidins-rich fraction (**C**).*

5.4.2 Inhibition of tyrosinase activity

Considering the copper chelating activity of CSS extracts, were evaluated for their potential to inhibit tyrosinase. A mushroom tyrosinase inhibitory test is the most frequently used method for determining the potential skin-protective activity of natural compounds and plant extracts (Zolghadri *et al.*, 2029).

Tyrosinase is a copper-dependent enzyme involved in the phenolic oxidation of L-tyrosine to L-DOPA (monophenolase activity) and the conversion of L-DOPA to L-dopaquinone (diphenolase activity).

The tyrosinase inhibition activity of each CSS sample was tested at concentrations of 100 µg/mL. The monophenolase tyrosinase inhibition activity from Tl and Ml samples was found to be 56.67 ± 0.43% ($p < 0.001$ vs. Ctrl) and 76.33 ± 0.14% ($p < 0.001$ vs. Ctrl; $p < 0.05$ vs. K. acid), respectively.

Meanwhile, the diphenolase tyrosinase inhibition activity for the same samples was 35.87 ± 0.56% ($p < 0.01$ vs. Ctrl) and 60.19 ± 0.21% ($p < 0.001$ vs. Ctrl; $p < 0.05$ vs. Kojic acid), respectively. All values were comparable to the positive control kojic acid (**Figure 5.4 C**).

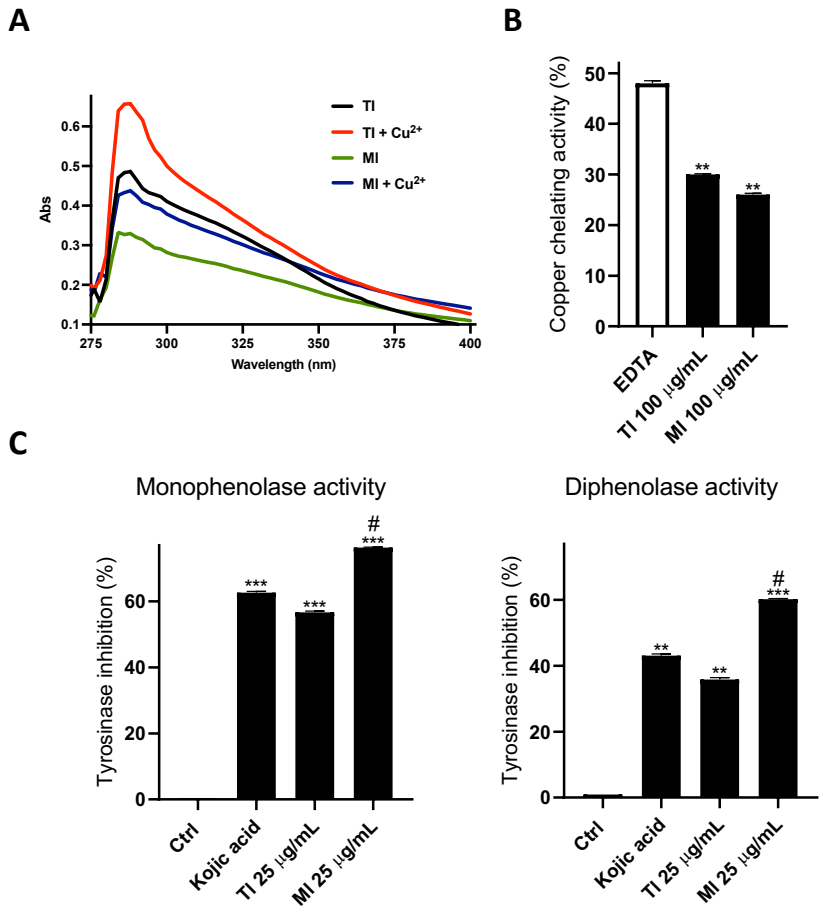

***Figure 5.4**. Bioactive effects of CSS extracts. (**A**) Spectrophotometric assay for copper chelation activity. (**B**) Quantitative analysis of copper chelation. (**C**) Inhibitory activity of extracts on tyrosinase.*
Data are shown as mean ± SD of three different experiments performed in triplicate.
***, *** denote respectively $p < 0.01$ and $p < 0.001$ vs. Ctrl. # denotes $p < 0.05$ vs. kojic acid.*

5.4.3 In-Cell UVA-cytoprotection

The protective activity of CSS extracts was then evaluated in HaCaT cells.

First, the extracts were analysed to assess their effect on cell viability. Experimental results showed that CSS extracts (6-50 µg/mL) did not cause a decrease in cell viability in the tested cell line (**Figure S5.1 A**).

Subsequently, the protective effects of CSS extracts on cell viability in UVA-irradiated HaCaT cells were measured. In the absence of CSS extracts, UVA-irradiated cells showed a reduction in cell viability ($p < 0.01$ vs. Ctrl), while with the extracts, particularly at 25 µg/mL, cell viability increased (Tl: $p < 0.01$ vs. UVA; Ml: $p < 0.01$ vs. UVA) (**Figure 5.5 A**).

Accordingly, with MTT assay, the cells treated with CSS extracts before UVA treatment showed a significant reduction in LDH release (UVA: $p < 0.001$ vs. Ctrl; Tl: $p < 0.01$ vs. UVA; Ml: $p < 0.05$ vs. UVA) (**Figure 5.5 B**).

The increase in LDH release into the extracellular medium, following UVA treatment, compared to the control, is indicative of a loss of plasma membrane integrity and, consequently, of cellular damage consistent with necrosis.

This result was supported by Annexin V-FITC/PI staining, FACS analysis showed that UVA irradiation of HaCaT cells induced a significant increase in PI-positive cells (UVA: $p < 0.001$ vs. Ctrl). In contrast, after Tl and Ml treatment, a reduction in necrotic rate was determined (Tl: $p < 0.01$ vs. UVA; Ml: $p < 0.05$ vs. UVA) suggesting a protective effect against UVA-induced necrosis (**Figures 5.5 C, D**).

At this point, western blot analyses were conducted to corroborate the protective effects against cell death. Specifically, p53 and PARP, two key markes of DNA damage and repair, were analyzed. As shown in **Figure 5.5 E**, UVA treatment led to the activation of elevated levels of p53 ($p < 0.01$ vs. Ctrl) and evident PARP cleavage ($p < 0.001$ vs. Ctrl) only in cells exposed to UVA radiation, consistent with DNA damage and oxidative stress.

However, treatment with both extracts reversed their expression patterns, restoring levels comparable to that observable in the control group (p53: Tl: $p < 0.01$ vs. UVA; Ml: $p < 0.01$ vs. UVA; PARP: Tl: $p < 0.001$ vs. UVA; Ml: $p < 0.001$ vs. UVA) (**Figures 5.5 E, F**).

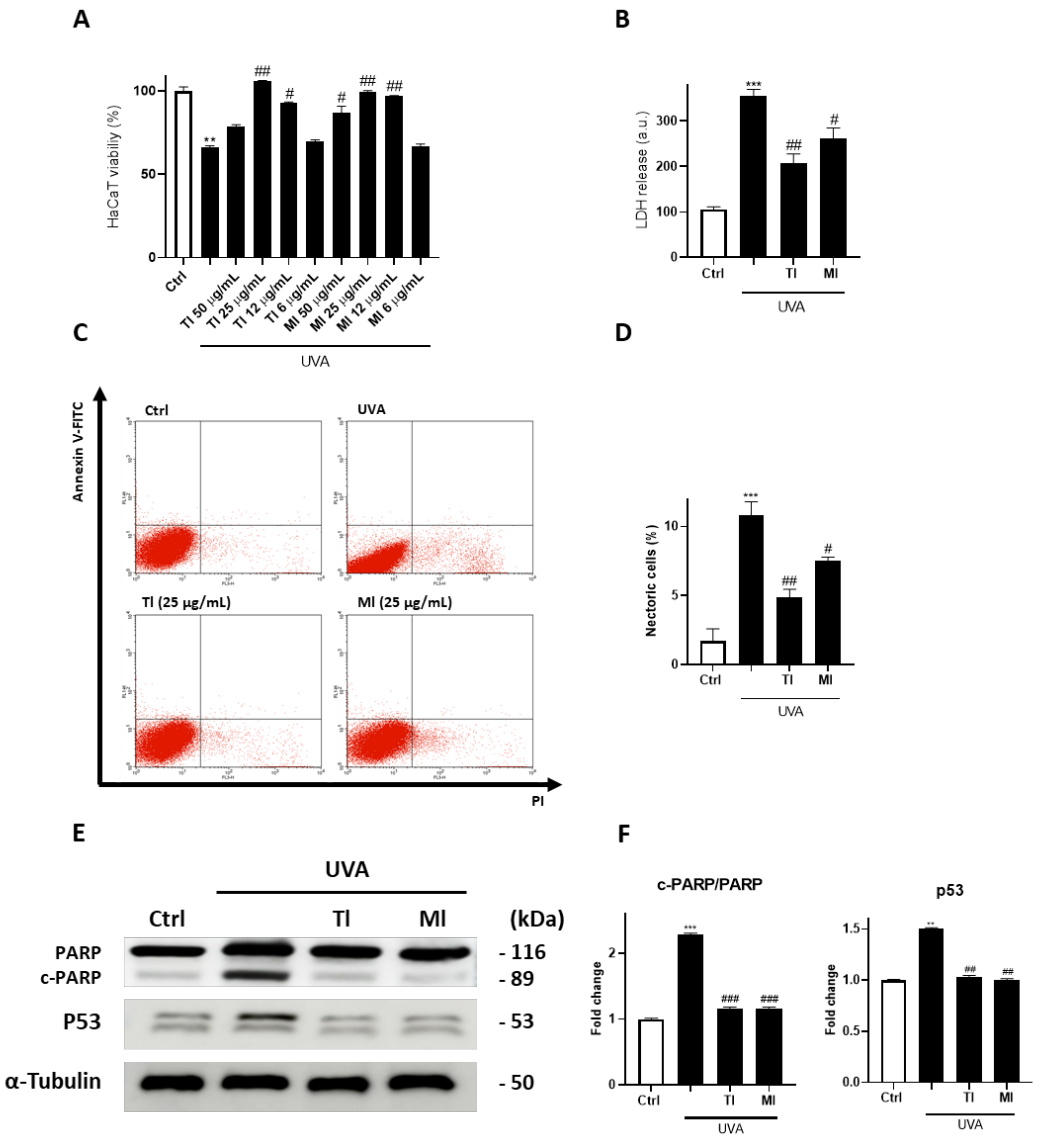

Figure 5.5. *Cytoprotective activity of CSS extracts against UVA-induced cell death. (**A**) MTT assay. (**B**) LDH release. (**C**) Representative images of HaCaT cells stained with Annexin-V-FITC/PI, to detect apoptosis and necrosis. (**D**) Quantitative analysis of cytofluorimetric analysis. (**E**) Western blot of p53 and PARP with corresponding densitometric analysis (**F**). Data are shown as mean ± SD of three different experiments performed in triplicate.*
***, *** denote respectively p < 0.01 and p < 0.001 vs. Ctrl.*
#, ##, ### denote respectively p < 0.05, p < 0.01 and p < 0.001 vs. UVA.

5.4.4 Antioxidant activity and ER stress protection

UVA irradiation is a potent inducer of ROS and RNS, which play a crucial role in modulating cell death. Therefore, the removal of excess reactive species or the suppression of their generation by antioxidants can be effective in preventing UVA-induced cellular damage.

For this reason, the antioxidant activity of CSS extracts in cells was evaluated. By using the probes DCFH and DAF, it was found that both extracts significantly reduced reactive oxygen (UVA: $p < 0.001$ vs. Ctrl; Tl: $p < 0.01$ vs. UVA; Ml: $p < 0.05$ vs. UVA) (**Figures 5.6 A, B**) and nitrogen species (UVA: $p < 0.001$ vs. Ctrl; Tl: $p < 0.001$ vs. UVA; Ml: $p < 0.01$ vs. UVA) (**Figures 5.6 C, D**) generated by UVA irradiation.

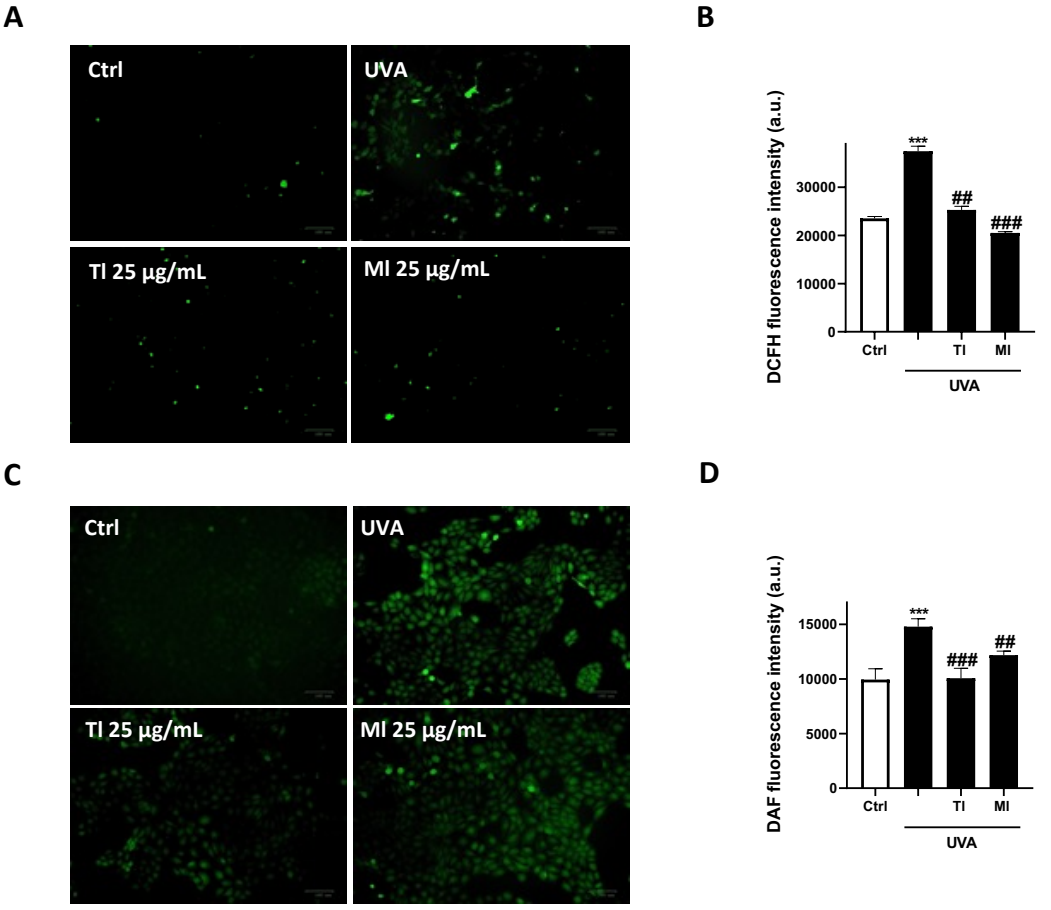

Figure 5.6. *Protective in vitro activity of Tl and Ml CSS extracts against UVA-induced oxidative stress. (**A**) Representative images of HaCaT cells stained with DCFH-DA to detect ROS production. (**B**) Quantitative analysis of ROS production. (**C**) Representative images of HaCaT cells stained with DAF-FM-DA to detect NO production. (**D**) Quantitative analysis of NO production. (Magnification, 20x. N ≥ 10. Scale bars: 100 µm).*
Data are shown as mean ± SD of three different experiments performed in triplicate.
, **, * denote respectively p < 0.05, p < 0.01 and p < 0.001 vs. Ctrl.*
#, ##, ### denote respectively p < 0.05, p < 0.01 and p < 0.001 vs. UVA.

To corroborate these data, the presence and activity of three main antioxidant targets, GSH, GST and GPx, was assessed (**Figures 5.7 A, B, C**).

The groups treated with UVA irradiation showed a significant reduction in GSH content ($p < 0.001$ vs. Ctrl), GST activity ($p < 0.01$ vs. Ctrl) and GPx activity ($p < 0.01$ vs. Ctrl).

However, when treated with CSS extracts, there was a significant increase (GSH content: Tl, $p < 0.001$ vs. UVA; Ml, $p < 0.01$ vs. UVA. GST activity: Tl, $p < 0.01$ vs. UVA; Ml, $p < 0.05$ vs. UVA. GPx activity: Tl, $p < 0.01$ vs. UVA; Ml, $p < 0.05$ vs. UVA) compared to the UVA, indicating that the extracts have potential antioxidant properties by inducing antioxidant response to protect cells from oxidative stress.

Multiple damages, such as UVA rays, can induce oxidative stress, disrupting ER homeostasis and leading to protein misfolding, which in turn activates the unfolded protein response and may result in different forms of cell death (McGrath *et al*., 2021).

Through ThT staining (Beriault *et al.*, 2013), was investigated whether CSS could provide protection against protein misfolding caused by UV radiation.

As illustrated in **Figures 5.7 D, E**, UVA-irradiated cells exhibit a high ThT fluorescence compared to control (UVA: $p < 0.001$ vs. Ctrl), indicating severe and maladaptive ER stress. In contrast, treatment with both CSS extracts markedly reduces protein misfolding (Tl: $p < 0.001$ vs. UVA; Ml: $p < 0.001$ vs. UVA) highlighting their ability in alleviating ER stress.

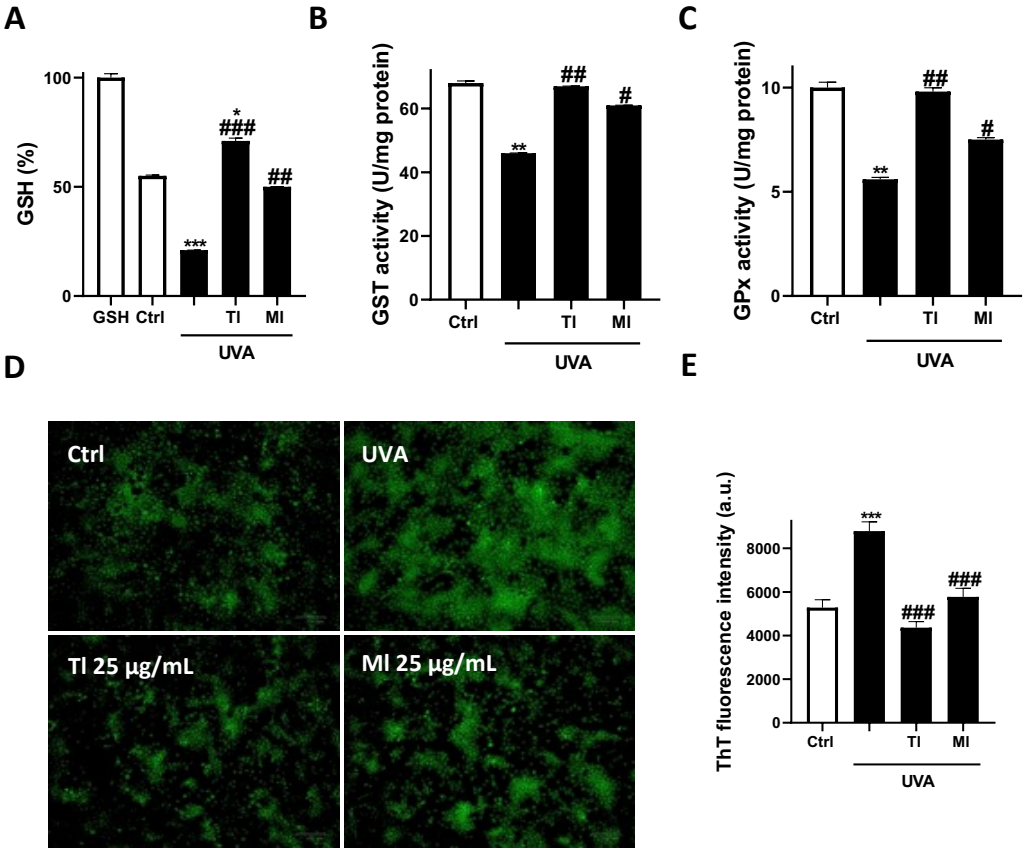

***Figure 5.7**. Protective in vitro activity of Tl and Ml CSS extracts against UVA-induced oxidative and ER stress. Determination of HaCaT GSH content (**A**), GST activity (**B**) and GPx activity (**C**). (**D**) Representative images of HaCaT cells stained with Thioflavin T (ThT) to detect misfolding protein production. (**E**) Quantitative analysis of misfolding protein production. (Magnification, 20×. N ≥ 10. Scale bar: 100 µm).*
Data are shown as mean ± SD of three different experiments performed in triplicate.
, **, * denote respectively $p < 0.05$, $p < 0.01$ and $p < 0.001$ vs. Ctrl.*
#, ##, ### denote respectively $p < 0.05$, $p < 0.01$ and $p < 0.001$ vs. UVA.

5.4.5 Molecular analysis of CSS extracts antioxidant mechanism

To further investigate the molecular mechanisms underlying the antioxidant effects of CSS extracts observed in previous experiments, was examined the activation of the Nrf2/HO-1 pathway.

Western blot analysis (**Figure 5.8 A**) showed that both extracts upregulated Nrf2 and HO-1 protein expression, with Tl eliciting a stronger effect than Ml, a trend confirmed by densitometric analysis (Tl: Nrf2: $p < 0.01$ vs. UVA; HO-1: $p < 0.01$ vs. UVA. Ml: HO-1: $p < 0.05$ vs. UVA) (**Figure 5.8 B**).

These results indicate that CSS extracts enhance cellular antioxidant defenses that are otherwise impaired by UVA exposure.

Confocal microscopy with z-stack projections (**Figure 5.8 C**) showed enhanced nuclear translocation of Nrf2 upon Tl treatment ($p < 0.001$ vs. UVA), with Ml having a moderate effect ($p < 0.01$ vs. UVA).

On the other hand, UVA alone reduced Nrf2 nuclear localization ($p < 0.01$ vs. Ctrl), whereas pre-treatment with CSS extracts restored it, Tl being the most effective. Quantitative analysis of the confocal images corroborated these findings (**Figure 5.8 D**). Importantly, the Nrf2 pathway is closely linked to ER stress signaling via PERK.

Previous ThT-based evaluation demonstrated that CSS extracts reduce deleterious ER stress by decreasing protein misfolding. This suggests that PERK activation may play a crucial role in mediating Nrf2 nuclear translocation and, at least in part, in driving the antioxidant effects of CSS extracts.

Overall, these results indicate that CSS extracts may exert antioxidant activity not only by upregulating Nrf2/HO-1 but also potentially via modulation of ER stress-PERK signaling, providing a mechanistic link between ER homeostasis and the activation of cellular antioxidant defenses.

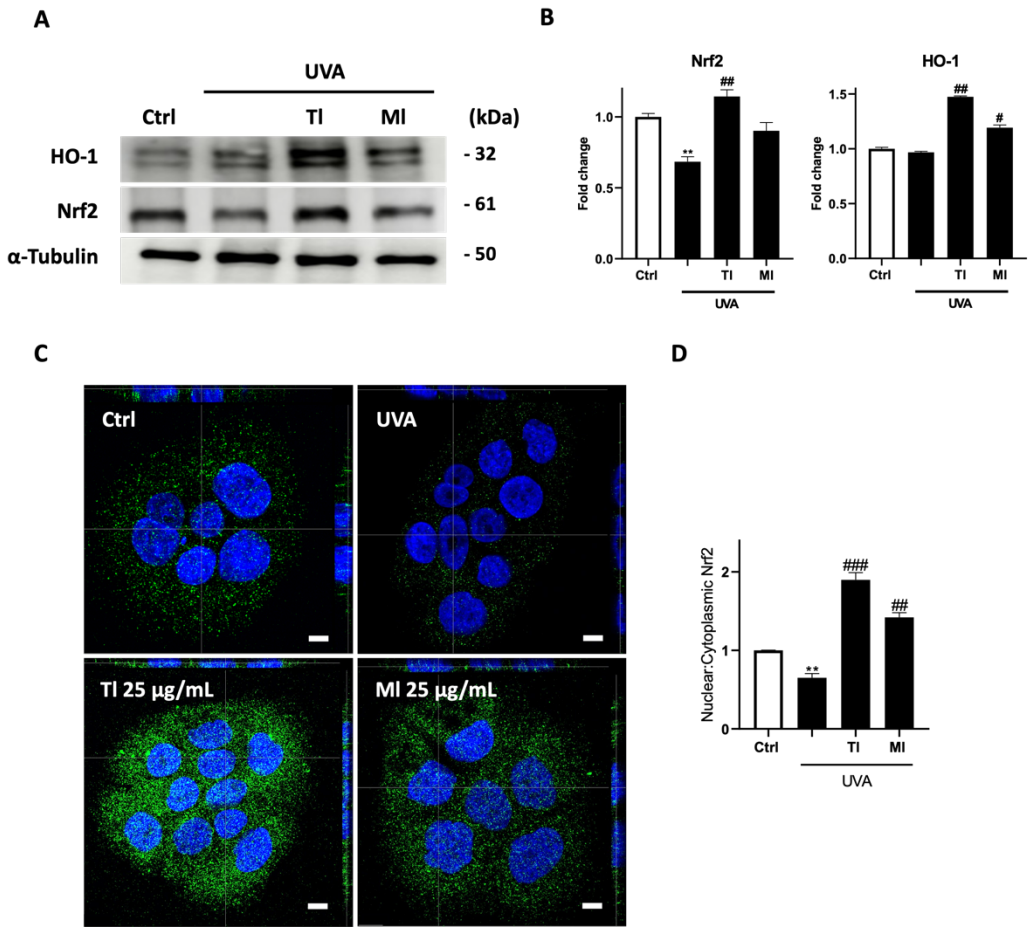

Figure 5.8. *Antioxidant proteins modulated by Tl and Ml CSS extracts against UVA-induced oxidative stress. (**A**) Western blot of Nrf2 and HO-1 with corresponding densitometric analysis (**B**). (**C**) Representative images from a confocal z-stack with orthogonal side-views of HaCaT cells. (**D**) Quantitative analysis of nuclear/cytoplasmic ratios of Nrf2 staining calculated as described in methods section (Magnification, 63×. N ≥ 10. Scale bar: 10 µm).*
Data are shown as mean ± SD of three different experiments performed in triplicate.
**, ** denote respectively $p < 0.05$ and $p < 0.01$ vs. Ctrl.*
##, ### denote respectively $p < 0.01$ and $p < 0.001$ vs. UVA.

Based on the previously described results, was investigated whether Nrf2 activation may be functionally linked to the PERK signaling pathway.

Therefore, MTT assay was performed using the selective PERK inhibitor GSK2606414 (GSK), in combination with CSS extracts and UVA irradiation.

Unlike the CSS protective effects observed in the absence of the inhibitor, co-treatment with GSK led to a significant reduction in mitochondrial activity for both Tl + GSK (Tl + GSK: $p < 0.01$ vs. Tl) and Ml + GSK (Ml + GSK: $p < 0.01$ vs. Ml) extracts compared to Tl and Ml alone (**Figure 5.9 A**).

Furthermore, these co-administration of CSS extracts with GSK are even lower than those observed with UVA treatment alone (UVA: $p < 0.001$ vs. Ctrl) (**Figure 5.9 A**). The cell metabolic activity observed with combined UVA and GSK treatment (UVA + GSK: $p < 0.001$ vs. Ctrl) was akin to UVA, because probably the cellular stress induced by UVA is already saturated, so PERK inhibition does not further affect cell mitochondrial metabolism under these conditions (**Figure 5.9 A**).

A similar trend emerged from LDH release assays, reflecting the cytotoxicity results. Specifically, LDH levels increased in Tl + GSK ($p < 0.001$ vs. Tl) compared to Tl ($p < 0.01$ vs. UVA), and Ml + GSK ($p < 0.01$ vs. Ml) to Ml ($p < 0.01$ vs. UVA) (**Figure 5.9 B**). Furthermore, unlike the MTT results, in this case GSK + UVA induced a significantly higher LDH release compared to UVA alone ($p < 0.05$ vs. UVA) (**Figure 5.9 B**).

Collectively, these findings suggest that the cytoprotective effects of CSS extracts strictly depend on an intact PERK pathway.

While UVA stress alone already triggers a basal PERK response that partially sustains cell survival, pharmacological inhibition of PERK not only abolishes the protective activity of CSS but even exacerbates cell damage, resulting in lower mitochondrial activity and higher cytotoxicity than UVA alone.

This indicates that CSS extracts fine-tune ER stress, attenuating its harmful, maladaptive aspects while maintaining a controlled activation of PERK sufficient to drive Nrf2-mediated antioxidant responses. Therefore, PERK emerges as a critical upstream regulator required for the beneficial effects of CSS under oxidative stress conditions.

To further investigate the involvement of PERK pathway, we performed real-time PCR analyses of BiP, PERK, and ATF4, as well as the antioxidant genes catalase and GPX, both regulated by Nrf2. Gene expression was evaluated at 4- and 24-hours post-treatment.

At 4 h, BiP, PERK and ATF4 expression levels increased in UVA-treated cells (BiP: $p < 0.001$ vs. Ctrl; PERK: $p < 0.01$ vs. Ctrl; ATF4: $p < 0.01$ vs. Ctrl) compared to untreated ones, consistent with the expected early activation of the UPR in response to UVA-induced ER stress. On the other hand, keratinocytes co-treated with CSS extracts displayed no significant induction of these genes compared to control, indicating an

early protective effect of the extracts (Tl + UVA: BiP: $p < 0.001$ vs. UVA; PERK: $p < 0.05$ vs. UVA. Ml + UVA: BiP: $p < 0.01$ vs. UVA; PERK: $p < 0.05$ vs. UVA) (**Figure 5.9 C "4h"**).

At 24 h, this divergence became even more pronounced, considering that both genes displayed an even greater expression in the UVA group (BiP: $p < 0.001$ vs. Ctrl; PERK: $p < 0.001$ vs. Ctrl; ATF4: $p < 0.05$ vs. Ctrl), while their expression remained consistently reduced under co-treatment with CSS extracts (Tl + UVA: BiP: $p < 0.001$ vs. UVA; PERK: $p < 0.001$ vs. UVA; ATF4: $p < 0.05$ vs. UVA. Ml + UVA: BiP: $p < 0.001$ vs. UVA; PERK: $p < 0.001$ vs. UVA; ATF4: $p < 0.05$ vs. UVA), thereby highlighting the protective effect of the extracts (**Figure 5.9 D "24 h"**).

To confirm the involvement of PERK in this regulatory mechanism, the same experimental setup was repeated in the presence of the PERK inhibitor GSK.

In this case, at 4 h BiP expression is significantly more increased in the UVA + GSK group ($p < 0.001$ vs. Ctrl), probably as a compensatory response to PERK inhibition, whereas in the CSS + UVA groups, BiP expression remained still reduced (Tl: $p < 0.001$ vs. UVA; Ml: $p < 0.001$ vs. UVA) (**Figure 5.9 C "4h + GSK"**).

At 24 h, BiP levels showed general attenuation across all conditions; as expected, given its stronger protective effect, the Tl + UVA group displayed the most pronounced reduction in BiP expression compared to UVA-treated cells ($p < 0.05$ vs. UVA) (**Figure 5.9 "24h + GSK"**).

In contrast, PERK expression was effectively suppressed by GSK treatment at both timepoints, confirming the inhibitor's efficacy (**Figure 5.9 C "4h + GSK"**).

This supported the hypothesis that PERK was initially activated as part of a protective response. In the presence of CSS extracts, the reduced cellular stress likely allowed for a timely resolution of the PERK-mediated signaling, leading to its downregulation at 24 h. In contrast, under UVA alone, the persistent stress maintained PERK activation over time.

Next, we evaluated the expression of the transcription factor ATF4, a key downstream effector of the PERK pathway that can mediate both adaptive and pro-death responses depending on the cellular context. At 4 h, ATF4 expression was already elevated in the UVA + GSK group ($p < 0.01$ vs. Ctrl), despite PERK inhibition (**Figure 5.9 C "4h + GSK"**).

This early induction is likely due to alternative kinases of the integrated stress response (e.g., GCN2, PKR, HRI) that also converge on eIF2α phosphorylation (Ryoo, 2024), in line with the concomitant increase of BiP observed under these conditions. At 24 h, ATF4 expression was markedly high in UVA + GSK ($p < 0.05$ vs. Ctrl), indicating that, when PERK signaling is blocked, prolonged ATF4 activation becomes part of a maladaptive stress program. A similar trend was observed with CSS + UVA + GSK, where ATF4 levels were further increased (UVA: $p < 0.05$ vs. Ctrl; Tl: $p < 0.05$ vs. UVA), in contrast to the reduction observed without the inhibitor (**Figure 5.9 D "24h + GSK"**). These results suggest that CSS extracts, unable to restore PERK activity under GSK inhibition, cannot prevent the sustained ATF4 induction, which in this context likely contributes to enhanced cytotoxicity rather than protection.

Finally, the expression of the antioxidant genes catalase (CAT) and GPx was assessed.

At 4 h, both genes were upregulated in the UVA + CSS extract groups (Tl: $p < 0.05$ vs. UVA; Ml: $p < 0.05$ vs. UVA) compared to UVA alone, where levels remained similar to control (**Figure 5.9 C "4 h"**).

While GPX expression remained elevated at 24 h in the CSS-treated groups (Tl: $p < 0.05$ vs. UVA; Ml: $p < 0.05$ vs. UVA), CAT expression declined and showed no significant differences among treatment groups at this timepoint (**Figure 5.9 D "24 h"**). This transient CAT induction may reflect an early adaptive response to oxidative stress that is downregulated at later timepoints (Valerio *et al.*, 2021), possibly due to feedback regulation or the temporal specificity of catalase expression in response to UVA-induced ROS.

In the presence of the PERK inhibitor GSK, CAT expression was downregulated at both 4 h and 24 h across all treatment conditions, indicating a strong dependence on PERK-Nrf2 signaling for its transcriptional regulation. Conversely, GPx expression displayed a more variable response: in the Tl + UVA + GSK group, GPx levels were reduced at 4 h compared to UVA alone (UVA: $p < 0.01$ vs. Ctrl; Tl: $p < 0.01$ vs. UVA) (**Figure 5.9 C "4h + GSK"**) but increased again at 24 h (Tl: $p < 0.05$ vs. UVA) (**Figure 5.9 D "24h + GSK"**).

This delayed upregulation may suggest that GPx is less strictly dependent on PERK activation than CAT, and that Tl extract is capable of promoting GPx expression over time, possibly through alternative signaling pathways or through delayed Nrf2 activation that becomes effective once the initial impact of PERK inhibition is overcome.

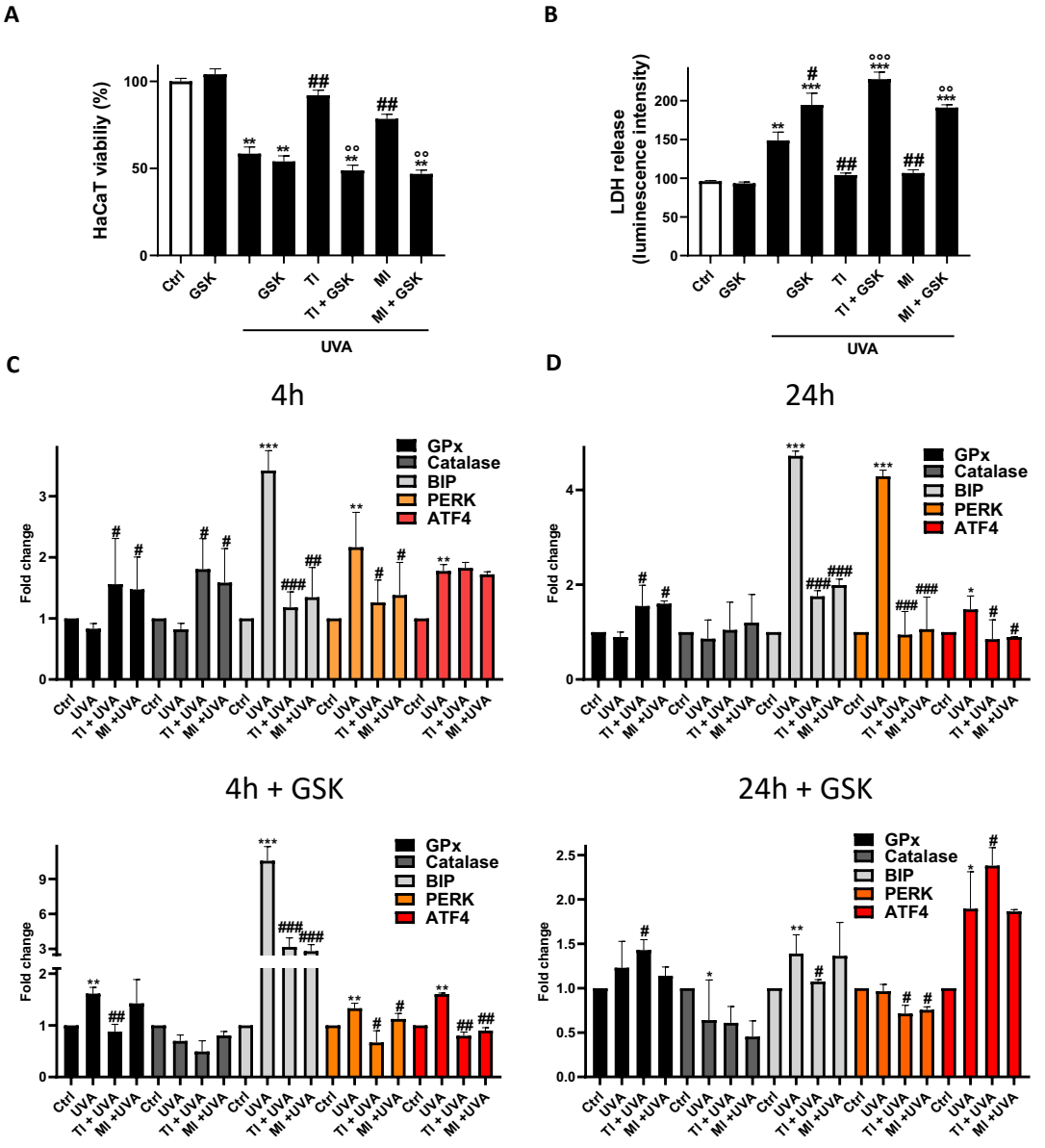

Figure 5.9. *Molecular mechanism of CSS extracts against UVA-induced oxidative stress. (**A**) MTT assay. (**B**) LDH release. (**C**) Gene expression fold change at 4 h post-treatment (RT-qPCR). (**D**) Gene expression fold change at 24 h post-treatment (RT-qPCR).*
Data are shown as mean ± SD of three different experiments performed in triplicate.
, **, * denote respectively p < 0.05, p < 0.01 and p < 0.001 vs. Ctrl.*
#, ##, ### denote respectively p < 0.05, p < 0.01 and p < 0.001 vs. UVA.

°°, °°° denote respectively p < 0.01 and p < 0.001 vs extracts (Tl or Ml in presence of UVA).

5.4.6 Protective role of CSS extracts against ferroptosis triggered by UVA radiation

Ferroptosis is a form of regulated, iron-dependent cell death characterized by excessive lipid peroxidation (Yu *et al.*, 2021) and the overexposure to UVA radiation can induce ferroptosis in skin cells through the accumulation of ROS (Yi *et al.*, 2023). Considering the antioxidant power of CSS extracts and the known anti-ferroptotic role of Nrf2, it was evaluated whether they could mitigate this process, assessing intracellular levels of Fe^{2+} labile iron.

The results showed that treatment with CSS extracts (Tl: $p < 0.001$ vs. UVA; Ml: $p < 0.001$ vs. UVA) led to a significant reduction in fluorescence compared to the UVA-irradiated group ($p < 0.001$ vs. Ctrl), indicating a decrease in intracellular Fe^{2+} levels (**Figures 5.19 A, B**).

The same assay was performed in the presence of GSK and using ferrostatin-1 as a positive control for ferroptosis inhibition.

Under these conditions, while ferrostatin-1 effectively reduced UVA-induced Fe^{2+} accumulation, co-treatment with the extracts and GSK under UVA exposure increased intracellular iron levels, comparable to UVA treatment, confirming the crucial role of PERK in the antioxidant response and counteracting ferroptosis (**Figure S5.1 B**).

Malondialdehyde (MDA) is a well-established marker of ferroptosis, a form of cell death characterized by iron-dependent lipid peroxidation (Chen *et al.*, 2024). Therefore, MDA accumulation was measured as an additional indicator of ferroptotic activity. Consistent with previous findings, treatment with CSS extracts significantly reduced MDA levels (Tl: $p < 0.001$ vs. UVA; Ml: $p < 0.001$ vs. UVA) compared to UVA alone (UVA: $p < 0.01$ vs. Ctrl) (**Figure 5.10 C**). The lipid peroxidation assay was also performed in the presence of the GSK and ferrostatin-1, confirming the same trend observed previously for the Fe^{2+} labile iron (**Figure S5.1 C**).

Furthermore, to confirm the involvement of lipid peroxidation in UVA-induced stress, C11-BODIPY fluorescent probe was employed to specifically detect oxidized

phospholipids within cellular membranes, a hallmark of ferroptotic cell death (Wiernicki *et al.*, 2020).

After exposure to UVA rays, a marked increase in lipid peroxidation was observed, as indicated by the shift in C11-BODIPY fluorescence. Treatment with CSS extracts significantly attenuated this oxidative change, suggesting effective inhibition of lipid peroxidation (UVA: $p < 0.001$ vs. Ctrl; Tl: $p < 0.001$ vs. UVA; Ml: $p < 0.001$ vs. UVA) (**Figures 5.10 D, E**). In line with previous tests, the protective effect of the extracts was lost when cells were co-treated with GSK under UVA irradiation.

In contrast, ferrostatin-1 effectively prevented lipid oxidation, confirming the activation of ferroptosis in our model (**Figure S5.1 D**). These results further confirm that CSS extracts mitigate ferroptosis by reducing lipid peroxidation and that this effect depends, at least in part, on the activation of the PERK pathway.

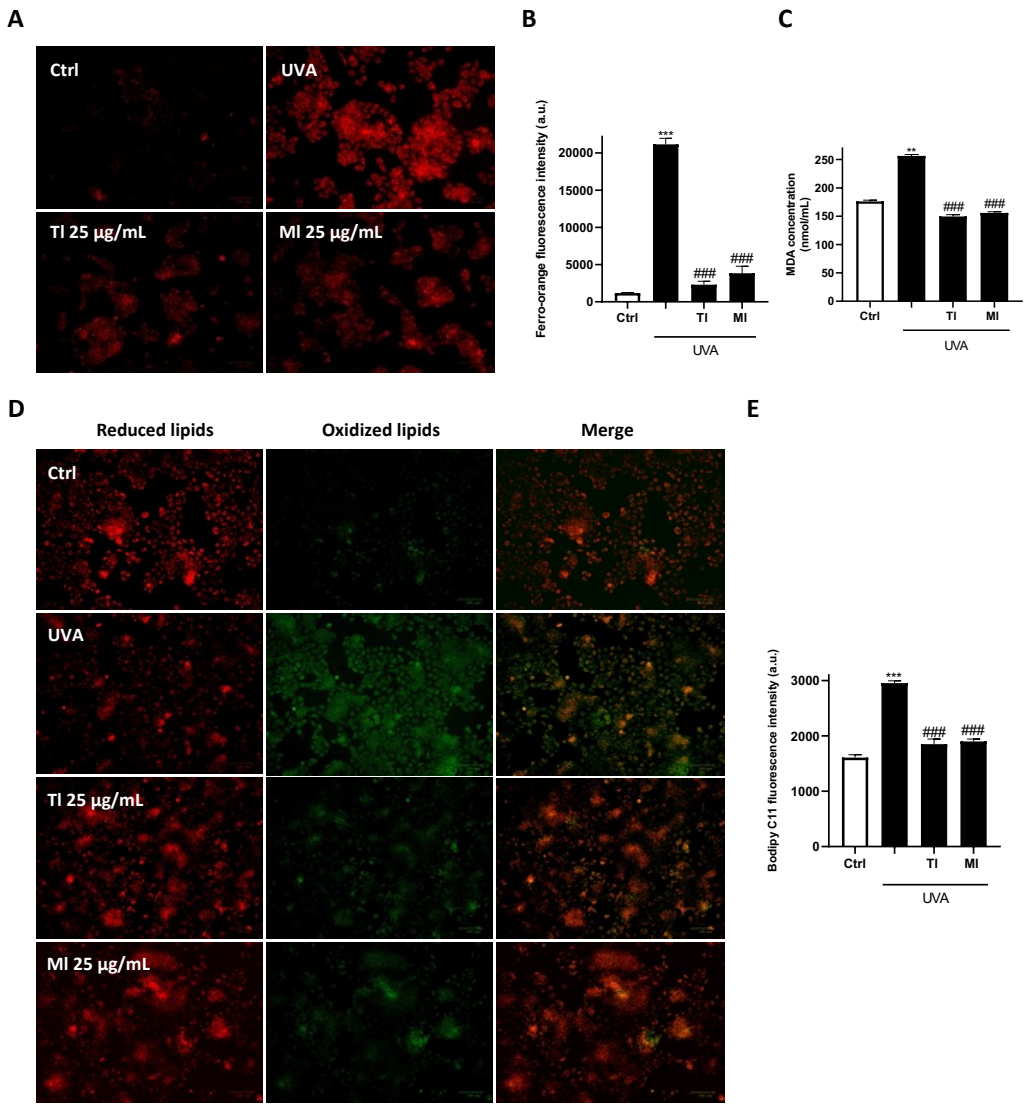

Figure 5.10. *Protection from UVA-induced ferroptosis by CSS extracts. (**A**) Representative images of HaCaT cells stained with FerroOrange to detect intracellular Fe^{2+} levels. (**B**) Quantification of FerroOrange fluorescence. (**C**) Malondialdehyde (MDA) levels as a marker of lipid peroxidation. (**D**) Representative images of HaCaT cells stained with C11 BODIPY to detect lipid ROS. (**E**) Quantification of C11 BODIPY fluorescence. (Magnification, 20×. N ≥ 10. Scale bars: 100 µm).*
Data are shown as mean ± SD of three different experiments performed in triplicate.
, **, * denote respectively $p < 0.05$, $p < 0.01$ and $p < 0.001$ vs. Ctrl.*
#, ##, ### denote respectively $p < 0.05$, $p < 0.01$ and $p < 0.001$ vs. UVA.

5.4.7 In vivo protective effects against UVA-induced photodamage

To further validate the protective effects of CSS extracts in vivo, was employed the zebrafish model, which represents a widely used system for studying melanogenesis, photodamage, and drug screening thanks to its genetic similarity

to humans, transparent embryos, and rapid development (Wang *et al.*, 2023; Issac *et al.*, 2021).

The *in vivo* photoprotective role of CSS was therefore evaluated in zebrafish exposed to UVA irradiation. As shown in **Figure 5.11**, UVA irradiation significantly induced morphological alterations of yolk sac and melanin accumulation, as well as intracellular ROS generation.

However, CSS Tl and Ml (50 µg/mL) remarkably restored the size of the yolk sac extracts (Tl: $p < 0.01$ vs. UVA; Ml: $p < 0.01$ vs. UVA) (**Figures 5.11 A**, **B**), an indicator of malabsorption (Sant et al., 2028; Kalasekar et al., 2015), reduced intracellular ROS level (Tl: $p < 0.01$ vs. UVA; Ml: $p < 0.05$ vs. UVA) (**Figures 5.11 A, C**), melanin accumulation (Tl: $p < 0.001$ vs. UVA; Ml: $p < 0.01$ vs. UVA) (**Figure 5.11 D**), and tyrosinase activity (Tl: $p < 0.05$ vs. Ctrl; Ml: $p < 0.05$ vs. Ctrl) (**Figure 5.11 E**) in accordance with *in vitro* studies.

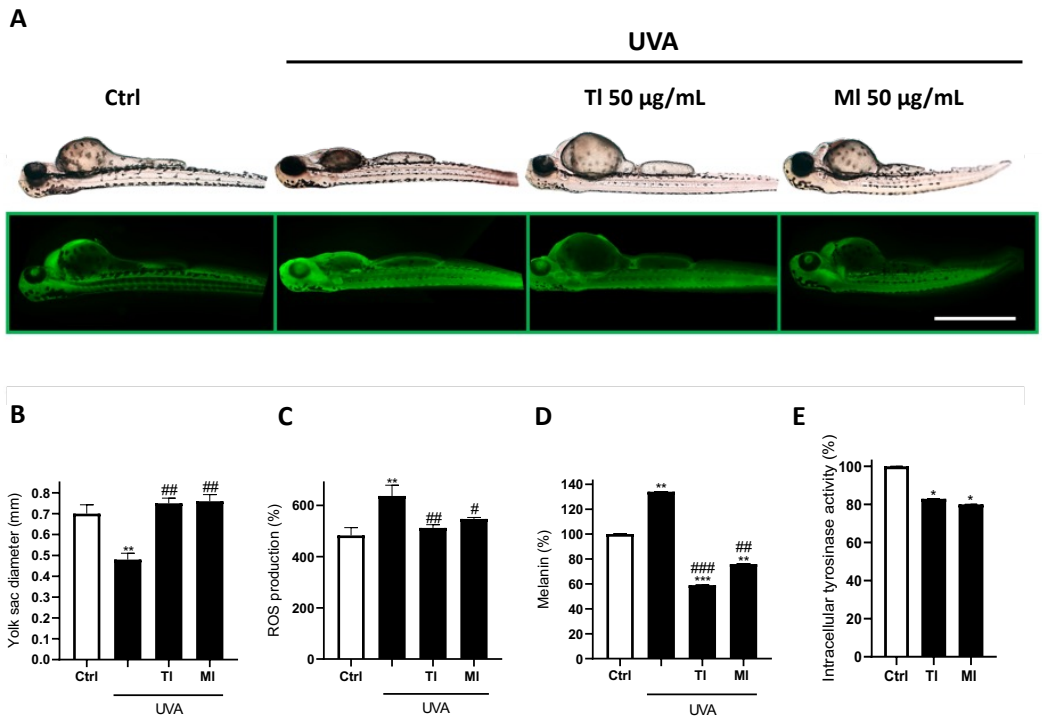

Figure 5.11. *Protective in vivo activity of Tl and Ml CSS extracts against UVA-induced photodamage. Representative images of 72 hpf zebrafish fish larvae in phase contrast (**A**) and stained with DCFH-DA (**B**). Quantitative analysis of (**B**) yolk sac diameter, (**C**) ROS production, (**D**) melanin content, (**E**) intracellular tyrosinase activity. Scale bars: 1 mm. N ≥ 5. Data are shown as mean ± SD of three different experiments performed in triplicate.*
, **, * denote respectively p < 0.05, p < 0.01 and p < 0.001 vs. Ctrl.*

#, ##, ### denote respectively p < 0.05, p < 0.01 and p < 0.001 vs. UVA.

Since external morphology alone cannot reveal the full extent of cellular damage or its prevention, histopathological analysis with H&E staining was performed to characterize tissue-level changes and assess the protective effect of CSS more directly. Histopathological analysis of zebrafish larvae did not reveal any abnormalities in the control group (**Figure 5.12**). However, several lesions were observed in larvae exposed to UVA (**Figure 5.12**); the yolk sac was shrunken, shriveled, with a severe, and diffuse edema. Skeletal muscle fibers were disorganized, fragmented and multifocally shortened, angulated and degenerated with homogeneous, hypereosinophilic, hyalinized sarcoplasm and occasionally pyknotic nuclei. The eyes showed severe and diffuse loss of the normal retinal architecture with variation in thickness of the outer and inner nuclear layers, extensive loss and thinning of the outer plexiform layer, retinal detachment and a peripheral clear space consistent with severe edema surrounding eosinophilic fibrils (rods and cones). Tl and Ml larvae didn't show relevant pathologic alterations (**Figure 5.12**).

Collectively, these results indicate that CSS extracts have also strong positive effects on our zebrafish model corroborating its photoprotective effects.

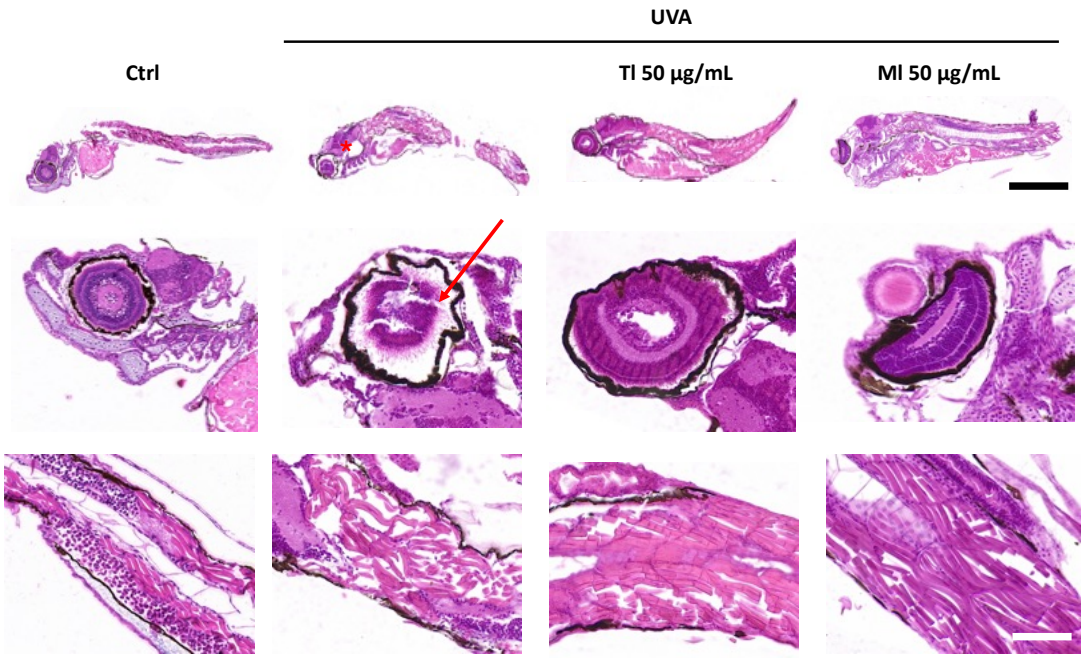

Figure 5.12. *Representative images of 72 hpf zebrafish fish larvae. In control group, histopathological analysis did not reveal relevant pathologic alterations. In UVA-exposed larvae, the yolk sac appeared shrunken, with a severe and diffuse edema (red asterisk). Retinal architecture was severely effaced with retinal detachment and a peripheral clear space consistent with severe edema surrounding eosinophilic fibrils (red arrow).*
Skeletal muscle fibers were disorganized, fragmented and degenerated. Tl and Ml larvae didn't show relevant pathologic alterations. Hematoxylin and Eosin staining. Scale bars: 100 mm.

To further investigate the underlying mechanism of CSS protection, it was evaluated the contribution of ER stress, previously identified *in vitro*.

For this purpose, zebrafish larval sections were subjected to ThT staining and analyzed by confocal microscopy to visualize protein misfolding (**Figure 5.13**). UVA exposure markedly increased ThT fluorescence (UVA: $p < 0.001$ vs. Ctrl), indicating enhanced protein misfolding, whereas both CSS extracts significantly reduced this signal (Tl: $p < 0.001$ vs. UVA; Ml: $p < 0.01$ vs. UVA).

The effect was particularly evident in Tl-treated larvae, confirming its stronger ability to counteract ER stress–associated protein aggregation *in vivo*. This evaluation highlights the relevance of ER stress modulation as a protective mechanism and supports the translational potential of CSS extracts in mitigating cellular damage under phototoxic conditions.

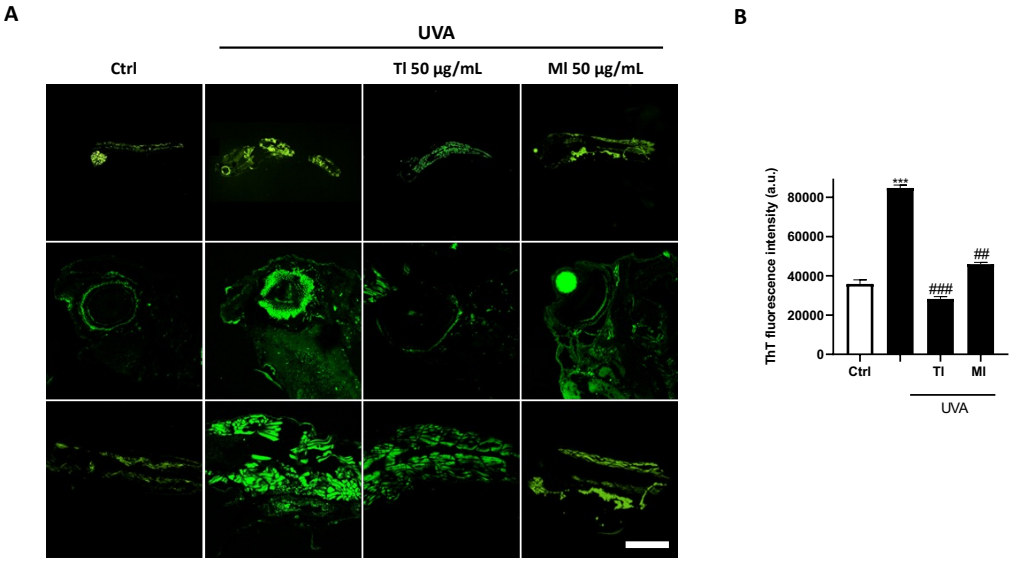

Figure 5.13*. Protective in vivo activity of Tl and Ml CSS extracts against UVA-induced ER stress. (**A**) ThT representative images of 72 hpf zebrafish fish larvae acquired by confocal microscopy. (**B**) Quantitative analysis of ThT staining. (Magnification, 40×. N≥5. Scale bars: 50 µm).*

Data are shown as mean ± SD of three different experiments performed in triplicate.
**** denotes p < 0.001 vs. Ctrl. ##, ### denote respectively p < 0.01 and p < 0.001 vs. UVA.*

Finally, the mechanism of CSS protection in vivo was deepened performing an evaluation of ferroptosis modulation, previously observed in vitro.

Zebrafish larvae were analyzed using FerroOrange to detect labile iron accumulation and BODIPY C11 to assess lipid peroxidation (**Figure 5.14**).

UVA exposure markedly increased both labile iron ($p < 0.001$ vs. Ctrl) and lipid ROS levels ($p < 0.001$ vs. Ctrl), whereas treatment with both CSS extracts significantly mitigated these effects (labile iron: Tl: $p < 0.001$ vs. UVA; Ml: $p < 0.001$ vs. UVA. Lipid ROS levels: Tl: $p < 0.01$ vs. UVA; Ml: $p < 0.01$ vs. UVA). These results suggest that the protective mechanisms identified *in vitro* are relevant in the whole organism and warrant further detailed investigation.

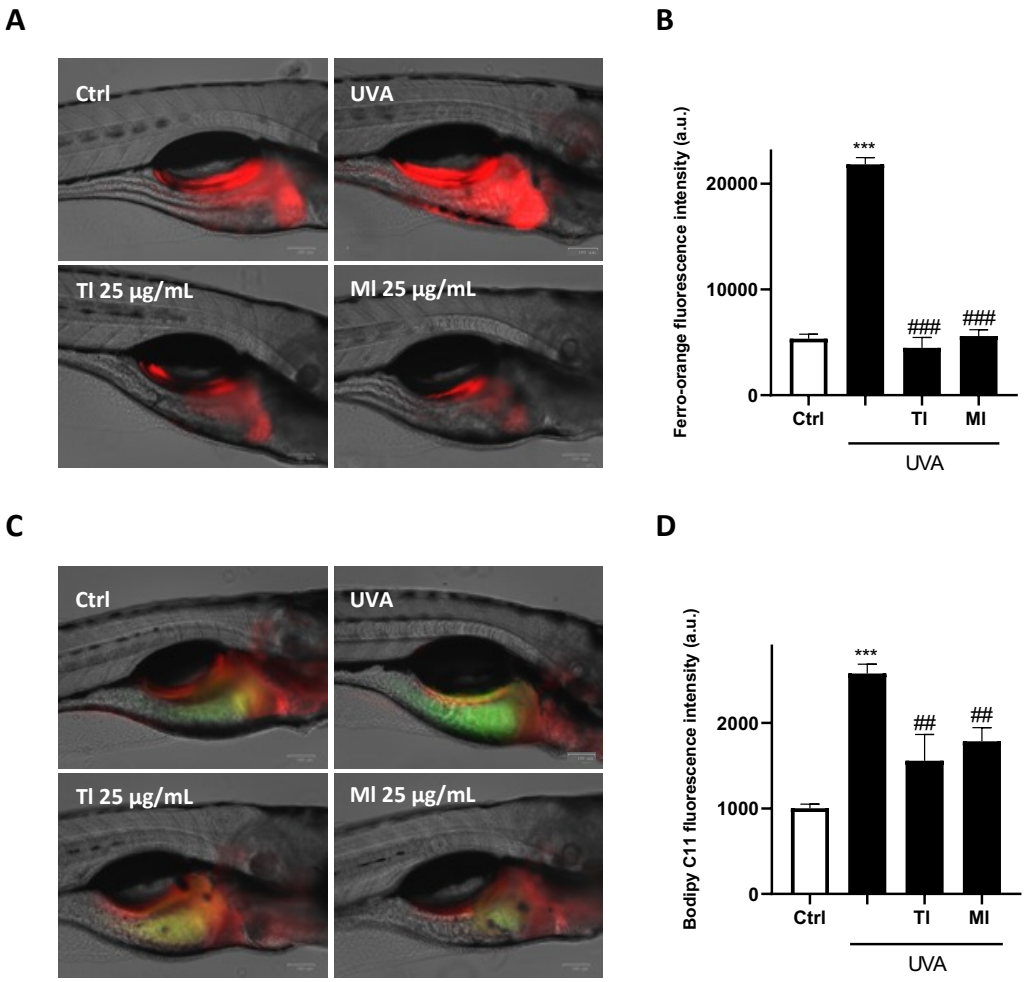

Figure 5.14. *In vivo protection from UVA-induced ferroptosis by CSS extracts. (**A**) Representative images of 72 hpf zebrafish fish larvae stained with FerroOrange to detect intracellular Fe^{2+} levels. (**B**) Quantification of FerroOrange fluorescence. (**C**) Representative images of 72 hpf zebrafish fish larvae stained with C11 BODIPY to detect lipid ROS. (**D**) Quantification of C11 BODIPY fluorescence (Magnification, 20×. N ≥ 5. Scale bars: 100 µm). Data are shown as mean ± SD of three different experiments performed in triplicate.*
**** denotes p < 0.001 vs. Ctrl. ##, ### denote respectively p < 0.01 and p < 0.001 vs. UVA.*

5.5 Conclusions

Natural substances are increasingly recognized for their potential as UV protectors, offering additional benefits that traditional sunscreens may not provide. Commercial sunscreen products featuring natural ingredients or plant extracts are gaining popularity due to their antioxidant, anti-inflammatory, and protective properties. Among these, the byproduct of coffee roasting CSS, stands out for its rich content of polyphenols and phenolic acids. CSS extracts were obtained using

microwave-assisted water-based extraction (MAE), a green technology that enables high yields in a short time while minimizing environmental impact.

CSS extracts have demonstrated promising properties as a UVA protector, showcasing their antioxidant potential as natural agents for skin protection. Through *in vitro* testing in a HaCaT cell model, the extract exhibited antioxidant activity, effectively mitigating oxidative stress and protecting cells against UVA-induced damage. Furthermore, this study provided new insight into the role of ER stress in UV-induced skin damage and to investigate how CSS extracts modulate this response. UVA exposure alone induced excessive ER stress that contributed to oxidative damage and ferroptotic cell death. In contrast, CSS extracts fine-tuned the ER stress response, promoting an adaptive, PERK-mediated activation that enhanced Nrf2-driven antioxidant gene expression and protected cells from ferroptosis. Pharmacological inhibition of PERK abolished these protective effects, confirming that the cytoprotective action of CSS depends on functional ER stress signaling. Their ability to guide ER stress toward a protective, adaptive response underscores the multifunctional mechanism of CSS. Enzymatic assays and *in vivo* testing in zebrafish confirmed its efficacy, inhibiting tyrosinase activity while preventing maladaptive ER stress and ferroptosis. These findings suggest that CSS could serve as a novel, sustainable ingredient in skincare formulations, with a multifaceted role aimed at combating UVA-induced skin damage and promoting overall skin health.

5.6 Supporting information

Table S5.1. *Tentative identification of secondary metabolites in coffee silver skin (CSS) extract using UHPLC-ESI-Orbitrap-MS/MS platform.*

Peak	Rt (min)	Name	m/z	MS2	Formula	Error (ppm)	Ion	Class	MSI level
1	0.77	Trigonelline	138.0547	68.8572; 78.2640; 94.0650	$C_7H_7NO_2$	0.73	[M+H]+1	Alkaloids	2
2	1.00	Isocitric Acid	191.0197	87.0089; 111.0089; 57.0347	$C_6H_8O_7$	-0.99	[M-H]-1	Carboxylic acids	2
3	2.09	Sucrose	341.1096	179.0558; 161.0461; 89.0245; 71.0140; 59.0139	$C_{12}H_{22}O_{11}$	1.49	[M-H]-1	Glycosyl compounds	2
4	2.75	Protocatechuic acid (2,6-Dihydroxybenoic acid)	153.0195	109.0296; 135.0455; 81.0346; 108.0218	$C_7H_6O_4$	0.89	[M-H]-1	Benzenoids	2
5	3.43	Theophylline	181.0719	134.0374;110.0714; 137.0826; 137.0250	$C_7H_8N_4O_2$	-0.95	[M+H]+1	Xanthines	2
6	3.78	Theobromine	181.0719	135.0804; 111.0804; 93.0698; 124.0505	$C_7H_8N_4O_2$	1.44	[M+H]+1	Xanthines	2
7	4.13	5-*O*-caffeoylquinic acid (chlorogenic acid)	353.0879	191.0552; 173.0458; 114,0196; 179.0354	$C_{16}H_{19}O_9$	2.34	[M-H]-1	Hydroxycinnamic acids	1
8	4.15	Theobromine (*isomer*)	181.0719	70.0651; 111.2830; 124.0505; 163.0865	$C_7H_8N_4O_2$	0.87	[M+H]+1	Xanthines	2
9	4.60	Caffeic acid	179.0351	135.0452;151.0400; 80.2994	$C_9H_8O_4$	0.24	[M-H]-1	Hydroxycinnamic acids	2
10	4.77	Caffeine	195.0874	138.0660; 110.0712; 123.0441; 82.7016	$C_8H_{10}N_4O_2$	0.73	[M+H]+1	Xanthines	1
11	4.79	3-*O*-feruloylquinic acid	367.1037	193.0509; 173.0458;	$C_{17}H_{20}O_9$	-0.99	[M-H]-1	Hydroxycinnamic acids	2

				93.0347; 349.2076					
12	4.82	Dihydroferulic acid 4-*O*-glucuronide	371.0985	191.0350; 147.0453; 137.0242; 209.0458; 59.0138	$C_{16}H_{20}O_{10}$	1.28	[M-H]-1	Phenilpropanoids glucuronides	2
13	4.83	*N*-Feruloylglycine	250.0794	132.0303; 88.0405; 115.0038; 91.0553; 206.0823	$C_{12}H_{13}NO_5$	0.58	[M-H]-1	Amino acids, peptides, and analogues	2
14	4.84	5-*O*-caffeoylquinic acid (chlorogenic acid)	353.0879	191.0552; 173.0458; 114,0196; 135.0439	$C_{16}H_{19}O_9$	0.68	[M-H]-1	Hydroxycinnamic acids	1
15	4.86	Caffeic acid	179.0351	191.0351;151.0400;124.1919; 353.0878	$C_9H_8O_4$	0.58	[M-H]-1	Hydroxycinnamic acids	2
16	5.25	*N*-Feruloyl-L-aspartate	308.078	246.0777; 264.0888; 149.0609; 193.0506; 134.0376	$C_{14}H_{15}NO_7$	-1.19	[M-H]-1	Amino acids, peptides, and analogues	2
17	5.46	Caffeoylshikimic acid	335.0775	179.0354; 161.0246; 135.0456	$C_{16}H_{16}O_8$	-0.97	[M-H]-1	Hydroxycinnamic acids	2
18	5.50	3-*O*-feruloylquinic acid	367.1037	193.0509; 173.0458; 93.0347; 349.2068	$C_{17}H_{20}O_9$	-1.13	[M-H]-1	Hydroxycinnamic acids	2
19	5.56	4-*O*-feruloylquinic acid + 5-*O*-feruloylquinic acid	367.1037	191.05528; 173.0445; 349.2039; 93.0347;	$C_{17}H_{20}O_9$	0.27	[M-H]-1	Hydroxycinnamic acids	2
20	5.64	Dimethyl-caffeoylquinic acid	381.1193	207.0664; 173.0458; 163.0763	$C_{18}H_{22}O_9$	0.56	[M-H]-1	Hydroxycinnamic acids	2

21	5.83	Atractyligenin-*O*-hexoside	481.2444	319.1908; 301.1817; 59.0139; 89.0245	$C_{25}H_{38}O_9$	1.49	[M-H]-1	Diterpenoids	2
22	5.85	Caffeoyl tyrosine	342.0985	206.0464 ; 163.0403; 119.0505; 135.0453	$C_{18}H_{17}NO_6$	2.35	[M-H]-1	Amino acids, peptides, and analogues	2
23	5.88	3-sinapoyl-4 caffeoylquinic acid	559.2772	351.2178; 193.0510; 321.2076	$C_{27}H_{28}O_{13}$	0.79	[M-H]-1	Hydroxycinnamic acids	2
24	6.06	*N*-Coumaroyl-L-glutamate	292.1189	274.1084; 248.1285; 119.2333	$C_{14}H_{15}NO_6$	0.72	[M-H]-1	Amino acids, peptides, and analogues	2
25	6.12	Methyl-*O*-feruloyl quinic acid	381.1196	173.0456; 207.0663; 137.0250; 155.0347	$C_{18}H_{22}O_9$	-1.12	[M-H]-1	Hydroxycinnamic acids	2
26	6.19	3-dimethoxycinnamoyl quinic acid	381.1919	335.1865; 363.1797; 273.1872; 319.1917; 207.0665; 173.0461	$C_{18}H_{22}O_9$	0.74	[M-H]-1	Hydroxycinnamic acids	2
27	6.36	Carboxytractyligenin	363.1813	319.192	$C_{20}H_{28}O_6$	-1.14	[M-H]-1	Diterpenoids	2
28	6.42	3,5-*O*-dicaffeoylquinic acid	515.1199	173.0457; 179.0352; 135.0454; 353.0881; 191.0563	$C_{25}H_{23}O_{12}$	0.50	[M-H]-1	Hydroxycinnamic acids	2
29	6.65	3-*O*-Feruloyl-4-*O*-caffeoylquinic acid	529.1361	173.0457; 193.0509; 161.0243; 349.1189; 351.2181	$C_{26}H_{25}O_{12}$	0.73	[M-H]-1	Hydroxycinnamic acids	2
30	6.93	*N*-Caffeoyl tryptophan	365.1147	229.0620; 186.0563; 203.0827	$C_{20}H_{18}O_5N_2$	0.21	[M-H]-1	Amino acids, peptides, and analogues	2
31	7.02	Desoxyatractyligenin-O hexoside	727.3542	643.2977; 625.2871;	$C_{36}H_{56}O_{15}$	0.24	[M-H]-1	Diterpenoids	2

				481.2442; 113.0245				
32	7.20	Caffeoyl-dimethoxy cinnamoylquinic acid	543.1525	335.2231; 349.0931; 381.1208	$C_{27}H_{28}O_{12}$	0.72	[M-H]-1	Hydroxycinnamic acids	2
33	7.28	Atractyligenin + FA	365.1971	319.1920; 347.1869; 275.0928; 231.1031; 257.1917; 83.6236	$C_{19}H_{28}O_4$	1.58	[M-H+FA]-1	Diterpenoids	2
34	7.33	*p*-Coumaroyl-*N*-tryptophan	349.1189	229.0620; 186.0564; 142.0669;	$C_{20}H_{17}N_2O_4$	1.42	[M-H]-1	Amino acids, peptides, and analogues	2
35	7.44	Feruloyl tryptophan	379.1312	229.0617; 142.0661; 186.0563; 175.0402; 149.0610; 100.0041	$C_{21}H_{20}N_2O_5$	1.12	[M-H]-1	Amino acids, peptides, and analogues	2
36	7.60	Feruloyl-dimethoxycinnamoylquinic acid	557.1682	382.4771; 349.0915; 207.0663; 193.0506; 173.0457	$C_{28}H_{30}O_{12}$	0.27	[M-H]-1	Hydroxycinnamic acids	2
37	7.73	Unknown chlorogenic acid derivative	451.1638	173.0457; 275.1143; 349.0929	$C_{22}H_{28}O_{10}$	-0.96	[M-H]-1	Hydroxycinnamic acids	3
38	7.95	Trihydroxy-octadecaenoic acid	329.2336	139.1130; 171.1028; 311.2234; 229.1447; 293.2123	$C_{18}H_{34}O_5$	1.13	[M-H]-1	Fatty acids	2
39	9.02	Linoleic acid methylester	293.1768	236.1056; 221.1545; 59.0139	$C_{17}H_{26}O_4$	0.65	[M-H]-1	Fatty acid esters	2
40	10.60	Ceramide conjugate I	496.3396	184.0733; 478.3289; 104.1069	$C_{22}H_{48}O_6N_4P$	0.21	[M+H]+1	Sphingolipids	2

41	13.72	*p*-Coumaric acid	164.0471	119.9077 ; 89.9259 ;81.7428 ; 61.9885	$C_9H_9O_3$	1.12	[M-H]-1	Hydroxycinnamic acids	2
42	14.01	*N*-eicosanoyl hydroxytryptamide	471.3939	160.0756; 177.1021; 454.3681	$C_{30}H_{50}N_2O_2$	1.12	[M+H]+1	Fatty acids	2
43	14.21	Docosenamide	338.3413	303.3044; 321.3149; 97.1011	$C_{22}H_{43}NO$	2.34	[M+H]+1	Fatty amides	2
44	14.64	Hydroxy-docosanoic acid	355.3221	309.3166; 337.3119; 168.8907	$C_{22}H_{44}O_3$	0.84	[M-H]-1	Fatty acids	2
45	15.30	Hydroxy-tetracosanoic acid	383.3535	337.3483; 365.3433; 256.0236; 146.3402	$C_{24}H_{48}O_3$	-0.96	[M-H]-1	Fatty acids	2

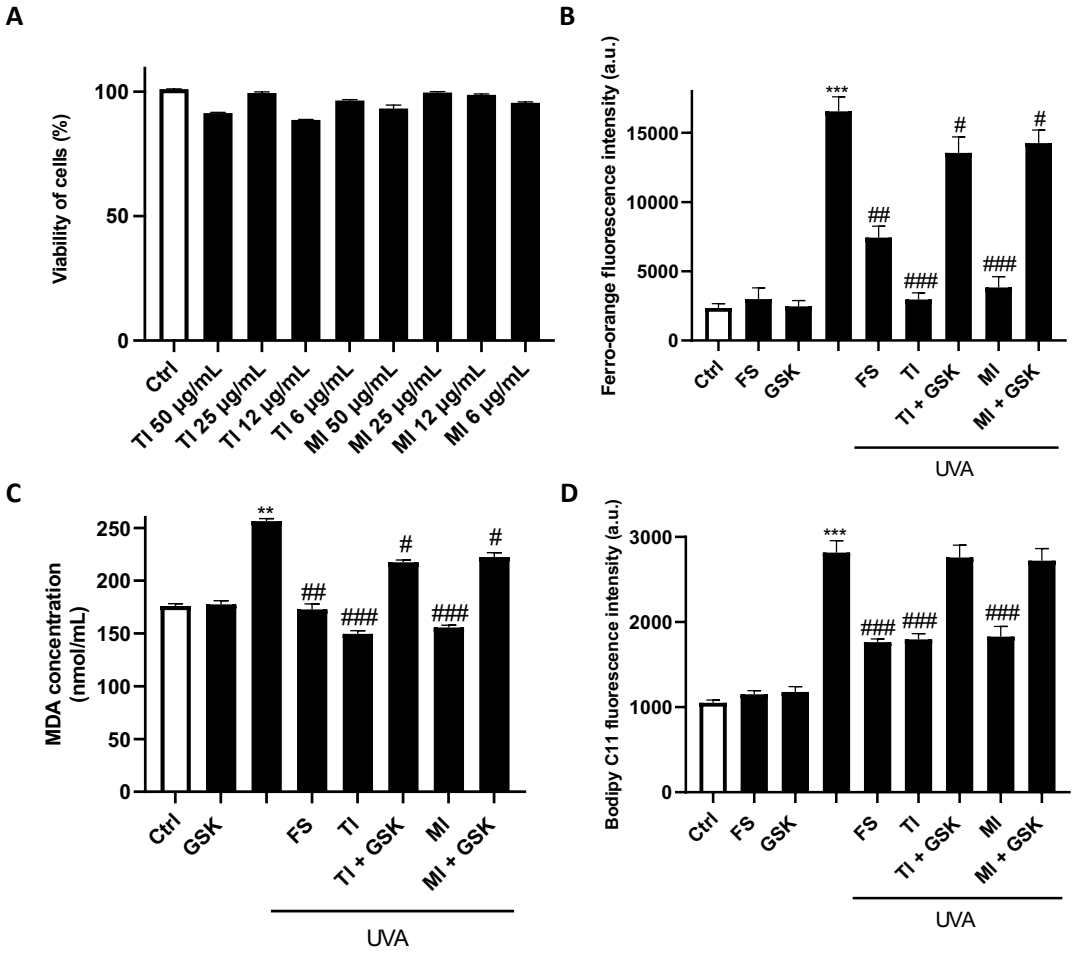

Figure S5.1. *(**A**) Cell viability was examined by the MTT assay. HaCaT cells were exposed to CN in the range of 6-50 µg/mL. (**B**) Quantification of FerroOrange fluorescence. (B) Malondialdehyde (MDA) levels as a marker of lipid peroxidation. (**C**) Quantification of C11 BODIPY fluorescence.*
Data are shown as mean ± SD of three different experiments performed in triplicate.
, **, * denote respectively p < 0.05, p < 0.01 and p < 0.001 vs. Ctrl.*
#, ##, ### denote respectively p < 0.05, p < 0.01 and p < 0.001 vs. UVA.

5.7 References

Agalou, A., Thrapsianiotis, M., Angelis, A., Papakyriakou, A., Skaltsounis, A.L., Aligiannis, N. and Beis, D. (2018). Identification of novel melanin synthesis inhibitors from *Crataegus pycnoloba* using an in vivo zebrafish phenotypic assay. *Frontiers in Pharmacology*, 9, 265.

Arteaga, C., Boix, N., Teixido, E., Marizande, F., Cadena, S. and Bustillos, A. (2021). The zebrafish embryo as a model to test protective effects of food antioxidant compounds. *Molecules*, 26, 5786.

Beriault, D.R. and Werstuck, G.H. (2013). Detection and quantification of endoplasmic reticulum stress in living cells using the fluorescent compound, Thioflavin T. *Biochimica et Biophysica Acta – Molecular Cell Research*, 1833, 2293–2301.

Bessada, S.M.F., Alves, R.C. and Oliveira, M.B.P.P. (2018). Coffee silverskin: A review on potential cosmetic applications. *Cosmetics*, 5, 5.

Borrella, I., Mataix, C. and Carrasco-Gallego, R. (2015). Smallholder farmers in the speciality coffee industry: Opportunities, constraints and the businesses that are making it possible. *IDS Bulletin*, 46, 29–44.

Briganti, S., Camera, E. and Picardo, M. (2003). Chemical and instrumental approaches to treat hyperpigmentation. *Pigment Cell Research*, 16, 101–110.

Chen, Z., Lin, H., Wang, X., Li, G., Liu, N., Zhang, M. and Shen, Y. (2024). The application of approaches in detecting ferroptosis. *Heliyon*, 10, e23507.

Chiang, H.M., Lin, T.J., Chiu, C.Y., Chang, C.W., Hsu, K.C., Fan, P.C. and Wen, K.C. (2011). *Coffea arabica* extract and its constituents prevent photoaging by suppressing MMPs expression and MAP kinase pathway. *Food and Chemical Toxicology*, 49, 309–318.

Clifford, M.N. and Knight, S. (2004). The cinnamoyl–amino acid conjugates of green robusta coffee beans. *Food Chemistry*, 87, 457–463.

Del Pozo, C., Rego, F., Yang, Y., Puy, N., Bartrolí, J., Fàbregas, E. and Bridgwater, A.V. (2019). Converting coffee silverskin to value-added products by a slow pyrolysis-based biorefinery process. *Journal of Analytical and Applied Pyrolysis*, 140, 143–154.

D'Mello, S.A., Finlay, G.J., Baguley, B.C. and Askarian-Amiri, M.E. (2016). Signaling pathways in melanogenesis. *International Journal of Molecular Sciences*, 17, 1144.

El-Hawary, E.A., Zayed, A., Laub, A., Modolo, L.V., Wessjohann, L. and Farag, M.A. (2022). How does LC/MS compare to UV in coffee authentication and determination of antioxidant effects? Brazilian and Middle Eastern coffee as case studies. *Antioxidants*, 11, 131.

Elias, M.L., Israeli, A.F. and Madan, R. (2023). Caffeine in skincare: Its role in skin cancer, sun protection and cosmetics. *Indian Journal of Dermatology*, 68, 546–550.

Fukushima, Y., Takahashi, Y., Hori, Y., Kishimoto, Y., Shiga, K., Tanaka, Y., Masunaga, E., Tani, M., Yokoyama, M. and Kondo, K. (2015). Skin photoprotection and consumption of coffee and polyphenols in healthy middle-aged Japanese females. *International Journal of Dermatology*, 54, 410–418.

Grabs, J. (2018). Assessing the institutionalization of private sustainability governance in a changing coffee sector. *Regional Studies, Regional Science*, 5, 335–353.

Herman, A. and Herman, A.P. (2013). Caffeine's mechanisms of action and its cosmetic use. *Skin Pharmacology and Physiology*, 26, 8–14.

Hoang-Minh, T., Le, T.L., Kasbohm, J. and Gieré, R. (2010). UV-protection characteristics of some clays. *Applied Clay Science*, 47, 349–357.

Hong, S.D., Yoon, D.Y., Lee, S., Han, S.B. and Kim, Y. (2014). Antimelanogenic chemicals with in vivo efficacy against skin pigmentation in guinea pigs. *Archives of Pharmacal Research*, 37, 1241–1251.

Iriondo-DeHond, A., Rodríguez Casas, A. and del Castillo, M.D. (2021). Interest of coffee melanoidins as sustainable healthier food ingredients. *Frontiers in Nutrition*, 8, 730343.

Issac, P.K., Guru, A., Velayutham, M., Pachaiappan, R., Arasu, M.V., Al-Dhabi, N.A., Choi, K.C., Harikrishnan, R. and Arockiaraj, J. (2021). Oxidative stress induced antioxidant and neurotoxicity demonstrated in vivo zebrafish embryo or larval model and their normalization due to morin showing therapeutic implications. *Life Sciences*, 283, 119864.

Juan-García, A., Caprioli, G., Sagratini, G., Mañes, J. and Juan, C. (2021). Coffee silverskin and spent coffee suitable as neuroprotectors against cell death by beauvericin and α-zearalenol: Evaluating strategies of treatment. *Toxins*, 13, 132.

Kalasekar, S.M., Zacharia, E., Kessler, N., Ducharme, N.A., Gustafsson, J.-Å., Kakadiaris, I.A. and Bondesson, M. (2015). Identification of environmental chemicals that induce yolk malabsorption in zebrafish using automated image segmentation. *Reproductive Toxicology*, 55, 20–29.

Kumar, K.J., Vani, M.G., Wang, S.Y., Liao, J.W., Hsu, L.S., Yang, H.L. and Hseu, Y.C. (2013). In vitro and in vivo studies disclosed the depigmenting effects of gallic acid: A novel skin lightening agent for hyperpigmentary skin diseases. *BioFactors*, 39, 259–270.

Lajis, A.F.B. (2018). A zebrafish embryo as an animal model for the treatment of hyperpigmentation in cosmetic dermatology medicine. *Medicina*, 54, 35.

Martuscelli, M., Esposito, L., Di Mattia, C.D., Ricci, A. and Mastrocola, D. (2021). Characterization of coffee silver skin as potential food-safe ingredient. *Foods*, 10, 1367.

McGrath, E.P., Centonze, F.G., Chevet, E., Avril, T. and Lafont, E. (2021). Death sentence: The tale of a fallen endoplasmic reticulum. *Biochimica et Biophysica Acta – Molecular Cell Research*, 1868, 119001.

Metro, D., Cernaro, V., Santoro, D., Papa, M., Buemi, M., Benvenga, S. and Manasseri, L. (2017). Beneficial effects of oral pure caffeine on oxidative stress. *Journal of Clinical and Translational Endocrinology*, 10, 22–27.

Milutinov, J., Pavlović, N., Ćirin, D., Atanacković Krstonošić, M. and Krstonošić, V. (2024). The potential of natural compounds in UV protection products. *Molecules*, 29, 5409.

Mohsin, G.F., Schmitt, F.-J., Kanzler, C., Epping, J.D., Flemig, S. and Hornemann, A. (2018). Structural characterization of melanoidin formed from d-glucose and l-alanine at different temperatures applying FTIR, NMR, EPR and MALDI-ToF-MS. *Food Chemistry*, 245, 761–767.

Pangestuti, R., Siahaan, E.A. and Kim, S.-K. (2018). Photoprotective substances derived from marine algae. *Marine Drugs*, 16, 399.

Panusa, A., Petrucci, R., Lavecchia, R. and Zuorro, A. (2017). UHPLC-PDA-ESI-TOF/MS metabolic profiling and antioxidant capacity of arabica and robusta coffee silverskin: Antioxidants vs phytotoxins. *Food Research International*, 99, 155–165.

Pojero, F., Gervasi, F., Fiore, S.D., Aiello, A., Bonacci, S., Caldarella, R., Attanzio, A., Candore, G., Caruso, C., Ligotti, M.E., Procopio, A., Restivo, I., Tesoriere, L., Allegra, M. and Accardi, G. (2023). Anti-inflammatory effects of nutritionally relevant concentrations of oleuropein and hydroxytyrosol on peripheral blood mononuclear cells: An age-related analysis. *International Journal of Molecular Sciences*, 24, 11029.

Restivo, I., Attanzio, A., Tesoriere, L., Allegra, M., Garcia-Llatas, G. and Cilla, A. (2022). Anti-eryptotic activity of food-derived phytochemicals and natural compounds. *International Journal of Molecular Sciences*, 23, 3019.

Rojas-González, A., Figueroa-Hernández, C.Y., González-Rios, O., Suárez-Quiroz, M.L., González-Amaro, R.M., Hernández-Estrada, Z.J. and Rayas-Duarte, P. (2022). Coffee chlorogenic acids incorporation for bioactivity enhancement of foods: A review. *Molecules*, 27, 3400.

Ryoo, H.D. (2024). The integrated stress response in metabolic adaptation. *Journal of Biological Chemistry*, 300, 107151.

Saleem, S. and Kannan, R.R. (2018). Zebrafish: An emerging real-time model system to study Alzheimer's disease and neurospecific drug discovery. *Cell Death Discovery*, 4, 45.

Sant, K.E. and Timme-Laragy, A.R. (2018). Zebrafish as a model for toxicological perturbation of yolk and nutrition in the early embryo. *Current Environmental Health Reports*, 5, 125–133.

Seo, M.D., Kang, T.J., Lee, C.H., Lee, A.Y. and Noh, M. (2012). HaCaT keratinocytes and primary epidermal keratinocytes have different transcriptional profiles of cornified envelope-associated genes to T helper cell cytokines. *Biomolecules & Therapeutics*, 20, 171–176.

Solano, F. (2020). Photoprotection and skin pigmentation: Melanin-related molecules and some other new agents obtained from natural sources. *Molecules*, 25, 1537.

Sumner, L.W., Amberg, A., Barrett, D. et al. (2007). Proposed minimum reporting standards for chemical analysis. *Metabolomics*, 3, 211–221.

Surma, S., Sahebkar, A. and Banach, M. (2023). Coffee or tea: Anti-inflammatory properties in the context of atherosclerotic cardiovascular disease prevention. *Pharmacological Research*, 187, 106596.

Valerio, H.P., Ravagnani, F.G., Ronsein, G.E. et al. (2021). A single dose of Ultraviolet-A induces proteome remodeling and senescence in primary human keratinocytes. *Scientific Reports*, 11, 23355.

Wang, W., Gao, X., Liu, L., Guo, S., Duan, J.A. and Xiao, P. (2025). Zebrafish as a vertebrate model for high-throughput drug toxicity screening: Mechanisms, novel techniques, and future perspectives. *Journal of Pharmaceutical Analysis*, 15, 101195.

Wang, Y., Hao, M.-M., Sun, Y., Wang, L.-F., Wang, H., Zhang, Y.-J., Li, H.-Y., Zhuang, P.-W. and Yang, Z. (2018). Synergistic promotion on tyrosinase inhibition by antioxidants. *Molecules*, 23, 106.

Widelski, J., Gaweł-Bęben, K., Czech, K., Paluch, E., Bortkiewicz, O., Kozachok, S., Mroczek, T. and Okińczyc, P. (2023). Extracts from European propolises as potent tyrosinase inhibitors. *Molecules*, 28, 55.

Wiernicki, B., Dubois, H., Tyurina, Y.Y. et al. (2020). Excessive phospholipid peroxidation distinguishes ferroptosis from other cell death modes including pyroptosis. *Cell Death & Disease*, 11, 922.

Yashin, A., Yashin, Y., Wang, J.Y. and Nemzer, B. (2013). Antioxidant and antiradical activity of coffee. *Antioxidants*, 2, 230–245.

Yi, P., Huang, Y., Zhao, X., Qin, Z., Zhu, D., Liu, L., Zheng, Y., Feng, J. and Long, M. (2023). A novel UVA-associated circUBE2I mediates ferroptosis in HaCaT cells. *Photochemistry and Photobiology*, 99, 1485–1496.

Yosboonruang, A., Ontawong, A., Thapmamang, J. and Duangjai, A. (2022). Antibacterial activity of Coffea robusta leaf extract against foodborne pathogens. *Journal of Microbiology and Biotechnology*, 32, 1003–1010.

Yu, Y., Yan, Y., Niu, F., Wang, Y., Chen, X., Su, G., Liu, Y., Zhao, X., Qian, L., Liu, P. and Xiong, Y. (2021). Ferroptosis: A cell death connecting oxidative stress, inflammation and cardiovascular diseases. *Cell Death Discovery*, 7, 193.

Yulianti, Y., Adawiyah, D.R., Herawati, D., Indrasti, D. and Andarwulan, N. (2023). Detection of markers in green beans and roasted beans of Kalosi-Enrekang Arabica coffee with different postharvest processing using LC-MS/MS. *Journal of Food Quality*, 2023, 6696808.

Zolghadri, S., Bahrami, A., Hassan Khan, M.T., Munoz-Munoz, J., Garcia-Molina, F., Garcia-Canovas, F. and Saboury, A.A. (2019). A comprehensive review on tyrosinase inhibitors. *Journal of Enzyme Inhibition and Medicinal Chemistry*, 34, 279–309.

6. Chapter VI: Conclusions

This PhD project was developed within the framework of Mediterranean biodiversity valorisation, with the primary objective of identifying and mechanistically validating bioactive phytocomplexes derived from agri-food matrices traditionally underexplored.

The overarching aim was to establish experimental platforms capable of linking phytochemical complexity to specific biochemical pathways involved in chronic disorders characterized by oxidative stress, metabolic imbalance, and cellular stress responses.

The integrated strategy combined analytical characterization with validation in disease-relevant *in vitro* and *in vivo* models, allowing a mechanistic interpretation of the biological effects exerted by the studied matrices.

The phytochemical profiling revealed chemically complex extracts rich in polyphenols, lipophilic components, and redox-active molecules, supporting the concept that biodiversity-derived phytocomplexes act through multi-target modulation rather than single-molecule mechanisms.

In oncological models, *Lycium barbarum* extract demonstrated context-dependent redox modulation, promoting pro-oxidant and pyroptosis-related mechanisms selectively in tumorigenic cells while preserving physiological redox balance in non-tumorigenic cells.

In the MAFLD model, olive and Cipollotto Nocerino leaves extracts reduced lipid accumulation and oxidative stress in steatotic HepG2 cells, with evidence supporting the involvement of SIRT1 signaling, ER stress modulation, and lipid metabolism regulation.

In the UVA-induced skin damage model, coffee silverskin extracts exerted photoprotective effects associated with Nrf2 activation, unfolded protein response modulation, lipid peroxidation control, and ferroptosis pathway regulation.

Collectively, these findings demonstrate that biodiversity-derived phytocomplexes can modulate key biochemical nodes, including redox regulation, ER stress, lipid metabolism, pyroptosis, and ferroptosis, across different pathological contexts. Importantly, this work establishes reproducible and mechanistically grounded experimental models suitable for the evaluation of nutraceutical candidates in chronic disorder settings.

However, this thesis represents only the first step of a broader research trajectory. While the present work focused on whole extracts and phytocomplexes, future objectives include systematic fractionation of the investigated matrices in order to reduce chemical complexity and isolate sub-fractions with enriched biological activity. Then, dentification and structural characterization of the most active molecules responsible for the observed biochemical effects, and validation of these bioactive fractions and isolated compounds in advanced *in vivo* models to confirm efficacy, safety, and pathway specificity.

The transition from complex extract evaluation to molecular resolution and *in vivo* validation will be essential to translate biodiversity research into rational nutraceutical development.

In this perspective, the current work provides the mechanistic and methodological foundation upon which future fractionation, molecular targeting, and translational studies can be built.

Ultimately, the valorisation of Mediterranean biodiversity should not be limited to descriptive phytochemistry but should evolve toward pathway-oriented and model-driven approaches capable of bridging natural product research with chronic disease prevention and management strategies.